Flow-Mediated Interaction Between a Vibrating and an Elastically-Mounted Cylinder

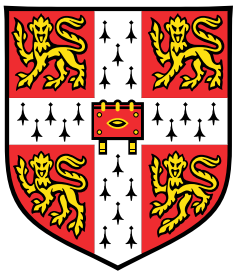

Zhonglu Lin

Department of Engineering
University of Cambridge

This dissertation is submitted for the degree of
Doctor of Philosophy

Jesus College September 2019

I would like to dedicate this thesis to my loving parents.

Declaration

I hereby declare that except where specific reference is made to the work of others, the contents of this dissertation are original and have not been submitted in whole or in part for consideration for any other degree or qualification in this, or any other university. This dissertation is my own work and contains nothing which is the outcome of work done in collaboration with others, except as specified in the text and Acknowledgements. This dissertation contains fewer than 65,000 words including appendices, bibliography, footnotes, tables and equations and has fewer than 150 figures.

This thesis includes the content already published in 3 journal papers and 3 conference papers, where the I am the first author and the major contributor. The included publications are listed below:

Journal papers

Lin, Z., Liang, D. & Zhao, M. Effects of Reynolds Number on Flow Mediated Interaction Between Two Cylinders. *J. Eng. Mech. - ASCE* (2019). (Accepted) doi:10.17863/CAM.38404

Lin, Z., Liang, D. & Zhao, M. Flow-mediated interaction between a vibrating cylinder and an elastically-mounted cylinder. *Ocean Eng.* (2018). doi:10.1016/j.oceaneng.2018.04.019

Lin, Z., Liang, D. & Zhao, M. Effects of Damping on Flow-Mediated Interaction Between Two Cylinders. *J. Fluids Eng. - ASME* (2018). doi:10.1115/1.4039712

Conference proceedings

Lin, Z., Liang. D. & Zhao, M. Numerical simulation of fluid coupling between two elastic support cylinders. In Proceedings of the *29th China National Hydrodynamics Symposium* (Volume 1) (2018).

Lin, Z., Liang, D. & Zhao, M. Interaction Between Two Vibrating Cylinders Immersed in Fluid. in *The 27th International Ocean and Polar Engineering Conference* (International Society of Offshore and Polar Engineers, 2017).

Lin, Z., Liang, D. & Zhao, M. Numerical Study of the Interaction between Two Immersed Cylinders. in *The 12th International Conference on Hydrodynamics* (2016).

Zhonglu Lin
September 2019

Acknowledgements

I would like to thank my supervisor, Dr. Dongfang Liang, for his academic support on my research. My PhD study could not be successful without his support.

I would like to express my sincere gratitude to Prof. Ming Zhao from Western Sydney University for his support over my works.

I would like to thank my advisor, Dr. Fehmi Cirak, for his critical review over my PhD works.

I would like to thank all my friends who supported me during this once seemingly unending journey of PhD study. I cannot go this far without your help.

The study was primarily funded by Fuzhou Nuocheng Construction Project Management Ltd. This work has been performed using resources provided by the Cambridge Tier-2 system operated by the University of Cambridge Research Computing Service (http://www.hpc.cam.ac.uk) funded by Engineering and Physical Sciences Research Council (EPSRC) Tier-2 capital grant (EP/P020259/1). The computing at Cirrus is funded by EPSRC Tier-2 Open Access Call. This study used the ARCHER UK National Supercomputing Service (http://www.archer.ac.uk). This study used the Cambridge Service for Data Driven Discovery (https://www.hpc.cam.ac.uk) hosted by the Research Computing Services at the University of Cambridge. I am very grateful for the technical support from the team at the University of Cambridge's Research Computing Services.

Thanks are due to my beloved parents. I thank them dearly for their support and encouragement for my pursuit of PhD.

Abstract

This study investigates the interaction between two cylinders of an identical diameter immersed in still fluid: the active cylinder is subject to forced vibration, while the adjacent passive cylinder is elastically-mounted with a damper and has only one-degree-of-freedom along the centreline of the two cylinders. The hydrodynamic interaction is simulated with an extensively-validated 2D Navier-Stokes solver that is based on the finite element method and the Arbitrary Lagrangian-Eulerian method. In total, 23,400 simulation cases are conducted for a range of combinations of parameters. The active cylinder's oscillation frequency f_1/f_n ranges from 0.05 to 3.2; the amplitude of the active cylinder A_1/D varies from 0.025 to 1.432; the mass ratio of the passive cylinder m^* takes the value of 1.5, 1.7, 2.0, 2.2 or 2.5; the structural damping factor of the passive cylinder ranging from 0 to 1.4; the Reynolds number Re_m varies from 10 to 315; the gap ratio G/D ranges from 0.2 to 3. This parametric space is chosen to reflect the values usually seen in engineering applications. With considered ranges of parameters, the solid-solid contact does not occur. The flows corresponding to regimes A, A*, C, E, F and G as classified by Tatsuno and Bearman (1990) are investigated. In all these regimes, harmonic frequency components in the response of the passive cylinder are found to persist in all regimes, causing the major and minor resonance. Even though the flow instability in regimes E, F, G causes the significant irregular frequency components to appear in low frequency. In the periodic regimes, the vibration centre of the passive cylinder can be attracted or repelled away from the active cylinder by varying the Reynolds number. The phase difference between the active cylinder and the passive cylinder's fundamental frequency component experiences a 180° shift with the increase of the active cylinder's oscillation frequency. All 6 non-dimensional parameters influence the the behaviour of the passive cylinder in different ways and will be discussed in detail in this thesis. Flow patterns in the current two-cylinder case are at large similar to the single-cylinder case, although at regime C, the flow pattern is fundamentally different due to a pulse beating passive cylinder. Overall the existence of the passive cylinder adds irregularity to the flow.

Table of contents

List of figures **xiii**

List of tables **xxvii**

Nomenclature **xxix**

1 Introduction **1**

1.1 Literature Review 1

1.1.1 Single Cylinder Oscillating in Still Fluid 3

1.1.2 A Oscillating Cylinder Actuating a Free Cylinder in Still Fluid . . . 5

1.2 Aims and Objectives 9

1.3 Outline of Thesis 9

2 Methodology **11**

2.1 Problem Setup and Dimensional Analysis 11

2.2 Computational Method 14

2.2.1 Governing Equations 14

2.2.2 Streamline Upwind Petrov-Galerkin FEM 15

2.2.3 Arbitrary Lagrangian-Eulerian Method 18

2.3 Mesh Independence Study 19

2.4 Validation 26

2.5 Data Processing Techniques 28

2.6 Chapter Summary 30

3 Effects of Parameters Associated With the Active Cylinder in Periodic Regimes 31

3.1 Resonance of Passive Cylinder 31

3.2 Phase Lag Shift from Anti-phase to In-phase 36

3.3 Effects on Flow Field 36

3.4 Chapter Summary 43

4 Effects of Parameters Associated With the Passive Cylinder in Periodic Regimes 45
4.1 Structural Damping Ratio 45
4.1.1 Approximating the Passive Cylinder's Motion to be Harmonic in the Context of Varied Structural Damping 46
4.1.2 Effects of Structural Damping on the Vibration of the Passive Cylinder 48
4.1.3 Force Acting on the Passive Cylinder 52
4.1.4 Effect of Structural Damping on Flow Field 55
4.2 Mass Ratio of the Passive Cylinder 59
4.3 Chapter Summary 61

5 Effects of Intermediate Fluid and Gap in Periodic Regimes 65
5.1 Reynolds Number 65
5.1.1 Effects of Reynolds Number on the Passive Cylinder's Vibration Centre Drift 66
5.1.2 Effects of Reynolds Number on Passive Cylinder's Vibration Amplitude 70
5.2 Flow Fields Around the Two Cylinders 72
5.3 Gap Distance 87
5.4 Chapter Summary 90

6 Effects of Active Cylinder's Amplitude and Frequency in Less Regular Regimes 93
6.1 Overview of *KC* Effects 93
6.2 Regime C 99
6.3 Regime E 108
6.4 Regime F 115
6.5 Regime G 121
6.6 Chapter Summary 126

7 Conclusions 127
7.1 Overview 127
7.2 Parametric Study in Periodic Regimes A and A* 128
7.3 Interactions in Less Regular Regimes C, E, F and G 128
7.4 Future Work 129

References 131

Appendix A Data Processing Scripts 137
A.1 Generation of Time History and Amplitude Spectra 137
A.2 Mesh Generation by Gmsh 142

List of figures

1.1 An offshore oil drilling platform with multiple cylindrical structures (Credit: Chesroc Nigeria Limited) 2

1.2 (a) Classical Huygens' pendulum clocks setup (Huygens, 1660) (b) Idealised model by Peña Ramirez et al. (2014). 2

1.3 Flow regimes classified by Tatsuno and Bearman (1990). In this thesis, the values of KC and β lies well within regimes A and A^*, and the flow characteristics in all the simulations do coincide with the regimes A and A^*: two symmetric vortices shed per half cycle. 4

1.4 Simulated flow patterns represented by streaklines in different flow regimes for oscillatory flow past a single cylinder, conducted under the same condition as the experiments carried out by Tatsuno and Bearman (1990). It was simulated by Zhao and Cheng (2014) using the code of current study. (a) Regime A* at $KC = 3.14$ and $\beta = 52.8$ (b) Regime A at $KC = 11$ and $\beta = 7.4$ (c) Regime D at $KC = 6.28$, and $\beta = 18$ (upper) and $\beta = 22.1$ (lower) (d) Regime E at $KC = 6.28$ and $\beta = 25.6$ in the 72nd period (left) and 200th period (right). (e) Regime F at $KC = 8.16, \beta = 27$ (upper), $KC = 12.6, \beta = 17.8$ (lower). (a-e) The oscillation direction is horizontal in all the sub-figures. 6

1.5 (a) The setup sketch of Case B (Gazzola et al., 2012). The active cylinder is forced to oscillated harmonically along the centreline of two cylinders, whereas the passive cylinder is free. This is different from the present study, where the passive cylinder is attached to a spring. (b) Threshold Reynolds number illustrated as a function of d/D_m and D_s/D_m (Gazzola et al., 2012). 7

1.6 In inviscid fluid, time history of the passive cylinder's normalised displacement from its initial position $\Delta x/D_m$ at initial phase of the active cylinder vibration at (a) 0° and (b) 180°, as demonstrated by Nair and Kanso (2007). (c)In viscous fluid, time history of slave's normalised displacement from its initial position $\Delta x/D_m$ at initial phase of the active cylinder vibration at 0° (solid line) and 180° (dashed line), as illustrated by Gazzola et al. (2012). The initial condition of the active cylinder can affect the drifting direction of the passive cylinder in inviscid fluid, but not in viscous fluid. 8

2.1 A sketch of interaction between the two cylinders: While the active cylinder undergoes harmonic forced vibration along the centreline of the two identical rigid cylinders, the passive cylinder is elastically mounted with a damper, vibrating in response to the active cylinder with 1DOF along the centreline as well. 12

2.2 Computational meshes for interaction between two cylinders with $G/D = 0.2$ and $\Delta r \leq 1.38 \times 10^{-3}$ and $N_c \geq 152$. 20

2.3 Effect of Δr on the responding amplitude A_2 with $N_c = 116$ and Effect of N_c on the responding amplitude A_2 with $\Delta r = 1.25 \times 10^{-3}$, for the case $G/D = 0.2, A_1/D = 0.1, f_1/f_n = 0.825, m^* = 2.5$. 21

2.4 Comparison of the passive cylinder's displacement time histories from different meshes for $G/D = 0.9, A_1/D = 0.477, m^* = 1.5, \zeta = 0$ and (a) $Re_m = 10, f_1/f_n = 3.2$, where the passive cylinder drifts towards the near side (b) $Re_m = 150, f_1/f_n = 3.2$, where the passive cylinder drifts towards the far side (c) $Re_m = 150, f_1/f_n = 0.725$, where the vibration amplitude is large due to the resonance. 23

2.5 Computational meshes for interaction between two cylinders with $G/D = 0.9$ with $\Delta r \leq 1.30 \times 10^{-3}$ and $N_c \geq 152$. 24

2.6 Vorticity contours of the mesh independence case at $KC = 9, G/D = 2.5, A_1/D = 1.432, f_1/f_n = 2.8, m^* = 2, \zeta = 0, Re_m = 315$. (a-d) Coarse mesh (e-h) Normal mesh (i-l) Dense mesh. 25

2.7 Comparison of fluid velocity distribution between the numerical simulation results and the experimental data by Dütsch et al. (1998). The horizontal & vertical velocity components (u & v) of the simulation results (continuous lines) and measured data (discrete symbols) are compared along four horizontal lines (i.e. $y/D = 0.6, 0, -0.6$ and -1.2) at three different phases (i.e. $\phi = 180^\circ, 210^\circ$ and 330°). 27

2.8 Computational meshes for validation case of a single cylinder vibrating in an otherwise still fluid with $N_c = 134$ and $\Delta r = 1.83 \times 10^{-3}$. 28
2.9 (a) Threshold Reynolds numbers as function of the normalised centre-to-centre distance d/D, where $m^* = 1, A_1/D = 1$, and the active and the passive cylinders have identical diameters. The present simulation output agree well with the results from Gazzola et al. (2012). (b) Passive cylinder's non-dimensional displacement Y_2/D versus the time normalized by the active cylinder vibration frequency tf_1, for a series of Reynolds numbers (from top to bottom curves $Re_m = 100, 60, 50, 40, 30, 27, 25, 20, 19, 18, 15, 10$), with $A_1/D = 1, d/D = 3.5$. Here, the threshold Reynolds number is 20. 29

3.1 Convergence time history for a case in periodic regime A/A^*. After a few initial steps, the vibration amplitude of the passive cylinder converges. . . . 32
3.2 Variation in A_2/A_1 with f_1/f_n at $G/D = 0.4, A_1/D = 0.025 - 0.1, m^* = 1.5$, and (a) undamped $\zeta = 0$ (b)damped $\zeta = 0.2$. A_2 and A_1 are linearly correlated unless when the resonance occurs or the damping ratio $\zeta >= 0.2$. 33
3.3 Amplitude spectra showing the response of the passive cylinder with various f_1/f_n at $G/D = 0.4,\ A_1/D = 0.075,\ m^* = 1.5$. (a) FFT spectra at $f_1 = f_w/3 \approx 0.25$ (b) FFT spectra at $f_1 = f_w/2 \approx 0.375$ (c) FFT spectra at $f_1 = f_w \approx 0.75$ (d) An overview of FFT spectra. It can be seen that, at $f_1 = f_w/2$, there are two distinct frequencies while at $f_1 = f_w$ there is only one. The red dashed thin line tracks the dominant frequencies. The red dashed thick squares highlight the resonating frequency component. 34
3.4 Amplitude spectra showing (a) responding displacement of the passive cylinder and (b) force coefficient upon the passive cylinder at $0.95 \leq f_1/f_n \leq 1.1,\ G/D = 0.4,\ A_1/D = 0.075,\ m^* = 1.5,\ \zeta = 0,\ Re_m = 100$. The dominant frequencies for displacement and force are different. 35
3.5 Variation of the oscillation phase difference $\Delta\phi_{21}$ between the passive and the active cylinder (for the fundamental frequency components) with f_1/f_n at $A_1/D = 0.025 - 0.100, m^* = 1.5, G/D = 0.4, Re_m = 100$ and (a) $\zeta = 0$ (b) $\zeta = 0.2$. The increase of the active cylinder oscillation frequency causes the phase difference to shift from anti-phase to in-phase at the immersed natural frequency. $\Delta\phi_{21}$ decreases with A_1/D. At $\zeta = 0, A_1/D$ affects more the phase difference at low frequencies compared with that at $\zeta = 0.2$. . . 36

3.6 Velocity vectors on the left of the passive cylinder at $G/D = 0.4, A_1/D = 0.075, m^* = 1.5, \zeta = 0, Re_m = 100$, and $\phi_1 = 45^\circ$ with (a) $f_1/f_n = 0.74$, $\Delta\phi_{21} = 90.7^\circ$ and (b) $f_1/f_n = 1.00$, $\Delta\phi_{21} = 0.58^\circ$. The vortex is always attached to the surface of the cylinders on their two sides, but it is dissipated before they can detach from the surface. $\Delta\phi_{21}$ is found to have significant influence on the flow field. The velocity vector is drawn on every grid point and the vector scale factors are (a) 0.06 grid units/magnitude and (b) 0.6 grid units/magnitude. 37

3.7 Velocity vectors ($u_i^* = u_i/f_n D$) at $f_1/f_n = 1.00$, $\phi_1 = 0^\circ$. A pair of small vortices show up in the wake of the passive cylinder when the passive cylinder reaches its highest or lowest position. These tiny vortices only exist for a short period of time in each cycle. The velocity vector is drawn on every grid point. The vector scale factor is 1.6 grid units/magnitude. 38

3.8 Velocity vectors at $f_1/f_n = 0.74$ and $\phi_1 = 135^\circ$ with $G/D = 0.4, A_1/D = 0.075, m^* = 1.5, \zeta = 0, Re_m = 100$. At exactly $90^\circ < \phi_1 < 180^\circ$, the zero-velocity point travels from the bottom of the passive cylinder (at $\phi_1 = 90^\circ$) to the top of the active cylinder (at $\phi_1 = 180^\circ$). The velocity vector is drawn on every grid point. 38

3.9 Non-dimensional pressure p^* contours at $\phi_1 =$ (a & e & i) 0°, (b & f & j) 90°, (c & g & k) 180°, (d & h & l) 270°. (a-d) $f_1/f_n = 0.55$, $\Delta\phi_{21} = 168.71^\circ$; (e-h) $f_1/f_n = 0.74$, $\Delta\phi_{21} = 90.673^\circ$; (i-l) $f_1/f_n = 1.0$, $\Delta\phi_{21} = 0.582^\circ$ with $G/D = 0.4, A_1/D = 0.075, m^* = 1.5, \zeta = 0, Re_m = 100$. The motion of the passive cylinder is found to have great influence on the distribution of pressure. Streamlines are plotted to show the status of the fluid. 39

4.1 (a) Variation in magnification factor of the passive cylinder $A_2/(F_0/k)$ with f_1/f_n, and (b) variation in force-displacement phase difference for the passive cylinder (for frequency components with $f/f_n = f_1/f_n$) with f_1/f_n at $G/D = 0.2$, $A_1/D = 0.1$, $m^* = 2.0$, and $\zeta = 0 - 1.4$. The red dashed line is the locus of maxima by assuming harmonic force input. 46

4.2 (a) Variation of A_2/A_1 and (b) variation of phase difference between the two cylinders $\Delta\phi_{21}$ with f_1/f_n (for the frequency components with $f/f_n = f_1/f_n$) with f_1/f_n at $G/D = 0.2$,$A_1/D = 0.1$, $m^* = 2.0$, and $\zeta = 0 - 1.4$. A_2/A_1 is negatively correlated with ζ, particularly within the regime of resonance. The phase difference curve converges at $\Delta\phi_{21} \approx 80^\circ, f_1/f_n \approx 0.775$. The increase in damping slows down the 180° phase shift of the passive cylinder as f_1/f_n reaches its immersed natural frequency. 49

4.3 Amplitude spectra showing the responding displacement of the passive cylinder with various f_1/f_n at $G/D = 0.2$, $A_1/D = 0.1$, and $m^* = 2.0$. (a) An overview of the FFT spectra (b) the FFT spectra at $f_1 = f_w/2 \approx 0.375$. The red dashed thin line tracks the dominant frequencies. It can be seen that, at $f_1 = f_w/2$, the high frequency component is always smaller than the fundamental component, whereas for the undamped cases, a high-frequency component becomes larger than the fundamental frequency, thus causing a minor peak of resonance. 51

4.4 (a) Zoom-in at peaks for variation of A_2/A_1 at $\zeta = 0.2$, and (b) zoom-in at peaks for variation of A_2/A_1 at $\zeta = 0.4$ for $G/D = 0.4$, $A_1/D = 0.025 - 0.1$, $m^* = 1.5$. A threshold damping ratio of the passive cylinder is discovered, beyond which its peak amplification factor decreases with the active cylinder vibration amplitude, and under which the peak increases with the amplitude. In this scenario, the threshold lies in $\zeta = 0.2 - 0.4$. . . . 52

4.5 (a–d) Non-dimensional pressure contours $p^* = p/\rho f_n^2 D^2$ at $G/D = 0.4, A_1/D = 0.075, m^* = 1.5, f_1/f_n = 0.74, \zeta = 0, Re_m = 100$, and $\Delta\phi_{21} = 90.673^\circ$. The dashed lines indicate negative values of non-dimensional pressure. The colour map shows corresponding colour for each value of non-dimensional pressure. The velocity vectors are plotted every 20 points. The vector scale factor is 0.3 grid units/magnitude. (e) The y-direction force coefficient upon the passive cylinder and its shear and pressure components were examined. Pressure rather than viscosity is the main contributor to the force acting on the passive cylinder. 53

4.6 Non-dimensional pressure contours $p^* = p/\rho f_n^2 D^2$ at $G/D = 0.2$; $A_1/D = 0.1$; $m^* = 1.5$; $f_1/f_n = 0.78$; and $\phi_1 = 0^\circ$ (a, e, and i), 90° (b, f, and j), 180° (c, g, and k) and 270° (d, h, and l). (a–d) $\zeta = 0$, $\Delta\phi_{21} = 46.6^\circ$; (e–h) $\zeta = 0.1$, $\Delta\phi_{21} = 50.0928^\circ$; (i–l) $\zeta = 0.8$, $\Delta\phi_{21} = 68.309^\circ$. The cylinder on the top is the passive passive cylinder. The cylinder on the bottom is the active active cylinder. The dashed lines indicate negative values of non-dimensional pressure. The color map shows corresponding color for each value of non-dimensional pressure. With the increase in damping, the main driver of the passive cylinder changes from the pressure fluctuation at the far side of the passive cylinder to that within the gap. The black sticks and the dots indicate the displacement of the cylinder in one cycle. 56

4.7 Velocity vectors on the left of the passive cylinder at $G/D = 0.2$, $A_1/D = 0.1$, $m^* = 1.5$, and $f_1/f_n = 0.75$, with (a) $\zeta = 0$, $\Delta\phi_{21} = 108.4°$; (b) $\zeta = 0.1$, $\Delta\phi_{21} = 95.62°$; (c) $\zeta = 0.8$, $\Delta\phi_{21} = 68.309°$ and (1) $\phi_1 = 90°$; (2) $\phi_1 = 180°$. The velocity vector is drawn on every grid point and the vector scale factors are 0.15 grid units/magnitude. The lifespan and the strength of vortices both decrease with damping. The black sticks and the dots indicate the displacement of the cylinder in one cycle. 57

4.8 Velocity vectors in the gap at $G/D = 0.2$, $A_1/D = 0.1$, $m^* = 1.5$, and $f_1/f_n = 0.75$, with (a) $\zeta = 0$, $\Delta\phi_{21} = 108.4°$; (b) $\zeta = 0.1$, $\Delta\phi_{21} = 95.62°$; and (1) $\phi_1 = 158°$; (2) $\phi_1 = 189°$. The velocity vector is drawn on every grid point and the vector scale factors are 0.011 grid units/magnitude. The zero-velocity point (see dashed circle in b1) travels from the bottom of the passive cylinder to the top of the active cylinder. For the damped case with $\zeta = 0.1$, the stagnant flow point appears earlier than the undamped case and has a longer lifespan. For both the damped and undamped cases, the stagnant flow point disappears at $\phi_1 = 189°$. The black sticks and the dots indicate the displacement of the cylinder in one cycle. 58

4.9 Variation of A_2/A_1 with f_1/f_n and m^* at $G/D = 0.2, A_1/D = 0.1, Re_m = 100, \zeta = 0$. m^* affects the resonance frequency. The red dashed rectangle highlights the convergence point. 60

4.10 Variation of the oscillation phase difference between the two cylinders with f_1/f_n at $A_1/D = 0.1, m^* = 1.5-2.5, G/D = 0.2, Re_m = 100, \zeta = 0$ the phase change occurs. G/D does not affect much the phase difference 61

4.11 (a) Variation in A_2/A_1 with f_1/f_n, and (b) variation in displacement phase difference $\Delta\phi_{21}$ between the passive cylinder and the active cylinder (for the frequency components with $f/f_n = f_1/f_n$) with f_1/f_n at $G/D = 0.2, A_1/D = 0.1, m^* = 1.5-2.5, Re_m = 100$ and $\zeta = 0-0.2$. The color and line type denote ζ, whereas the marker type denotes m^*. With a non-zero damping, the peak A_2/A_1 decreases with m^*. The curve of $\Delta\phi_{21}$ disperses at resonance, which follows the same pattern as the undamped cases. 62

5.1 Convergence time history for a case with $Re = 140$. After a few initial steps, the vibration amplitude and the centre drift of the passive cylinder converges to constant values. 66

5.2 (a) Variation in vibration centre drift $\Delta\overline{Y}_2$ with f_1/f_n at $G/D = 0.9, A_1/D = 0.477, m^* = 1.5, \zeta = 0$ and $Re_m = 10-150$. (b) Zoom-in at the secondary and the primary resonance regime (c) Further zoom-in at the primary resonance regime (d) Variation in vibration centre drift $\Delta\overline{Y}_2$ with Re_m at $G/D = 0.9, A_1/D = 0.477, m^* = 1.5, \zeta = 0$ and $f_1/f_n = 1-3.2$. 67

5.3 (a) Variation in $\Delta\overline{Y}_2/A_1$ with f_1/f_n and (b) Zoom-in for its resonance regime at $G/D = 0.9, A_1/D = 0.477, m^* = 1.5, Re_m = 10, 70$ and $\zeta = 0-0.2$. The marker type denotes ζ, whereas the line type denotes Re_m. 68

5.4 (a) Variation in $\Delta\overline{Y}_2/A_1$ with f_1/f_n and (b) Zoom-in for its resonance regime at $G/D = 0.9, A_1/D = 0.477, \zeta = 0.2, Re_m = 10, 70$ and $m^* = 1.5-2.5$. The marker type denotes m^*, whereas the line type denotes Re_m. 69

5.5 Amplitude spectra showing the responding displacement of the passive cylinder with $f_1/f_n = 0.05-3.2$ at $G/D = 0.9, A_1/D = 0.477, m^* = 1.5, \zeta = 0$ with (a) $Re_m = 10$ (b) $Re_m = 30$ (c) $Re_m = 50$ (d) $Re_m = 110$. The dashed thin line tracks the dominant frequencies. 71

5.6 (a) Variation of passive cylinder's amplification factor A_2/A_1 with active cylinder's oscillation frequency f_1/f_n at $G/D = 0.9, A_1/D = 0.477, m^* = 2.0, Re_m = 10-110$ and $\zeta = 0-0.2$. (b) Zoom-in at resonance regimes. The marker type denotes damping factor ζ, whereas the line type denotes the Reynolds number Re_m. 71

5.7 (a) Variation of amplification factor A_2/A_1 with active cylinder's oscillation frequency f_1/f_n (b) Zoom-in at primary and secondary resonance regimes and (c) Variation of phase difference between the two cylinders $\Delta\phi_{21}$ with f_1/f_n (for the frequency components with $f/f_n = f_1/f_n$) with f_1/f_n at $G/D = 0.9$, $A_1/D = 0.477$, $m^* = 1.5, \zeta = 0, Re_m = 10-150$, i.e. $KC = 3, \beta = 3.3-50$. A_2/A_1 is positively correlated with Re_m, particularly within the regime of resonance, and the resonance frequency increases with Re_m. The resonance amplitude at $Re_m = 150$ is as large as 1.6 times of that at $Re_m = 10$. The phase difference is shifted towards the positive side with the increase of Re_m. 73

5.8 (a) Variation of passive cylinder's amplification factor A_2/A_1 with active cylinder's oscillation frequency f_1/f_n at $G/D = 0.9, A_1/D = 0.477, \zeta = 0, m^* = 1.5-2.5, Re_m = 10-110$ and (b) Zoom-in at resonance regimes. The marker type denotes mass ratio m^*, whereas the line type denotes the Reynolds number Re_m. 74

5.9 Contours of pressure coefficient C_p and velocity vectors (1) in the gap at $\phi_1 = 180^\circ$ and (2) in the far side of the active cylinder at $\phi_1 = 0^\circ$, given $G/D = 0.9, A_1/D = 0.477, m^* = 1.5, f_1/f_n = 2.8$, with (a) $Re_m = 10$, $\Delta\phi_{21} = -30.6^\circ$; (b) $Re_m = 50$, $\Delta\phi_{21} = -16.8^\circ$; (c) $Re_m = 110$, $\Delta\phi_{21} = -12.22^\circ$. The velocity vector is drawn on every two grid points and the vector scale factors are 0.1 grid units/magnitude. 75

5.10 Pressure coefficient contours and velocity vectors in the gap at $G/D = 0.9, A_1/D = 0.477, m^* = 1.5, \zeta = 0$, and $\phi_1 = 180^\circ$ with (a) $Re_m = 10, f_1/f_n = 0.65, \Delta\phi_{21} = 27.05^\circ$, (b) $Re_m = 50, f_1/f_n = 0.7, \Delta\phi_{21} = 64.66^\circ$, (c) $Re_m = 110, f_1/f_n = 0.72, \Delta\phi_{21} = 71.42^\circ$, The velocity vector is drawn on every two grid points and the vector scale factors are 0.1 grid units/magnitude. 76

5.11 Pressure coefficient contours and streamlines at $G/D = 0.9, A_1/D = 0.477, m^* = 1.5, \zeta = 0$, and (1) $Re_m = 10, f_1/f_n = 2.8, \Delta\phi_{21} = -30.64^\circ$, (2) $Re_m = 50, f_1/f_n = 2.8, \Delta\phi_{21} = -16.77^\circ$, (3) $Re_m = 110, f_1/f_n = 2.8, \Delta\phi_{21} = -12.22^\circ$, (a) $\phi_1 = 0^\circ$ (b) $\phi_1 = 90^\circ$ (c) $\phi_1 = 180^\circ$ (d) $\phi_1 = 270^\circ$. The numbers [1-4] identify the case with different *Re*, whereas the alphabets [a-d] indicate the instances in one cycle of the active cylinder oscillation. The dots on the sticks indicate the position of the cylinders in one cycle of motion. 78

5.12 Evolution of non-dimensional vorticity contours at $G/D = 0.9, A_1/D = 0.477, m^* = 1.5, \zeta = 0, f_1/f_n = 3.2$, and (1) $Re_m = 10$, (2) $Re_m = 150$, (a) $\phi_1 = 0^\circ$ (b) $\phi_1 = 90^\circ$ (c) $\phi_1 = 180^\circ$ (d) $\phi_1 = 270^\circ$. The numbers [1-2] identify the case with different *Re*, whereas the alphabets [a-d] indicate the instances in one cycle of the active cylinder oscillation. 79

5.13 Streamlines and non-dimensional vorticity contours at $G/D = 0.9, A_1/D = 0.477, m^* = 1.5, \zeta = 0, f_1/f_n = 3.2, \phi_1 = 180^\circ$, and (a) $Re_m = 10$, (b) $Re_m = 150$. 80

5.14 Time histories of hydraulic force acting on the passive cylinder at primary or secondary resonance with $G/D = 0.9, A_1/D = 0.477, m^* = 2$, and (a) $\zeta = 0$, $Re_m = 10$, $f_1/f_n = 0.7$ (b) $\zeta = 0$, $Re_m = 50$, $f_1/f_n = 0.745$ (c) $\zeta = 0$, $Re_m = 110$, $f_1/f_n = 0.765$ (d) $\zeta = 0.2$, $Re_m = 10$, $f_1/f_n = 0.73$ (e) $\zeta = 0.2$, $Re_m = 50$, $f_1/f_n = 0.775$ (f) $\zeta = 0.2$, $Re_m = 110$, $f_1/f_n = 0.795$ (g) $\zeta = 0$, $Re_m = 10$, $f_1/f_n = 0.39$ (h) $\zeta = 0$, $Re_m = 50$, $f_1/f_n = 0.39$ (i) $\zeta = 0$, $Re_m = 110$, $f_1/f_n = 0.39$ (j) $\zeta = 0.2$, $Re_m = 10$, $f_1/f_n = 0.39$ (k) $\zeta = 0.2$, $Re_m = 50$, $f_1/f_n = 0.39$ (l) $\zeta = 0.2$, $Re_m = 110$, $f_1/f_n = 0.39$. . . 82

5.15 Pressure coefficient contours and velocity vectors at $G/D = 0.9, A_1/D = 0.477, m^* = 2, \zeta = 0$ and (1) $Re_m = 10, f_1/f_n = 0.7$, (2) $Re_m = 50, f_1/f_n = 0.745$, (3) $Re_m = 110, f_1/f_n = 0.765$, (a) $\phi_1 = 0^\circ$ (b) $\phi_1 = 90^\circ$ (c) $\phi_1 = 180^\circ$ (d) $\phi_1 = 270^\circ$. Primary resonance occurs at around $f_1/f_n = 0.75$ and the damping factor is zero. 83

5.16 Pressure coefficient contours and velocity vectors at $G/D = 0.9, A_1/D = 0.477, m^* = 2, \zeta = 0.2$ and (1) $Re_m = 10, f_1/f_n = 0.73$, (2) $Re_m = 50, f_1/f_n = 0.775$, (3) $Re_m = 110, f_1/f_n = 0.795$, (a) $\phi_1 = 0^\circ$ (b) $\phi_1 = 90^\circ$ (c) $\phi_1 = 180^\circ$ (d) $\phi_1 = 270^\circ$. Primary resonance occurs at around $f_1/f_n = 0.75$ and the damping factor is relatively high at $\zeta = 0.2$. 84

5.17 Pressure coefficient contours and velocity vectors at $G/D = 0.9, A_1/D = 0.477, m^* = 2, \zeta = 0, f_1/f_n = 0.39$ and (1) $Re_m = 10$, (2) $Re_m = 50$, (3) $Re_m = 110$, (a) $\phi_1 = 0^\circ$ (b) $\phi_1 = 90^\circ$ (c) $\phi_1 = 180^\circ$ (d) $\phi_1 = 270^\circ$. Secondary resonance occurs at $f_1/f_n = 0.39$ and the damping factor is zero. 85

5.18 Pressure coefficient contours and velocity vectors at $G/D = 0.9, A_1/D = 0.477, m^* = 2, \zeta = 0.2, f_1/f_n = 0.39$ and (1) $Re_m = 10$, (2) $Re_m = 50$, (3) $Re_m = 110$, (a) $\phi_1 = 0^\circ$ (b) $\phi_1 = 90^\circ$ (c) $\phi_1 = 180^\circ$ (d) $\phi_1 = 270^\circ$. Secondary resonance occurs at $f_1/f_n = 0.39$ and the damping factor is relatively high at $\zeta = 0.2$. 86

5.19 Variation of A_2/A_1 with f_1/f_n and G/D at $m^* = 2.5, A_1/D = 0.05, Re_m = 100, \zeta = 0$. A_2/D decreases with G/D. 88

5.20 Variation of the oscillation phase difference between the two cylinders with f_1/f_n at $A_1/D = 0.05, m^* = 2.5, G/D = 0.2 - 1.0, Re_m = 100, \zeta = 0$. G/D does not affect much the phase difference. 88

5.21 (a) Variation of A_2/A_1 with f_1/f_n, and (b) variation of displacement phase difference $\Delta\phi_{21}$ between the passive cylinder and the active cylinder (for frequency components with $f/f_n = f_1/f_n$) with f_1/f_n at $G/D = 0.3 - 0.9, A_1/D = 0.05, m^* = 2.5$, and $\zeta = 0.2$. A_2/A_1 decreases with G/D, but the initial gap distance has little effect on $\Delta\phi_{21}$. This pattern is exactly the same as the undamped cases. 89

6.1 Typical time histories of passive cylinder's vibration for $G/D = 2.5, m^* = 2, \zeta = 0, \beta = 35, f_1/f_n = 2.8$, (a) $KC = 1, Re_m = 35, A_1/D = 0.159$, (b) $KC = 4, Re_m = 140, A_1/D = 0.637$, (c) $KC = 5, Re_m = 175, A_1/D = 0.796$, (d) $KC = 6, Re_m = 210, A_1/D = 0.955$, (e) $KC = 7, Re_m = 245, A_1/D = 1.114$, (f) $KC = 8, Re_m = 280, A_1/D = 1.273$ 94

6.2 Amplitude spectra for the displacement histories of the passive cylinder at $G/D = 2.5, m^* = 2, \zeta = 0, \beta = 35$, (a) $KC = 3$ in regime A, (b) $KC = 4$ in regime A, (c) $KC = 5$ in regime C, (d) $KC = 6$ in regime E, (e) $KC = 7$ in regime F, (f) $KC = 8$ in regime F 96

6.3 At structural damping $\zeta = 0$, (a) Variation of amplification factor A_2/A_1 for only the harmonic components with f_1/f_n (b) Zoom-in for resonance (c) Variation of oscillation phase difference between the two cylinders $\Delta\phi_{21}$ with f_1/f_n (for the frequency components with $f/f_n = f_1/f_n$) with f_1/f_n at $G/D = 3.0, A_1/D = 0.159 - 1.114, m^* = 2.0, \zeta = 0, Re_m = 35 - 245$ and $KC = 1 - 7, \beta = 35$. The amplitude of the harmonic components is extracted by filter out the low-frequency components by FFT. The data processing method is discussed in Section 2.5. 97

6.4 At structural damping $\zeta = 0.02$, (a)Overview and (b)Zoom-in for variation of amplification factor A_2/A_1 with f_1/f_n and KC. (c) Variation of oscillation phase difference between two cylinders $\Delta\phi_{21}$ (for the harmonic component with $f/f_n = f_1/f_n$) with f_1/f_n and KC at $G/D = 3.0, A_1/D = 0.159 - 1.114, m^* = 2.0, Re_m = 35 - 245$ and $KC = 1 - 7, \beta = 35$. 98

6.5 Displacement time history of the passive cylinder in regime C with $KC = 5, \beta = 35, G/D = 2.5, A_1/D = 0.796, m^* = 2, \zeta = 0, Re_m = 175$ with (a)$f_1/f_n = 0.05$, (b)$f_1/f_n = 0.35$, (c)$f_1/f_n = 0.77$, (d)$f_1/f_n = 0.82$, (e)$f_1/f_n = 1.0$, (f)$f_1/f_n = 1.2$, (g)$f_1/f_n = 1.4$, (h)$f_1/f_n = 1.8$, (i)$f_1/f_n = 2.0$, (j)$f_1/f_n = 2.4$, (k)$f_1/f_n = 2.8$, (l)$f_1/f_n = 3.2$. $KC = 5$ is a critical value that above which the irregularity of the displacement time history is significantly increased. With the increase of frequency ratio, the vibration of the passive cylinder gradually changes from a repetitive pattern to pulsed beating. . . . 100

6.6 Amplitude spectra of the passive cylinder's displacement In regime C with $KC = 5, \beta = 35, G/D = 2.5, A_1/D = 0.796, m^* = 2, \zeta = 0, Re_m = 175$ with (a)$f_1/f_n = 0.05$, (b)$f_1/f_n = 0.35$, (c)$f_1/f_n = 0.77$, (d)$f_1/f_n = 0.82$, (e)$f_1/f_n = 1.0$, (f)$f_1/f_n = 1.2$, (g)$f_1/f_n = 1.4$, (h)$f_1/f_n = 1.8$, (i)$f_1/f_n = 2.0$, (j)$f_1/f_n = 2.4$, (k)$f_1/f_n = 2.8$, (l)$f_1/f_n = 3.2$. 101

6.7 Vorticity contours In regime C with (a-d) $f_1/f_n = 0.05$, (e-h) $f_1/f_n = 0.77$, and (i-l) $f_1/f_n = 2.8$ with (a & e & i) $\phi = 0^\circ$ (b & f & j) $\phi = 90^\circ$ (c & g & k) $\phi = 180^\circ$ (d & h & l) $\phi = 270^\circ$ at $KC = 5, \beta = 35, G/D = 2.5, A_1/D = 0.796, m^* = 2, \zeta = 0, Re_m = 175$. 102

6.8 Non-dimensional Vorticity Contours in Regime C with $f_1/f_n = 0.05$ and $KC = 5, \beta = 35, G/D = 2.5, A_1/D = 0.796, m^* = 2, \zeta = 0, Re_m = 175$, corresponding to instants (a)A (b)B (c)C (d)D in Fig. 6.9. The shape of vorticity contours switch the direction of skewing for approximately every 10 periods. 104

6.9 (a)Displacement time history and (b) amplitude spectra of the passive cylinder in Regime C with $f_1/f_n = 0.05$ and $KC = 5, \beta = 35, G/D = 2.5, A_1/D = 0.796, m^* = 2, \zeta = 0, Re_m = 175$. The marked locations in (a) corresponds to the instants $a-d$ in Fig. 6.8. 105

6.10 Displacement time history of the passive cylinder in Regime C with $f_1/f_n = 3.2$ and $KC = 5, \beta = 35, G/D = 2.5, A_1/D = 0.796, m^* = 2, \zeta = 0, Re_m = 175$. The marked locations $A-F$ corresponds to the Figs. 6.11a-6.11f. . . . 106

6.11 Vorticity Contours for a typical cycle of beating in Regime C, corresponding to instants (a)A (b)B (c)C (d)D (e)E (f)F in Fig. 6.10 with $f_1/f_n = 3.2$ and $KC = 5, \beta = 35, G/D = 2.5, A_1/D = 0.796, m^* = 2, \zeta = 0, Re_m = 175$. The passive cylinder is pushed further away when the streaming direction is pointing at it. 107

6.12 Displacement time history of the passive cylinder in Regime E with $KC = 6, \beta = 35, G/D = 2.5, A_1/D = 0.955, m^* = 2, \zeta = 0, Re_m = 210$ with (a)$f_1/f_n = 0.05$, (b)$f_1/f_n = 0.35$, (c)$f_1/f_n = 0.77$, (d)$f_1/f_n = 0.82$, (e)$f_1/f_n = 1.0$, (f)$f_1/f_n = 1.2$, (g)$f_1/f_n = 1.4$, (h)$f_1/f_n = 1.8$, (i)$f_1/f_n = 2.0$, (j)$f_1/f_n = 2.4$, (k)$f_1/f_n = 2.8$, (l)$f_1/f_n = 3.2$. At $KC = 6$, the time histories become more irregular compared with $KC = 5$, especially at high frequency f_1/f_n. 109

6.13 Amplitude spectra of the passive cylinder's displacement in Regime E with $KC = 6, \beta = 35, G/D = 2.5, A_1/D = 0.955, m^* = 2, \zeta = 0, Re_m = 210$ with (a)$f_1/f_n = 0.05$, (b)$f_1/f_n = 0.35$, (c)$f_1/f_n = 0.77$, (d)$f_1/f_n = 0.82$, (e)$f_1/f_n = 1.0$, (f)$f_1/f_n = 1.2$, (g)$f_1/f_n = 1.4$, (h)$f_1/f_n = 1.8$, (i)$f_1/f_n = 2.0$, (j)$f_1/f_n = 2.4$, (k)$f_1/f_n = 2.8$, (l)$f_1/f_n = 3.2$. 110

6.14 Vorticity contours in Regime E with $f_1/f_n = 0.05$ at $KC = 6, \beta = 35, G/D = 2.5, A_1/D = 0.955, m^* = 2, \zeta = 0, Re_m = 210$. The flow pattern changes between one pattern and its mirror-image intermittently. With the increase of the f_1/f_n, the interaction remains steady for less cycles of the active cylinder oscillation and the passive cylinder's vibration becomes more irregular as well. 111

6.15 Vorticity contours in Regime E with (a-d) $f_1/f_n = 0.05$, (e-h) $f_1/f_n = 0.77$, and (i-l) $f_1/f_n = 3.2$ at $KC = 6, \beta = 35, G/D = 2.5, A_1/D = 0.955, m^* = 2, \zeta = 0, Re_m = 210$. Sub-figures in the same column are at the similar state of vortex shedding process. With the increase in f_1/f_n, the vortex shedding at the temporary steady state becomes more curved, and the streaming more circular. 113

6.16 Typical time histories of passive cylinder vibration for $G/D = 2.5, m^* = 2, \zeta = 0, \beta = 35$ (a)$KC = 5$ with $\zeta = 0$ and $\zeta = 0.02$, (b)$KC = 6$ with $\zeta = 0$ and $\zeta = 0.02$. In (a), we see that the time histories with $\zeta = 0$ and $\zeta = 0.02$ almost exactly overlap each other despite the difference of damping factor, whereas, in (b), we see that the minor difference of initial condition, i.e. damping factor, leads to dramatic deviation of time history after $tf_n = 18$, which is an indication of chaos. 114

6.17 Displacement time history of the passive cylinder in Regime F with $KC = 8, \beta = 35, G/D = 2.5, A_1/D = 1.273, m^* = 2, \zeta = 0, Re_m = 280$ with (a)$f_1/f_n = 0.05$, (b)$f_1/f_n = 0.35$, (c)$f_1/f_n = 0.77$, (d)$f_1/f_n = 0.82$, (e)$f_1/f_n = 1.0$, (f)$f_1/f_n = 1.2$, (g)$f_1/f_n = 1.4$, (h)$f_1/f_n = 1.8$, (i)$f_1/f_n = 2.0$, (j)$f_1/f_n = 2.4$, (k)$f_1/f_n = 2.8$, (l)$f_1/f_n = 3.2$. At $KC = 8$, irregularity is apparent even at very low frequency. 116

6.18 Amplitude spectra of the passive cylinder's displacement in Regime F with $KC = 8, \beta = 35, G/D = 2.5, A_1/D = 1.273, m^* = 2, \zeta = 0, Re_m = 280$ with (a)$f_1/f_n = 0.05$, (b)$f_1/f_n = 0.35$, (c)$f_1/f_n = 0.77$, (d)$f_1/f_n = 0.82$, (e)$f_1/f_n = 1.0$, (f)$f_1/f_n = 1.2$, (g)$f_1/f_n = 1.4$, (h)$f_1/f_n = 1.8$, (i)$f_1/f_n = 2.0$, (j)$f_1/f_n = 2.4$, (k)$f_1/f_n = 2.8$, (l)$f_1/f_n = 3.2$. At $KC = 8$, irregularity is apparent even at very low frequency. 117

6.19 Vorticity contours for a typical regime F flow with only one forced oscillating cylinder at $Re = 150$, $KC = 12$ and $\beta = 12.5$. (Zhao and Cheng, 2014). The flow oscillates on the horizontal direction. 118

6.20 Vorticity contours for vortex shedding patterns in Regime F with $f_1/f_n = 0.05, KC = 8, \beta = 35, G/D = 2.5, A_1/D = 1.273, m^* = 2, \zeta = 0, Re_m = 280$ (a-d) Pattern F1, one vortex pair shed from both sides convected upward and another pair shed from the left side convected downward (e-h) Pattern F2, one pair + one negative vortex shed upward and one pair shed downwards from the left side (i-l) Pattern F3, one pair shed upwards from the left side, and one pair + one negative vortex shed downward. The mirror-images of these patterns can also occur. 119

6.21 Displacement time history of the passive cylinder in Regime G with $KC = 9, \beta = 35, G/D = 2.5, A_1/D = 1.432, m^* = 2, \zeta = 0, Re_m = 315$ with (a)$f_1/f_n = 0.05$, (b)$f_1/f_n = 0.35$, (c)$f_1/f_n = 0.77$, (d)$f_1/f_n = 0.82$, (e)$f_1/f_n = 1.0$, (f)$f_1/f_n = 1.2$, (g)$f_1/f_n = 1.4$, (h)$f_1/f_n = 1.6$, (i)$f_1/f_n = 1.8$, (j)$f_1/f_n = 2.0$, (k)$f_1/f_n = 2.4$, (l)$f_1/f_n = 2.8$. 122

6.22 Amplitude spectra of the passive cylinder's displacement in Regime G with $KC = 9, \beta = 35, G/D = 2.5, A_1/D = 1.432, m^* = 2, \zeta = 0, Re_m = 315$ with (a)$f_1/f_n = 0.05$, (b)$f_1/f_n = 0.35$, (c)$f_1/f_n = 0.77$, (d)$f_1/f_n = 0.82$, (e)$f_1/f_n = 1.0$, (f)$f_1/f_n = 1.2$, (g)$f_1/f_n = 1.4$, (h)$f_1/f_n = 1.6$, (i)$f_1/f_n = 1.8$, (j)$f_1/f_n = 2.0$, (k)$f_1/f_n = 2.4$, (l)$f_1/f_n = 2.8$. The dominant frequency of the passive cylinder's vibration becomes equivalent to its immersed natural frequency at $f_1/f_n \geq 1.0$. 123

6.23 Non-dimensional vorticity contours for regime G with $KC = 9, \beta = 35, G/D = 2.5, A_1/D = 1.432, m^* = 2, \zeta = 0, Re_m = 315, f_1/f_n = 2.0$. 124

6.24 Passive cylinder's vibration time history in Regime G with $KC = 9, \beta = 35, G/D = 2.5, A_1/D = 1.432, m^* = 2, \zeta = 0, Re_m = 315, f_1/f_n = 2.0$. The instants *A* and *P* corresponds to Figs. 6.25a and 6.25p, respectively. 124

6.25 Non-dimensional vorticity contours in Regime G with $KC = 9, \beta = 35, G/D = 2.5, A_1/D = 1.432, m^* = 2, \zeta = 0, Re_m = 315, f_1/f_n = 2.0$. (a-h) Multiple negative vortices shed from the active cylinder merges around the passive cylinder and pushes it away. (i-p) The vortex pairs shed from the active cylinder goes around the passive cylinder without causing its significant displacement. Instants A and P in Fig. 6.25 corresponds to Figs. 6.25a and 6.25p, respectively. 125

List of tables

2.1 Non-dimensional groups and the range of value in this thesis 13
2.2 Comparison of the passive cylinder's displacement with different meshes for $KC = 3, G/D = 0.9, A_1/D = 0.477, f_1/f_n = 3.2, m^* = 1.5, \zeta = 0, Re_m = 10$. 22
2.3 Comparison of the passive cylinder's displacement with different meshes for $KC = 9, G/D = 2.5, A_1/D = 1.432, f_1/f_n = 2.8, m^* = 2, \zeta = 0, Re_m = 315$. 22

Nomenclature

Non-dimensional Groups

ζ $= \frac{c}{2\sqrt{mk}} = \frac{c}{4\pi f_n m}$, damping ratio of the passive cylinder

A_1/D amplitude ratio of the active cylinder

f_1/f_n frequency ratio of the active cylinder

G/D initial clear gap distance ratio

m^* $= m_c/m_{disp}$, mass ratio of the passive cylinder

Re_m $= U_m D/\nu$, Reynolds number regarding the maximum oscillation velocity

Symbols

β $= Re_m/KC$, Stokes number

$\Delta\phi_{21}$ $= \phi_2 - \phi_1$, the vibration phase of the passive cylinder minus that of the active cylinder

Δr^* the minimum non-dimensional mesh size in the radial direction of the cylinder

Δt^* non-dimensional computational time step

ν fluid kinematic viscosity

ω arbitrary velocity of a moving reference frame in arbitrary Lagrangian-Eulerian description

ϕ vibration phase for the single cylinder oscillation

ϕ_1 phase of the vibrating active cylinder

ϕ_2 phase of the vibrating passive cylinder

ζ damping ratio of the passive cylinder mass-spring system

A amplitude of a displacement frequency component obtained from fast Fourier transform

A_2 $= (Y_{max} - Y_{min})/2$, passive cylinder vibration amplitude during the steady state

C_A added mass coefficient, the added mass divided by the displaced fluid mass by the cylinder

C_{Y2A} amplitude of a force coefficient frequency component obtained from fast Fourier transform

C_{Y2} the force coefficient on the passive cylinder along the y-axis

D diameter for both the active and the passive cylinders

d initial centre to centre distance between the two cylinders

f frequency of a frequency component obtained from fast Fourier transform

f_1 frequency of the active cylinder oscillation

f_2 frequency of the passive cylinder vibration during the steady state

f_n $= (1/2\pi) * \sqrt{k/m_c}$, structural (vacuum) natural frequency for the elastically mounted passive cylinder

f_w $= f_n * \sqrt{m^*/(m^* + C_A)}$, the immersed natural frequency of the passive cylinder in water

f_{peak} the resonance frequency obtained directly from the numerical simulations

F_{Y2} the force acting on the passive cylinder along the y-axis

G initial clear gap distance between the two cylinders

k stiffness of the passive cylinder mass-spring system

KC $= U_m T/D$, Keulegan-Carpenter number

m_c mass of the passive cylinder

m_{disp} $= \rho \pi D^2/4$ mass of the fluid displaced by the cylinder

N_c the number of computational elements along the circumference of a cylinder

p pressure

p^* $= p/\rho f_n^2 D^2$, normalised pressure

T the period of forced vibration

t time

t^* $= f_n t$, normalised time

u horizontal fluid velocity component

$u^*_{j,mesh}$ the non-dimensional velocity of the mesh movement

u_i fluid velocity component in the x_i direction

u_i^* $= u_i/f_nD$, normalised velocity

U_m $= 2\pi A_1 f_1$, maximum velocity of the active cylinder relative to the fluid

v vertical fluid velocity component

x_i Cartesian coordinates with $x_1 = x$ and $x_2 = y$

x_i^* $= x_i/D$, normalised Cartesian coordinates

Y_1 the displacement of the active cylinder

Y_2 the displacement of the passive cylinder

$Y_{max,min}$ the maximum and the minimum of the passive cylinder displacement Y_2 in the last 50 periods of steady oscillations

Y_{max} maximum of the Y_2 values in the last 50 periods of steady oscillations

Y_{min} minimum of the Y_2 values in the last 50 periods of steady oscillations

Acronyms

ALE Arbitrary Lagrangian-Eulerian method

CFD Computational Fluid Dynamics

DEM Discrete Element Method

DNS Direct Numerical Simulation

DOF Degree Of Freedom

FEM Finite Element Method

FVM Finite Volume Method

HPC High-Performance Computing

PDE Partial Differential Equations

VIV Vortex-Induced Vibration

Chapter 1

Introduction

This chapter presents the background of this study by discussing the most relevant research. The aims and objectives of this work are stated. An outline of the entire thesis is provided at the end of this chapter.

1.1 Literature Review

Flow-mediated interaction is a phenomenon concerning objects moving in a fluid which interact with the nearby objects via the perturbed fluid. The ensuing movement of the neighbouring objects is more complicated compared with traditional scenarios with objects under a steady or a periodic flow.

The significance of researching flow-mediated interaction relies on its wide occurrence in both natural and artificial situations, for example, sperm-egg interaction (Riffell and Zimmer, 2007), fish schooling (Liao, 2003; Gazzola et al., 2011, 2016), dolphin drafting (Weihs, 2004), swimming of micro-organisms (Gyrya et al., 2010; Ishikawa et al., 2006; Koch and Subramanian, 2011), formation of solid particle clusters (Voth et al., 2002), and dispersion of particle clouds (Metzger et al., 2007), interference between immersed risers (Bampalas and Graham, 2008), seismic pile water interaction (Pang et al., 2015). Extensive and elaborate studies have been carried out on this topic, for the purpose of comprehending the mechanism of the interactions. The revelations from these studies can thus be exploited in engineering applications, e.g. vortex-induced vibration energy harvesting (Bernitsas et al., 2008), self-propulsion device design (Van Rees et al., 2015), and the cyber octopus being developed by US Department of Defense Office of Naval Research. Figures 1.1 and 1.2 show some examples of phenomena and applications that is relevant to the present study.

This thesis focuses on the flow-mediated interaction between two rigid cylinders immersed in a quiescent incompressible fluid. One cylinder, the active cylinder, carries out

Fig. 1.1 An offshore oil drilling platform with multiple cylindrical structures (Credit: Chesroc Nigeria Limited)

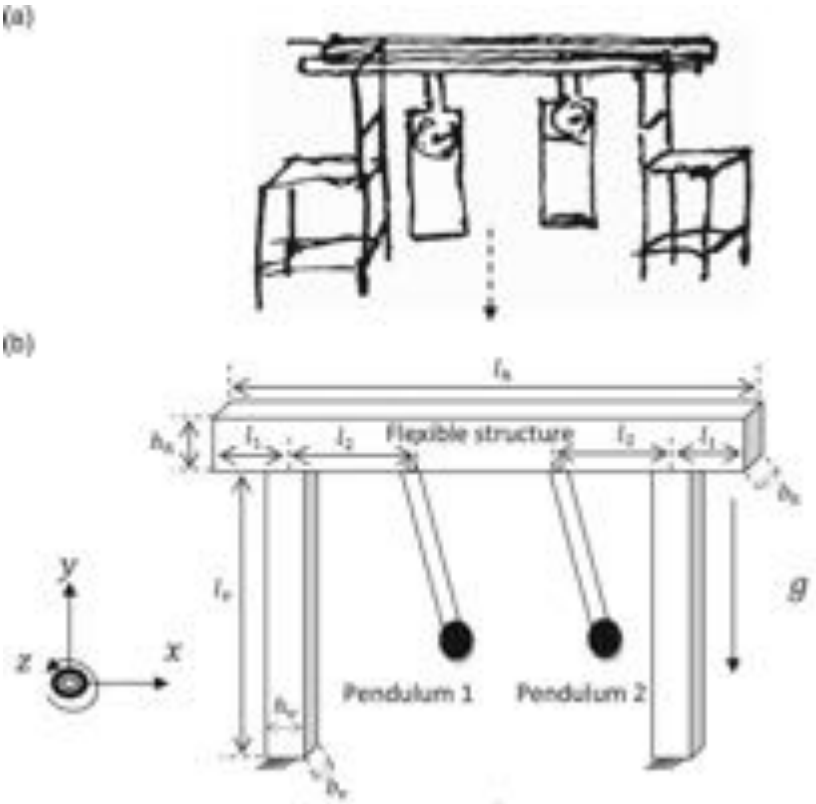

Fig. 1.2 (a) Classical Huygens' pendulum clocks setup (Huygens, 1660) (b) Idealised model by Peña Ramirez et al. (2014).

sinusoidal forced vibration to perturb the surrounding fluid, and the generated periodic flow thus interacts with the other cylinder, the passive cylinder, which is elastically-mounted with a damper. Despite the basic geometry, this problem involves a rich spectrum of physics and carries practical implications in many fields of research and engineering.

Due to the necessity to check the flow-mediated interactions between multiple cylinders, various studies have already been conducted over the past decades to analyse the fluid-structure interactions involving solely one periodically oscillating cylinder.

1.1.1 Single Cylinder Oscillating in Still Fluid

The scenario of a cylinder oscillating in a fluid is physically equivalent to a cylinder immersed in an oscillatory flow, which can be determined by two dimensionless parameters, i.e. the Keulegan-Carpenter number and Reynolds number. The Keulegan-Carpenter number can be defined as $KC = U_m T/D$ (Keulegan and Carpenter, 1958), where U_m is the amplitude of the oscillatory flow velocity, T the period of oscillatory flow, and D the diameter of the cylinder. Given a sinusoidal flow we have $KC = 2\pi A_1/D$. The Reynolds number is defined as $Re_m = U_m D/\nu$, where ν is the fluid kinematic viscosity. The Stokes number, β, is dependent on the Reynolds number and the Keulegan-Carpenter number and is defined as $\beta = Re_m/KC$. In engineering applications, the prediction of fluid-induced drag forces for a circular cylinder in oscillating or wave flow is predicted by the Morrison Equation (Morison et al., 1950), which represent the in-line force per unit length as

$$F = \frac{1}{2}\rho D C_D U|U| + \frac{1}{4}\pi\rho D^2 C_m \dot{U} \tag{1.1}$$

where ρ is the fluid density, D is the body diameter, U is the fluid velocity, $C_m = 1 + C_a$ is the inertia coefficient, C_a the added mass coefficient, and C_D is the drag coefficient. C_m and C_D are found to depend on both KC (Keulegan and Carpenter, 1958) and $\beta = Re/KC$ (Sarpkaya, 1977). Williamson (1985) further studied the effects of vortex motions on the forces upon a single cylinder in the range of $0 < KC < 35$ with β fixed at 730. Williamson (1985) reported reasonable symmetry at $KC < 4$. Several regimes were classified according to the vortex patterns and KC. Specifically, at $0 < KC < 7$ a pair of small attached vortices are observed, which is similar to the flow pattern generated by the active cylinder in the present study. Based on this pattern, five flow regimes were defined according to KC. While Williamson (1985) carried out experiments at a fixed β, Tatsuno and Bearman (1990) further explored in the range of $KC < 15$ and $\beta < 160$. They classified eight flow regimes based on flow visualization, which were referred to as regimes A^*, A, B, C, D, E, F, G. The flows in regimes A and A^* are entirely two-dimensional (2D). The flow regimes discussed

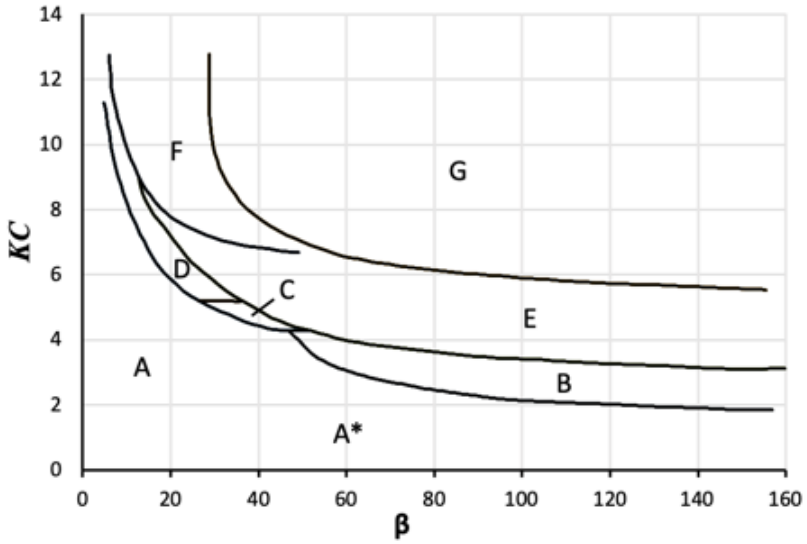

Fig. 1.3 Flow regimes classified by Tatsuno and Bearman (1990). In this thesis, the values of KC and β lies well within regimes A and A^*, and the flow characteristics in all the simulations do coincide with the regimes A and A^*: two symmetric vortices shed per half cycle.

in this thesis are within regimes A, A^*, C, E, F, G. Based on the useful flow regime map from Tatsuno and Bearman (1990), Elston et al. (2004, 2006) further examined the symmetry breaking phenomenon, and identified the parameters related to the breakage of different types of symmetries for this case, including the onset of both 2D and 3D instability. Many researchers investigated the flow transition from 2D to 3D as well (Honji, 2006; Hall, 1984; Sarpkaya, 1986, 2002, 2005, 2006). The present study is within regimes A and A^*, and for all the involved cases, the flow field is symmetric. Dütsch et al. (1998) carried out laser Doppler anemometry measurements of a laminar flow generated by the harmonic oscillation of a circular cylinder in otherwise still water. By comparing with these experimental results, an in-house 2D Navier-Stokes model is validated in Lin et al. (2017), which is the basic tool for the present study.

In addition to the experimental efforts, with the continuous enhancement of computational power, fluid mechanics problems are increasingly studied in a numerical manner. The problem of oscillatory flow past a circular cylinder is not an exception. Many researchers have used 2D simulations to predict the flow field. Justesen (1991) conducted numerical simulation on this problem for $\beta = 196, 483, 1035$ and $0 < KC < 26$. By solving 2D NS equations, they achieved good agreement with the experimental data. Lin et al. (1996) utilised a 2D discrete vortex method to carry out numerical simulation at $\beta = 76$ and $KC < 30$. They successfully reproduced all the major vortex-shedding regimes found in previous experiments. Iliadis and Anagnostopoulos (2002) focused on an aperiodic flow case of oscillatory flow

past a circular cylinder at $Re_m = 200$ and $KC = 20$ using 2D finite element method. They observed intermittent changes between different vortex shedding modes.

Also, Zhao and Cheng (2014) numerically studied the oscillatory flow past two circular cylinders. They found that, in the side-by-side arrangement with small gap ratios, the vortex shedding from the gap of the two cylinders dominates, resulting in the unique gap vortex shedding (GVS) regime, which cannot be found for a single cylinder case. In the tandem arrangement with a very small gap between the two cylinders, the flow regimes are similar to that of a single cylinder. A strong interaction between the vortex shedding flows from the two cylinders makes the flow notably irregular at large KC values in both side-by-side and tandem arrangements. Zhao and Cheng (2014) used the same code used in this study to simulate the single-cylinder case and achieved very good agreement with the experimental results by Tatsuno and Bearman (1990), as seen in Fig. 1.4.

1.1.2 A Oscillating Cylinder Actuating a Free Cylinder in Still Fluid

In contrast to the abundant research on cylinders vibrating in a still fluid, the research related to the flow-mediated interaction between multiple immersed cylinders is relatively scarce. Lamb (1932) studied the interaction between two spheres immersed in *inviscid* fluid. One sphere is forced to oscillate along the centre-line, whereas the other nearby sphere of neutral buoyancy responds freely to the disturbed fluid. By theoretical analysis, Lamb (1932) stated that the free sphere is "on the whole" attracted towards the forcedly oscillating sphere due to the imbalanced pressure force. By both analytical and numerical methods, Nair and Kanso (2007) studied an identical configuration in greater detail, but for the case of two circular cylinders rather than two spheres. One cylinder is started impulsively and is forced to oscillate along the centre-line between two cylinders, whereas the second responds freely without any constraints. By contrast, in the present study, the second (passive) cylinder is constrained by the spring and the damper. Nair and Kanso (2007) discovered that the free cylinder can be either repelled away or attracted towards the forcedly oscillating cylinder, depending on the initial velocity direction of the oscillating cylinder. They further suggested that this should also be the case for the sphere scenario analysed by Lamb (1932), who only captured the attraction due to a mathematical mistreatment.

The flow-mediated interaction between two cylinders was further investigated by Gazzola et al. (2012), as seen in Fig. 1.5a, but the fluid was taken to be *viscous* rather than *inviscid*. They found a threshold Reynolds number, beyond which the passive cylinder is repelled by the active cylinder, and under which the passive is attracted to the active cylinder. An increase in Reynolds number, i.e. , a decrease in viscosity, slows down the dissipation of the secondary flow, which favours the repulsion of the passive cylinder by the active cylinder.

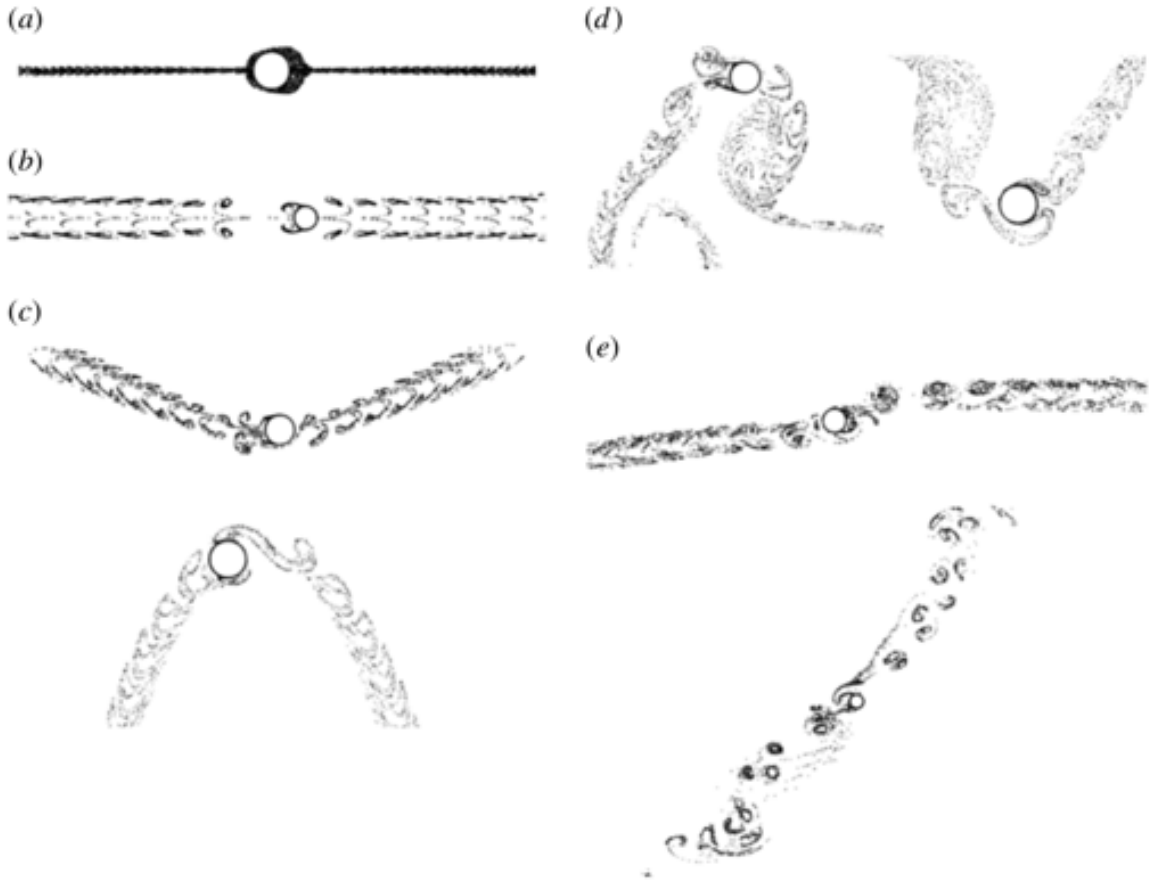

Fig. 1.4 Simulated flow patterns represented by streaklines in different flow regimes for oscillatory flow past a single cylinder, conducted under the same condition as the experiments carried out by Tatsuno and Bearman (1990). It was simulated by Zhao and Cheng (2014) using the code of current study. (a) Regime A* at $KC = 3.14$ and $\beta = 52.8$ (b) Regime A at $KC = 11$ and $\beta = 7.4$ (c) Regime D at $KC = 6.28$, and $\beta = 18$ (upper) and $\beta = 22.1$ (lower) (d) Regime E at $KC = 6.28$ and $\beta = 25.6$ in the 72nd period (left) and 200th period (right). (e) Regime F at $KC = 8.16, \beta = 27$ (upper), $KC = 12.6, \beta = 17.8$ (lower). (a-e) The oscillation direction is horizontal in all the sub-figures.

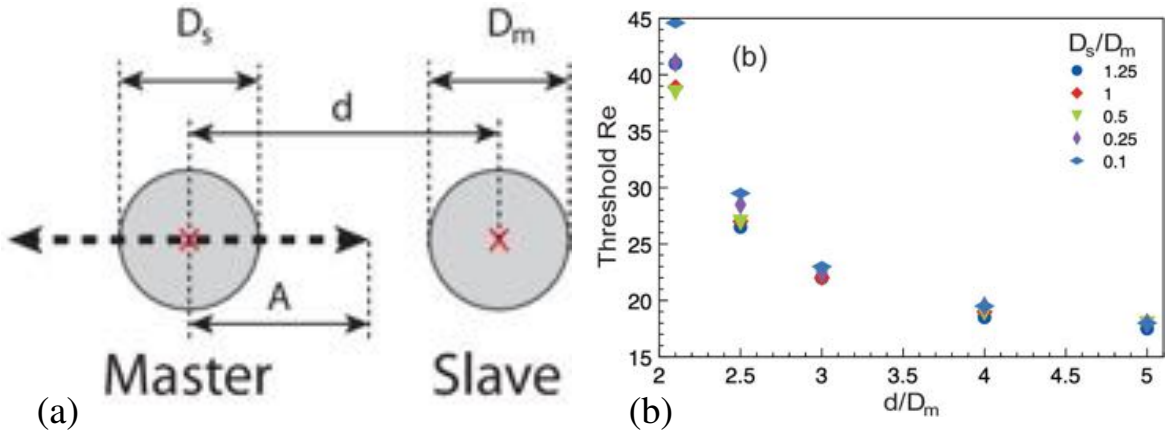

Fig. 1.5 (a) The setup sketch of Case B (Gazzola et al., 2012). The active cylinder is forced to oscillated harmonically along the centreline of two cylinders, whereas the passive cylinder is free. This is different from the present study, where the passive cylinder is attached to a spring. (b) Threshold Reynolds number illustrated as a function of d/D_m and D_s/D_m (Gazzola et al., 2012).

When the repelling effect prevails, a secondary flow structure is discovered between the two cylinders. They further discovered that the threshold Reynolds number is indifferent to the initial phase of the active cylinder, i.e. , the direction of the initial velocity of the active cylinder. This conclusion is different from that drawn in Nair and Kanso (2007) concerning the inviscid flow, where the initial phase of the movement governs the repulsion or attraction. Fig. 1.6 compares the effect of initial phase between inviscid and viscous fluid. With the increase in the initial gap, the threshold Reynolds number decreases exponentially, whereas it is less sensitive to the size difference between the two cylinders, as seen in Fig. 1.5b. Based on these observations, Gazzola et al. (2012) concluded that the flow features have a greater influence than the inertia of the passive cylinder. As a result, in the present study, the diameters of the passive cylinder and the active cylinders are identical. They also found that, given a very small vibration amplitude of the active cylinder, the level of repulsion or attraction is significantly reduced. Therefore, in the present study, the active cylinder oscillates at an amplitude of 0.477D, i.e. $KC = 3$, allowing convenient observation and study of the repulsion and attraction.

In summary, a large amount of research has been carried out on oscillatory flow past a single cylinder, but there is only limited research on the flow-mediated interaction between immersed objects despite the rich physics involved and the potential engineering applications.

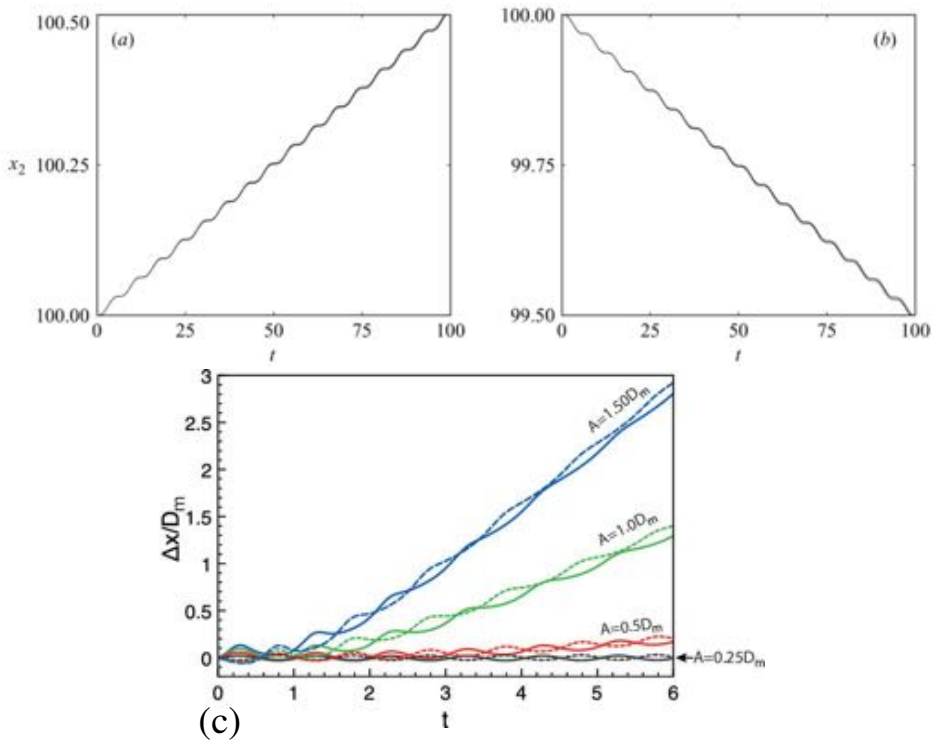

Fig. 1.6 In inviscid fluid, time history of the passive cylinder's normalised displacement from its initial position $\Delta x/D_m$ at initial phase of the active cylinder vibration at (a) 0° and (b) 180°, as demonstrated by Nair and Kanso (2007). (c)In viscous fluid, time history of slave's normalised displacement from its initial position $\Delta x/D_m$ at initial phase of the active cylinder vibration at 0° (solid line) and 180° (dashed line), as illustrated by Gazzola et al. (2012). The initial condition of the active cylinder can affect the drifting direction of the passive cylinder in inviscid fluid, but not in viscous fluid.

1.2 Aims and Objectives

The interaction between two vibrating cylinders immersed in a fluid has never been carefully studied in the past, despite many relevant natural phenomena and engineering applications. The aim of this work is to understand the mechanism of the flow-mediated interaction among multiple vibrating cylinders.

To investigate this mechanism, this thesis focuses on a representative case with two cylinders immersed in otherwise static fluid. An active cylinder is forced to oscillate harmonically, whereas a nearby passive cylinder is elastically-mounted with a damper and responds to the actuated flowing fluid. Both cylinders vibrate only along the centreline connecting the two cylinders.

The achievements of this study are listed here:

- Review the existing literature
- Validate the numerical method
- Non-dimensionalise the representative case
- Design the parametric space to be explored
- Run extensive amount of simulation cases on high performance computing facilities
- Process huge amount of data by scripting, and analyse the processed data
- Summarise the discoveries and contribute to the physical understanding

1.3 Outline of Thesis

Chapter 2 describes computational methods for the in-house finite element method (FEM) code applied in this study. The dimensional analysis and governing equations are presented followed by the mesh independence study and validation of the numerical model.

Chapters 3 to 5 present the parametric studies for the non-dimensional groups associated with the active cylinder, the passive cylinder, and the intermediate fluid, respectively.

Chapter 3 focuses on the effects of the parameters relevant to the active cylinder, i.e. the frequency and amplitude of its forced oscillation.

Chapter 4 investigates the influence parameters related to the passive cylinder, i.e. its damping ratio and mass ratio.

Chapter 5 studies the roles played by the parameters related to the intermediate fluid, i.e. the Reynolds number and the gap distance between the two cylinders.

In Chapters 3 to 5, the representative cases selected from 23,400 simulations are demonstrated and interesting phenomena are discussed, including the primary and secondary resonance, drifting of the passive cylinder, the shift of phase difference between the two cylinders and the characteristic flow field around the cylinders.

Chapter 2

Methodology

This chapter discusses the methodology of this thesis. Section 2.1 demonstrates the problem setup for the interested physical case of the multi-cylinder interaction in fluid and also the corresponding dimensional analysis. Simulation of this physical problem was carried out using an in-house FORTRAN code. The two-dimensional (2D) Navier-Stokes equations are directly solved to simulate the flow-mediated interaction, as seen in Section 2.2.1. The simulation code applies the streamlined upwind Petrov-Galerkin finite element method (FEM), as described in Section 2.2.2, with arbitrary Lagrangian-Eulerian (ALE) method, as demonstrated in Section 2.2.3. The mesh independence study and the validation were conducted in Section 2.3 and Section 2.4, respectively, to check the validity of the model.

2.1 Problem Setup and Dimensional Analysis

In this study, two identical rigid cylinders are immersed in otherwise still fluid, as seen in Fig. 2.1. At time zero, the active cylinder impulsively starts and vibrates harmonically disturbing the surrounding fluid, whereas the passive cylinder vibrates correspondingly with 1 degree of freedom (1DOF) along the y-axis in response to the imbalanced hydrodynamic force due to the actuation of the active cylinder. In all the studied cases, the passive cylinder and the active cylinder are always separated by the fluid, with no occurrence of solid-solid contact.

Here, dimensional analysis is carried out to simplify the targeted problem by reducing variables involved, as seen in Figure 2.1. Buckingham theorem is applied to find out the dimensionless groups influencing the simulation results. The detailed procedure is as follows:

For this case, 9 quantities and 3 dimensions are involved:

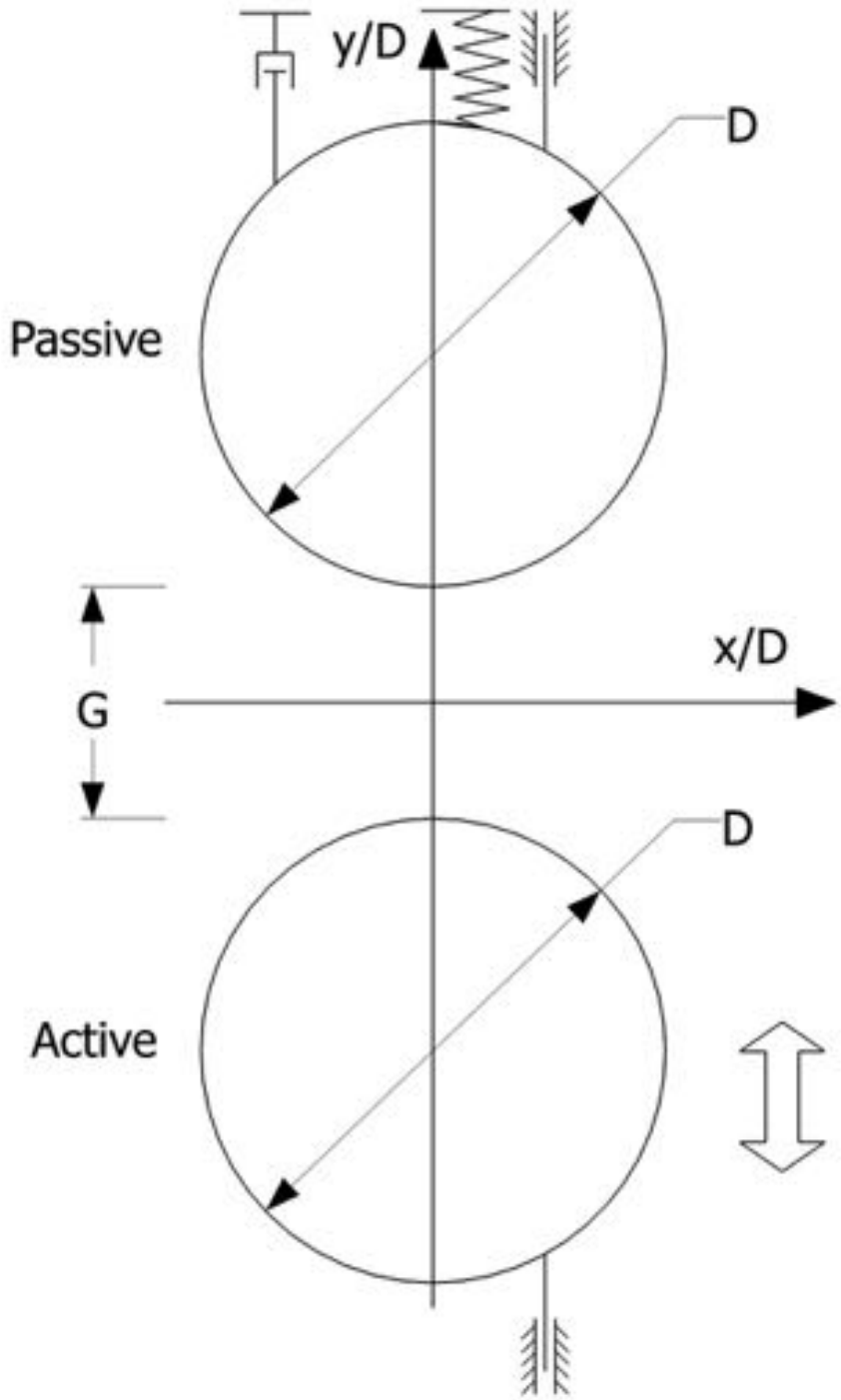

Fig. 2.1 A sketch of interaction between the two cylinders: While the active cylinder undergoes harmonic forced vibration along the centreline of the two identical rigid cylinders, the passive cylinder is elastically mounted with a damper, vibrating in response to the active cylinder with 1DOF along the centreline as well.

$$\begin{bmatrix} D & f_n & m & A_1 & f_1 & G & \rho & \nu & c \\ 0 & 0 & 1 & 0 & 0 & 0 & 1 & 0 & 1 \\ 1 & 0 & 0 & 1 & 0 & 1 & -2 & 2 & 0 \\ 0 & -1 & 0 & 0 & -1 & 0 & 0 & -1 & -1 \end{bmatrix} \begin{matrix} \\ M \\ L \\ T \end{matrix}$$

where D is the diameter of the cylinder; $f_n = \sqrt{k/m}/2\pi$ is structural natural frequency of the passive cylinder; m is mass of the passive cylinder; k is the stiffness of the spring mounted to the passive cylinder; A_1 is the oscillation amplitude of the active cylinder; f_1 is oscillation frequency of the active cylinder; G is initial gap distance between the two cylinder; ρ is density of fluid; ν is kinematic viscosity of fluid; c is viscous structural damping coefficient of the passive cylinder; M, L and T represent dimensions of mass, length and time, respectively.

According to Buckingham theorem, these quantities can be reduced to $9-3=6$ independent dimensionless groups.

If D, f_n, and m are selected as repeating variables, the 6 groups can be written as follows:

$$\pi_1 = \frac{A_1}{D}, \qquad \pi_2 = \frac{f_1}{f_n}, \qquad \pi_3 = \frac{G}{D},$$
$$\pi_4 = \frac{\rho}{mD^{-2}} = \frac{4}{\pi m^*}, \qquad \pi_6 = \frac{c}{4\pi f_n m} = \zeta, \qquad \pi_5 = \frac{\nu}{f_n D^2} = \frac{2\pi(A_1/D)(f_1/f_n)}{Re_m}.$$

In other words, any case can be determined by 6 independent dimensionless groups: A_1/D, f_1/f_n, G/D, m^*, Re_m and ζ as seen in Table 2.1:

Table 2.1 Non-dimensional groups and the range of value in this thesis

Frequency ratio of active cylinder	f_1/f_n		$0.05-3.2$
Amplitude ratio of active cylinder	A_1/D		$0.025-0.477$
Damping ratio of passive cylinder	ζ	$\frac{c}{4\pi f_n m}$	$0-1.4$
Mass ratio of passive cylinder	m^*	$\frac{m_c}{\rho D^2\pi/4}$	$1.5-2.5$
Reynolds number regarding U_m	Re_m	$\frac{2\pi A_1 f_1 D}{\nu}$	$10-315$
Gap ratio	G/D		$0.2-1.0$

Simulations are conducted for a range of combinations in both regular and irregular regimes. As seen in Table 2.1, the active cylinder's frequency f_1/f_n ranges from 0.05 to

3.2; the amplitude of the active cylinder A_1/D varies from 0.025 to 1.432; the damping ratio ranges from 0 to 1.4; the mass ratio m^* takes the value of 1.5, 1.7, 2.0, 2.2 or 2.5; the Reynolds number Re_m varies from 10 to 315; the gap ratio G/D ranges from 0.2 to 2.5. The corresponding Keulegan-Carpenter number and the Stokes number of the active cylinder can be calculated as $KC = 2\pi A_1/D = 0.157 - 9$ and $\beta = Re_m/KC = 3.3 - 110$, respectively. In total, 21224 combinations of periodic regime are examined.

The tested range of the active cylinder's oscillation frequency allows clear demonstration of all the resonating frequencies of the passive cylinder's response, which will be discussed later in Chapter 3. The range of Reynolds number Re_m involves both the repelling and attraction regimes for the passive cylinder, which will be discussed later in Chapter 5. The range of the active cylinder's amplitude and the Reynolds number together constrain the involved flow regimes to A^*, A, C, E, F, G as defined by Tatsuno and Bearman (1990). The mass ratios are typical for engineering structures immersed in water, e.g. the mass ratio of concrete in water is about 2.5.

2.2 Computational Method

This section describes the governing equations of the current numerical model. The streamline upwind Petrov-Galerkin finite element method was implemented to discretise the governing equations. Arbitrary Lagrangian-Eulerian method was used to handle the moving boundary.

2.2.1 Governing Equations

The two-dimensional Navier-Stokes equations are solved by the Streamline Upwind Petrov-Galerkin finite-element method (Brooks and Hughes, 1982). The moving cylinder boundaries are handled through the use of an arbitrary Lagrangian-Eulerian (ALE) scheme, as seen in Section 2.2.3. In the governing equations, the length, time, velocity and pressure are non-dimensional quantities according to:

$$x_i^* = \frac{x_i}{D},\ t^* = t f_n,\ u_i^* = \frac{u_i}{f_n D},\ p^* = \frac{p}{\rho f_n^2 D^2} \tag{2.1}$$

where $x_1^* = x/D$ and $x_2^* = y/D$ are the Cartesian coordinates, as shown in Fig. 2.1. t is time, $f_n = \sqrt{k/m}/2\pi$ is the structural natural frequency in vacuum determined by the passive cylinder's mass and spring stiffness as explained before, u_i is the fluid velocity component in the x_i direction, and p is the pressure. The variables with stars represent the non-dimensional quantities. The non-dimensional incompressible two-dimensional Navier-Stokes equations in the ALE framework are

$$\frac{\partial u_i^*}{\partial x_i^*} = 0, \tag{2.2}$$

$$\frac{\partial u_i^*}{\partial t^*} + (u_j^* - u_{j,mesh}^*)\frac{\partial u_j^*}{\partial x_j^*} + \frac{\partial p^*}{\partial x_i^*} = \frac{U_m}{Re_m f_n D}\frac{\partial^2 u_i^*}{\partial x_j^* \partial x_j^*} \tag{2.3}$$

where $u_{j,mesh}^*$ is the velocity of the mesh movement.

The motion equations for the active and the passive cylinders are

$$Y_1 = A_1 \sin(2\pi f_1 t) \tag{2.4}$$

$$\frac{\partial^2 Y_2}{\partial t^2} + 4\pi f_n \zeta \frac{\partial Y_2}{\partial t} + 4\pi^2 f_n^2 Y_2 = \frac{2}{\pi}\frac{U_m^2}{m^* D} C_{Y2} \tag{2.5}$$

where Y_1 and Y_2 are the y direction displacements of the active and passive cylinders, respectively, ζ stands for the damping factor, $C_{Y2} = F_{Y2}/(0.5\rho D U_m^2)$ is the force coefficient for the passive cylinder, F_{Y2} is the y direction force on the passive cylinder.

These equations can also be written in a non-dimensional form:

$$Y_2^* = Y_2/D \tag{2.6}$$

$$\frac{Y_1}{D} = \frac{A_1}{D}\sin(2\pi\frac{f_1}{f_n}t^*) \tag{2.7}$$

$$\frac{\partial^2 Y_2^*}{\partial t^{*2}} + 4\pi\zeta\frac{\partial Y_2^*}{\partial t^*} + 4\pi^2 Y_2^* = \frac{8\pi}{m^*}(\frac{A_1}{D})^2(\frac{f_1}{f_n})^2 C_{Y2} \tag{2.8}$$

2.2.2 Streamline Upwind Petrov-Galerkin FEM

Finite element method (FEM) is often exploited to solve the problems where the governing equations are known, but analytical solutions are difficult or impossible to achieve. The popularity and fame of FEM can be attributed to its various advantages. First and foremost, FEM can accurately represent very complex geometries and can include dissimilar material properties, which enables FEM to deal with a wide range of engineering problems, for example, solid mechanics, fluid dynamics, heat transfer and electrostatic problems. FEM can also handle complex restraints and complex loadings, for example, nodal loading, element loading and time or frequency dependent loading (Weck et al., 2016). FEM discretises the governing equations into small elements and uses a weighted residual formulation to obtain a system of matrix equations. An approximate solution of the original problem can thus be achieved by FEM.

Bubnov-Galerkin method is the most common weighted residual formulation. The Galerkin method is capable of achieving good results while applying it to most structures or heat conduction problems, since it can minimise the difference between the finite element solution and the exact solution (Brooks and Hughes, 1982). When it comes to fluid flow simulations, Bubnov-Galerkin method was initially applied as well, but sometimes, significant unphysical oscillation of the flow velocity were discovered. This problem can only be fixed by excessive refinement of the computational mesh, which is not desirable in most cases. This disadvantage of the Bubnov-Galerkin method demands a new formulation without such unphysical oscillations at any level of mesh refinement. The upwind difference method can produce simulation results without the unphysical oscillations, but has the disadvantaged of only first degree of accuracy. To solve this problem, Brooks and Hughes (1982) developed a new Navier-Stokes solution algorithm with streamline upwind Petrov-Galerkin formulation, which possesses both the robust qualities of an upwind method and the accuracy of Petrov-Galerkin method. The principal idea of this formulation is to add a streamline upwind perturbation to the standard Bubnov-Galerkin weighting functions, acting only in the flow direction. This formulation is employed in the present simulation code (Zhao et al., 2007, 2009; Zhao, 2013).

In the present study, a Galerkin finite element method is used to discretise the governing equations in space. The conventional Galerkin discretisation equals to the central-difference approximation in finite difference method. Since central-difference discretisation has negative artificial diffusion, numerical instabilities often take place in central-difference solutions of the convective-diffusive equations. In the present study, by introducing an artificial diffusion term to the momentum equations, a streamline upwind scheme is applied. In the momentum equations, the added diffusion term can be written as (Brooks and Hughes, 1982):

$$\tilde{k}\frac{\partial}{\partial x_k}(u'_j u'_k \frac{\partial u_i}{\partial x_j}), \tag{2.9}$$

where $u'_i = u_i/\|\boldsymbol{u}\|$, $\|\boldsymbol{u}\|$ is the magnitude of the velocity defined as $\|\boldsymbol{u}\|^2 = \sum_i u_i u_i$, $\tilde{k}$ is defined as (Brooks and Hughes, 1982; Jester and Kallinderis, 2003):

$$\tilde{k} = \tilde{\xi}\|u_e\|h_e/2, \tag{2.10}$$

$$\tilde{\xi} = \begin{cases} Re_h/3, & Re_h \leq 3, \\ 1, & Re_h > 3, \end{cases} \tag{2.11}$$

where $\|u_e\|$ is the magnitude of the velocity at the element centroid, h_e is the element's average edge length, $Re_h(=\|u_e\|h_e/\nu)$ is the cell Reynolds number.

For the time integration of the momentum equation Eq. (2.3), a fractional step formulation is applied (Meting et al., 1997; Meneghini et al., 2001). First, by neglecting the pressure gradient terms, an intermediate velocity is computed. The pressure field is then obtained by solving the pressure Poisson equation. The final velocity is achieved by including the pressure effect. In the intermediate velocity computation, the streamline upwind scheme is applied. During a time increment from $t = n\Delta t$ to $(n+1)\Delta t$, with Δt being the computational time step, the algorithm of the time advancement scheme for the equations is as follows:

1. Solving the momentum equations without pressure terms, the intermediate velocity $\tilde{u}_i^{n+1}$ is computed at time $t = (n+1)\Delta t$. The diffusion terms are considered implicitly whereas the convection terms are considered explicitly from the previous time step. The parameter $\tilde{k}$ is evaluated at the time level $n\Delta t$. The equation for computing $\tilde{u}_i^{n+1}$ is:

$$\tilde{u}_i^{n+1} - \Delta t \frac{\partial}{\partial x_j}[\frac{1}{Re}(\frac{\partial \tilde{u}_i^{n+1}}{\partial x_j} + \frac{\partial \tilde{u}_j^{n+1}}{\partial x_i})] - \Delta t \tilde{k} \frac{\partial}{\partial x_k}(u_j^n u_k^n \frac{\partial \tilde{u}_i^{n+1}}{\partial x_j}) = u_i^n - \Delta t u_j^n \frac{\partial u_i^n}{\partial x_j}, \quad (2.12)$$

2. In general, the intermediate velocity field does not satify the continuity equation. At the time $t = (n+1)\Delta t$, the pressure is computed to enforce the continuity in the final velocity field. The pressure is computed by solving the following pressure Poisson equation,

$$\frac{\partial^2 p^{n+1}}{\partial x_j \partial x_j} = \frac{1}{\Delta t} \frac{\partial \tilde{u}_j^{n+1}}{\partial x_j}, \quad (2.13)$$

3. The final velocity is obtained by including the pressure terms

$$u_i^{n+1} = \tilde{u}_i^{n+1} - \Delta t \frac{\partial p^{n+1}}{\partial x_i}. \quad (2.14)$$

The computational domain Ω is divided into linear finite elements. In an element, the velocity components, pressure and the turbulence quantities can be approximated as:

$$u_i \approx \boldsymbol{N}\boldsymbol{U}_i, p \approx \boldsymbol{N}\boldsymbol{P}, \quad (2.15)$$

where $\boldsymbol{N}$ is the shape function vector, $\boldsymbol{U}_i$ and $\boldsymbol{P}$ are the nodal values of u_i and p, respectively. By selecting the shape function as the weighting function and applying a weighted residual

formulation to Eqs. (2.12–14), the following set of matrix equations is obtained:

$$[\boldsymbol{M}+\Delta t(\boldsymbol{D}^n+\boldsymbol{D}_u^n)]\tilde{\boldsymbol{U}}_i^{n+1}=\boldsymbol{M}\boldsymbol{U}_i^n+\Delta t\boldsymbol{C}^n\boldsymbol{U}_i^n, \tag{2.16}$$

$$\boldsymbol{S}\boldsymbol{P}^{n+1}=-\frac{1}{\Delta t}\boldsymbol{A}_i\tilde{\boldsymbol{U}}_i^{n+1}, \tag{2.17}$$

$$\boldsymbol{M}\boldsymbol{U}_i^{n+1}=\boldsymbol{M}\tilde{\boldsymbol{U}}_i^{n+1}-\Delta t\boldsymbol{A}_i\boldsymbol{P}^{n+1}, \tag{2.18}$$

where

$$\boldsymbol{M}=\int_{\boldsymbol{\Omega}}\boldsymbol{N}^T\boldsymbol{N}d\boldsymbol{\Omega},\qquad \boldsymbol{D}^n=\int_{\boldsymbol{\Omega}}\tilde{k}^n u_i^n u_j^n\frac{\partial\boldsymbol{N}^T}{\partial x_i}\frac{\partial\boldsymbol{N}}{\partial x_j}d\boldsymbol{\Omega},$$

$$\boldsymbol{A}_i=\int_{\boldsymbol{\Omega}}\boldsymbol{N}^T\frac{\partial\boldsymbol{N}}{\partial x_i}d\boldsymbol{\Omega},\qquad \boldsymbol{S}=\int_{\boldsymbol{\Omega}}\frac{\partial\boldsymbol{N}^T}{\partial x_i}\frac{\partial\boldsymbol{N}}{\partial x_i}d\boldsymbol{\Omega}$$

$$\boldsymbol{D}_u^n=\int_{\boldsymbol{\Omega}}\nu\frac{\partial\boldsymbol{N}^T}{\partial x_j}\frac{\partial\boldsymbol{N}}{\partial x_j}d\boldsymbol{\Omega},\qquad \boldsymbol{C}^n=\int_{\boldsymbol{\Omega}}-u_j^n\boldsymbol{N}^T\frac{\partial\boldsymbol{N}}{\partial x_j}d\boldsymbol{\Omega}$$

In summary, the computational procedure is:

1. Calculate the intermediate velocity by Eq. (2.16);
2. Solve the pressure Eq. (2.17)
3. Obtain the final velocity by Eq. (2.18)
4. Return to step 1 and repeat the procedure till the flow is fully developed.

2.2.3 Arbitrary Lagrangian-Eulerian Method

The current numerical model uses the Arbitrary Lagrangian-Eulerian (ALE) method to deal with the moving boundaries due to the fluid-structure interaction. ALE method was originally developed for inviscid flows in finite difference formats by Noh (1964), Trulio (1966) and Hirt et al. (1974). Hughes et al. (1981) later presents the theoretical framework of ALE for incompressible viscous flows. Donea et al. (1982) proposed the ALE method in FEM format for the fluid-structure interaction problems.

The Lagrangian and the Eulerian description are the two most basic viewpoints in the algorithms of fluid mechanics. In Lagrangian description, the computational mesh moves with the associated material particle. In Eulerian, the computational mesh is treated as a fixed reference frame and the fluid moves with respect to the grid. The ALE description was developed to represent the generalisation of the two classical concepts. The ALE description does not depend on the assumption of fluid particles and consider the mesh as a reference

frame travelling with an arbitrary velocity ω in the space. Donea et al. (1982) summarised that, those descriptions can be classified by ω as follows:

1. $\omega = 0$, the reference frame is static, corresponding to the Eulerian description, where motion is represented by velocity distribution on fixed nodes on the mesh.
2. $\omega = v$, where v is the actual particle velocity. The reference frame moves with the particle, corresponding to the Lagrangian decription.
3. $0 < \omega < v$, the reference frame is not static and travels at a velocity ω different from the particle velocity v, corresponding to the arbitrary Lagrangian-Eulerian description.

The ALE algorithm allows the computational mesh inside the domains to move arbitrarily to optimize the shapes of elements, while the mesh on the boundaries and interfaces of the domains can move along with materials to precisely track the boundaries and interfaces of a multi-material system. Also, ALE formulations can be reduced to either Lagrangian formulations by equating mesh motion to material motion or Eulerian formulations by fixing mesh in space. As a result, the versatility of ALE method allows it to perform comprehensive engineering simulations, including heat transfer, fluid flow, fluid-structure interactions and metal-manufacturing.

In the present code, the location of each finite element node is updated at every time step according to the motion of the cylinder. The FEM node displacements are governed by (Zhao, 2013):

$$\nabla \cdot (\gamma \nabla S_y) = 0, \tag{2.19}$$

where S_y is the displacement of the nodal points in the y-direction and γ is a constant that controls the mesh deformation. To avoid excessive distortion of the near-wall elements, in each finite element, it is configured that $\gamma = 1/A_{element}$, with $A_{element}$ being the area of the element. A Galerkin FEM is applied to solve Equation (2.19) by specifying the displacements at all boundaries. On the cylinder surfaces, the nodal displacement S_y is identical to the displacement of the cylinder whereas $S_y = 0$ on all other non-cylinder boundaries.

2.3 Mesh Independence Study

Mesh independence study is conducted to ensure that the mesh is sufficiently dense to obtain converged results. A close-up of the typical computational mesh around the cylinders is illustrated in Fig. 2.2. It has $16,407$ nodes in total. The complete computational domain is of a square shape with a sufficiently large side length of $30D$ to eliminate the boundary effects

(Zhao and Cheng, 2014). The mesh is a combination of structured (around the cylinders) and unstructured (far from the cylinders) types. The number of elements along each cylinder circumference N_c is 152, and the minimum non-dimensional mesh size in the radial direction Δr^* is 1.30×10^{-3}. The non-dimensional time step Δt^* in the simulation is chosen based on the Courant condition $\Delta t^* = 0.00025/U_m^* = 0.00025 D f_n/(2\pi A_1 f_1)$, i.e., the Courant number is $\Delta t^* U_m^*/\Delta r^* = 0.19 < 1$, where U_m^* is the non-dimensional maximum vibration velocity of the active cylinder.

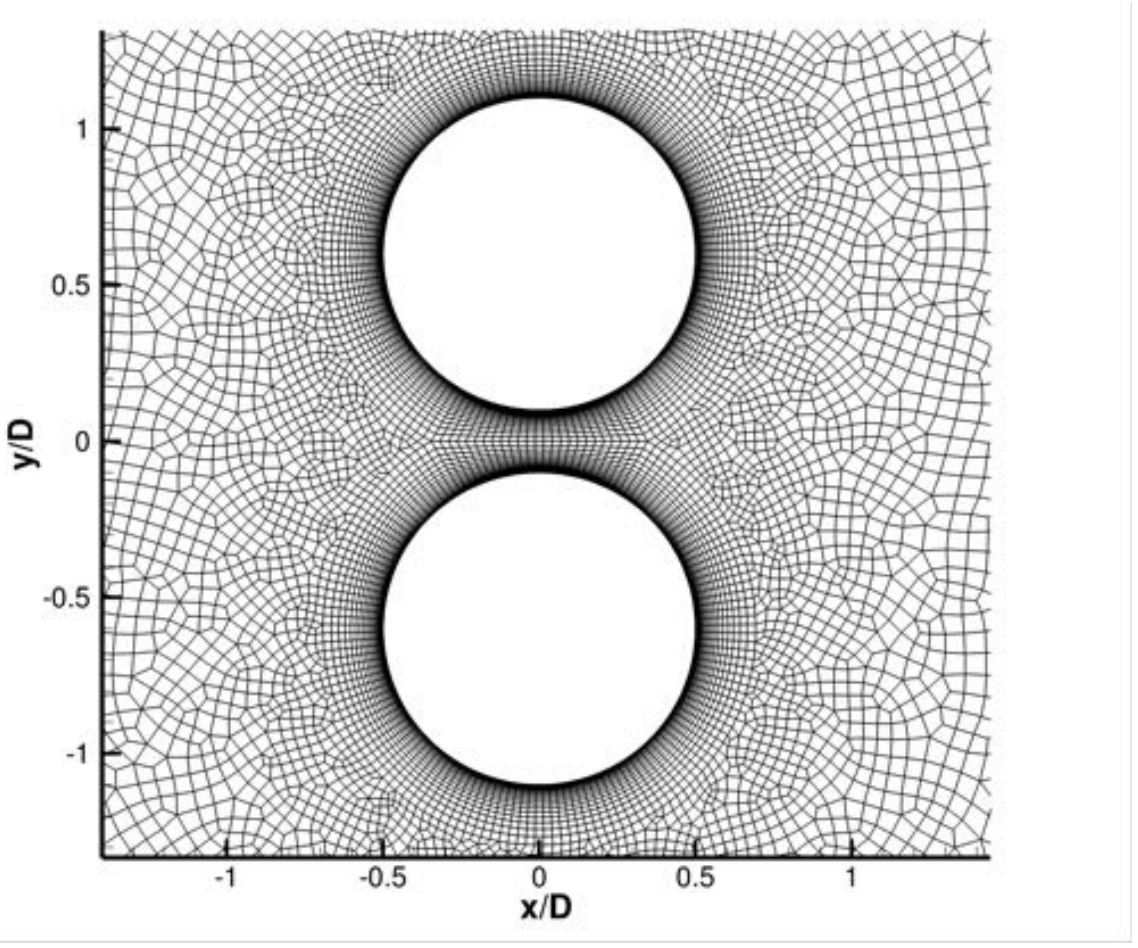

Fig. 2.2 Computational meshes for interaction between two cylinders with $G/D = 0.2$ and $\Delta r \leq 1.38 \times 10^{-3}$ and $N_c \geq 152$.

The test case in $G/D = 0.2,\ A_1/D = 0.1,\ f_1/f_n = 0.825,\ \zeta = 0$ and $m^* = 2.5$ is chosen for the mesh independence study. This is a challenging case, because of the large vibration amplitude of the passive cylinder, which results in a very small distance between the two cylinder at certain instances. The temporarily small proximity of the two cylinders adversely affects the accuracy of the computation, as the computational cells in the gap are greatly

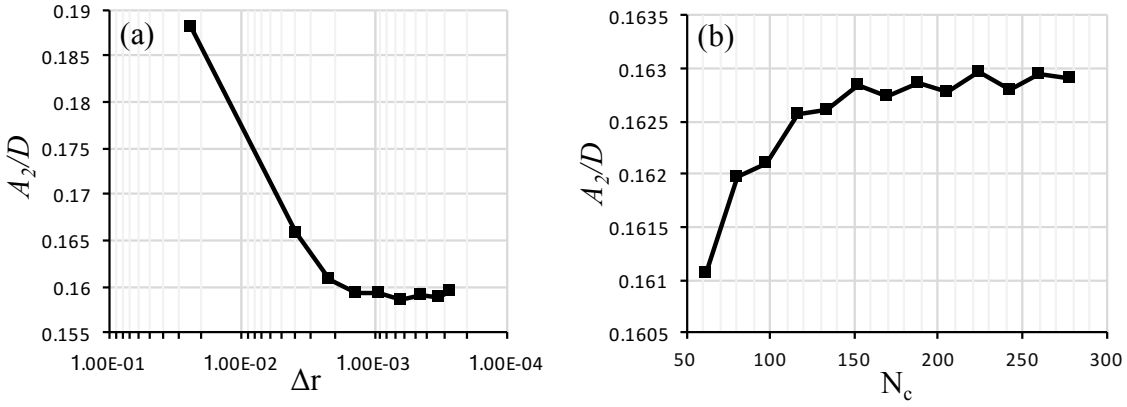

Fig. 2.3 Effect of Δr on the responding amplitude A_2 with $N_c = 116$ and Effect of N_c on the responding amplitude A_2 with $\Delta r = 1.25 \times 10^{-3}$, for the case $G/D = 0.2, A_1/D = 0.1, f_1/f_n = 0.825, m^* = 2.5$.

squeezed and stretched periodically. Simulations are conducted in two scenarios. Scenario (a) has a constant $N_c = 116$, with $\Delta r = 2.65 \times 10^{-4}$, 3.22×10^{-4}, 4.49×10^{-4}, 6.36×10^{-4}, 9.21×10^{-4}, 1.38×10^{-3}, 2.21×10^{-3}, 3.87×10^{-3} and 2.43×10^{-2} in a series of meshes with different resolutions. Scenario (b) has constant $\Delta r = 9 \times 10^{-4}$, while $N_c = 62$, 80, 98, 116, 134, 152, 170, 188, 206, 224, 242, 260 and 278 in a series of meshes with different resolutions. Figs. 2.3a and 2.3b show the variations of A_2/D with Δr and N_c, respectively. A_2 is calculated to be $(Y_{max} - Y_{min})/2$, where Y_{max} and Y_{min} are the maximum and minimum, respectively, of the Y_2 values in the last 50 periods of steady oscillations. It can be seen that the change in A_2/D is negligible when $\Delta r \leq 1.38 \times 10^{-3}$ and $N_c \geq 152$. In conclusion, a mesh with $\Delta r = 1.30 \times 10^{-3}$ and $N_c = 152$ would be sufficiently fine to achieve converged results. Hence, all the simulations with $A_1/D \leq 0.02$ adopted a resolution no coarser than this.

To ensure the mesh independence of cases with larger oscillation amplitude of the active cylinder. Mesh independence study has been conducted for the scenario of $G/D = 0.9, A_1/D = 0.477, f_1/f_n = 3.2, m^* = 1.5, \zeta = 0, Re_m = 10$ with a variety of mesh density as listed in Table 2.2. Based on these meshes, typical cases were tested as seen in Fig. 2.4. It can be seen that the mesh with normal density can already provide a decent accuracy. In order to be conservative, the dense mesh is chosen to run all the simulations with $0.02 < A_1/D \leq 0.477$, which is illustrated in Fig. 2.5.

An additional mesh independence study is carried out at $KC = 9, G/D = 2.5, A_1/D = 1.432, f_1/f_n = 2.8, m^* = 2, \zeta = 0, Re_m = 315$ where the active cylinder's amplitude is larger. Three sets of meshes were tested and compared for the suitability of the mesh density, as seen in Table 2.3. The amplitude in the first 200 oscillation periods of the active cylinder is

Table 2.2 Comparison of the passive cylinder's displacement with different meshes for $KC = 3, G/D = 0.9, A_1/D = 0.477, f_1/f_n = 3.2, m^* = 1.5, \zeta = 0, Re_m = 10$.

Mesh Resolution	Fine	Normal	Coarse	Very Coarse
N_c	152	134	86	50
Δr	0.00130	0.00144	0.00192	0.00597
N_{node}	30280	24050	15971	9722
$Y_{2,min}/D$	-0.04893	-0.04804	-0.04684	-0.04463
$Y_{2,max}/D$	-0.1982	-0.1972	-0.1955	-0.1930

calculated, and considering the irregular nature in regime G, the convergence is quite good. In addition, as seen in Fig. 2.6, the vortex shedding pattern is quite coherent already for three sets of the meshes. As a result, the dense mesh is chosen for the cases with large KC.

Table 2.3 Comparison of the passive cylinder's displacement with different meshes for $KC = 9, G/D = 2.5, A_1/D = 1.432, f_1/f_n = 2.8, m^* = 2, \zeta = 0, Re_m = 315$.

Mesh Resolution	Fine	Normal	Coarse
N_c	164	140	128
Δr	0.0030	0.0050	0.0058
N_{node}	33874	27625	22389
$Y_{2,min}/D$	-0.6871	-0.6645	-1.1603
$Y_{2,max}/D$	0.4568	0.4593	1.1915
$(Y_{2,max} - Y_{2,min})/2D$	0.5720	0.5619	1.1759

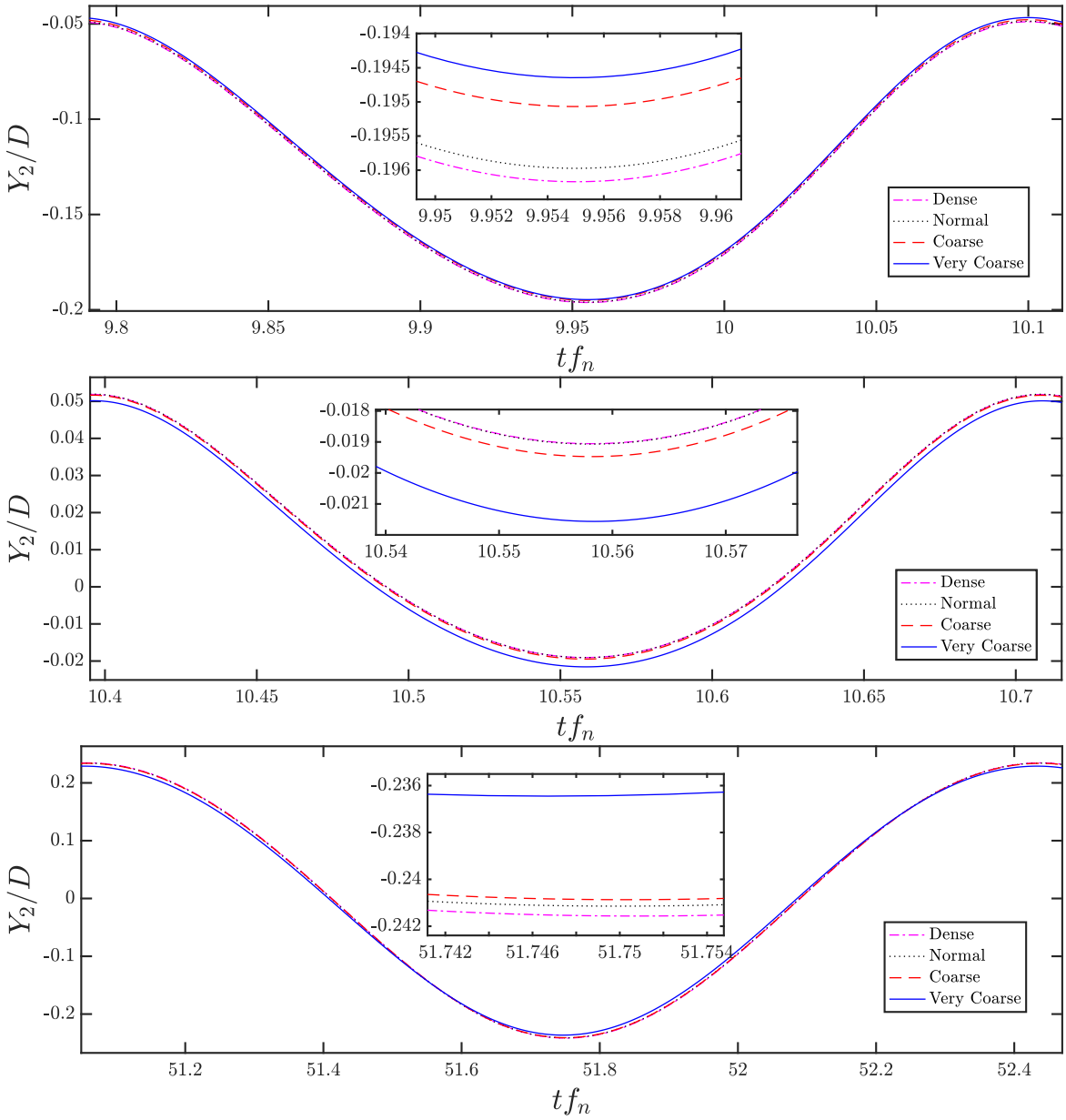

Fig. 2.4 Comparison of the passive cylinder's displacement time histories from different meshes for $G/D = 0.9, A_1/D = 0.477, m^* = 1.5, \zeta = 0$ and (a) $Re_m = 10, f_1/f_n = 3.2$, where the passive cylinder drifts towards the near side (b) $Re_m = 150, f_1/f_n = 3.2$, where the passive cylinder drifts towards the far side (c) $Re_m = 150, f_1/f_n = 0.725$, where the vibration amplitude is large due to the resonance.

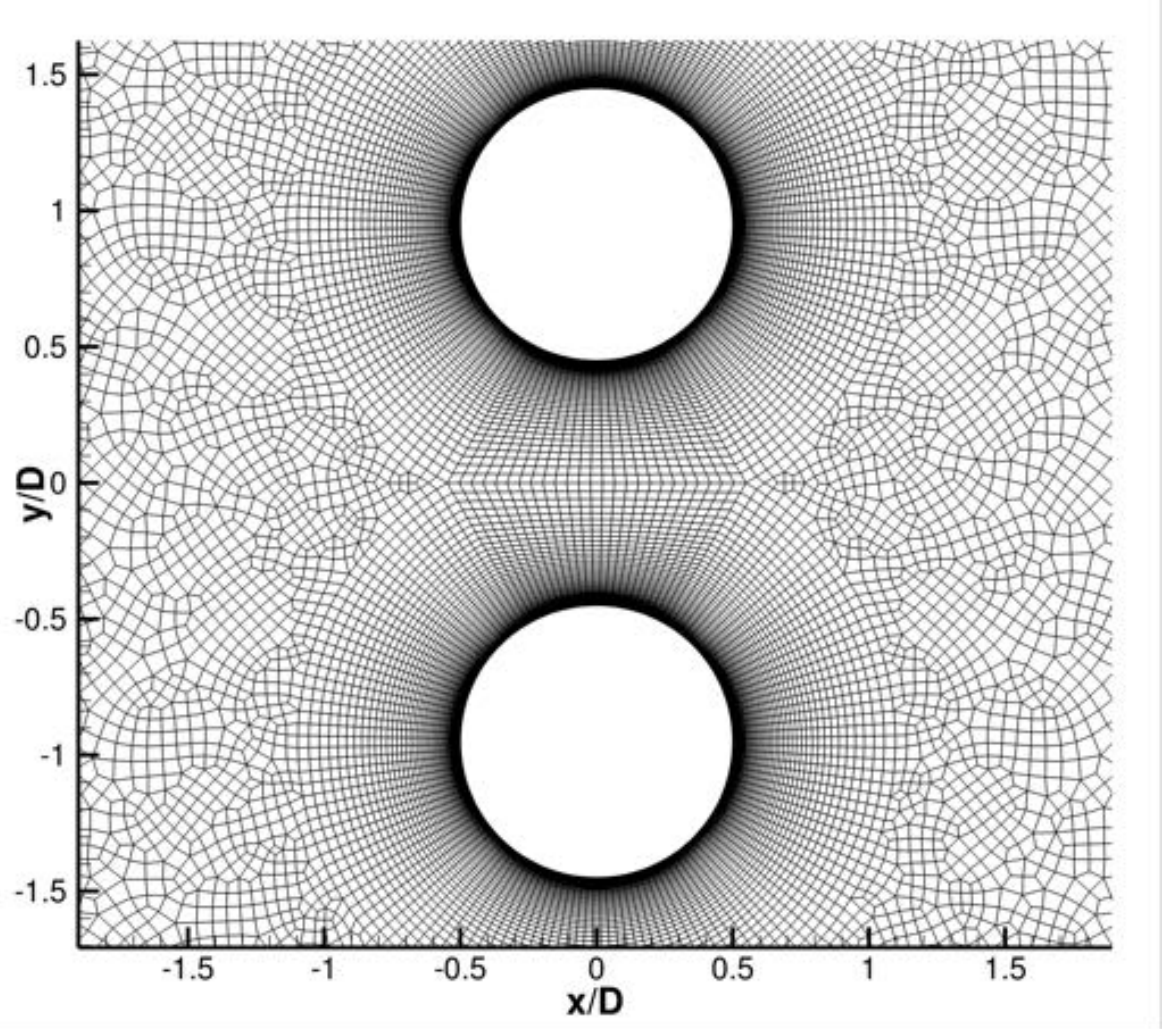

Fig. 2.5 Computational meshes for interaction between two cylinders with $G/D = 0.9$ with $\Delta r \leq 1.30 \times 10^{-3}$ and $N_c \geq 152$.

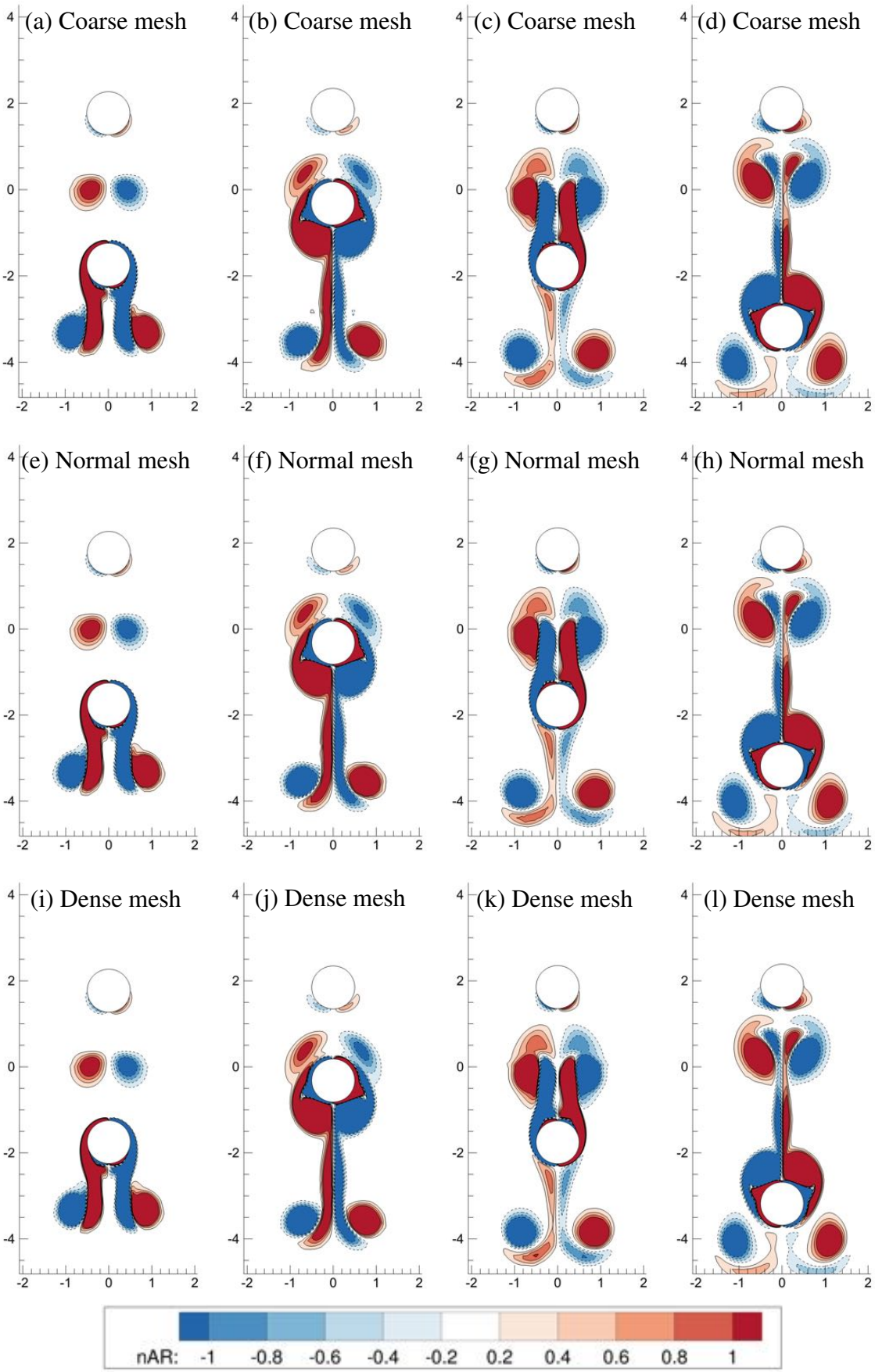

Fig. 2.6 Vorticity contours of the mesh independence case at $KC = 9, G/D = 2.5, A_1/D = 1.432, f_1/f_n = 2.8, m^* = 2, \zeta = 0, Re_m = 315$. (a-d) Coarse mesh (e-h) Normal mesh (i-l) Dense mesh.

2.4 Validation

The numerical methods, including the streamline upwind Petrov-Galerkin FEM, the solution of the vibration equation, treatment of the moving boundary and adaptation of the mesh close to the boundary, have all been validated in many previous studies (Zhao, 2013; Zhao and Yan, 2013; Zhao et al., 2013; Cui et al., 2014; Zhao and Cheng, 2014; Lin et al., 2016). With regard to this thesis, the problem of interest is a single cylinder oscillating harmonically in an otherwise still fluid at $KC = 5, Re_m = 100$ to validate our numerical method. The simulation is conducted on a mesh shown in Fig. 2.8, and the simulation results are compared with the experimental data obtained by Dütsch et al. (1998), as shown in figure 2.7. The horizontal and vertical components (u & v) of the simulated and measured velocities are compared along four horizontal sections (i.e. $y/D = 0.6, 0, -0.6$ and -1.2) at three phases (i.e. $\phi = 180^\circ, 210^\circ$ and 330°). It can be seen that the simulation results match well with the experimental data. These experimental data from Dütsch et al. (1998) are commonly used to validate numerical models regarding flow past cylinder scenarios (Guilmineau and Queutey, 2002; Yang and Balaras, 2006; Kim and Choi, 2006; Choi et al., 2007; Kim and Choi, 2019).

In addition to the harmonic oscillation of a single-cylinder, simulations were conducted upon a case study that involves the interaction between two cylinders to validate the present numerical method. In this case study, the active cylinder is forced to oscillate along the centre line of the two cylinders, whereas the passive cylinder is neutrally buoyant ($m^* = 1$) and is free to move in the fluid subject to unbalanced hydrodynamic force without any constraint of spring or damper. Initially, both cylinders are at rest, and the active cylinder impulsively starts the oscillation by moving towards the passive cylinder. The diameters of the two cylinders are identical, while the active cylinder's vibration amplitude is fixed at $A_1/D = 1.0$. The simulation results of the present numerical model are compared with that of Gazzola et al. (2012), who discovered the threshold Reynolds numbers, above which the passive cylinder is repelled away from the active cylinder, and below which the passive cylinder is attracted towards the active cylinder. The threshold Reynolds number is shown to be a function of the initial distance between the two cylinders, as seen in Fig. 2.9a. To illustrate how the threshold Reynolds number is obtained from the present simulations, the passive cylinder's displacements are plotted at a series of Reynolds numbers in Fig. 2.9b. The threshold Reynolds numbers obtained from the present model agree well with the results in Gazzola et al. (2012).

In addition, the current numerical model has also been validated extensively for simulations in regime A, A*, C, E, F and G by Zhao and Cheng (2014), and achieved very good agreement with the experimental results by Tatsuno and Bearman (1990).

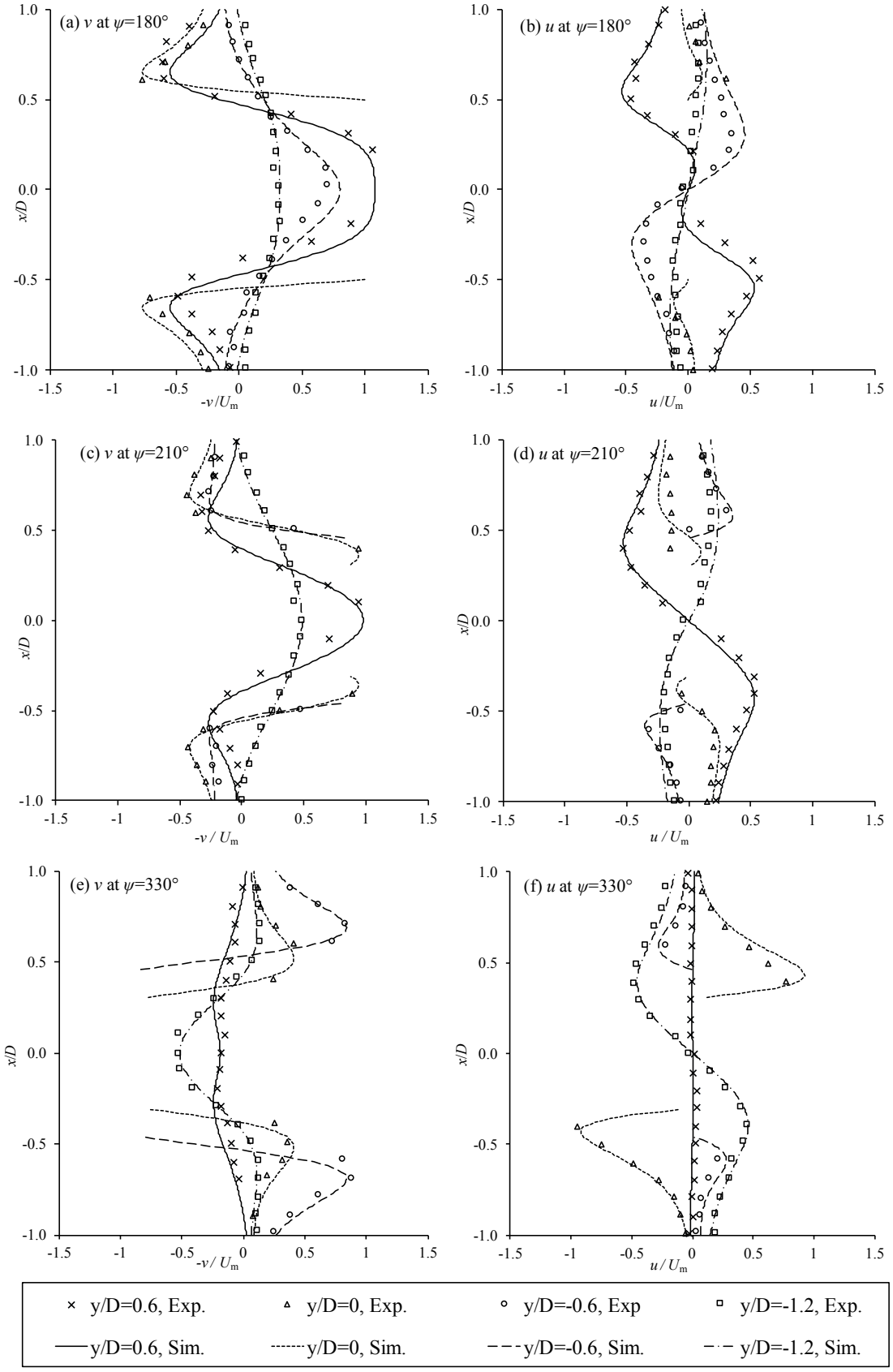

Fig. 2.7 Comparison of fluid velocity distribution between the numerical simulation results and the experimental data by Dütsch et al. (1998). The horizontal & vertical velocity components (u & v) of the simulation results (continuous lines) and measured data (discrete symbols) are compared along four horizontal lines (i.e. $y/D = 0.6, 0, -0.6$ and -1.2) at three different phases (i.e. $\phi = 180°, 210°$ and $330°$).

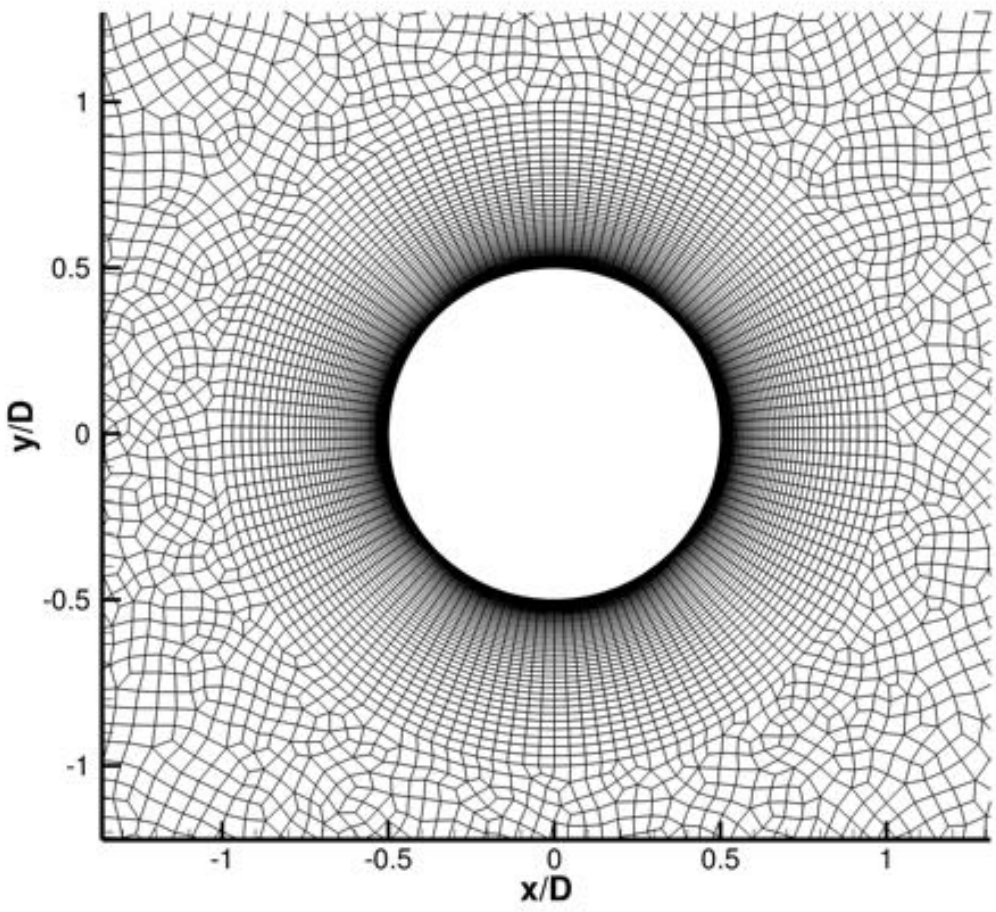

Fig. 2.8 Computational meshes for validation case of a single cylinder vibrating in an otherwise still fluid with $N_c = 134$ and $\Delta r = 1.83 \times 10^{-3}$.

2.5 Data Processing Techniques

This section explains the techniques to process and make sense of the data generated by a large number of simulations. Many scripts are created to automatically generate the input files, to efficiently exploit the high performance computing facilities and to aggregate the simulation results of 23,400 cases. Example data processing scripts are listed in Appendix A.

Chapters 3 to 5 only discuss a few representative cases to illustrate the physical pattern. However, the generality of the conclusions is ensured by scrutinisation on all 23,400 cases that has been simulated. The simulation results were automatically summarised into figures by small programmes and then manually examined.

This research deliberately implements the serial computing rather than parallel computing to eliminate the inefficiency due to additional data transfer cost. The simulations were all executed on HPC facilities. So the strategy was to run a large amount of serial cases at the

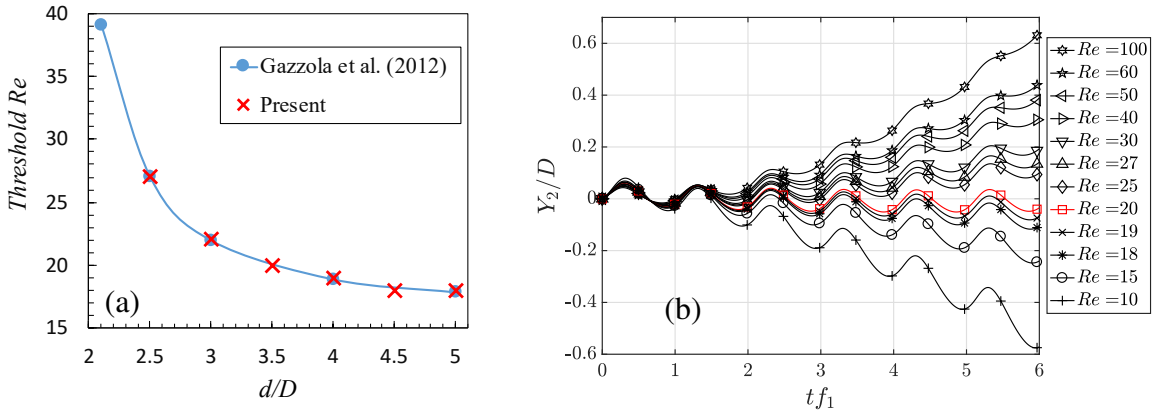

Fig. 2.9 (a) Threshold Reynolds numbers as function of the normalised centre-to-centre distance d/D, where $m^* = 1, A_1/D = 1$, and the active and the passive cylinders have identical diameters. The present simulation output agree well with the results from Gazzola et al. (2012). (b) Passive cylinder's non-dimensional displacement Y_2/D versus the time normalized by the active cylinder vibration frequency tf_1, for a series of Reynolds numbers (from top to bottom curves $Re_m = 100, 60, 50, 40, 30, 27, 25, 20, 19, 18, 15, 10$), with $A_1/D = 1, d/D = 3.5$. Here, the threshold Reynolds number is 20.

same time, typically hundreds or thousands of cases for each batch. Many bash scripts were created to execute the simulation on HPC and to transfer the large amount of data back to local nodes efficiently by compressing the files.

Many figures in the results chapters Chapters 3 to 5 illustrate the variation of the passive cylinder's responding amplitude. In this thesis, for the cases with periodical interaction, the amplitude of passive cylinder's vibration is calculated as $A_2 = (Y_{2,max} - Y_{2,min})/2$, where $Y_{2,max}$ and $Y_{2,min}$ are the maximum and minimum displacement in the last 50 periods of steady vibration. The vibration centre drift of the passive cylinder in Chapter 5 is calculated as $\Delta\overline{Y}_2 = (Y_{max} + Y_{min})/2$.

The displacement/force spectra of the passive cylinder's vibration were auto-generated by programmes. The displacement spectra are produced by conducting Fast Fourier Transform (FFT) to the original displacement time history. FFT is an algorithm of signal processing to quickly execute the discrete Fourier transform. It can be used to investigate the time histories on the frequency domain and thus to identify patterns that is usually undistinguishable in the time domain. It can be understood as using many sinusoidal components like $y = Asin(\omega t + \phi)$ to fit the time histories. The results of FFT can be demonstrated by two figures. The first figure's x-axis is the frequency ω for all the components with its y-axis being the amplitude A of each corresponding components. The second figure has the same x-axis with y-axis being the phase ϕ of each corresponding components. A series of FFT results can be combined together by adding a third axis. In Chapters 3 to 5, the third axis will be the

active cylinder's oscillation frequency f_1/f_n and thus a three-dimensional figure is plotted to demonstrate the physical pattern. Since FFT can also extract ϕ of the frequency components, the phase difference between the passive cylinder and the active cylinder is also extracted by FFT. To ensure the accuracy of the FFT analysis, in this thesis, at least 50 periods of steady-state periodical vibrations time history are used in the transform. Zero padding is also applied during the transform, which, although adds some noise to the low amplitude regime in the frequency domain, greatly increases the accuracy while extracting the peak amplitude.

In Chapter 6, for cases with relatively high KC and thus with irregular time history, the vibration amplitude and the vibration centre shift may both be functions of time, and we calculate them by carrying out fast Fourier transform to converting the displacement time history from the time domain to the frequency domain. In the frequency domain, the low frequency part represents the vibration centre shift, while the high frequency part stands for the vibration relative to the vibration centre, i.e. harmonics. We extract the high frequency parts, and convert the high frequency part back to time domain, and then calculate its amplitude as $A_2 = (Y_{2,max} - Y_{2,min})/2$, since the extracted time history is very regular.

2.6 Chapter Summary

This chapter describes the methodology of this study. The problems setup is illustrated and the corresponding dimensional analysis is carried out to determine the 6 non-dimensional groups. The governing equation is presented and the computational methods are discussed. Detailed mesh independence study is conducted to choose the appropriate mesh density and validation is achieved by comparing to both experimental and numerical studies with similar case setups.

Chapter 3

Effects of Parameters Associated With the Active Cylinder in Periodic Regimes

This chapter examines the effects of the active cylinder's frequency f_1/f_n and its oscillation amplitude A_1/D on the passive cylinder's oscillation amplitude A_2/D. Here, the natural frequency f_n is defined as $f_n = \sqrt{k/m}/2\pi$. k is the stiffness of the spring mounted to the passive cylinder. m is mass of the passive cylinder. f_1/f_n is considered to be the most influential parameter for A_2/D. The resonance of the passive cylinder occurs at $f_1/f_n \approx f_w/f_n = \sqrt{m^*/(m^*+C_A)}$, where C_A is the added mass coefficient of the passive cylinder, i.e. the added mass divided by the displaced fluid mass by the cylinder, and f_w is the immersed natural frequency of the passive cylinder in water. The effects of A_1/D is presented together with f_1/f_n for a clear comparison between their effects and also to demonstrate their coupled effect.

To better demonstrate the meaning of the active cylinder's frequency f_1/f_n and its oscillation amplitude A_1/D, the forced oscillation equation of the active cylinder, i.e. Equation (2.4), is restated here:

$$Y_1 = A_1 \sin(2\pi f_1 t) \tag{3.1}$$

3.1 Resonance of Passive Cylinder

In the periodic regimes, the vibration of the passive cylinder will converge after a few initial periods, as seen in Figure 3.1, where the time history of the passive cylinder is illustrated. So the converged amplitude A_2 is a representative value to describe the vibration of the passive cylinder. In this thesis, for the cases with periodical interaction, the amplitude of

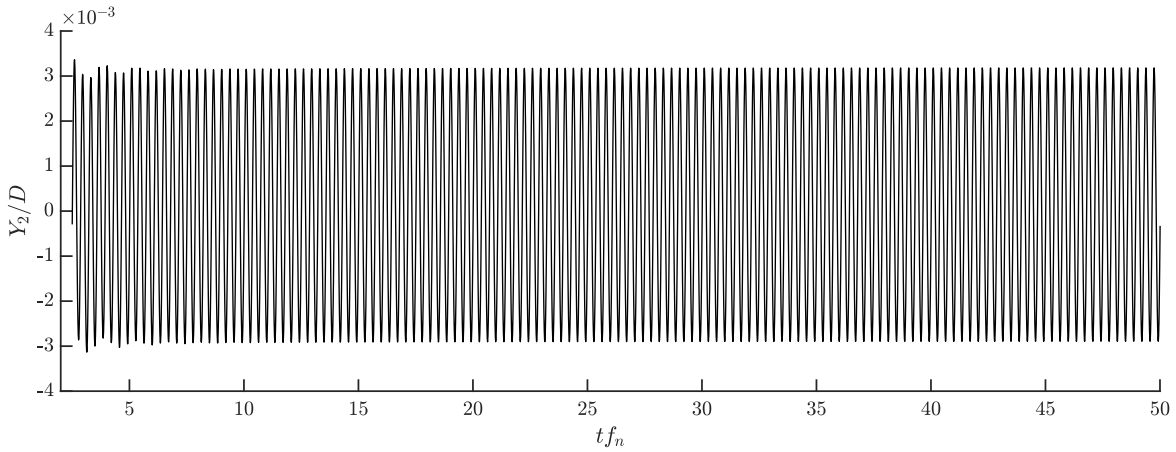

Fig. 3.1 Convergence time history for a case in periodic regime A/A^*. After a few initial steps, the vibration amplitude of the passive cylinder converges.

passive cylinder's vibration is calculated as $A_2 = (Y_{2,max} - Y_{2,min})/2$, where $Y_{2,max}$ and $Y_{2,min}$ are the maximum and minimum displacement in the last 50 periods of steady vibration. The amplification factor A_2/A_1 is often used to compare amplitude of the passive cylinder with that of the active cylinder. If $A_2/A_1 > 1$, it means that the vibration of the passive cylinder is even larger than that of the active cylinder. Figure 3.2 shows the variation of the amplification factor A_2/A_1 with f_1/f_n. The major resonance peak occurs at the immersed natural frequency $f_1/f_n = 0.775 \approx f_w/f_n = \sqrt{m^*/(m^* + C_A)}$ (assuming $C_A = 1$), whereas another minor peak of A_2/D takes place at *half* the immersed natural frequency $f_1/f_n = 0.375 \approx 0.5 f_w/f_n$. The reason for the existence of a minor peak will be discussed later.

The oscillation amplitude of the active cylinder and the passive cylinder is in general linearly correlated. Figure 3.2 demonstrates the relationship between the active cylinder vibration amplitude A_1/D and the passive cylinder vibration amplitude A_2/D at $\zeta = 0$ and 0.2. At $\zeta = 0$, it can be seen in Fig. 3.2a that A_2/D generally follows a linear relationship with A_1/D, except near the two resonance peaks. Other non-dimensional parameters have a much smaller influence on this $A_1 - A_2$ relationship than the f_1/f_n. At $\zeta \geq 0.2$, the linear correlation of vibration amplitude is strengthened between the passive cylinder A_2/D and the active cylinder A_1/D, as demonstrated in Fig. 3.2b. Here, this linear relationship is examined by the variation of amplification factor A_2/A_1 with the amplitude of the active cylinder A_1/D, as seen in Fig. 3.2b. The $A_2/A_1 - f_1/f_n$ curves overlap each other regardless of the varying A_1/D, which indicates a strong linear correlation, even at resonance.

Harmonics are discovered in the response vibration of the passive cylinder, and sometimes, the secondary harmonic can exhibit amplitude larger than the fundamental harmonic, causing secondary resonance at half the immersed natural frequency. In Fig. 3.3, the FFT-generated

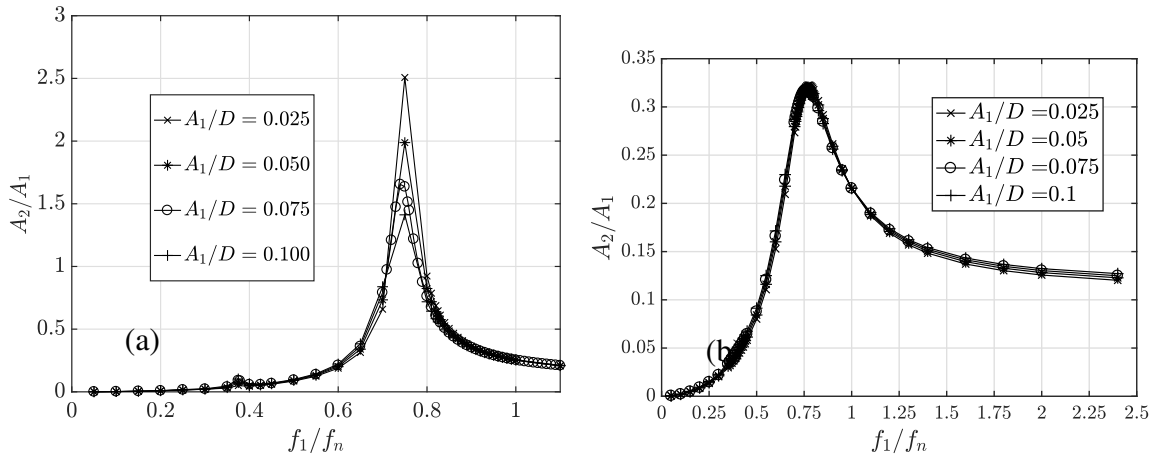

Fig. 3.2 Variation in A_2/A_1 with f_1/f_n at $G/D = 0.4, A_1/D = 0.025 - 0.1, m^* = 1.5$, and (a) undamped $\zeta = 0$ (b)damped $\zeta = 0.2$. A_2 and A_1 are linearly correlated unless when the resonance occurs or the damping ratio $\zeta >= 0.2$.

displacement amplitude spectra show that the vibration history of the passive cylinder in each case typically contains three distinct frequency components. The corresponding frequency for each frequency components is equal to one, two, or three times of f_1/f_n as $f/f_n = nf_1/f_n, n \in \{1,2,3\}$, i.e. at least three *harmonics* exist. As a result, when the active cylinder vibrates at a frequency with $f_1/f_n = (f_w/f_n)/n$ ($n \in \{1,2,3\}$), one of the harmonics thus reaches the immersed natural frequency, as $f/f_n = nf_1/f_n \approx n[(f_w/f_n)/n] = f_w/f_n$ ($n \in \{1,2,3\}$). Since $f/f_n = f_w/f_n$, resonance then occurs at that particular harmonic and yields a significant increase in its amplitude. For example, Fig. 3.3a, 3.3b, and 3.3c show the close-up of the amplitude spectra at $f_1/f_n \approx f_w/3f_n$, $f_1/f_n \approx f_w/2f_n$, and $f_1/f_n \approx f_w/f_n$, respectively. At $f_1/f_n = 0.25 \approx f_w/3f_n$, three rows of noticeable frequency components are observed, as seen in Fig. 3.3a. These rows, from the furthest to the nearest row, correspond to the harmonics with $f/f_n = f_1/f_n$, $f/f_n = 2f_1/f_n$ and $f/f_n = 3f_1/f_n$. Overall, the furthest row of $f/f_n = f_1/f_n$ has the largest amplitude. The middle row of $f/f_n = 2f_1/f_n$ has the second largest values of the amplitude. The nearest row of $f/f_n = 3f_1/f_n$ has the smallest values of the amplitude. In Fig. 3.3a, the amplitude values of the third harmonic with $f/f_n = f_w/3f_n$ reach their maximum at $f_1/f_n = 0.25 \approx f_w/3f_n$ due to resonance, as seen in the red dashed rectangle of Fig. 3.3a. Similarly, in Fig. 3.3b, two sets of harmonics are observed, i.e. $f/f_n = f_1/f_n$, $f/f_n = 2f_1/f_n$. The amplitude values of the harmonics with $f/f_n = 2f_1/f_n$ peak at $f_1/f_n = 0.375 \approx f_w/2f_n$, as seen in the red dashed rectangle of Fig. 3.3b. Here, the amplitude values of the components on the middle row also exceeds that of the furthest row, meaning that the second harmonic has an amplitude larger than the first harmonic. This results in the minor peak found in Fig. 3.2a. In Fig. 3.3c, only one

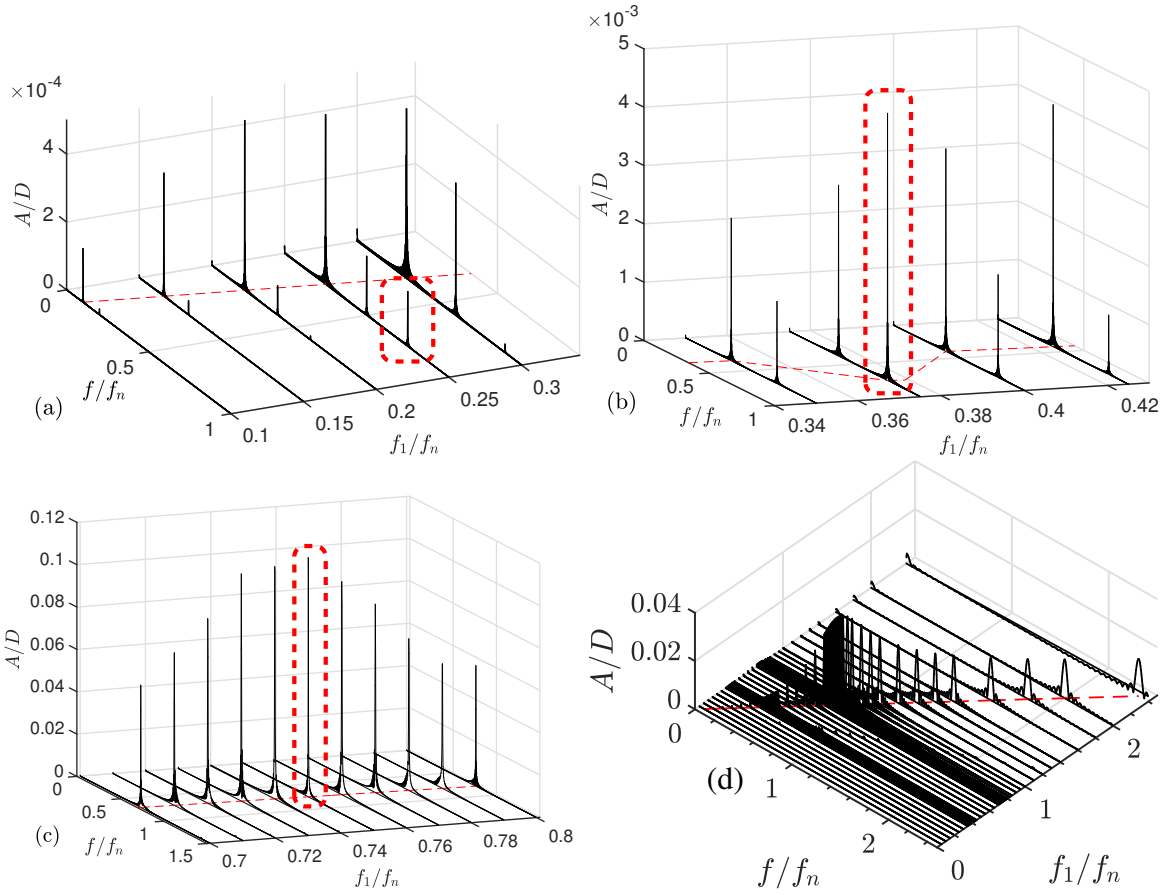

Fig. 3.3 Amplitude spectra showing the response of the passive cylinder with various f_1/f_n at $G/D = 0.4$, $A_1/D = 0.075$, $m^* = 1.5$. (a) FFT spectra at $f_1 = f_w/3 \approx 0.25$ (b) FFT spectra at $f_1 = f_w/2 \approx 0.375$ (c) FFT spectra at $f_1 = f_w \approx 0.75$ (d) An overview of FFT spectra. It can be seen that, at $f_1 = f_w/2$, there are two distinct frequencies while at $f_1 = f_w$ there is only one. The red dashed thin line tracks the dominant frequencies. The red dashed thick squares highlight the resonating frequency component.

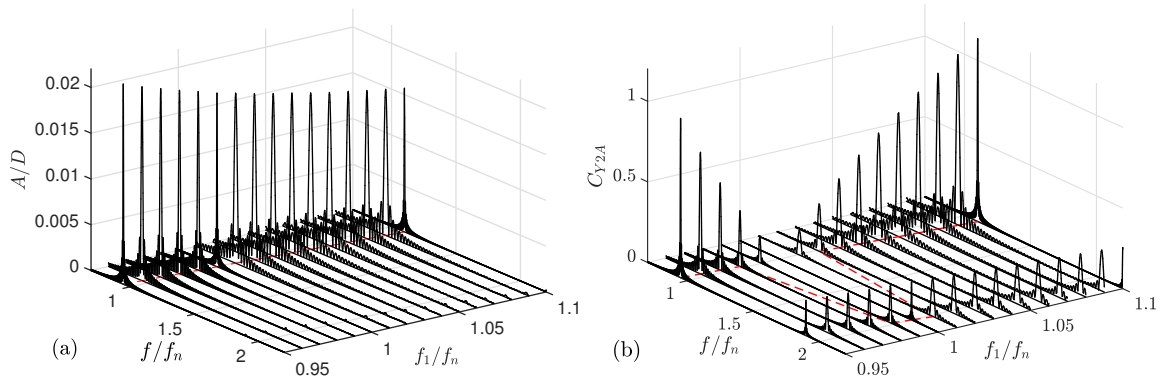

Fig. 3.4 Amplitude spectra showing (a) responding displacement of the passive cylinder and (b) force coefficient upon the passive cylinder at $0.95 \leq f_1/f_n \leq 1.1$, $G/D = 0.4$, $A_1/D = 0.075$, $m^* = 1.5$, $\zeta = 0$, $Re_m = 100$. The dominant frequencies for displacement and force are different.

row of the frequency components ($f/f_n = f_1/f_n$) is identified, whose values of amplitude reaches maximum at the immersed natural frequency $f_1/f_n = 0.75$. This constitutes the major resonance peak in Fig. 3.2. Fig. 3.3d provides an overview of the FFT spectra. The red dashed line denotes the dominant frequency in each case. It is clear that the dominant frequency is equal to f_1/f_n except at $f_1/f_n = 0.375 \approx f_w/2f_n$, where the minor resonance is observed. Although the above analysis is for a specific case with f_1/f_n being the only variable, all other cases simulated with various $A_1/D, G/D, f_1/f_n, m^*, Re_m, \zeta$ follow almost the same pattern. The multiple frequency components observed in the passive cylinder is as if the active cylinder is play a sound of a single tone and the passive cylinder responds with another sound of harmonics.

The variation of force acting on the passive cylinder C_{Y2} with f_1/f_n generally follows the same pattern as the displacement, except at $0.95 < f_1/f_n < 1.1$ with $\zeta = 0$. In this range, the displacement amplitude spectra only have one row of noticeable components for $f/f_n = f_1/f_n$, as shown in Fig. 3.4a, and their amplitude decreases steadily with the active cylinder frequency f_1/f_n. In contrast, at the same range of $0.95 < f_1/f_n < 1.1$, two rows of distinct frequency components, i.e. $f/f_n = f_1/f_n$ and $f/f_n = 2f_1/f_n$, are found in the force amplitude spectra shown in Fig. 3.4b. At $f_1/f_n = 1$, the amplitude of the further row with $f/f_n = f_1/f_n$ reaches its minimum and becomes much smaller than the nearer row. Meanwhile, the amplitude of nearest row $f = 2f_1$ increases slightly with f_1/f_n. It can be seen that a discrepancy between the dominant frequencies of Y_2 and C_{Y2} is discovered at $0.99 \leq f_1/f_n \leq 1.01$, which is demonstrated by the red dashed lines tracking the dominant frequencies at $0.99 \leq f_1/f_n \leq 1.01$.

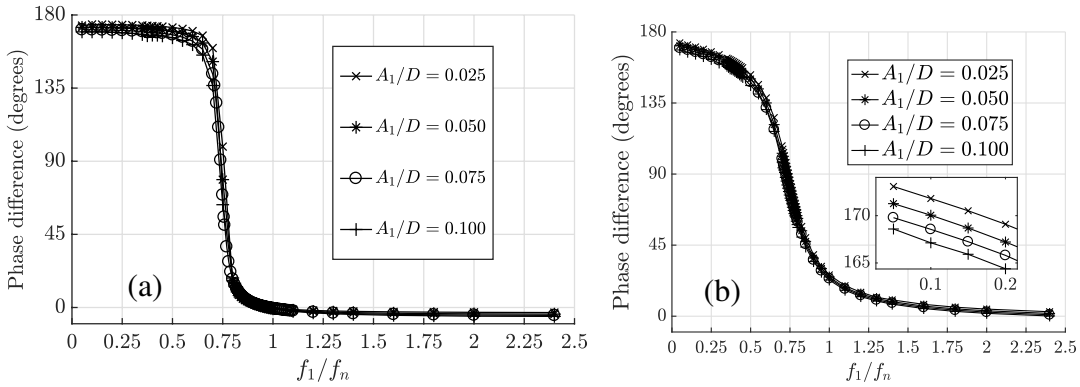

Fig. 3.5 Variation of the oscillation phase difference $\Delta\phi_{21}$ between the passive and the active cylinder (for the fundamental frequency components) with f_1/f_n at $A_1/D = 0.025 - 0.100, m^* = 1.5, G/D = 0.4, Re_m = 100$ and (a) $\zeta = 0$ (b) $\zeta = 0.2$. The increase of the active cylinder oscillation frequency causes the phase difference to shift from anti-phase to in-phase at the immersed natural frequency. $\Delta\phi_{21}$ decreases with A_1/D. At $\zeta = 0$, A_1/D affects more the phase difference at low frequencies compared with that at $\zeta = 0.2$.

3.2 Phase Lag Shift from Anti-phase to In-phase

The phase difference between the vibration of the passive cylinder and the active cylinder changes for 180° when the active cylinder's oscillation frequency increases beyond the passive cylinder's resonance frequency. The phase difference is defined as the vibration phase of the passive cylinder minus that of the active cylinder, i.e. $\Delta\phi_{21} = \phi_2 - \phi_1$, where the phases of the passive cylinder and the active cylinder are obtained through FFT. The phase difference is dominantly controlled by the active cylinder vibration frequency f_1/f_n. As seen in Figure 3.5, a 180° phase jump for $\Delta\phi_{21}$ occurs at the immersed natural frequency, below which the two cylinders vibrate in anti-phase, i.e. $\Delta\phi_{21} \approx 180°$, and above which they vibrate in phase, i.e. $\Delta\phi_{21} \approx 0°$. The phase jump frequency is equal to the resonance frequency, and the resonance occurs when $\Delta\phi_{21} \approx 90°$. The phase difference is not sensitive to other parameters except damping ratio ζ. $\Delta\phi_{21}$ decreases slightly with active cylinder vibration amplitude ratio A_1/D at low active cylinder frequency f_1/f_n. At $\zeta = 0$, this impact of A_1/D diminishes with f_1/f_n, demonstrated as the overlapped curves in Fig. 3.5a, whereas, at $\zeta = 0.2$, the impact of A_1/D remains constant, as seen in Fig. 3.5b.

3.3 Effects on Flow Field

In regimes A and A^*, no vortex shedding is identified and the flow is laminar and symmetrical, which reflects the feature of the regime A^* for single cylinder vibration. There are two types

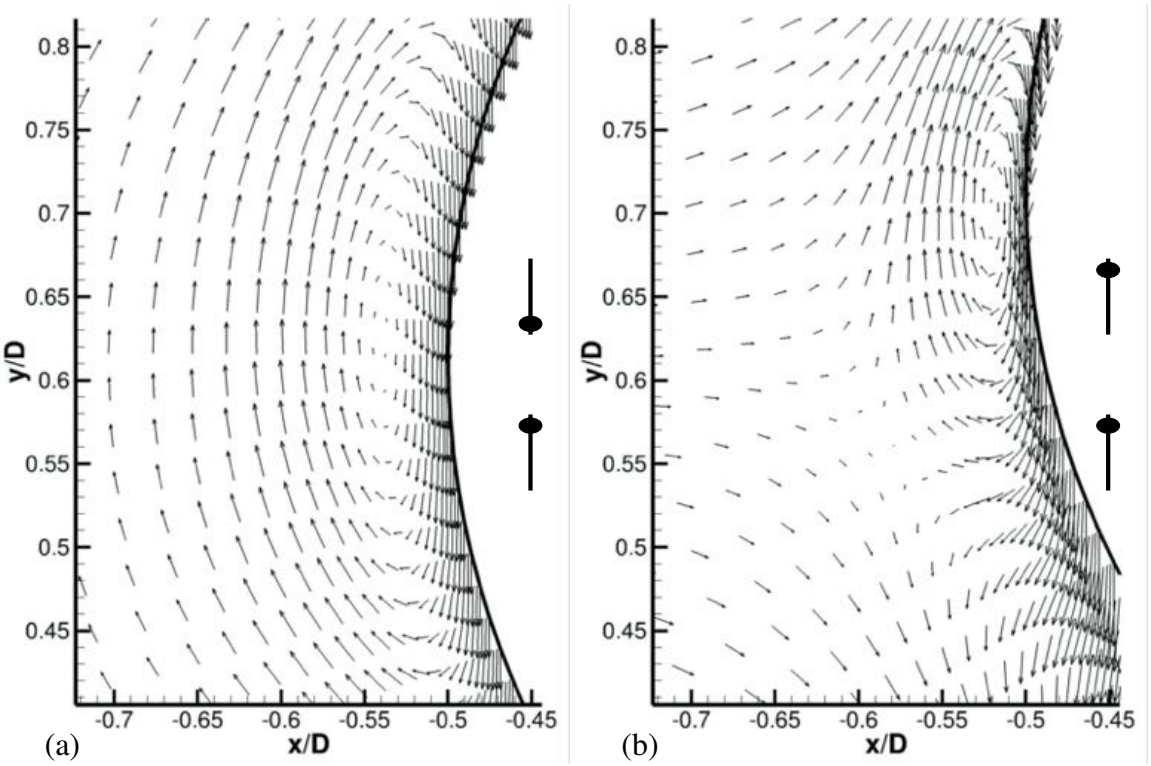

Fig. 3.6 Velocity vectors on the left of the passive cylinder at $G/D = 0.4, A_1/D = 0.075, m^* = 1.5, \zeta = 0, Re_m = 100$, and $\phi_1 = 45^\circ$ with (a) $f_1/f_n = 0.74$, $\Delta\phi_{21} = 90.7^\circ$ and (b) $f_1/f_n = 1.00$, $\Delta\phi_{21} = 0.58^\circ$. The vortex is always attached to the surface of the cylinders on their two sides, but it is dissipated before they can detach from the surface. $\Delta\phi_{21}$ is found to have significant influence on the flow field. The velocity vector is drawn on every grid point and the vector scale factors are (a) 0.06 grid units/magnitude and (b) 0.6 grid units/magnitude.

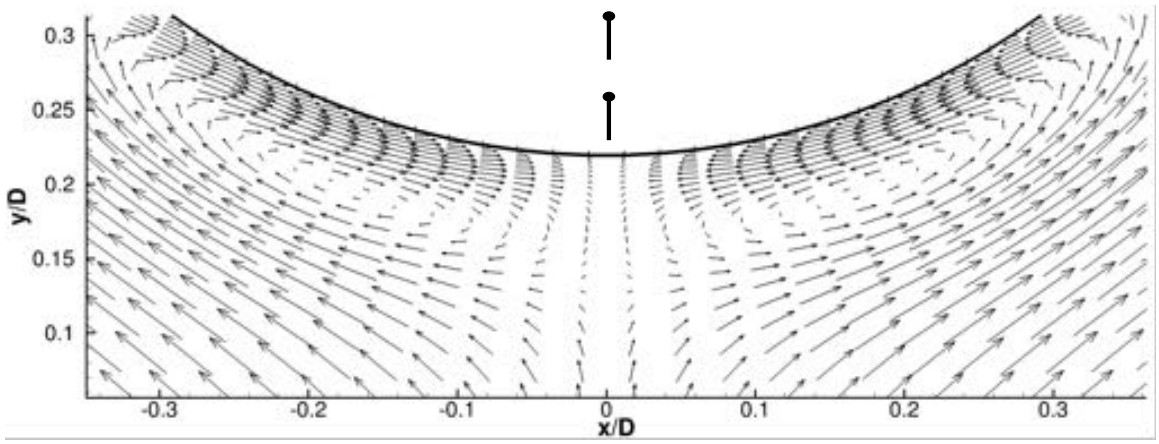

Fig. 3.7 Velocity vectors ($u_i^* = u_i/f_nD$) at $f_1/f_n = 1.00$, $\phi_1 = 0°$. A pair of small vortices show up in the wake of the passive cylinder when the passive cylinder reaches its highest or lowest position. These tiny vortices only exist for a short period of time in each cycle. The velocity vector is drawn on every grid point. The vector scale factor is 1.6 grid units/magnitude.

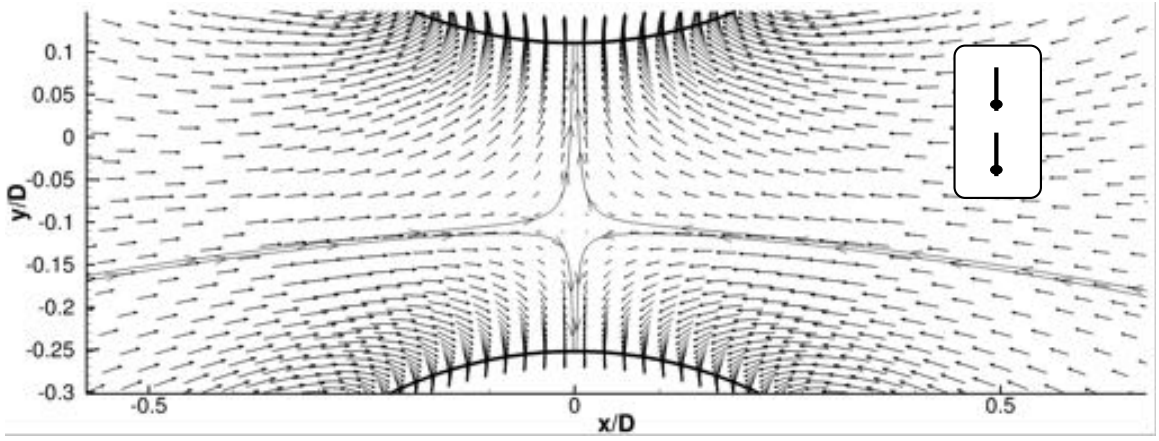

Fig. 3.8 Velocity vectors at $f_1/f_n = 0.74$ and $\phi_1 = 135°$ with $G/D = 0.4, A_1/D = 0.075, m^* = 1.5, \zeta = 0, Re_m = 100$. At exactly $90° < \phi_1 < 180°$, the zero-velocity point travels from the bottom of the passive cylinder (at $\phi_1 = 90°$) to the top of the active cylinder (at $\phi_1 = 180°$). The velocity vector is drawn on every grid point.

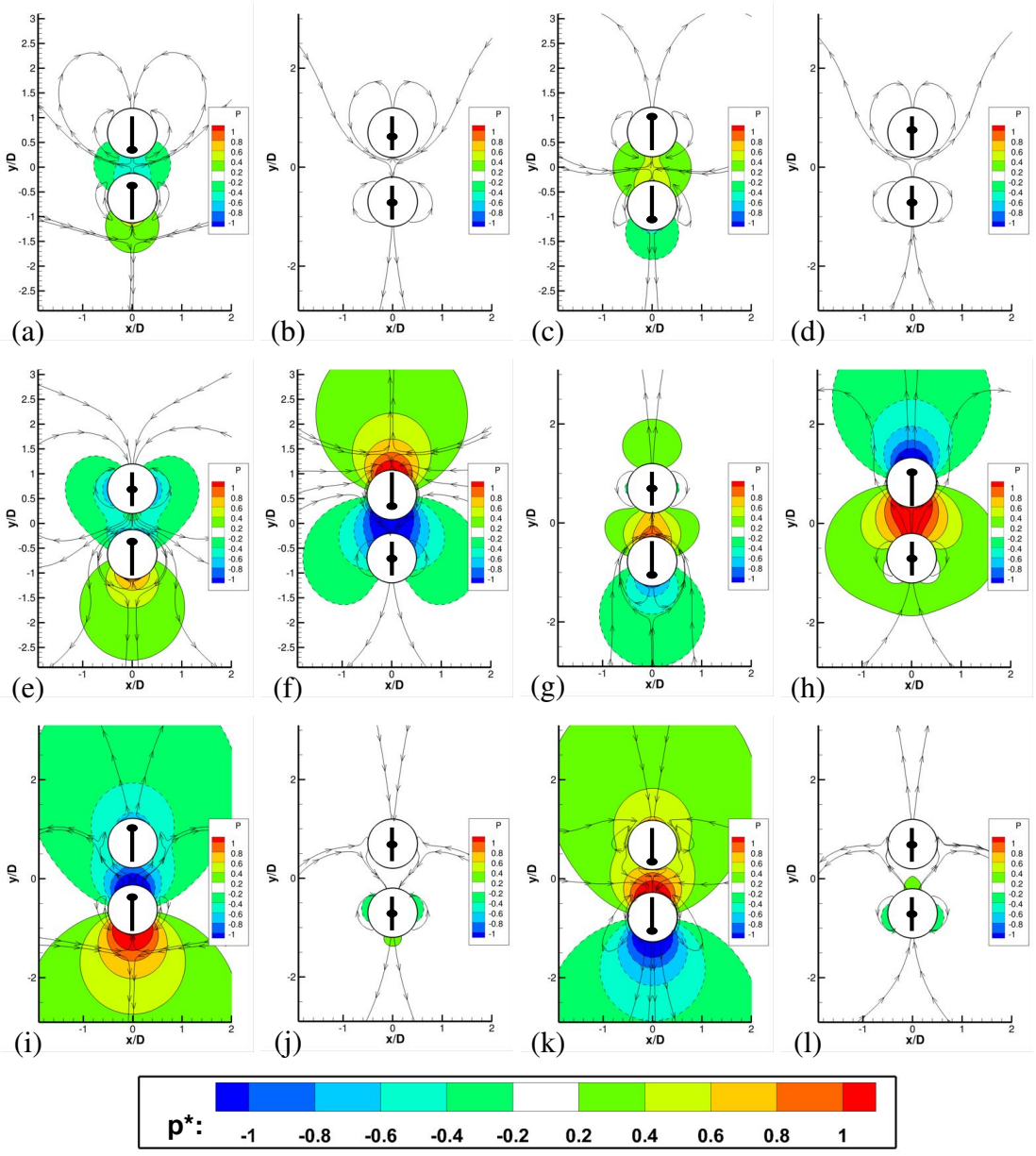

Fig. 3.9 Non-dimensional pressure p^* contours at $\phi_1 =$ (a & e & i) 0°, (b & f & j) 90°, (c & g & k) 180°, (d & h & l) 270°. (a-d) $f_1/f_n = 0.55$, $\Delta\phi_{21} = 168.71°$; (e-h) $f_1/f_n = 0.74$, $\Delta\phi_{21} = 90.673°$; (i-l) $f_1/f_n = 1.0$, $\Delta\phi_{21} = 0.582°$ with $G/D = 0.4, A_1/D = 0.075, m^* = 1.5, \zeta = 0, Re_m = 100$. The motion of the passive cylinder is found to have great influence on the distribution of pressure. Streamlines are plotted to show the status of the fluid.

of hydrodynamic forces upon the cylinder surface, i.e. shear and pressure forces. In the present study, the pressure force always has an amplitude larger than shear force, so the pressure force is the dominant contributor to the motion of the passive cylinder. Therefore, pressure contours are used to visualise the pressure distribution around the cylinders. For comparison purposes in different configurations, corresponding figures are with the same phase of the active cylinder's vibration, ϕ_1. $\phi_1 = 0^\circ$ is defined as the moment when the active cylinder is at its highest position. In the following discussion, the default condition is $G/D = 0.4$, $A_1/D = 0.075$, and $m^* = 1.5$. The flow fields at different values of f_1/f_n are examined because f_1/f_n has a dominant effect upon the flow field compared with other non-dimensional groups.

In regimes A and A^*, for both the active and the passive cylinders, vortices are generated on two sides of the cylinder at every f_1/f_n, but the vortices are dissipated before they can detach from the surface. This vortex generation-dissipation process occurs twice in each cycle of the vibration. Figure 3.6 shows two typical flow patterns observed at $f_1/f_n = 0.74$ and $f_1/f_n = 1.0$ respectively. At $f_1/f_n = 0.74$, the first type of the flow pattern is observed, as seen in figure 3.6a. When the passive cylinder moves downwards, the fluid is still moving upwards due to the previous upward motion of passive cylinder. This creates a vortex that moves outwards as well as upwards relative to the passive cylinder. The vortex grows larger as it moves out, but eventually, the streamlines can no longer be closed, and thus the vortex is dissipated. This process can be affected by f_1/f_n. At $f_1/f_n = 0.74$, the resonance occurs and the amplification factor is large, i.e. $A_2/A_1 \approx 1.7$. This means that the passive cylinder vibration amplitude is much larger than that for the active cylinder, and the flow field close to the passive cylinder is dominantly controlled by the passive cylinder itself. Consequently, the velocity vector field near the passive cylinder looks very similar to a single cylinder vibrating in still fluid. In contrast, at $f_1/f_n = 1.00$, we see the second type of the flow pattern, as demonstrated in figure 3.6b. Since the passive cylinder amplitude is much smaller than that for the active cylinder, as $A_2/A_1 \approx 0.25$, the flow around the passive cylinder is greatly influenced by the active cylinder, which results in a unique flow pattern. A zero-velocity point can be seen close to the vortex at the coordinate of about $(-0.58, 0.57)$. The fluid below that point has been dragged down due to the downward motion of the active cylinder while the fluid above is still moving up due to inertia, forming a vortex smaller and weaker than that at $f_1/f_n = 0.74$. It is also interesting that the position of the zero-velocity point is relatively stable throughout the entire cycle. If higher f_1/f_n is applied, the zero-velocity point appears upwards.

At $f_1/f_n = 1.00$, when the passive cylinder has either reached its highest or lowest position, i.e. $\phi_1 \approx 0^\circ$ or 180°, a pair of vortices appears below the passive cylinder, as seen

in figure 3.7. This is because the active and the passive cylinders move in phase and the upward motion of the passive cylinder causes the fluid to flow down along its surface and to collide with the fluid pushed up by the active cylinder. The two flows with opposite directions collide, and therefore a pair of vortices are generated. Conversely, if the active and the passive cylinders are both moving downward, reaching their lowest positions, a pair of vortices with opposite vorticity is produced.

At $f_1/f_n = 0.74$, a moving zero-velocity point is found in the gap and on the boundary dividing the fluids flowing upwards and the fluids going downwards, as seen in Fig. 3.8. This point is found to travel downward from the bottom of the passive cylinder to the top of the active cylinder only, which occurs twice in each cycle. At $f_1/f_n = 0.74$, the oscillation phase difference is $\Delta\phi_{21} = 90^\circ$. Therefore, for every 90°, the passive cylinder and the active cylinders switch between moving in the same direction and in the opposite direction. For example, in figure 3.8, the zero-velocity point appears when the passive cylinder and the active cylinders are moving in opposite directions, i.e. towards each other or away from each other, and that point travels only from the passive cylinder to the active cylinder. This is because A_2/D is larger than A_1/D, i.e. $A_2/A_1 \approx 1.7$, and thus the passive cylinder has a larger maximum velocity. At $90^\circ < \phi_1 < 180^\circ$, the passive cylinder is accelerating to its maximum upwards velocity, while the active cylinder is decelerating to zero velocity and moving downwards to its lowest position. The passive cylinder thus drives its surrounding fluid upwards, reversing the flow direction from the previous downwards movement. Here, a zero-velocity point appears. As this process carries on, more and more fluids are dragged upwards by the passive cylinder, and the boundary thus continues to move downwards. Consequently, the zero-velocity point moves downwards as well, which eventually touches the near-side surface of the active cylinder. At that moment, the active cylinder velocity reaches zero, and the zero-velocity point disappears. Conversely, when the passive cylinder and the active cylinders move towards each other, the same process repeats, although the fluid in the gap changes from flowing upwards to going downwards, as the zero-velocity point travels. The existence of zero-velocity point can be affected the structural damping factor ζ, which will be discussed later in Chapter 4.

Figure 3.9 depicts contours of non-dimensional pressure and streamlines of the flow around the cylinders. At $f_1/f_n = 0.55$, i.e. figure 3.9a-3.9d, since A_2/D and f_1/f_n are both low, the fluid is less disturbed and thus its pressure contours conduct much less fluctuation compared with that at $f_1/f_n = 0.74$ & 1.00. At $f_1/f_n = 0.55$, since the amplification factor is $A_2/A_1 \approx 0.25$, the active cylinder has more control over the pressure distribution compared with the passive cylinder. The active and the passive cylinders vibrate in anti-phase and thus always move in opposite directions. As a result, the streamlines do not connect the

active cylinder and the passive cylinder directly through the gap. In other words, the flow direction is reversed in the gap. At $f_1/f_n = 0.74,\ \phi_1 = 90^\circ$, as depicted in figure 3.9f, when two cylinders move close to each other, the fluid is pushed out of the gap and continues to flow due to inertia, and the pressure in the gap gradually becomes negative. When two cylinders move away from each other, the fluid flows back to fill the gap, where the pressure is increased. Since $\Delta\phi_{21} = 90.673^\circ$, the two cylinders switch periodically from moving in the same direction to moving in the opposite direction, which causes a unique pressure distribution, as demonstrated in figure 3.9e-3.9h. Correspondingly, the distribution of streamlines switches periodically from connecting the cylinders directly, e.g. figure 3.9f, to not being so, e.g. figure 3.9g. At $f_1/f_n = 1.00$, i.e. figure 3.9i-l, the two cylinders vibrate in phase and $A_2/A_1 \approx 0.25$. As a result, the pressure distribution is mainly controlled by the active cylinder while the passive cylinder only has a minor contribution. There are always streamlines directly connecting the two cylinders because they vibrate in phase.

Despite the identical phase ϕ_1 and amplitude A_1/D of the active cylinder, the pressure contours at $f_1/f_n = 0.74$ and that at $f_1/f_n = 1.0$, as seen in figures 3.9f and 3.9j, are drastically different, because the phase of the passive cylinder at $f_1/f_n = 1.0$ is 90° lagged behind that at $f_1/f_n = 0.74$. In other words, the pressure distribution on the surface of the passive cylinder is greatly influenced by the motion of the passive cylinder itself. The pressure contours caused by the active and the passive cylinders interfere each other. For example, at $f_1/f_n = 1.00$ and $\phi_1 = 0^\circ$, i.e. figures 3.9i, the two cylinders vibrate in phase and both reach their highest positions with their velocities decelerating to zero. Since the active cylinder has a much larger amplitude than the salve and they vibrate in phase, the pressure distribution is dominantly controlled by the active cylinder. For the same reason, the motion of the passive cylinder and the friction on its surface only slightly affects the distribution of the negative pressure and do not affect on the distribution at the far side of the active cylinder.

Some low pressure areas are attached to the left and right surfaces of the active cylinder or the passive cylinders. The vortices can be identified by the closed streamlines on the two sides of the cylinders. For example, for $f_1/f_n = 1.00$, at $\phi_1 = 90^\circ$ and $\phi_1 = 270^\circ$, i.e. figures 3.9j and 3.9l, the negative pressure (dashed lines) attached to the shoulders of the active cylinder corresponds to the vortices in figure 3.6. These vortices can also be identified by the streamlines in figure 3.9j and 3.9l.

In summary, although the passive cylinder is driven by the disturbed fluid around it, it also feeds back to the flow and changes the surrounding pressure distribution. When the passive cylinder is free to move, as in the past studies, its existence does not influence the disturbed flow much, and the flow pattern is similar to that of a single cylinder oscillating in a still fluid. When the passive cylinder has a different density from the fluid and is elastically-mounted,

its influence on the disturbed flow can be significant; therefore the coupling between the active and passive cylinders is more complex.

3.4 Chapter Summary

Detailed numerical simulations are conducted to investigate the effects of active cylinder's amplitude A_1/D and frequency f_1/f_n upon the mechanical interactions between two submerged cylinders. With considered cases in this chapter, all the interactions reach a periodic steady state after a few cycles. This chapter discusses only the characteristics of the interaction during the steady state.

Active cylinder's oscillation frequency f_1/f_n is found to play a major role in governing A_2/D and $\Delta\phi_{21}$. The integer multiples of the active cylinder's vibration frequency, i.e. harmonics, are distinguished by FFT in the responding vibration of the passive cylinder, and the magnitude of these harmonics is related to the hydrodynamic force acting on the passive cylinder. When $nf_1/f_n = f_w/f_n$, $n \in \{1,2,3\}$, resonance occurs at the corresponding harmonic. This explains the secondary resonance occurring at $f_1/f_n = (f_w/f_n)/2$, which takes place at the second harmonic $f/f_n = 2f_1/f_n$. At structural damping $\zeta = 0$, A_1 is linearly correlated with A_2 except when the resonance occurred. At $\zeta \leq 0.2$, the linear correlation can be assumed even at resonance.

At $\zeta = 0$, the pattern of the force acting on the passive cylinder is very similar to the pattern of the resulting displacement. However, at $0.99 \leq f_1/f_n \leq 1.01$, the dominant frequencies of the external force and the displacement are distinctively different.As f_1/f_n increases from 0.05 to 2.4, the phase difference $\Delta\phi_{21}$ between the passive cylinder and the active cylinders observes a 180° change, from being anti-phase to being in-phase, and the phase shift occurs abruptly at around $f_1/f_n = f_w/f_n$. At $\Delta\phi_{21} \approx 90^\circ$, the passive cylinder's vibration amplitude A_2/D reaches its maximum. Small vortices are generated on the left and right shoulders of the two cylinders, but no vortex shedding takes place, which is in line with the flow features in regime A^* (Tatsuno and Bearman, 1990). The variations in $\Delta\phi_{21}$ and A_2/A_1 are also reflected in the changes in the pressure distributions.

Chapter 4

Effects of Parameters Associated With the Passive Cylinder in Periodic Regimes

This chapter focuses on the effects of parameters relevant to the passive cylinder, i.e. the damping ratio ζ and the mass ratio m^* of the passive cylinder. Each parameter affects the cylinder-to-cylinder flow-mediated interaction in its unique way.

To better demonstrate the meaning of the damping ratio ζ and the mass ratio m^*, the mass-spring-damper system of the passive cylinder, i.e. Equation (2.5), is restated here:

$$\frac{\partial^2 Y_2}{\partial t^2} + 4\pi f_n \zeta \frac{\partial Y_2}{\partial t} + 4\pi^2 f_n^2 Y_2 = \frac{2}{\pi} \frac{U_m^2}{m^* D} C_{Y2} \tag{4.1}$$

Although this chapter focus on the effects of parameters related to the passive cylinder, the analysis on data are often presented in variation of the active cylinder's oscillation frequency f_1/f_n, because f_1/f_n is the most influential non-dimensional group due to resonance as mentioned in Chapter 3, so the display of results can be less meaningful if not shown with a variety of f_1/f_n. Such manner of demonstration will allow clear comparison between effects of different non-dimensional groups.

4.1 Structural Damping Ratio

The structural damping ratio ζ of the passive cylinder is an important non-dimensional group that it not only affects vibration amplitude of the salve but also alters the phase difference between the passive cylinder and the active cylinder. The increase in ζ can strengthen the linear relationship between the amplitude of the passive cylinder A_2 and that of the active cylinder A_1. A critical damping ratio is found that beyond which the resonance amplitude increases with the active cylinder's oscillation amplitude A_1/D, and

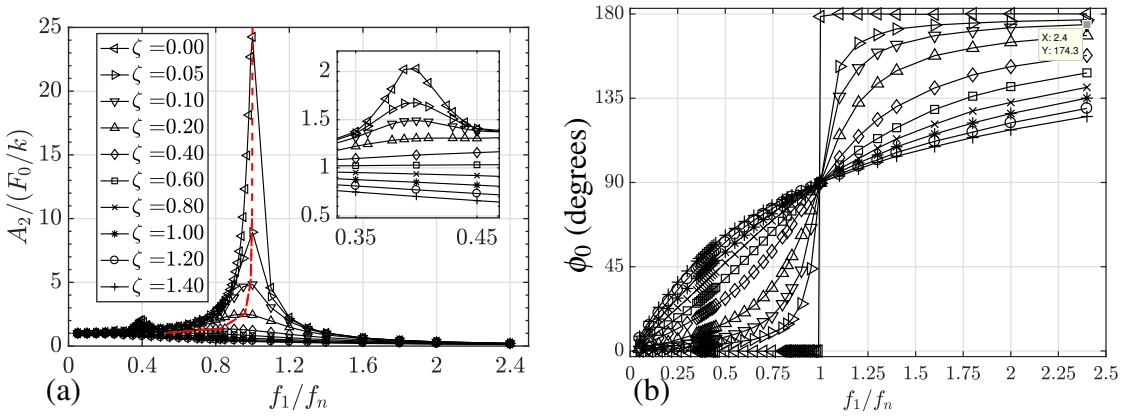

Fig. 4.1 (a) Variation in magnification factor of the passive cylinder $A_2/(F_0/k)$ with f_1/f_n, and (b) variation in force-displacement phase difference for the passive cylinder (for frequency components with $f/f_n = f_1/f_n$) with f_1/f_n at $G/D = 0.2$, $A_1/D = 0.1$, $m^* = 2.0$, and $\zeta = 0 - 1.4$. The red dashed line is the locus of maxima by assuming harmonic force input.

below which the resonance amplitude decreases with A_1/D. It is interesting to find that the flow characteristics are subtly influenced by ζ. Being counter-intuitive, the damping ratio of the passive cylinder affects the pressure distribution at the far side of the active cylinder. ζ also alters the timespan for the flow in the gap to reverse its direction.

4.1.1 Approximating the Passive Cylinder's Motion to be Harmonic in the Context of Varied Structural Damping

This section discusses the appropriateness to approximate the passive cylinder's vibration as sinusoidal with a frequency identical to that of the active cylinder in the context of varied structural damping factors by examining the magnification factor and the displacement-force phase difference.

With such an approximation, the response of the passive cylinder can be described as Eqs. (4.2) and (4.3):

$$F_{Y2}(t) = F_0 \sin(2\pi f_1 t) \tag{4.2}$$

$$Y_2 = A_2 \sin(2\pi f_1 t + \phi_0) \tag{4.3}$$

where the amplitude of the force acting on the passive cylinder is calculated as $F_0 = (F_{Y2,max} - F_{Y2,min})/2$. $F_{Y2,max}$ and $F_{Y2,min}$ are, respectively, the maximum and minimum force values in final 50 cycles of steady vibration. ϕ_0 is the phase difference between the sinusoidal force and the displacement.

In Fig. 4.1a, the magnification factor $A_2/(F_0/k)$ of the passive cylinder's displacement is calculated from the simulation results as:

$$\frac{A_2}{F_0/k} = (\frac{A_2}{D})/(\frac{F_0/(D/2)}{2\pi^3 m^* f_n^2 D^2 \rho}) \tag{4.4}$$

which shows the same pattern as that of a second-order linear system subject to harmonic forcing. The analytic maxima locus, Eqs. (4.5) and (4.6), can be deduced from substituting $F_{Y2}(t) = F_0 \sin(2\pi f_1 t)$ into Eq. (2.5), the motion equation of the passive cylinder.

$$(f_1/f_n)_{peak} = \sqrt{1-2\zeta^2} \tag{4.5}$$

$$(A_2/(F_0/k))_{peak} = \frac{1}{2\zeta\sqrt{1-\zeta^2}} \tag{4.6}$$

The peaks of the simulated magnification factor match the above analytic maxima loci very well as indicated by the red dashed line in Fig. 4.1a. This corresponds to the approximation of the harmonic response of the passive cylinder.

Moreover, as seen in Fig. 4.1b, the simulated displacement-force phase difference ϕ_0 agrees exactly with the analytic phase difference described in Eq. (4.7):

$$\phi_0 = \arctan\frac{-2\zeta(f_1/f_n)}{1-(f_1/f_n)^2} \tag{4.7}$$

which is deduced from Eqs. (2.5) and (4.2). Due to the almost perfect matching between the numerical and analytical results, the curves are nearly indistinguishable. Therefore, only the simulated curves are demonstrated in Fig. 4.1b. The harmonic assumption of Eq. (4.2) can capture the major dynamic features of the passive cylinder regardless of the varying damping factor.

The harmonic assumption of Eq. (4.2) leads to minor inaccuracies, since the vibration of the passive cylinder is predominantly but not entirely harmonic. For example, It leads to a discrepancy at $f_1/f_n = 0.4$, where secondary resonance exists. However, the secondary resonance can be explained by multiple superimposed harmonic input forces (discussed further in Section 4.1.2). Another difference from the analytic solution is that $A_2/(F_0/k)$ does not reach infinity at $f_1/f_n = 1$ and $\zeta = 0$, which means that the input force is not purely harmonic in that situation. Despite these minor discrepancies, the harmonic assumption is capable of capturing the general features of the passive cylinder vibration for all the cases.

4.1.2 Effects of Structural Damping on the Vibration of the Passive Cylinder

The structural damping can significantly affect passive cylinder's vibration amplitude and phase lag. It can also alter the relationship between other non-dimensional groups and the passive cylinder's vibration pattern.

The amplification factor A_2/A_1 decreases with the damping factor ζ, as seen in Fig. 4.2a. This decrease is most dramatic when the response is close to resonance. For example, the resonance amplitude at $\zeta = 0.4$ is only a seventh of that at $\zeta = 0$. The resonance amplitude is highly sensitive to ζ when damping is small, but it becomes less sensitive to ζ, with the increase of the damping factor. For example, the resonance amplitude decreases by half with the increase of ζ from 0 to 0.05, whereas the resonance amplitude decreases by only a third from $\zeta = 0.05$ to $\zeta = 0.10$. At $\zeta \geq 0.8$, a resonance peak can no longer be observed. Instead, the responding amplitude increases with the frequency monotonically. At $\zeta \leq 0.10$, the secondary resonance increases with the vibration amplitude of the active cylinder. However, at $\zeta \geq 0.20$, A_1/D can no longer affect the pattern of the minor resonance. As the active cylinder vibrates at a very low frequency, the responding amplitude of the passive cylinder, regardless of ζ, converges to zero. If the active cylinder vibrates at a very high frequency, the responding amplitude converges to a certain value above zero, i.e. $A_2/A_1 = 0.2$. This means that at either a very low or a very high vibrating frequency, the effect of damping on the responding amplitude of the passive cylinder becomes very small, which is in contrast with that at resonance. These patterns apply to all the cases.

As demonstrated in Section 4.1.1, the passive cylinder response can be approximated as harmonic with a frequency equal to the active cylinder frequency, with its frequency identical to that of the active cylinder. The passive cylinder actually vibrates with more than one frequency components according to the FFT results, although the dominant frequency component is, in most cases, the first harmonic with $f/f_n = f_1/f_n$, i.e. the fundamental frequency component. The amplitude of the frequency component with $f/f_n = f_1/f_n$ is usually much larger than other frequency components. This is why the passive cylinder response can be approximated as harmonic with a frequency of the active cylinder.

For example, in the amplitude spectra plotted in Fig. 4.3, two harmonics are typically observed in the response of the passive cylinder. The one having the same frequency as the active cylinder $f/f_n = f_1/f_n$ is the dominant component, whereas the amplitude of the second harmonic, i.e., component with a double frequency $f/f_n = 2f_1/f_n$, is much lower. The amplitude of the second harmonic is generally small, but it becomes comparable with the amplitude of the first harmonic as the active cylinder's frequency is about $f_1/f_n = 0.375$ as shown in Fig. 4.3. Such large amplitude occurs because the frequency of the second

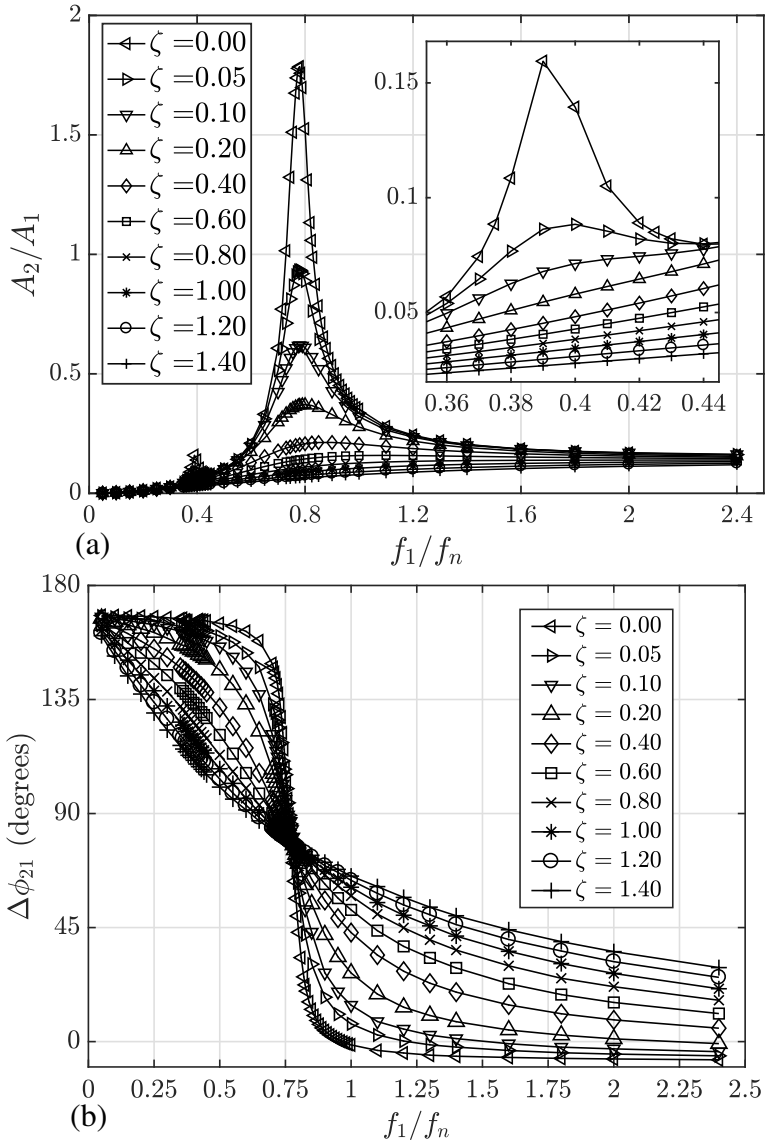

Fig. 4.2 (a) Variation of A_2/A_1 and (b) variation of phase difference between the two cylinders $\Delta\phi_{21}$ with f_1/f_n (for the frequency components with $f/f_n = f_1/f_n$) with f_1/f_n at $G/D = 0.2$,$A_1/D = 0.1$, $m^* = 2.0$, and $\zeta = 0 - 1.4$. A_2/A_1 is negatively correlated with ζ, particularly within the regime of resonance. The phase difference curve converges at $\Delta\phi_{21} \approx 80^\circ, f_1/f_n \approx 0.775$. The increase in damping slows down the 180° phase shift of the passive cylinder as f_1/f_n reaches its immersed natural frequency.

harmonic $f = 2f_1/f_n$ coincides with the immersed natural frequency. As mentioned before, the displacement amplitude of the passive cylinder decreases with ζ. At half the submerged natural frequency, a threshold ζ is found, under which the amplitude of the second harmonic is greater than that of the first harmonic, and beyond which it is lower than that of the first harmonic. Fig. 4.3b illustrates a case with the damping coefficient above the threshold. From

the curves demonstrated in Fig. 4.2a, the threshold damping coefficient for such a setup is found to be around $\zeta = 0.1$. Dominant influence of the second harmonic can be observed in Fig. 4.2a and Fig. 3.3 at half the immersed natural frequency with $\zeta < 0.1$, but they are not observed with $\zeta > 0.1$. In other words, the secondary resonance can be suppressed by adding value to the structural damping factor. The existence of this threshold damping coefficient signifies that the two harmonics are not equally influenced by damping. Because the displacement is more sensitive to damping at resonance than at other situations. When the active cylinder vibrates at $1/2$ the immersed natural frequency of the passive cylinder, the second harmonic of the passive cylinder's displacement with $f/f_n = 2f_1/f_n$ coincides with the immersed natural frequency, causing resonance. The increase in damping causes more amplitude reduction for the second harmonic than that for the first harmonic, whose frequency does not coincide with the immersed natural frequency of the passive cylinder.

In the phase analysis, the vibration phase of the passive cylinder is represented by the phase of its first harmonic with $f/f_n = f_1/f_n$. This representation captures the predominant characteristics of the motion, except at the the secondary resonance, where the displacement of the passive cylinder has two harmonics with comparable magnitude. Such a representation enables us to compare the phases $\Delta\phi_{21}$ of the passive cylinder and the active cylinders, because the fundamental frequency of the passive cylinder synchronizes with the active cylinder vibration at the steady state. Fig. 4.2b illustrates the vibration phase difference $\Delta\phi_{21} = \phi_2 - \phi_1$ between the passive cylinder ϕ_2 and the active cylinder ϕ_1, at various ζ. Regardless of ζ, it is seen that, at a very low and very high f_1/f_n, the values of $\Delta\phi_{21}$ are approximately 180° and 0°, respectively. The two cylinders' vibration is in anti-phase at low frequencies and in phase at high frequencies. The phase of the passive cylinder changes abruptly at resonance when structural damping is low, but the phase change with the frequency becomes increasingly gradual with increasing damping. For example, at $\zeta = 0$, the phase change of the passive cylinder occurs with an almost vertical gradient at the immersed natural frequency, whereas at $\zeta = 1.4$, the phase difference reduces gradually with the increment of f_1/f_n. Although damping ratio affects the rate of the phase change, the phase difference remain constant at different ζ, as all the curves pass through $\Delta\phi_{21} \approx 80^\circ$ and $f_1/f_n \approx 0.775$. It means that the phase difference is independent of damping at resonance. Later in Section 4.1.4, the effects of damping on flow features at resonance are investigated.

In addition, it is seen that, at a low damping of $\zeta \leq 0.2$, the relative resonance amplitude decreases with the input amplitude A_1/D, e.g. Fig. 4.4a. Conversely, given a relatively high damping of $\zeta \geq 0.4$, the resonance amplitude increases with A_1/D, e.g. Fig. 4.4b. This reversal of the correlations indicates the existence of a threshold damping factor, under which A_2/A_1 decreases with A_1/D, and beyond which A_2/A_1 increases with A_1/D.

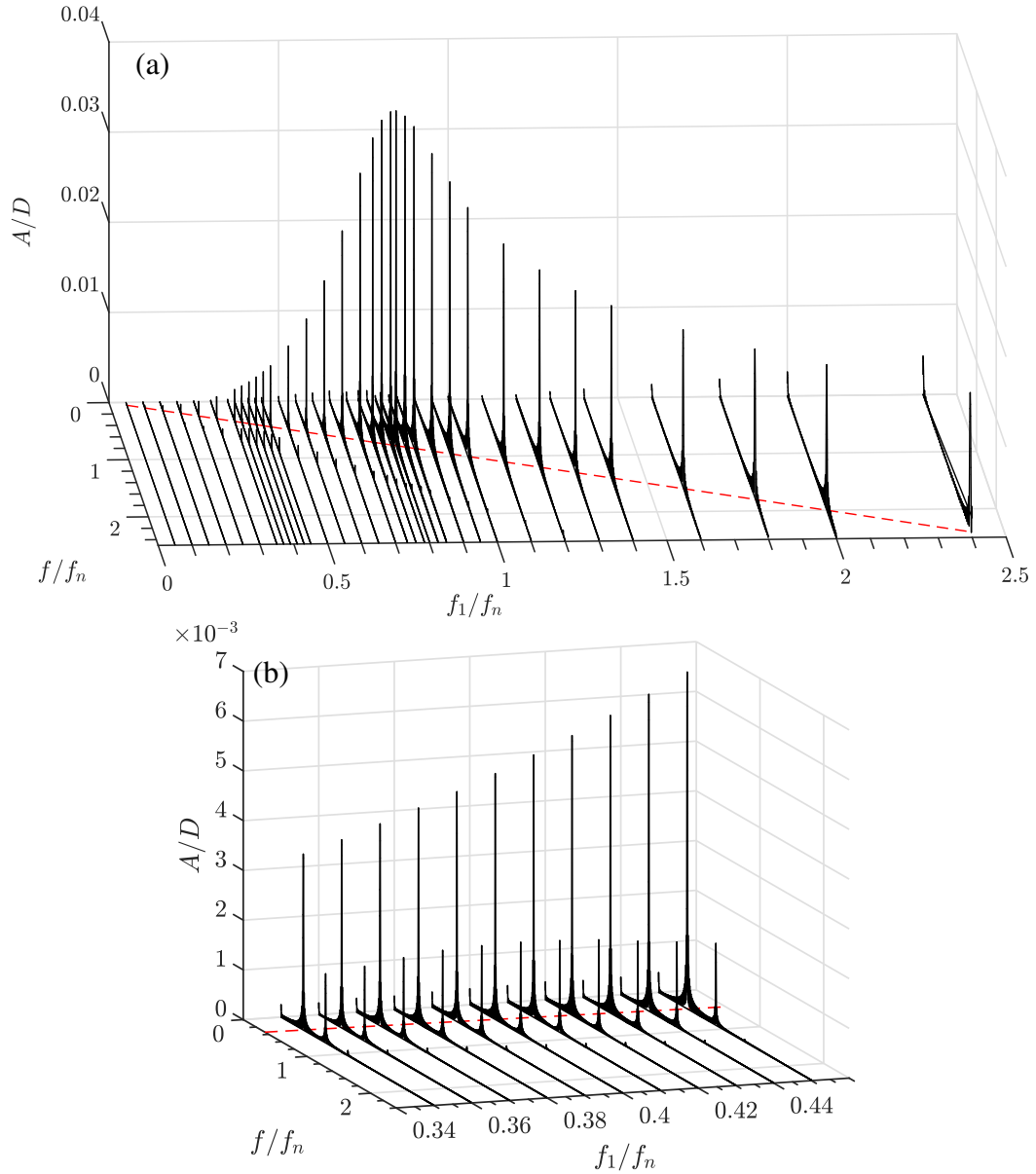

Fig. 4.3 Amplitude spectra showing the responding displacement of the passive cylinder with various f_1/f_n at $G/D = 0.2$, $A_1/D = 0.1$, and $m^* = 2.0$. (a) An overview of the FFT spectra (b) the FFT spectra at $f_1 = f_w/2 \approx 0.375$. The red dashed thin line tracks the dominant frequencies. It can be seen that, at $f_1 = f_w/2$, the high frequency component is always smaller than the fundamental component, whereas for the undamped cases, a high-frequency component becomes larger than the fundamental frequency, thus causing a minor peak of resonance.

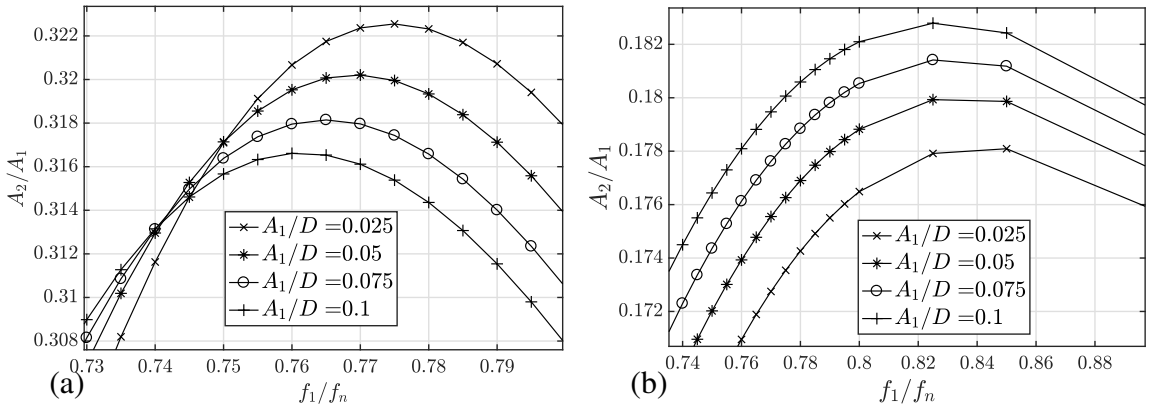

Fig. 4.4 (a) Zoom-in at peaks for variation of A_2/A_1 at $\zeta = 0.2$, and (b) zoom-in at peaks for variation of A_2/A_1 at $\zeta = 0.4$ for $G/D = 0.4$, $A_1/D = 0.025 - 0.1$, $m^* = 1.5$. A threshold damping ratio of the passive cylinder is discovered, beyond which its peak amplification factor decreases with the active cylinder vibration amplitude, and under which the peak increases with the amplitude. In this scenario, the threshold lies in $\zeta = 0.2 - 0.4$.

In summary, the vibration amplitude of the passive cylinder decreases with ζ, and the magnitude of this decrease drops with damping as well. The increase in damping reduces and can eventually eliminate the secondary resonance at half the immersed natural frequency. From Fig. 3.2b in Chapter 3, it is also known that the increase in damping strengthens the linear relationship between the active cylinder and the passive cylinder vibration amplitude. A threshold damping factor is found that, below which its peak amplification factor A_2/A_1 decreases with the active cylinder amplitude A_1/D, and beyond which the peak increases with A_1/D. The above results show that the relative amplitude can be affected by the damping factor in both a direct and an indirect way.

4.1.3 Force Acting on the Passive Cylinder

For the mass-spring system of the passive cylinder, the input force determines the time history of its displacement. The input force acting on the passive cylinder is controlled by the status of the surrounding fluid in the process of this flow-mediated interaction. In this section, the fluctuation of the pressure and the flow distributions in one cycle of the passive cylinder vibration is examined, and how the force acting on the passive cylinder changes correspondingly. The examined scenario is only one typical resonating case at $G/D = 0.4$, $A_1/D = 0.075$, $m^* = 1.5$, $f_1/f_n = 0.74, \zeta = 0, Re_m = 100$, and $\Delta\phi_{21} = 90.673°$, but it is capable to represent the most common situation encountered and to reveal the underlying principles in this process. It will be discussed later that the decrease of Re_m can enhance the contribution from shear force, but the pressure force is always significant.

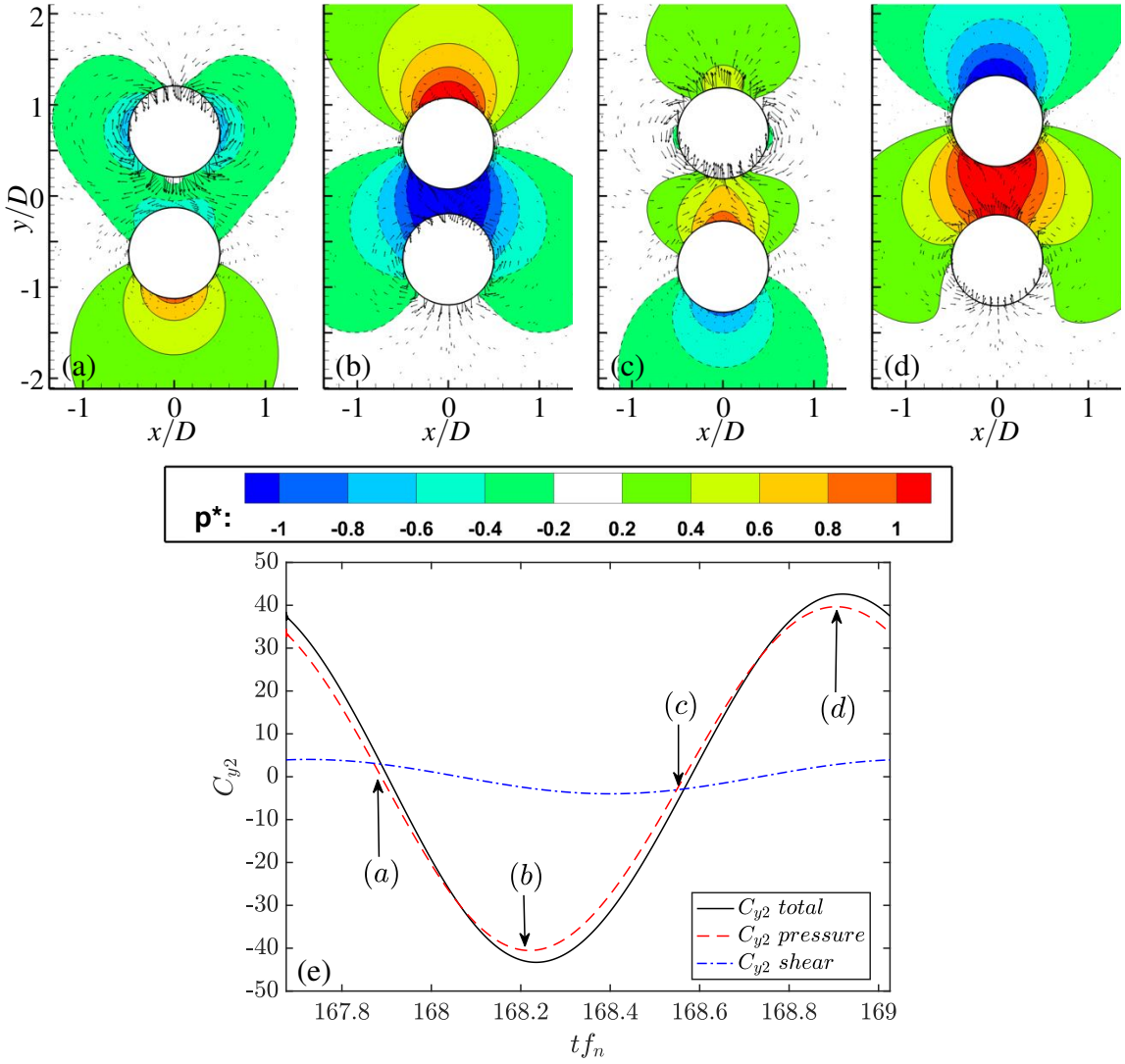

Fig. 4.5 (a–d) Non-dimensional pressure contours $p^* = p/\rho f_n^2 D^2$ at $G/D = 0.4, A_1/D = 0.075, m^* = 1.5, f_1/f_n = 0.74, \zeta = 0, Re_m = 100$, and $\Delta\phi_{21} = 90.673°$. The dashed lines indicate negative values of non-dimensional pressure. The colour map shows corresponding colour for each value of non-dimensional pressure. The velocity vectors are plotted every 20 points. The vector scale factor is 0.3 grid units/magnitude. (e) The y-direction force coefficient upon the passive cylinder and its shear and pressure components were examined. Pressure rather than viscosity is the main contributor to the force acting on the passive cylinder.

As discussed in Sections 4.1.1 and 4.1.2, the force acting on the passive cylinder can be treated as harmonic, especially at resonance. By examining the time history of the force coefficient C_{Y2} at resonance, i.e. see Fig. 4.5e, the pressure and the shear force components is predominantly sinusoidal. The pressure distributions at the maxima, minima, and transient equilibrium of the force are demonstrated in Figs. 4.5a-4.5d. The force acting on the passive cylinder is most significantly induced by pressure rather than viscosity, as seen in Fig. 4.5e. The pressure force is induced by the pressure distribution surrounding the passive cylinder, which is illustrated in Figs. 4.5a-4.5d. It is seen that the maximum attractive and repulsive forces occur when the pressure field within the gap is at its highest and lowest positions, as shown in figures 4.5b and 4.5d respectively. At these positions, the pressure gradients are at the steepest, which poses the greatest acceleration on the fluid surrounding the passive cylinder. In Figs. 4.5b and 4.5d, the pressure patterns are almost identical. If you reverse the sign of the pressure contours in Fig. 4.5b and adjust for the pressure reduction due to vortices, you can then obtain Fig. 4.5d.

The passive cylinder is at transient equilibrium in both Figs. 4.5a and 4.5c, where distinctively different patterns are observed. In Fig. 4.5a, the pressure magnitude is very low at the far side of the passive cylinder as well as within the gap, while in Fig. 4.5c, a higher magnitude of pressure is found at the same regions. The passive cylinder reaches its maximum velocity at both Figs. 4.5a and 4.5c, creating a pair of vortices much stronger than that in Figs. 4.5b and 4.5d. However, the direction of the velocity is opposite in Figs. 4.5a and 4.5c, which reverses the sign of the surrounding pressure contours. Nevertheless, the strong vortices can only decrease the pressure, which strengthens the negative pressure and weakens the positive pressure. The downward momentum of the passive cylinder in Fig. 4.5a results in a lower pressure at the far side of the passive cylinder, while in Fig. 4.5c, the upward momentum increases the pressure below the passive cylinder. On the circumference of the passive cylinder, the pressure distribution is negative in Fig. 4.5a and is positive in Fig. 4.5b except in the shoulder regions characterized by strong vortices. Nevertheless, the circumferential pressure distributions are symmetrical regarding the x-axis in both Figs. 4.5a and 4.5c. As a result, the passive cylinder reaches transient equilibrium in Figs. 4.5a and 4.5c. Compared with the pressure force, the shear force is also sinusoidal but has a very limited contribution to the force acting on the passive cylinder, since the shear force is much smaller than the pressure force. The shear force maintains a constant phase difference from the pressure force regardless of f_1/f_n and ζ. At resonance, the shear force slightly increases the amplitude of the force acting on the passive cylinder. In addition, the fluid flows in and out of the gap periodically in response to the sinusoidal vibration of the active cylinder and

the passive cylinder, which causes the horizontal and vertical components of the fluid velocity in the gap to change sinusoidally as well, as demonstrated in Figs.4.5a-4.5d.

4.1.4 Effect of Structural Damping on Flow Field

Section 4.1.3 has demonstrated that pressure is the main contributor to the passive cylinder vibration. This section further discusses the effects of ζ on the pressure and flow fields surrounding the cylinders at resonance, as seen in Fig. 4.6. As previously discussed in Section 4.1.2 with Fig. 4.2b, when resonance takes place, the variation of the damping does not affect the phase difference between the two cylinders, which facilitates the flow field comparison among the cases with different damping ratios.

The effect of ζ on the pressure and the streamline distributions is demonstrated in Fig. 4.6 by varying the value of ζ from 0, 0.1 to 0.8 while keeping other parameters unchanged. For comparison purposes in different configurations, corresponding figures on the same column are with the same phase of the active cylinder's vibration, ϕ_1. $\phi_1 = 0^\circ$ is defined as the moment when the active cylinder at its highest position.

When $\zeta = 0$, the pressure fluctuates most severely on the far side of the passive cylinder, as seen in Figs. 4.6a and 4.6c. With the increase in damping, the fluctuation at the far side of the passive cylinder becomes less severe, whereas the pressure fluctuation within the gap becomes significant as seen in Figs. 4.6a, 4.6e and 4.6i. This phenomenon indicates that, with the increase in structural damping, the main contributor of the passive cylinder's motion changes from the pressure fluctuation at the far side regime of the passive cylinder to that within the gap. This is because the increase in damping severely reduces the vibration amplitude of the passive cylinder, as demonstrated in Fig. 4.2a, and thus the pressure accumulated in the gap cannot be alleviated in time due to the inadequate displacement of the passive cylinder, resulting in a stronger pressure fluctuation in the gap. The restricted motion of the damped passive cylinder also prevents the generation of a strong vortex, corresponding to a shorter lifespan of the vortices attached on the left and right of the passive cylinder, as shown in Fig. 4.7. The weakened vortices increase the pressure on the left and right sides of the passive cylinder. Being counter-intuitive, although the structural damping ratio is entirely associated with the passive cylinder, the pressure fluctuation intensity below the active cylinder slightly decreases with structural damping, as seen in Figs. 4.6a, 4.6e and 4.6i. This is because a damped passive cylinder displaces less amount of the fluid, and thus smaller volumes of fluid are pushed down to flow past the active cylinder and to strengthen the pressure below it.

In the gap, a zero-velocity point travels downward from the passive cylinder to the active cylinder, as seen in the red dashed circle of Fig. 4.8b. That point appears when the passive

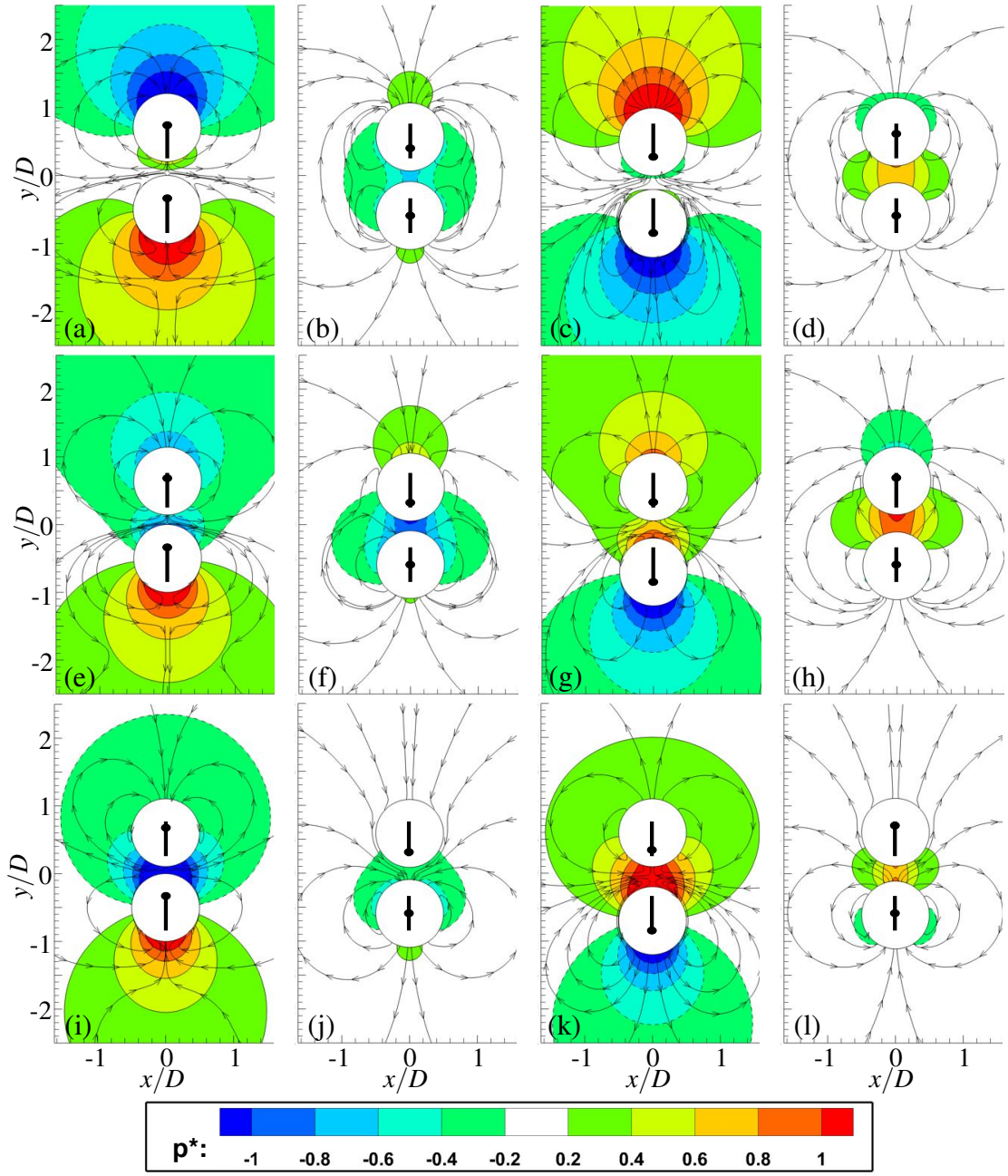

Fig. 4.6 Non-dimensional pressure contours $p^* = p/\rho f_n^2 D^2$ at $G/D = 0.2$; $A_1/D = 0.1$; $m^* = 1.5$; $f_1/f_n = 0.78$; and $\phi_1 = 0^\circ$ (a, e, and i), 90° (b, f, and j), 180° (c, g, and k) and 270° (d, h, and l). (a–d) $\zeta = 0$, $\Delta\phi_{21} = 46.6^\circ$; (e–h) $\zeta = 0.1$, $\Delta\phi_{21} = 50.0928^\circ$; (i–l) $\zeta = 0.8$, $\Delta\phi_{21} = 68.309^\circ$. The cylinder on the top is the passive passive cylinder. The cylinder on the bottom is the active active cylinder. The dashed lines indicate negative values of non-dimensional pressure. The color map shows corresponding color for each value of non-dimensional pressure. With the increase in damping, the main driver of the passive cylinder changes from the pressure fluctuation at the far side of the passive cylinder to that within the gap. The black sticks and the dots indicate the displacement of the cylinder in one cycle.

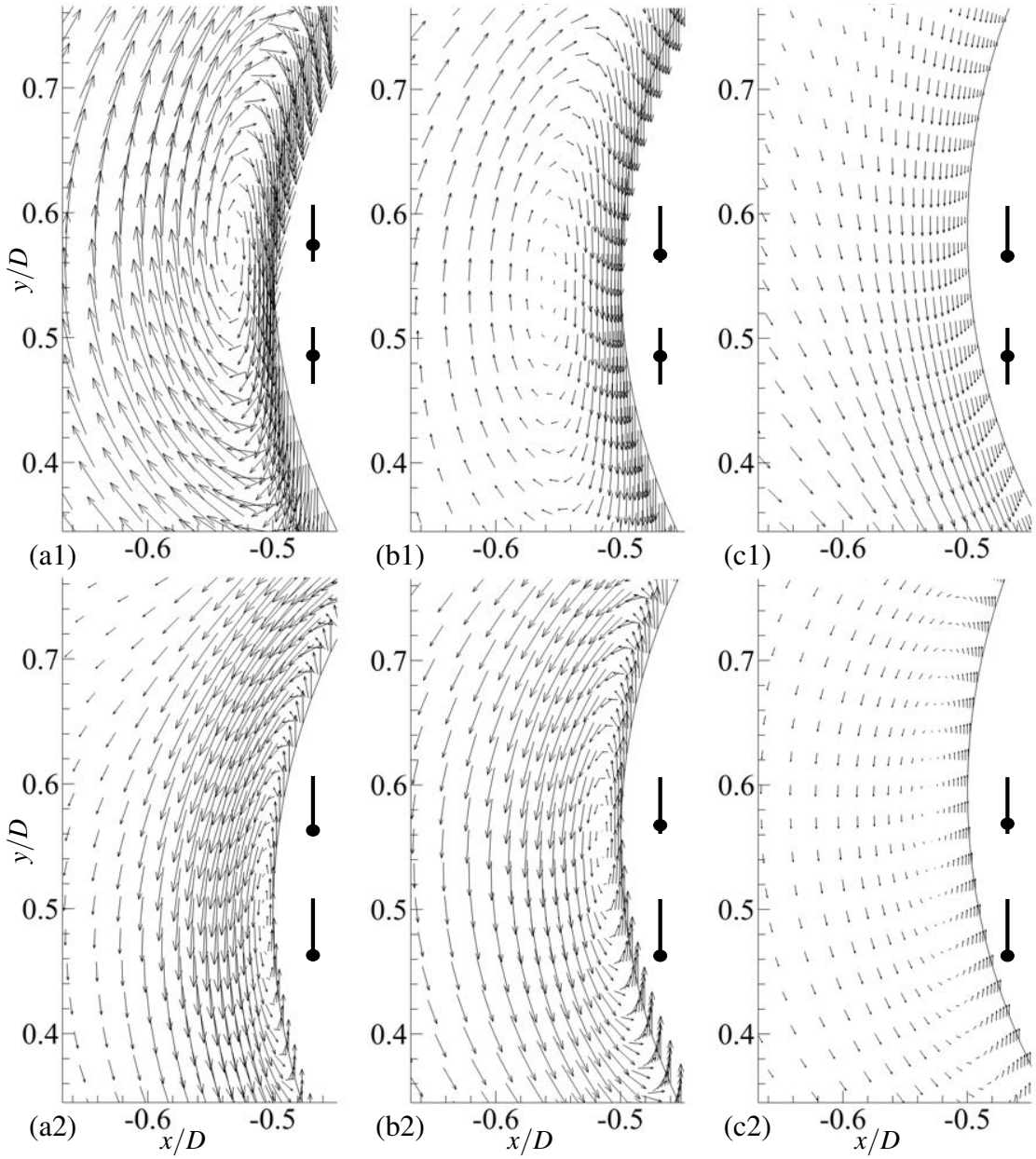

Fig. 4.7 Velocity vectors on the left of the passive cylinder at $G/D = 0.2$, $A_1/D = 0.1$, $m^* = 1.5$, and $f_1/f_n = 0.75$, with (a) $\zeta = 0$, $\Delta\phi_{21} = 108.4°$; (b) $\zeta = 0.1$, $\Delta\phi_{21} = 95.62°$; (c) $\zeta = 0.8$, $\Delta\phi_{21} = 68.309°$ and (1) $\phi_1 = 90°$; (2) $\phi_1 = 180°$. The velocity vector is drawn on every grid point and the vector scale factors are 0.15 grid units/magnitude. The lifespan and the strength of vortices both decrease with damping. The black sticks and the dots indicate the displacement of the cylinder in one cycle.

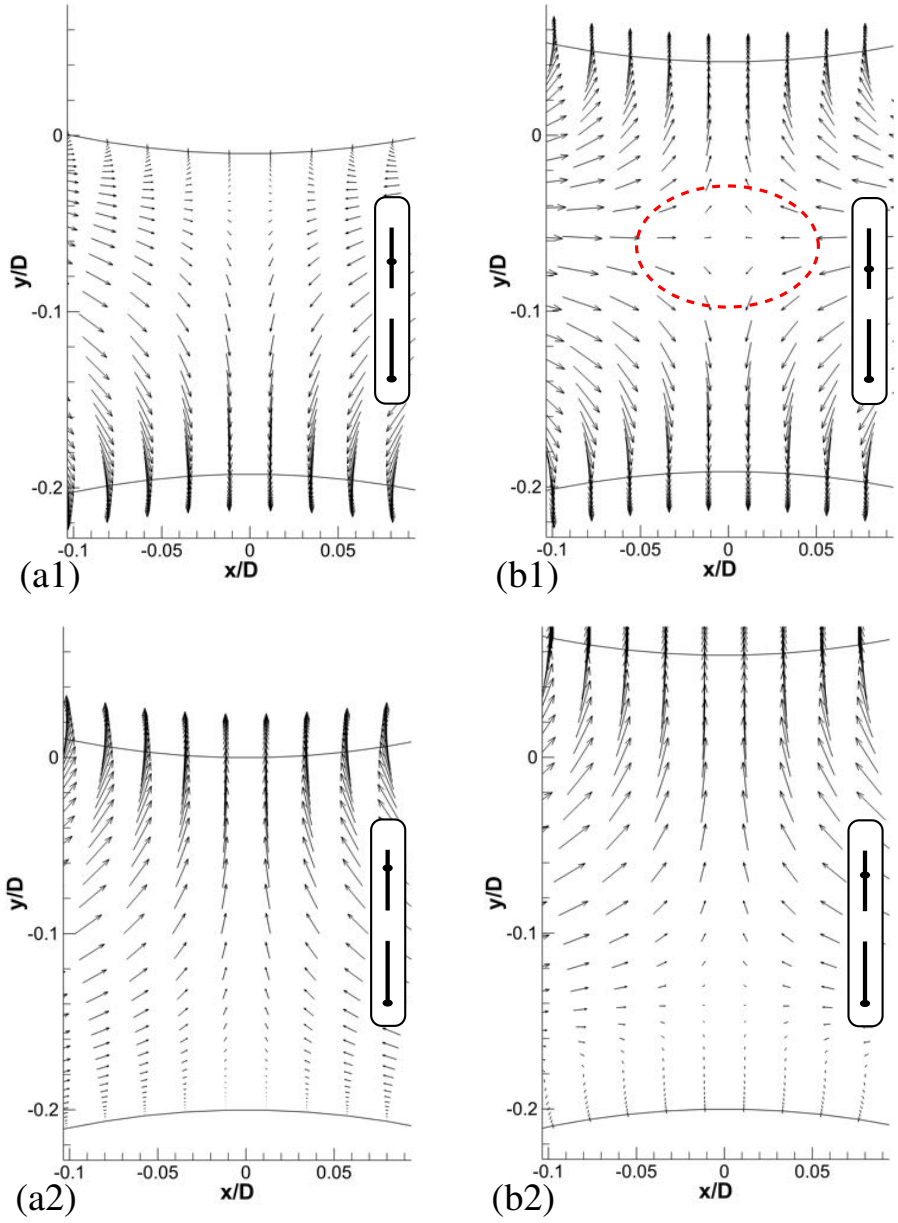

Fig. 4.8 Velocity vectors in the gap at $G/D = 0.2$, $A_1/D = 0.1$, $m^* = 1.5$, and $f_1/f_n = 0.75$, with (a) $\zeta = 0$, $\Delta\phi_{21} = 108.4°$; (b) $\zeta = 0.1$, $\Delta\phi_{21} = 95.62°$; and (1) $\phi_1 = 158°$; (2) $\phi_1 = 189°$. The velocity vector is drawn on every grid point and the vector scale factors are 0.011 grid units/magnitude. The zero-velocity point (see dashed circle in b1) travels from the bottom of the passive cylinder to the top of the active cylinder. For the damped case with $\zeta = 0.1$, the stagnant flow point appears earlier than the undamped case and has a longer lifespan. For both the damped and undamped cases, the stagnant flow point disappears at $\phi_1 = 189°$. The black sticks and the dots indicate the displacement of the cylinder in one cycle.

cylinder and the active cylinder move either closer to or farther away from each other and the fluid flow in the gap is changing direction. The increase in damping lengthens the lifespan of such a point. For example, at $\zeta = 0$, that point exists in the time frame $\phi_1 = 135^\circ - 184^\circ$, as shown in Figs.4.8a1 and 4.8a2. By comparison, at an increased damping $\zeta = 0.1$, that point exists in the time frame $\phi_1 = 161^\circ - 184^\circ$, as illustrated in Figs. 4.8b1 and 4.8b2. At the moment of $\phi_1 = 161^\circ$, the zero-velocity point of the undamped case has just been produced, as demonstrated in Fig. 4.8a1, whereas that of the damped case is already on the way downward, as seen in Figs.4.8b1. At the moment of $\phi_1 = 184^\circ$, for both the damped and the undamped cases, the zero-velocity point disappears, as seen in Figs. 4.8a2 and 4.8b2. It is clear that the lifespan of the zero-velocity point is lengthened due to the damping effect, indicating a sustained period of opposite flows within the gap. The longer lifespan of the zero-velocity point allows the pressure to accumulate in the gap for a longer period and, consequently, to generate a more violent pressure fluctuation, as shown in Figs. 4.6c, 4.6g and 4.6k. A larger damping ratio also results in a greater fluctuation of the transient gap distance between the two cylinders, which means the fluid is squeezed out of the gap rather than vibrating together with the passive cylinder and the active cylinder. This corresponds to the lower flow velocity in the gap and the increased lifespan of the zero-velocity point.

4.2 Mass Ratio of the Passive Cylinder

Another important parameter is the mass ratio m^*, which is the mass of the passive cylinder divided by that of the displaced water, i.e. $m^* = m_c/m_{disp} = m_c/(\rho D^2\pi/4)$. As seen in Fig. 4.9, the mass ratio influences the natural frequency of the passive cylinder in fluid as $f_w/f_n = \sqrt{m^*/(m^*+C_A)}$. This submerged natural frequency is approximately equal to the active cylinder frequency that causes the resonance of the passive cylinder. The resonance frequency increases with m^*, but m^* appears to have no effect on the resonance amplitude. As a result, the resonance frequency in Fig. 4.9 increases with m^*. It is also interesting to note that the curves with various m^* converges at the point $(A_2/A_1, f_1/f_n) = (1, 0.36)$, as seen in the dashed rectangle in Fig. 4.9. This convergence point is independent of A_1/D because A_2/D is linearly correlated with A_1/D at $f_1/f_n = 1$, as seen in Fig. 3.2. This convergence point is only affected by G/D. In other words, if $f_1/f_n = 1$, A_2/A_1 is solely dependent on G/D.

If we assume $C_A = 1$, the calculated $\sqrt{m^*/(m^*+C_A)}$ does not exactly match the resonance frequency f_w/f_n found in the simulations. There is always a discrepancy of the magnitude of 10^{-2}. Conversely, if we calculate the added mass coefficient as $C_A = m^*[1 - (f_{peak}/f_n)^2]$, where f_{peak} is the resonance frequency obtained directly from the simulations,

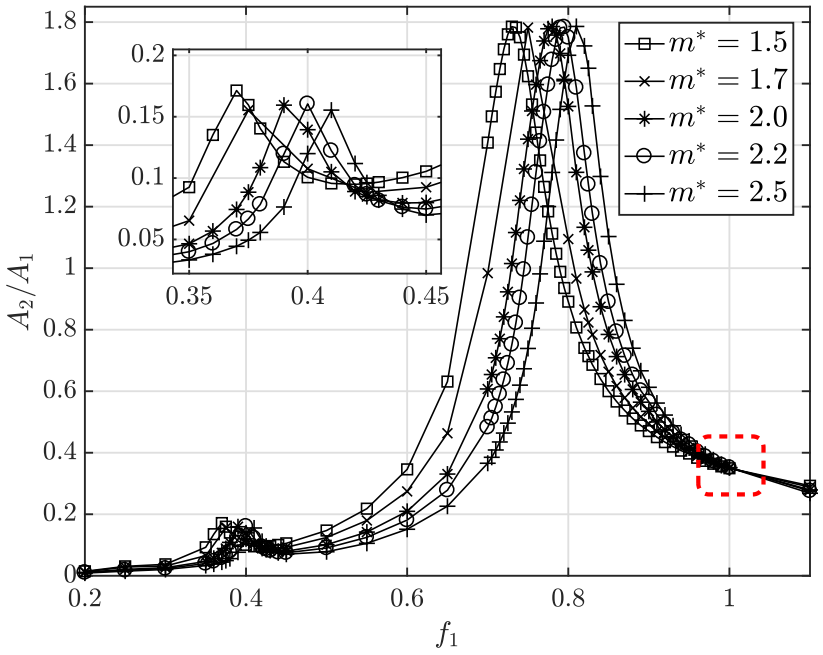

Fig. 4.9 Variation of A_2/A_1 with f_1/f_n and m^* at $G/D = 0.2, A_1/D = 0.1, Re_m = 100, \zeta = 0$. m^* affects the resonance frequency. The red dashed rectangle highlights the convergence point.

the C_A can be found to be in the range of $0.70 - 0.85$ for $m^* = 1.5 - 2.5$. The calculated C_A increases with m^*, G/D as well as with A_1/D.

In terms of the mass ratio's effect on phase difference, since phase jump frequency is equal to the resonance frequency, m^* determines at which f_1/f_n the vibration of the two cylinders abruptly changes from being in phase to being anti-phase, as seen in Fig. 4.10.

The structural damping factor affects the mass ratio's influence on the frequency-amplitude relationship, as seen in Fig. 4.11a. Given a damping factor larger than zero, the resonance amplitude of the passive cylinder decreases with its mass ratio, e.g. the dashed red lines. However, for undamped cases, the mass ratio does not affect the resonance amplitude at all, as demonstrated by the black solid lines. Despite the negative contribution to the peak amplitude, the increase in damping does not allow the mass ratio to affect the immersed resonance frequency. With $\zeta = 0$, the mass ratio is seen to be unable to affect the vibration amplitude at $f_1/f_n = 1.0$, because the black solid lines cross the same point at $f_1/f_n = 1.0$ as highlighted in the red dashed box in Fig. 4.9. However, with $\zeta > 0$, the lines representing different mass ratios give different amplitude at $f_1/f_n = 1.0$, and the separation of these lines increases with damping, as highlighted in the red dashed box in Fig. 4.11a. Hence, at $\zeta > 0$, the responding amplitude becomes dependent on the mass ratio. It is also observed that the frequency disparity between the force and the displacement at $f_1/f_n = 1.0$. For all cases, the

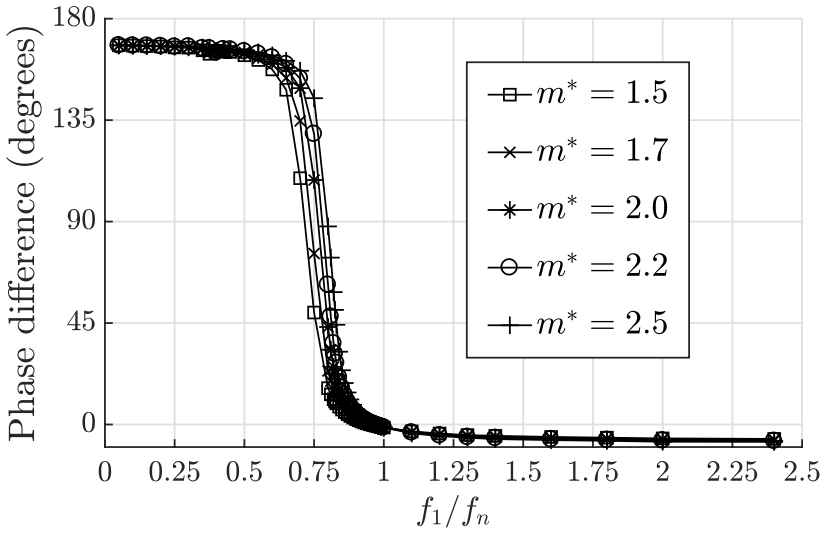

Fig. 4.10 Variation of the oscillation phase difference between the two cylinders with f_1/f_n at $A_1/D = 0.1, m^* = 1.5-2.5, G/D = 0.2, Re_m = 100, \zeta = 0$ the phase change occurs. G/D does not affect much the phase difference

mass ratio does not affect the phase lag $\Delta\phi_{21}$ at a very high or very low f_1/f_n, as shown by the lines converging at the far left and far right in Fig. 4.11b. However, the increase in mass ratio causes the phase change as well as the resonance to occur at a larger f_1/f_n, corresponding to the increase of the immersed natural frequency. This pattern is not influenced by the variation of the damping ratio. Additionally, at $\zeta = 0.2$, despite the variation of resonance frequency with m^*, the phase lag between the two cylinders at the resonance frequency remains constant regardless of m^*, e.g. $\Delta\phi_{21} \approx 70^\circ$ in Fig. 4.11. At $\zeta = 0$, the phase difference at resonance is observed to be lower as $\Delta\phi_{21} \approx 90^\circ$. This indicates that the phase difference at resonance decreases with damping ratio.

In a nutshell, a non-zero damping ratio leads to a negative correlation between the mass ratio and the relative resonance amplitude, whereas at zero damping ratio, mass ratio does not affect the resonance amplitude but only the resonance frequency of the passive cylinder.

4.3 Chapter Summary

This chapter carries out parametric study on the effects of the passive cylinder's structural damping and its mass ratio on its responding vibration. It is found that, with a variety of damping ratios, the motion of the passive cylinder can generally be regarded to be sinusoidal with a frequency identical to that of the active cylinder oscillation. Although multiple frequency components were discovered in some configurations, the dominant and

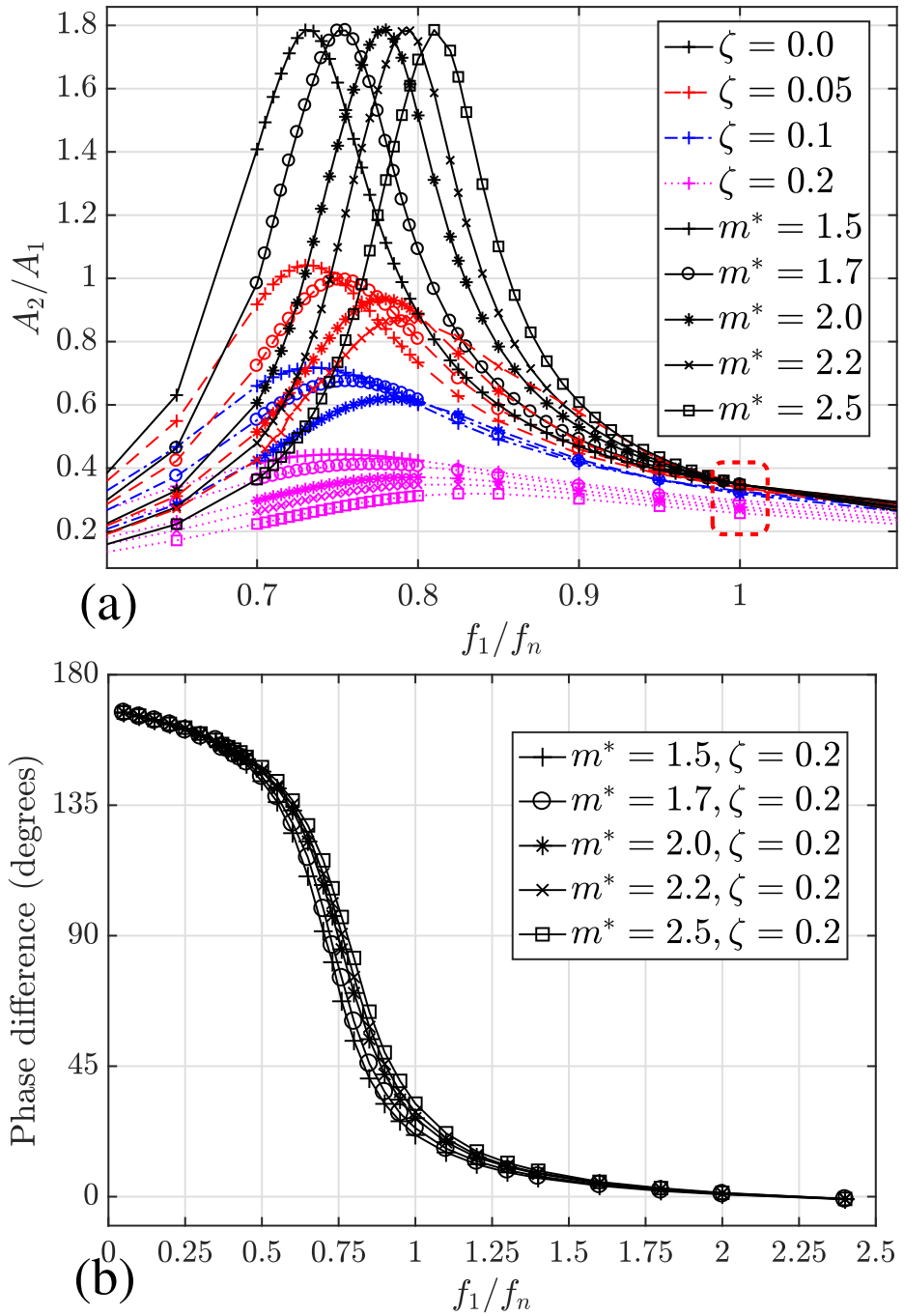

Fig. 4.11 (a) Variation in A_2/A_1 with f_1/f_n, and (b) variation in displacement phase difference $\Delta\phi_{21}$ between the passive cylinder and the active cylinder (for the frequency components with $f/f_n = f_1/f_n$) with f_1/f_n at $G/D = 0.2, A_1/D = 0.1, m^* = 1.5-2.5, Re_m = 100$ and $\zeta = 0-0.2$. The color and line type denote ζ, whereas the marker type denotes m^*. With a non-zero damping, the peak A_2/A_1 decreases with m^*. The curve of $\Delta\phi_{21}$ disperses at resonance, which follows the same pattern as the undamped cases.

fundamental frequencies are equal to the frequency of the active cylinder in most cases, so, in regimes A and A^*, it is usually accurate enough to simplify the vibration of the passive cylinder as harmonic.

The increase in damping reduces the passive cylinder vibration amplitude and particularly weakens the resonance. With the presence of damping, the resonance amplitude decreases with the mass ratio. The increase in damping strengthens the linear correlation between the active cylinder's amplitude and the passive cylinder's amplitude. It is discovered that a threshold damping ratio of the passive cylinder, beyond which the amplification factor A_2/A_1 decreases with the active cylinder's vibration amplitude A_1/D, and under which the factor increases with the amplitude. Damping also slows down the switch of the vibration phase of the passive cylinder near resonance, but the phase difference $\Delta\phi_{21}$ at resonance remains constant regardless of the damping ratio. The damping ratio does not significantly influence the dependence of $\Delta\phi_{21}$ on other parameters.

The force acting upon the passive cylinder mainly arises from the pressure gradient rather than viscous shearing. Hence, the pressure difference on the two sides of the passive cylinder determines its driving force. It is seen that the maximum attractive and repulsive forces occur when the pressure in the gap is at highest and lowest, respectively. With the increase in damping, the reduction in the vibration amplitude of the passive cylinder is accompanied by the increased variation of the gap size between the two cylinders. As a result, the magnitude of the pressure oscillation within the gap increases but the pressure change on the far side of the passive cylinder decreases. Correspondingly, the increase in damping gives rise to a sustained period of opposite flows within the gap, leading to an increased lifespan of a zero-velocity point within flow in the gap.

Mass ratio m^* determines the values of f_w/f_n and thus controls the the exact frequency for the resonance f_1/f_n. At $\zeta = 0$, mass ratio does not affect the resonance amplitude of the passive cylinder. However, at $\zeta > 0$, resonance amplitude decreases with mass ratio. Mass ratio affects the phase difference between the two cylinders only at resonance frequency regardless of the damping ratio. In other words, mass ratio does not affect the phase difference at very low or very high frequency f_1/f_n.

Chapter 5

Effects of Intermediate Fluid and Gap in Periodic Regimes

This chapter focuses on the effects of Reynolds numbers Re_m and gap ratio G/D on the interactions between the two cylinders. It is reminded here that the Reynolds number in this thesis is defined by maximum velocity of the active cylinder, diameter of the cylinder and the viscosity of the fluid, i.e. $Re_m = U_m D/\nu = 2\pi A_1 f_1 D/\nu$. The gap distance G is the *clear* distance between the active cylinder and the passive cylinder. In this chapter, Reynolds number ranges from 10 to 150. The Reynolds number is found to affect the vibration centre drift of the passive cylinder which can be repelled or attracted by the active cylinder with different Reynolds number. The correlation between the Reynolds number and the resonance amplitude can be altered by the change of structural damping factor. Gap ratio can in general reduce the vibration amplitude of the passive cylinder but it almost has no influence on the phase-lag, which is counter-intuitive.

5.1 Reynolds Number

Reynolds number significantly affects the interactions between the two cylinders, and thus the displacement of the passive cylinder. In general, with the increase of the Reynolds number, both the resonance vibration amplitude and the resonance frequency is increased, while the phase difference between the active cylinder and the passive cylinder is reduced. A threshold Reynolds number is discovered, beyond which the passive cylinder vibrates steadily about a position that is closer to the active cylinder than the initial stationary position, and below which the passive cylinder is repelled away from the active cylinder. This is similar to the critical Reynolds number discussed by Gazzola et al. (2012). The difference is that in the

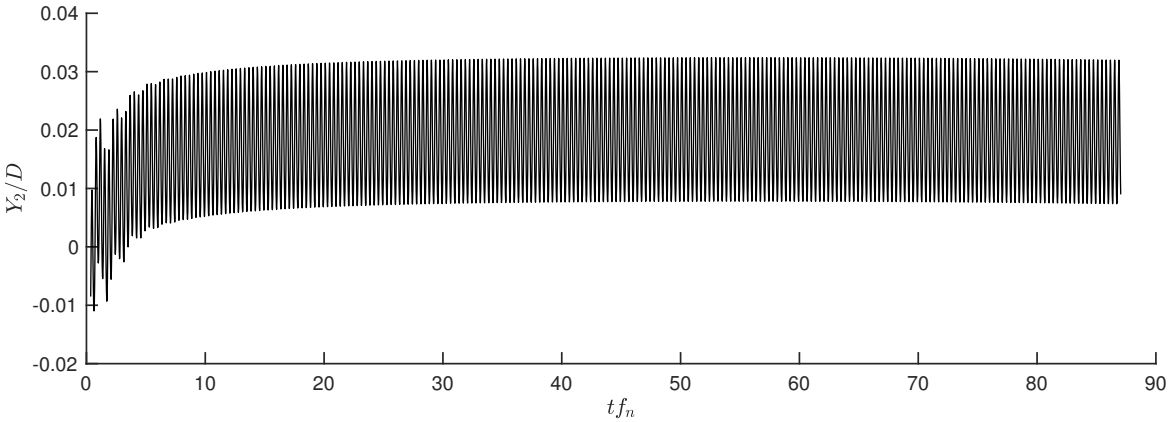

Fig. 5.1 Convergence time history for a case with $Re = 140$. After a few initial steps, the vibration amplitude and the centre drift of the passive cylinder converges to constant values.

current scenario, the passive cylinder is constrained by a spring rather than being free and it is not neutrally buoyant, so it is not carried away by the flowing fluid but vibrates about a constant position away from the initial position. The influence of the damping factor and the mass ratio on the relationship between the Reynolds number and the passive cylinder's displacement is also examined. We then further discuss the influence of the Reynolds number on the flow field adjacent to the two cylinders.

5.1.1 Effects of Reynolds Number on the Passive Cylinder's Vibration Centre Drift

Similar to Case B in Gazzola et al. (2012), the passive cylinder in the presented cases is also observed to be repelled away or attracted towards the active cylinder, depending on the value of Re_m. Nevertheless, it should be noted that the repelling and attraction discussed is referred to the centre of the passive cylinder's vibration relative to its stationary position at time zero - either closer or further away from the active cylinder. For this reason, in the following discussion, this phenomenon is addressed as "vibration centre drift".

In the periodic regimes, the vibration amplitude and the centre drift of the passive cylinder will converge after a few initial periods, as seen in Figure 5.1. So the converged amplitude A_2 and the vibration centre drift $\Delta\overline{Y}_2$ are useful to describe the general vibration patterns of the passive cylinder. In this thesis, for the cases with periodical interaction, the amplitude of the passive cylinder's vibration is calculated as $A_2 = (Y_{2,max} - Y_{2,min})/2$, where $Y_{2,max}$ and $Y_{2,min}$ are the maximum and minimum displacement in the last 50 periods of steady vibration. The vibration centre drift of the passive cylinder is calculated as $\Delta\overline{Y}_2 = (Y_{max} + Y_{min})/2$. At a very low Keulegan-Carpenter number of the active cylinder $KC = 0.157 - 0.628$ and a

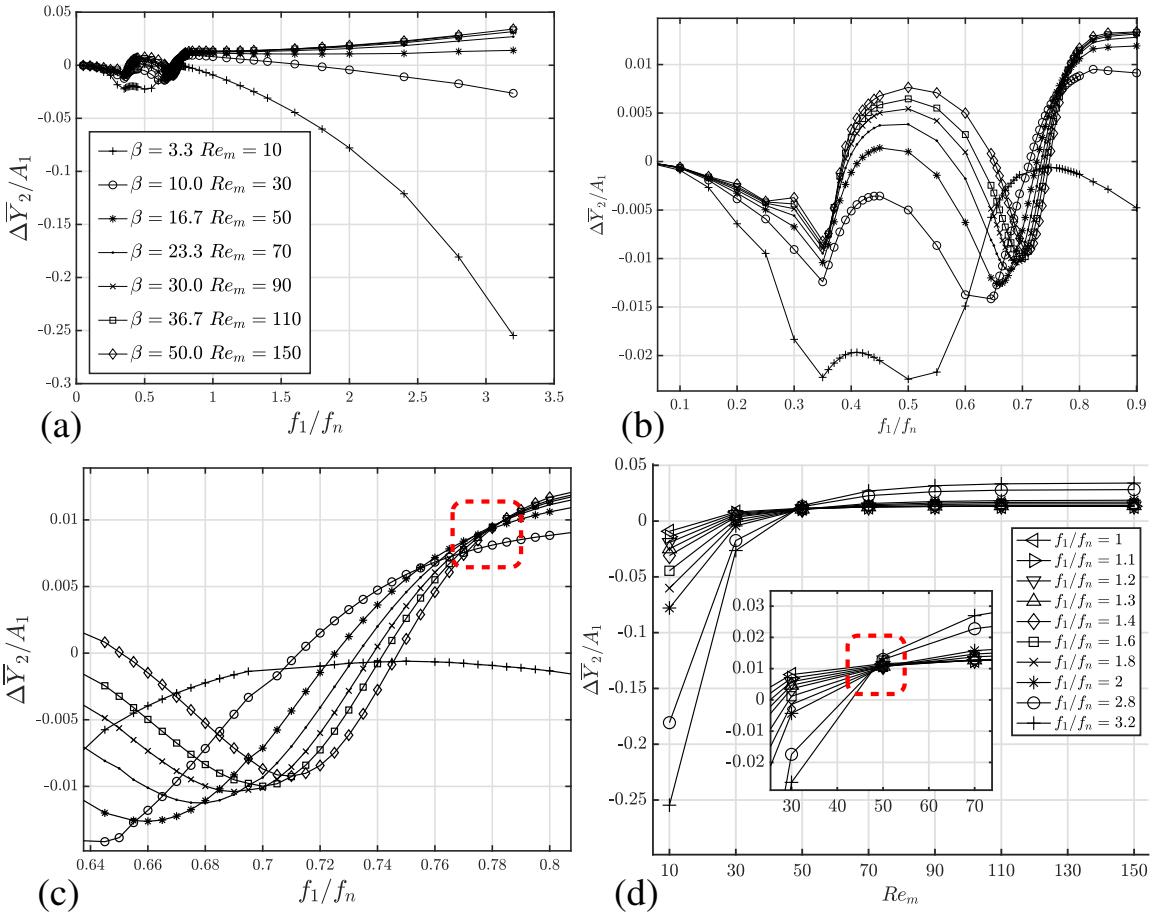

Fig. 5.2 (a) Variation in vibration centre drift $\Delta\overline{Y}_2$ with f_1/f_n at $G/D = 0.9, A_1/D = 0.477, m^* = 1.5, \zeta = 0$ and $Re_m = 10 - 150$. (b) Zoom-in at the secondary and the primary resonance regime (c) Further zoom-in at the primary resonance regime (d) Variation in vibration centre drift $\Delta\overline{Y}_2$ with Re_m at $G/D = 0.9, A_1/D = 0.477, m^* = 1.5, \zeta = 0$ and $f_1/f_n = 1 - 3.2$.

fixed Reynolds number of $Re_m = 100$, the phenomenon of vibration centre drift was hardly observed in the previous studies (Lin et al., 2018a,b). However, when the KC is increased to 3 and a variety of Re_m from 10 to 150 is tested, the vibration centre drift of the passive cylinder is clearly observed.

A critical Reynolds number is discovered that, beyond which the passive cylinder is repelled away from the active cylinder, and below which the the passive cylinder is attracted towards the active cylinder. For example, as seen in Fig. 5.2a, the critical Reynolds number is at about $Re_m = 40$, when the frequencies are relatively high at $f_1/f_n > 1$. The variation of the vibration centre drift demonstrates a unique pattern at both the secondary and the primary resonance regimes at $0.25 < f_1/f_n < 0.85$, as seen in Fig. 5.2b. The two drops in the curves at $f_1/f_n = 0.35$ and at $f_1/f_n = 0.7$ correspond to the secondary and primary resonance regimes,

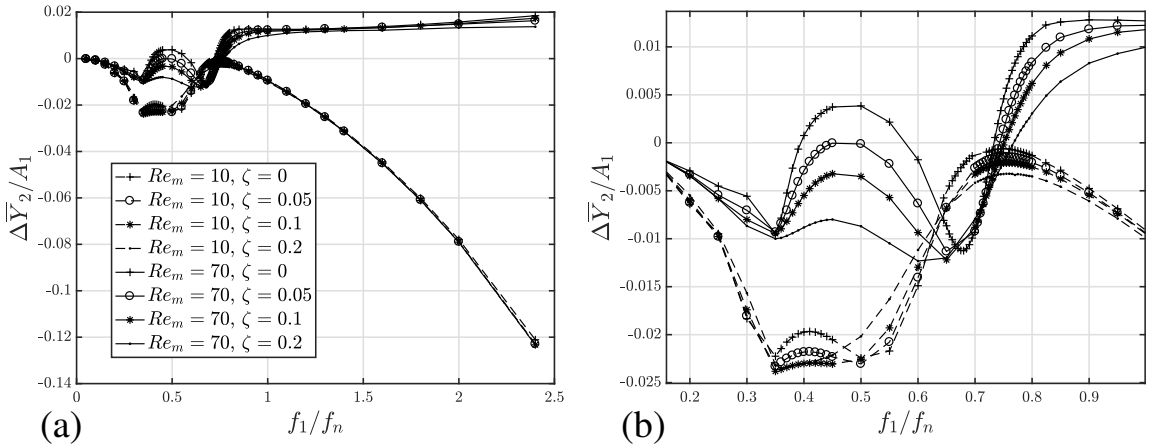

Fig. 5.3 (a) Variation in $\Delta\overline{Y}_2/A_1$ with f_1/f_n and (b) Zoom-in for its resonance regime at $G/D = 0.9, A_1/D = 0.477, m^* = 1.5, Re_m = 10, 70$ and $\zeta = 0 - 0.2$. The marker type denotes ζ, whereas the line type denotes Re_m.

respectively. This indicates that, when resonance occurs, the passive cylinder tends to be attracted towards the active cylinder. On the contrary, when the active cylinder oscillates at a relatively high frequency at $f_1/f_n > 1$, the resonance-induced drop in the curve is no longer observed. An increased frequency is found to amplify the effects of Re_m on the repelling or the attraction of the passive cylinder. Figure 5.2c is a close-up at the primary resonance at $f_1/f_n = 0.64 - 0.8$, where the attraction effect due to the resonance is clearly identified. In addition, the curves for $Re_m \geq 50$ converge at the point of $f_1/f_n = 0.78, A_2/A_1 = 0.01$. This indicates that, at $Re_m \geq 50$, when the active cylinder vibrates at the frequency of $f_1/f_n = 0.78$, the distance of the vibration centre drift is constantly $\Delta\overline{Y}_2 = 0.01A_1$, being independent of the Reynolds number. Nevertheless, at $Re_m = 10$, this pattern of convergence is not observed. Moreover, the information in Fig. 5.2c can be presented in another form. $\Delta\overline{Y}_2/A_1$ can be plotted against Re_m rather than f_1/f_n, as shown in Fig. 5.2. At a high frequency $f_1/f_n \geq 1$, the passive cylinder is increasingly repelled from the active cylinder with the rise of the Reynolds number, especially at $10 < Re_m < 100$. At $Re_m > 100$, the vibration centre drift $\Delta\overline{Y}_2$ becomes insensitive to the Reynolds number. A convergence point is observed at $Re_m = 50$ and $\Delta\overline{Y}_2/A_1 = 0.01$, which means that the vibration centre drift of the passive cylinder is independent of the active cylinder's vibration frequency at $Re_m = 50$ and $f_1/f_n > 1$. Also, it is notable that the critical Reynolds number, i.e. the Re_m corresponding to zero vibration centre drift, slightly increases with the active cylinder's vibration frequency.

The influence of the damping factor upon the passive cylinder's vibration centre drift is most significant at the resonance regime at $f_1/f_n = 0.3 - 0.8$, but is much less influential at low and high frequencies at $f_1/f_n < 0.25$ and $f_1/f_n > 1$, as seen in Fig. 5.3a. In other words,

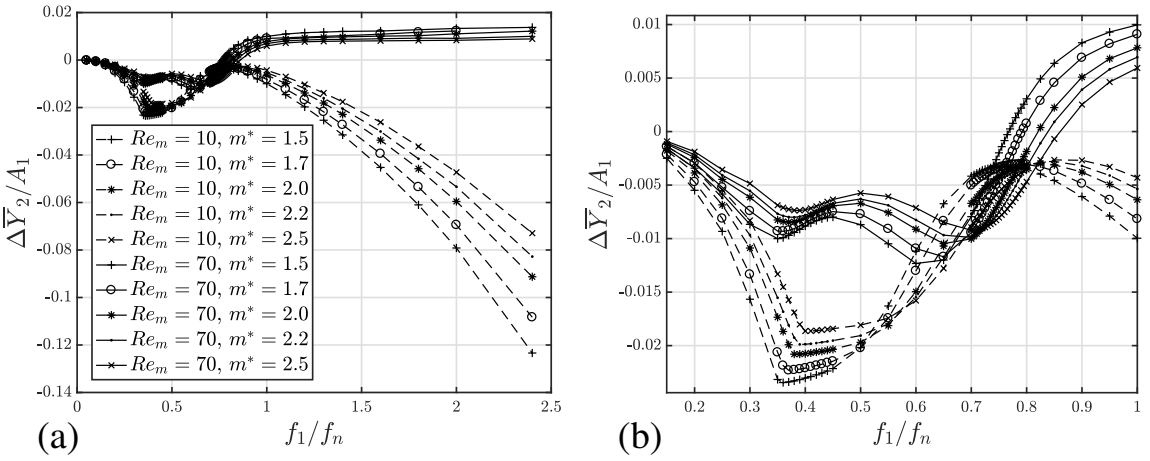

Fig. 5.4 (a) Variation in $\Delta\overline{Y}_2/A_1$ with f_1/f_n and (b) Zoom-in for its resonance regime at $G/D = 0.9, A_1/D = 0.477, \zeta = 0.2, Re_m = 10, 70$ and $m^* = 1.5 - 2.5$. The marker type denotes m^*, whereas the line type denotes Re_m.

at resonance, the passive cylinder tend to be attracted towards the active cylinder with a high damping factor. This pattern corresponds well to the damping factor's effect on the passive cylinder's responding amplitude, where the damping effect also becomes most significant at the resonance regimes and diminishes at both very high and very low frequency regimes, as demonstrated in Lin et al. (2018a). As seen in Fig. 5.3b, it is interesting that a higher damping factor can actually push the passive cylinder further away from the initial vibration centre, which is counter-intuitive.

The Reynolds number affects the damping factor's influence on the frequency-amplitude relationship, as seen in Fig. 5.3a. In general, at the resonance regime, the vibration centre drift is more sensitive to damping factor with a higher Reynolds number. For example, as seen in Fig. 5.3b, with the damping factor ζ rising from 0 to 0.2, the vibration centre drift $\Delta\overline{Y}_2$ increased by 0.003 from -0.023 to -0.020 at $Re_m = 10$, whereas it increases by 0.012 from -0.008 to 0.004 at $Re_m = 70$. The increment at $Re_m = 10$ is only 25% of that at $Re_m = 70$.

Mass ratio m^* also plays an important role on the vibration centre drift of the passive cylinder. In contrast to the damping factor, the mass ratio becomes more influential over the vibration centre drift when the frequency is beyond the resonance regime, as seen in Fig. 5.4a. With a further examination, it is found that the correlation between the mass ratio and the vibration centre drift reverses twice at $Re_m = 10$, but it reverses for only once at $Re_m = 70$, as seen in Fig. 5.4b. For cases with low $Re_m = 10$, vibration centre drift is positively correlated with m^* at low frequencies. As f_1/f_n goes beyond 0.5, the correlation is reversed that the vibration centre drift decreases with m^*. When f_1/f_n is further increased beyond 0.8, the correlation is reversed back to be positive again, and remains positive for larger frequencies.

Here, for $Re_m = 10$, the correlation is reversed twice at $f_1/f_n = 0.5$ and $f_1/f_n = 0.8$, and it ends up in positive correlation. For cases with high $Re_m = 70$, vibration centre drift is positively correlated with m^* at low frequencies, similar to low Re_m cases. When f_1/f_n goes above 0.7, the correlation becomes negative, and it remains negative for all frequencies at $f_1/f_n > 0.7$. Here, the correlation is reversed once, and it ends up in negative correlation.

In summary, at a low frequency $f_1/f_n < 0.5$ or a high frequency $f_1/f_n > 0.8$, with the increase of the mass ratio, the passive cylinder is dragged towards its initial position, where $\Delta\overline{Y}_2/A_1 = 0$. However, at the primary resonance regime $0.5 < f_1/f_n < 0.8$, the increase of mass ratio may cause the passive cylinder to be attracted towards the active cylinder, which is counter-intuitive.

5.1.2 Effects of Reynolds Number on Passive Cylinder's Vibration Amplitude

The amplitude spectra of passive cylinder's displacement offer an comprehensive overview to the dynamic characteristics of the passive cylinder, as depicted in Fig. 5.5. It is seen that the amplitude of the dominant frequency components at resonance increases exponentially with Re_m. As seen in Fig. 5.5a, a series of frequency components are observed with almost zero component frequencies $f/f_n \approx 0$. This indicates that the vibration centre of the passive cylinder at the periodic state shifts from its initial position, giving rise to a component with an extremely low f/f_n. It is also seen that the component amplitude at zero frequency increases with active cylinder's oscillation frequency f_1/f_n, which means when the active cylinder vibrates at a higher frequency, the passive cylinder drifts further away from the initial position. The influence of the Reynolds number on the component amplitude at zero frequency is more complicated. It initially decreases with Re_m at low Reynolds numbers and, when Re_m goes beyond a critical value, e.g. $Re_m = 50$ in Fig. 5.5c, the amplitude increases with Re_m again. The relationship between the Reynolds number and the vibration centre drift of the passive cylinder will be further discussed in Section 5.1.1.

A critical damping factor is discovered at $\zeta = 0.1$, below which the resonance amplification factor increases with the Reynolds number, and beyond which the factor decreases with the Reynolds number, as seen in Fig. 5.6a. It is also seen that the increase of the Reynolds number amplifies the effect of the damping factor. In other words, the peak amplification factor becomes more sensitive to the damping factor at a high Reynolds number. The same pattern applies to the secondary resonance regime as shown in the inset in Fig. 5.6b, although the secondary peak amplification factor has a critical damping factor of $\zeta = 0.025$, rather than $\zeta = 0.1$ for the primary resonance peak in this case. The effects of the damping factor

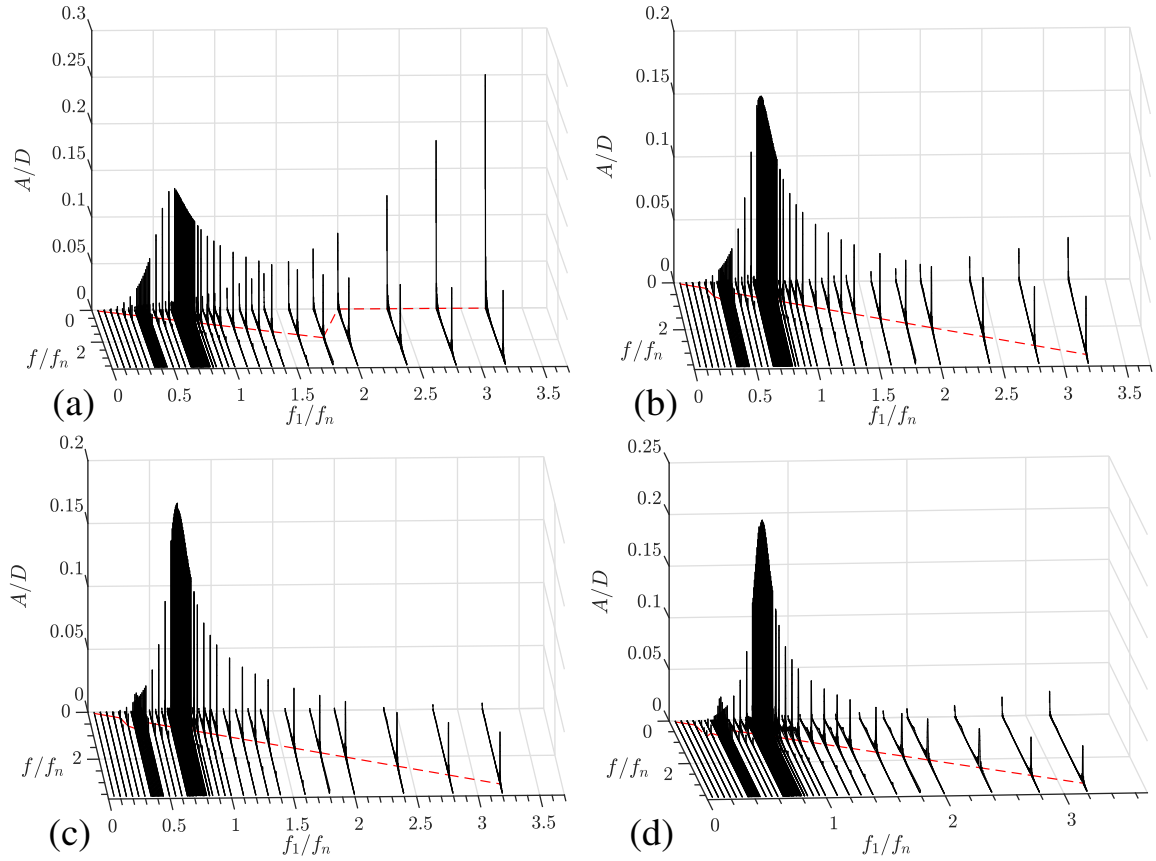

Fig. 5.5 Amplitude spectra showing the responding displacement of the passive cylinder with $f_1/f_n = 0.05-3.2$ at $G/D = 0.9, A_1/D = 0.477, m^* = 1.5, \zeta = 0$ with (a) $Re_m = 10$ (b) $Re_m = 30$ (c) $Re_m = 50$ (d) $Re_m = 110$. The dashed thin line tracks the dominant frequencies.

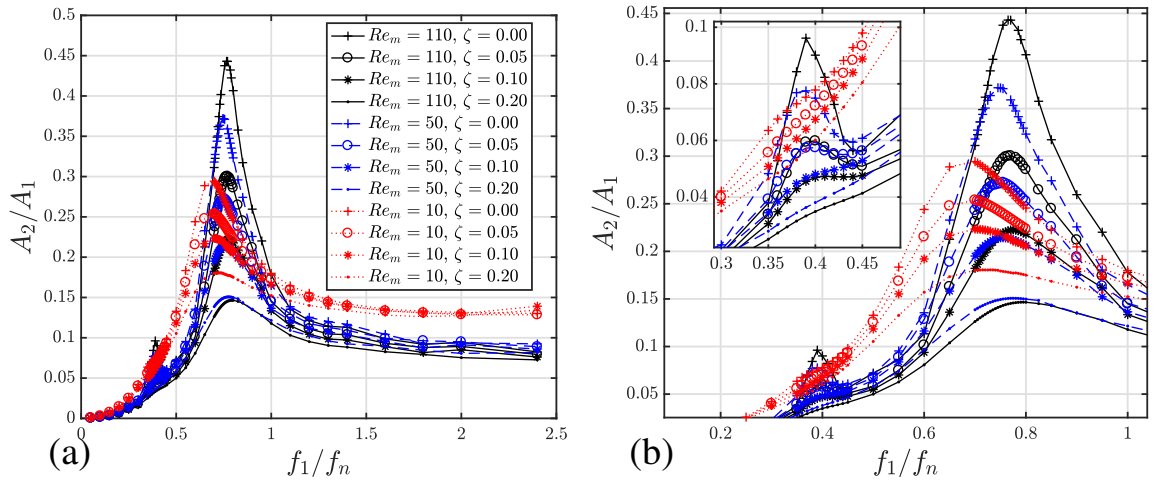

Fig. 5.6 (a) Variation of passive cylinder's amplification factor A_2/A_1 with active cylinder's oscillation frequency f_1/f_n at $G/D = 0.9, A_1/D = 0.477, m^* = 2.0, Re_m = 10-110$ and $\zeta = 0-0.2$. (b) Zoom-in at resonance regimes. The marker type denotes damping factor ζ, whereas the line type denotes the Reynolds number Re_m.

are weakened at very low or very high frequencies, which is consistent with the conclusion made by Lin et al. (2018a). The mechanism of the critical damping factor will be discussed in detail later.

With a damping ratio less than 0.1, the passive cylinder's resonance amplitude and the resonance frequency both increase with the Reynolds number, as seen in Fig. 5.7, which matches the pattern shown in Fig. 5.5. At $f_1/f_n < 1$, the passive cylinder's vibration amplitude generally increases with Reynolds number, whereas at $f_1/f_n > 1$ the amplitude decreases with Reynolds number, as demonstrated in Fig. 5.7a. As seen in Fig. 5.7b, when Re_m increases from 10 to 150, the resonance amplitude doubles from 0.3 to 0.6. Meanwhile, the resonance frequency increases from 0.625 to 0.74. In terms of secondary resonance at $0.34 < f_1/f_n < 0.4$, as Re_m rises from 30 to 150, the amplitude of the secondary resonance doubles from 0.075 to 0.14 and the secondary resonance frequency rises from 0.36 to 0.375. The situation at $Re_m = 10$ is special that the secondary resonance is not observed, and, here, the amplitude at $Re_m = 10$ is higher than those at $Re_m = 30 - 50$. The vibration phase difference between the two cylinders is demonstrated in Fig. 5.7c. Overall, the increase of Re_m causes the phase difference curves to shift upwards. The steepness of the phase change at resonance slightly increases with Re_m as well.

Reynolds number does not qualitatively affect the relationship between the mass ratio and the peak amplification factor, as seen in Fig. 5.8. The primary and secondary resonance frequencies increase with the mass ratio, regardless of the Reynolds number.

5.2 Flow Fields Around the Two Cylinders

This section examines the effect of the Reynolds number upon the flow fields surrounding the two cylinders. The typical cases with parameter combinations of $G/D = 0.9, A_1/D = 0.477, m^* = 1.5, f_1/f_n = 2.8$ and various Re_m are examined in detail. The major flow feature presented below is representative to other cases examined in this study.

The flow resulting from the flow-mediated interaction between the two cylinders moving along the vertical (y) axis has the following symmetry properties:

$$u_1(x,y,t) = -u_1(-x,y,t) \tag{5.1}$$

$$(u_1,u_2)(x,y,t) = (u_1,u_2)(x,y,t+T) \tag{5.2}$$

where Eq. 5.1 represents reflection symmetry about y-axis, while Eq. 5.2 stands for the periodic nature of the flow-mediated interaction in the current range of parametric space.

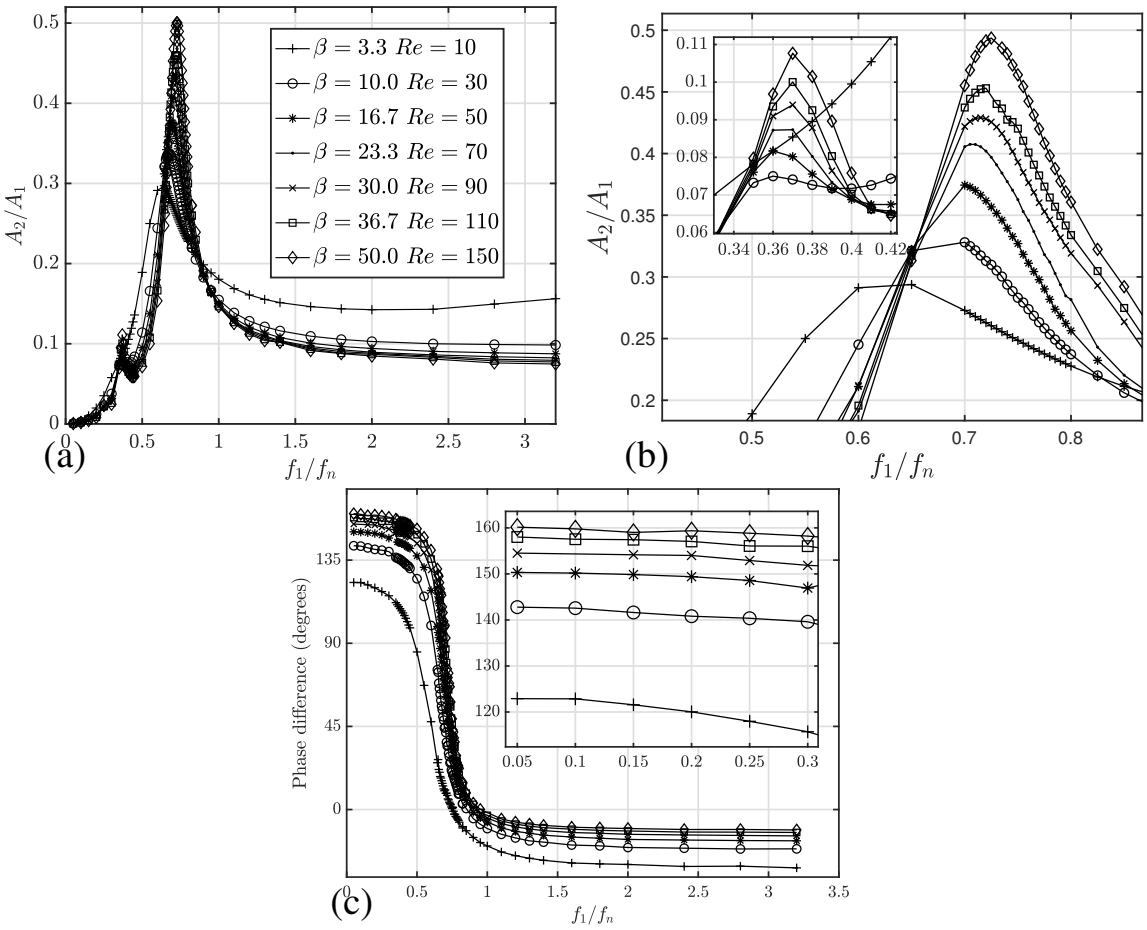

Fig. 5.7 (a) Variation of amplification factor A_2/A_1 with active cylinder's oscillation frequency f_1/f_n (b) Zoom-in at primary and secondary resonance regimes and (c) Variation of phase difference between the two cylinders $\Delta\phi_{21}$ with f_1/f_n (for the frequency components with $f/f_n = f_1/f_n$) with f_1/f_n at $G/D = 0.9$,$A_1/D = 0.477$, $m^* = 1.5, \zeta = 0, Re_m = 10-150$, i.e. $KC = 3, \beta = 3.3-50$. A_2/A_1 is positively correlated with Re_m, particularly within the regime of resonance, and the resonance frequency increases with Re_m. The resonance amplitude at $Re_m = 150$ is as large as 1.6 times of that at $Re_m = 10$. The phase difference is shifted towards the positive side with the increase of Re_m.

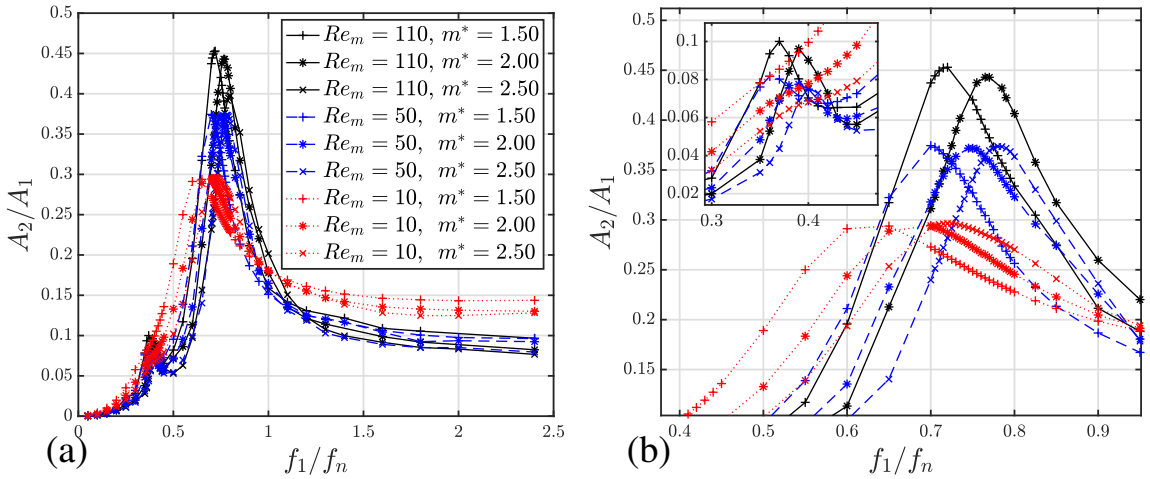

Fig. 5.8 (a) Variation of passive cylinder's amplification factor A_2/A_1 with active cylinder's oscillation frequency f_1/f_n at $G/D = 0.9, A_1/D = 0.477, \zeta = 0, m^* = 1.5-2.5, Re_m = 10-110$ and (b) Zoom-in at resonance regimes. The marker type denotes mass ratio m^*, whereas the line type denotes the Reynolds number Re_m.

Since the scenario is symmetric regarding y-axis, Figs. 5.9 and 5.10 present only the left half of the region around the two cylinders.

With the increase of the Reynolds number, more vortices are generated. For example, pressure coefficient and velocity vectors in the gap at a high frequency $f_1/f_n = 2.8$ with a constant phase of ϕ_1 are plotted in Fig. 5.9, where the pressure coefficient is calculated as $C_p = p^*/[2\pi(A_1/D)(f_1/f_n)]^2 = p/(\rho U_m^2)$. At $Re_m = 10$, no vortex is generated, as seen in Fig. 5.9a, whereas at $Re_m = 50$, a pair of vortices are generated in the gap, as shown in Fig. 5.9b. At a relatively high Reynolds number $Re_m = 150$, 2 pairs of vortices are generated in the gap, and another pair of vortices is observed at the far side of the active cylinder, as demonstrated in Fig. 5.9c. Although vortices are observed, vortex shedding does not occur at $Re_m = 10-150$, and the vortices are dissipated before they can be shed away from the two cylinders.

The pressure decreases at the near side of the active cylinder with the increase in the Reynolds number, because the generated vortices help reduce pressure. The increase of Reynolds number can also be interpreted as the relative reduction of viscosity, causing the fluid to flow out of the gap more easily and thus more rapidly reducing the pressure accumulated in the gap. Also, the vibration amplitude of the passive cylinder decreases with Reynolds number, corresponding to the reduced pressure fluctuation surrounding the passive cylinder.

The fluid around the passive cylinder tends to flow upwards with the progression of Reynolds number at $\phi_1 = 180°$, as seen in Fig. 5.9a1, 5.9b1 and 5.9c1. The increase of the

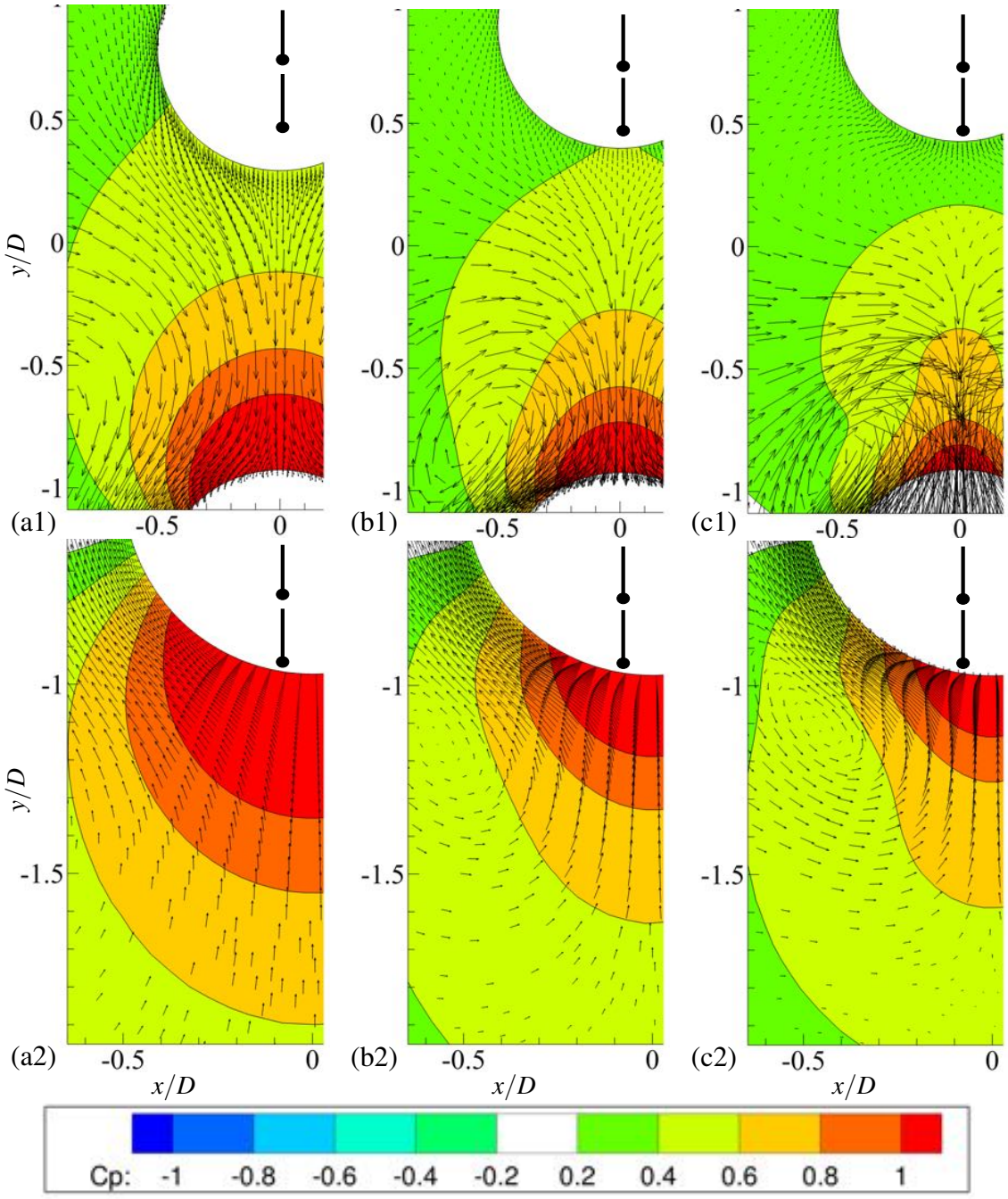

Fig. 5.9 Contours of pressure coefficient C_p and velocity vectors (1) in the gap at $\phi_1 = 180°$ and (2) in the far side of the active cylinder at $\phi_1 = 0°$, given $G/D = 0.9, A_1/D = 0.477, m^* = 1.5, f_1/f_n = 2.8$, with (a) $Re_m = 10$, $\Delta\phi_{21} = -30.6°$; (b) $Re_m = 50$, $\Delta\phi_{21} = -16.8°$; (c) $Re_m = 110$, $\Delta\phi_{21} = -12.22°$. The velocity vector is drawn on every two grid points and the vector scale factors are 0.1 grid units/magnitude.

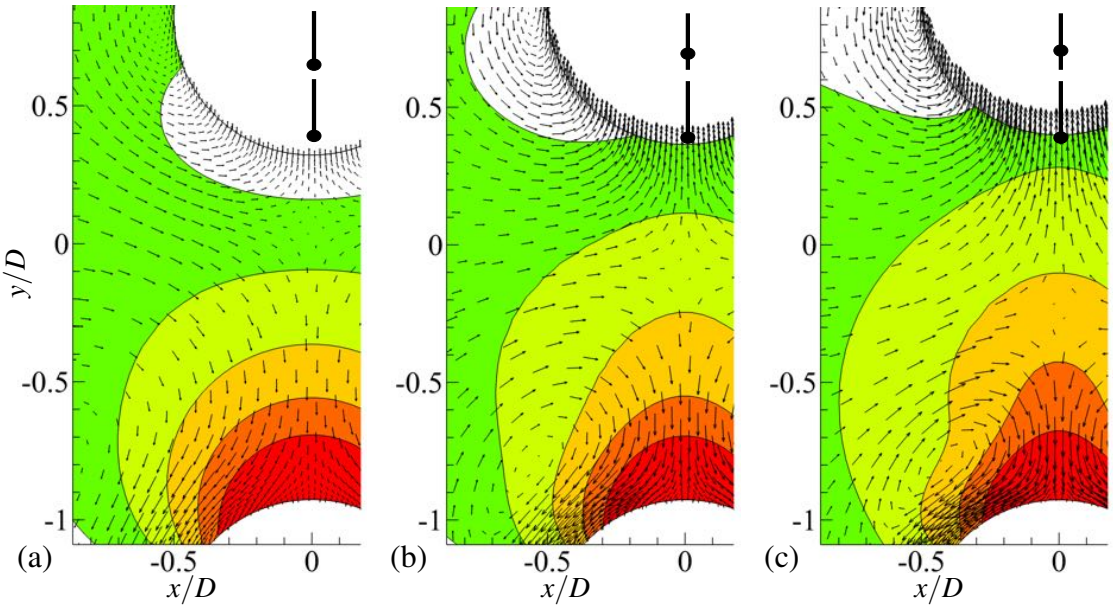

Fig. 5.10 Pressure coefficient contours and velocity vectors in the gap at $G/D = 0.9, A_1/D = 0.477, m^* = 1.5, \zeta = 0$, and $\phi_1 = 180^\circ$ with (a) $Re_m = 10, f_1/f_n = 0.65, \Delta\phi_{21} = 27.05^\circ$, (b) $Re_m = 50, f_1/f_n = 0.7, \Delta\phi_{21} = 64.66^\circ$, (c) $Re_m = 110, f_1/f_n = 0.72, \Delta\phi_{21} = 71.42^\circ$, The velocity vector is drawn on every two grid points and the vector scale factors are 0.1 grid units/magnitude.

Reynolds number, i.e. the decrease of viscous influence, contributes to the slow dissipation of the secondary vortices at the near side of the passive cylinder in Fig. 5.9c1, which causes the fluid to flow upwards, favouring the repelling of the passive cylinder. This explains the increase of the vibration centre drift with the Reynolds number as seen in Fig. 5.2d. This mechanism is very similar to the cases where the passive cylinder is not constrained by a spring (Gazzola et al., 2012, p. 14). This difference of flow structure will be further discussed later by vorticity plots and streamlines.

At the resonance regime, as seen in Fig. 5.10, less vortices are generated in the gap between the two cylinders, compared with the high frequency situation demonstrated in Fig. 5.9. At $Re_m = 150$, only one pair of vortices are generated in the gap at the resonance frequency, as shown in Fig. 5.9c1, while two pairs are observed at the high frequency as demonstrated in Fig. 5.10c. By comparing the velocity fields in Figs. 5.9 and 5.10, it is seen that the fluid flows more violently at a higher frequency, because the maximum velocity of the vibrating active cylinder U_m is increased, contributing more dynamic energy imparted to the surrounding fluid and thus amplifying attraction and repelling of the passive cylinder.

The secondary vortices at the near side of the passive cylinder is observed at the high frequency as seen in Fig. 5.9c1 but it is not seen at the resonance frequency Fig. 5.10c. The

reduction on the active cylinder's oscillation frequency weakens the secondary vortices in the gap, and thus reducing the repelling effect on the passive cylinder. This is consistent with the pattern shown in Fig. 5.2a.

Pressure coefficient and streamlines at a high frequency $f_1/f_n = 2.8$ are demonstrated in Fig. 5.11. With the increase of Reynolds number, the intensity of pressure fluctuation in the gap and at the far side of the passive cylinder both decreases, as seen in Fig. 5.11a1, 5.11a2 and 5.11a3. Since the pressure difference on the circumference of the passive cylinder is the main driver of its motion (Lin et al., 2018a), the vibration amplitude of the passive cylinder is reduced due to the increase in the Reynolds number. This confirms the results shown in Fig. 5.7, where the amplification factor decreases with the Reynolds number at a high frequency. Also, with the increase of Re_m, the influence of vortices on the pressure is strengthened. This effect is indicated in Fig. 5.11a3 as the two small local low pressure spots located symmetrical beneath the active cylinder and in Fig. 5.11c3 as the two small local low pressure spots located symmetrical above the active cylinder.

The vorticity contours, Figs. 5.12 and 5.13, demonstrate the flow pattern difference between the case with $Re_m = 10$, which is lower than the critical Reynolds number and the case with $Re_m = 150$, which is higher than the critical Reynolds number. The change of flow field is presented in Fig. 5.12 when Re_m is increased from 10 to 150, which means the viscous effect is reduced. At $Re_m = 10$, the vortices are in general much larger than those at $Re_m = 150$ due to high viscosity. As demonstrated in Fig. 5.13a, at $\phi = 180^\circ$, the large vortices drive the surrounding fluid to flow downwards. The passive cylinder is immersed in the downward flow, and it is driven towards the active cylinder. As mentioned before, at $Re_m = 10$, an extra pair of vortices is never observed during the periodical vibration of the passive cylinder.At $Re_m = 150$, low viscosity causes the vortices in the gap harder to dissipated, and the size of vortex also becomes smaller. Taking Fig. 5.12c2 for example, the pair of vortices in the gap can be seen throughout the whole cycle, see Fig. 5.12a2-5.12d2, of the flow-mediated interaction. This pair of vortices has opposite signs. The positive vortex is always on the left, whereas the negative vortex is always on the right. Together they propel a fluid flow to push away the passive cylinder. The flow structure is also demonstrated by the streamlines in Fig. 5.13b. The existence of these vortices throughout the periodical vibration of the salve cylinder causes its vibration centre to drift towards the far side.

The vortices at $Re_m = 10$ are in general much larger than those at $Re_m = 150$ due to high viscosity. As demonstrated in Fig. 5.13a, at $\phi = 180^\circ$, the large vortices drive the surrounding fluid to flow downwards, producing a strong attraction towards the active cylinder. The passive cylinder is immersed in the downward flow, and it is dragged towards the active cylinder. The high viscosity also leads to quicker dissipation of the vortices. At

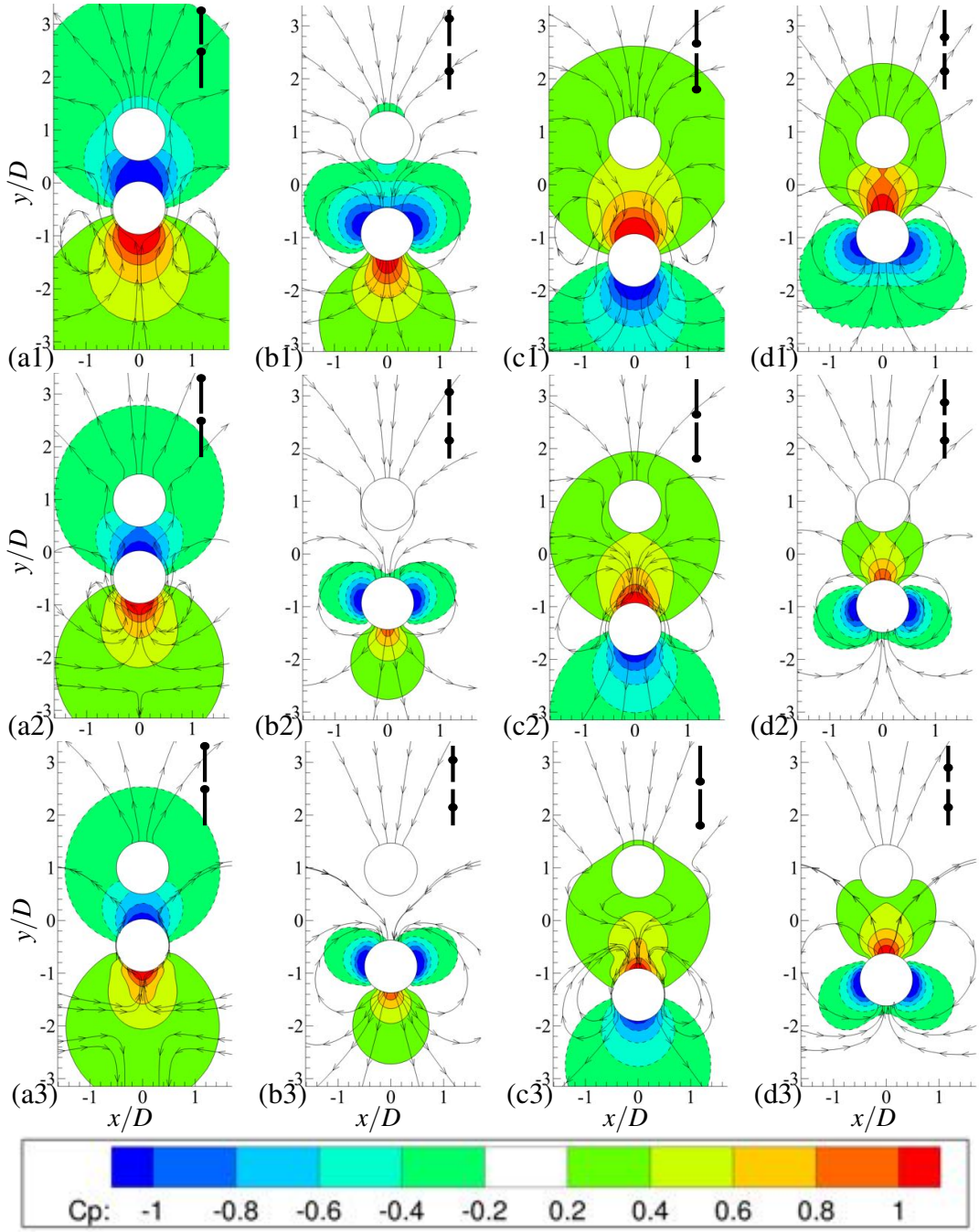

Fig. 5.11 Pressure coefficient contours and streamlines at $G/D = 0.9, A_1/D = 0.477, m^* = 1.5, \zeta = 0$, and (1) $Re_m = 10, f_1/f_n = 2.8, \Delta\phi_{21} = -30.64°$, (2) $Re_m = 50, f_1/f_n = 2.8, \Delta\phi_{21} = -16.77°$, (3) $Re_m = 110, f_1/f_n = 2.8, \Delta\phi_{21} = -12.22°$, (a) $\phi_1 = 0°$ (b) $\phi_1 = 90°$ (c) $\phi_1 = 180°$ (d) $\phi_1 = 270°$. The numbers [1-4] identify the case with different Re, whereas the alphabets [a-d] indicate the instances in one cycle of the active cylinder oscillation. The dots on the sticks indicate the position of the cylinders in one cycle of motion.

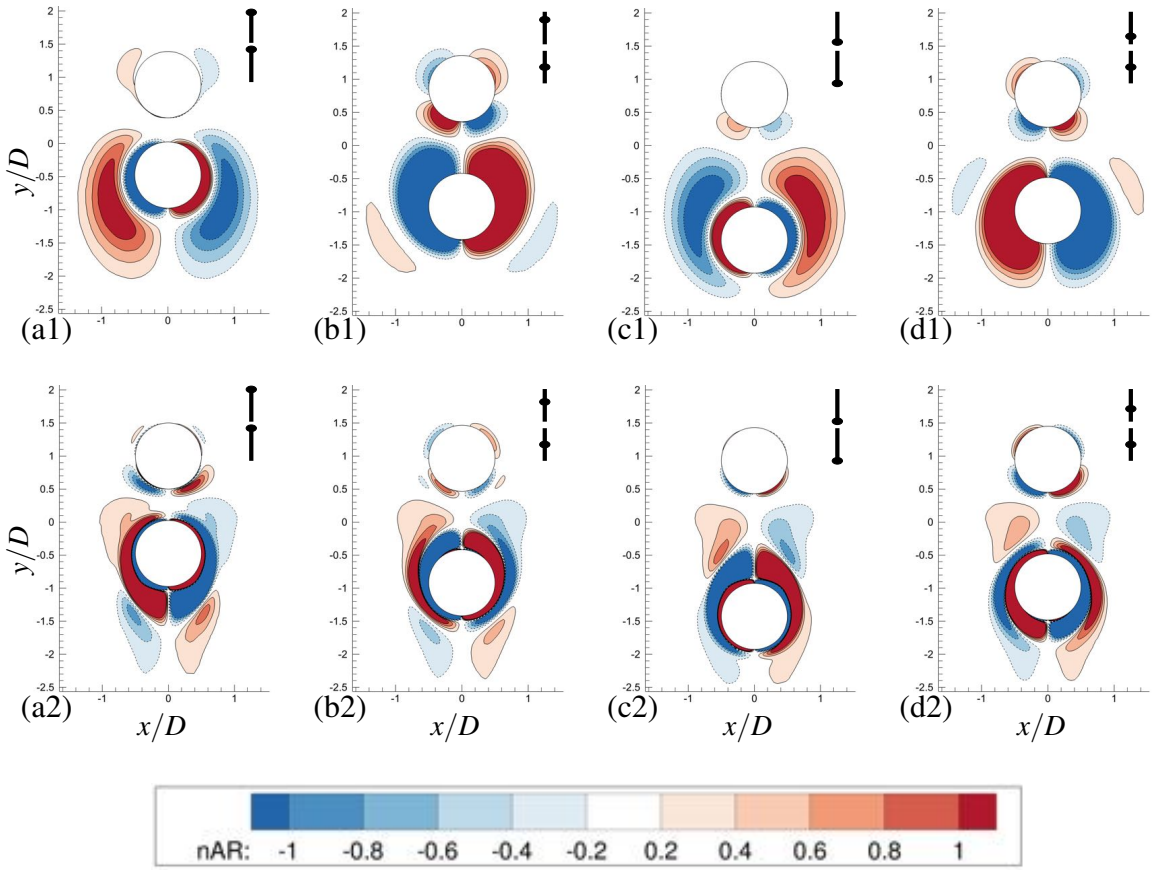

Fig. 5.12 Evolution of non-dimensional vorticity contours at $G/D = 0.9, A_1/D = 0.477, m^* = 1.5, \zeta = 0, f_1/f_n = 3.2$, and (1) $Re_m = 10$, (2) $Re_m = 150$, (a) $\phi_1 = 0^\circ$ (b) $\phi_1 = 90^\circ$ (c) $\phi_1 = 180^\circ$ (d) $\phi_1 = 270^\circ$. The numbers [1-2] identify the case with different Re, whereas the alphabets [a-d] indicate the instances in one cycle of the active cylinder oscillation.

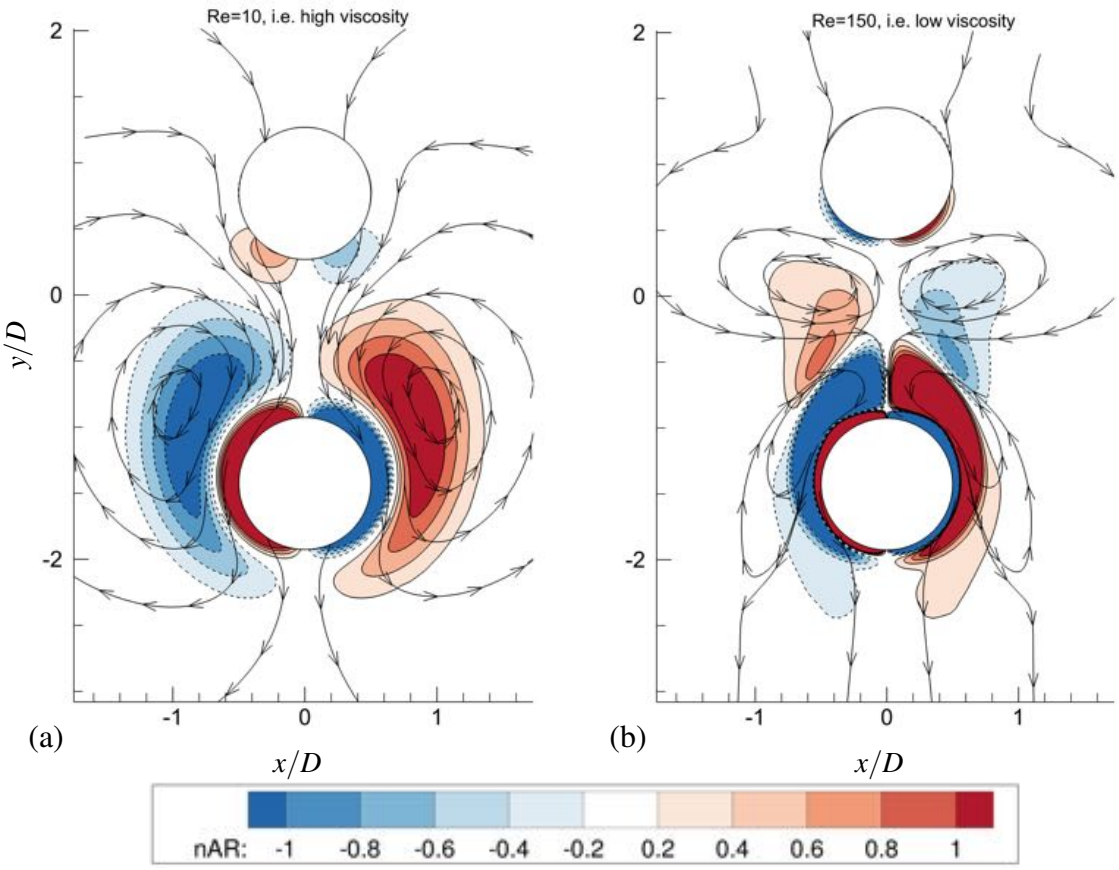

Fig. 5.13 Streamlines and non-dimensional vorticity contours at $G/D = 0.9, A_1/D = 0.477, m^* = 1.5, \zeta = 0, f_1/f_n = 3.2, \phi_1 = 180^\circ$, and (a) $Re_m = 10$, (b) $Re_m = 150$.

$Re_m = 10$ extra pair of vortices is never observed in the periodical vibration of the passive cylinder, favouring the attraction of the passive cylinder.

In summary, at $Re_m = 10$, the elastically-mounted passive cylinder's vibration centre drifts towards the active cylinder, whereas at $Re_m = 150$, the flow pattern favours the repelling of the passive cylinder. Also, at around $Re_m \approx 60$, where the effects contributing to repulsion and attraction are almost equal and the vibration centre of the passive cylinder stays at the initial position.

The time histories of the total hydraulic force coefficient show that the amplitude of the shear force decreases with Re_m due to the decreasing viscosity. The pressure force amplitude rises with the Re_m at $\zeta = 0$. The increase in pressure force exceeds the decrease in the shear force, so the amplitude of the force acting on the cylinder increases as well. Therefore, vibration amplitude increases with Re_m at $\zeta = 0$. At $\zeta = 0.2$, the shear force drops with Re_m, whereas the pressure force remains almost constant with the increase of Re_m. Consequently, the amplitude of the force acting on the cylinder reduces. As a result, the vibration amplitude decreases with Re_m at $\zeta = 0$. This applies for both the primary resonance, Fig. 5.14a-5.14f, and secondary resonance, Fig. 5.14g-5.14l.

The primary resonance, the pressure coefficient and velocity vector plots, Figs. 5.15 to 5.18, demonstrate that, at $\zeta = 0$, the intensity of pressure fluctuation around the passive cylinder increases with Re_m, whereas, at $\zeta = 0.2$, the intensity decreases with Re_m.

For example, as seen in Fig. 5.15b1-5.15b3, at $\zeta = 0$, the positive pressure above the passive cylinder increases as Re_m goes up from $Re_m = 10$ to $Re_m = 110$, whereas the negative pressure below the passive cylinder decreases only slightly. Similar patterns can be observed in other sub-figures in Fig. 5.15. So, at $\zeta = 0$, the pressure fluctuation, in general, is strengthened with Reynolds number. This is consistent with the time histories of the pressure coefficient shown in Fig. 5.14a-5.14c, where the pressure force acting on the passive cylinder fluctuates with smaller amplitude while Re_m goes up.

At $\zeta = 0.2$, as shown in Fig. 5.16b1-5.16b3, the positive pressure above the passive cylinder remains almost constant with the variation of Re_m, while the negative pressure below the passive cylinder is weakened with the increase of Re_m. Together with other sub-figures in Fig. 5.16, it is clear that the pressure fluctuation is weakened due to the increase of Re_m. This corresponds to the decrease in the amplitude of the pressure force with Re_m as seen in Fig. 5.14d-5.14f. Similar pattern can be found for the primary resonance pressure coefficient contours and velocity vectors shown in Figs. 5.17 and 5.18.

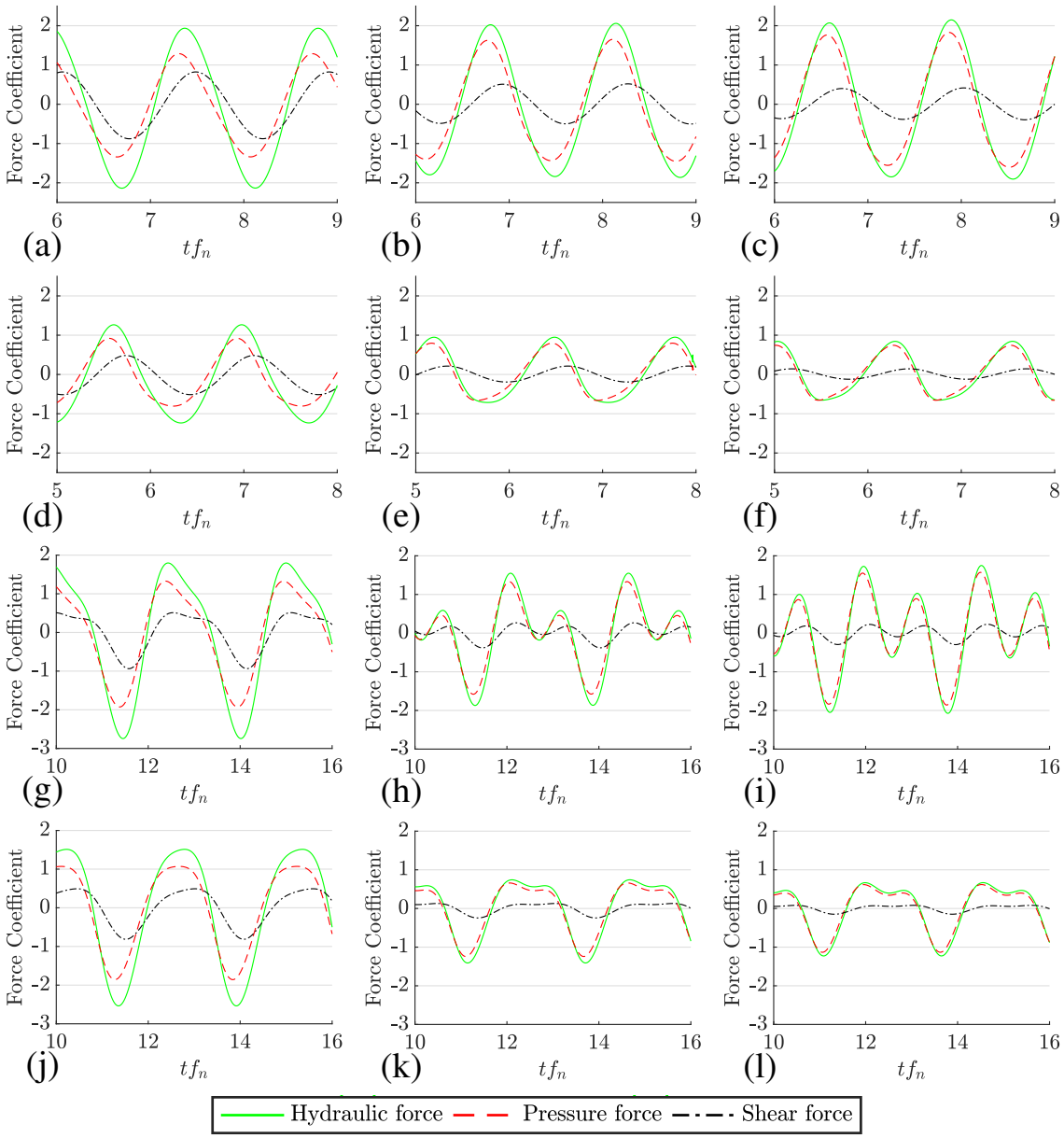

Fig. 5.14 Time histories of hydraulic force acting on the passive cylinder at primary or secondary resonance with $G/D = 0.9, A_1/D = 0.477, m^* = 2$, and (a) $\zeta = 0$, $Re_m = 10$, $f_1/f_n = 0.7$ (b) $\zeta = 0$, $Re_m = 50$, $f_1/f_n = 0.745$ (c) $\zeta = 0$, $Re_m = 110$, $f_1/f_n = 0.765$ (d) $\zeta = 0.2$, $Re_m = 10$, $f_1/f_n = 0.73$ (e) $\zeta = 0.2$, $Re_m = 50$, $f_1/f_n = 0.775$ (f) $\zeta = 0.2$, $Re_m = 110$, $f_1/f_n = 0.795$ (g) $\zeta = 0$, $Re_m = 10$, $f_1/f_n = 0.39$ (h) $\zeta = 0$, $Re_m = 50$, $f_1/f_n = 0.39$ (i) $\zeta = 0$, $Re_m = 110$, $f_1/f_n = 0.39$ (j) $\zeta = 0.2$, $Re_m = 10$, $f_1/f_n = 0.39$ (k) $\zeta = 0.2$, $Re_m = 50$, $f_1/f_n = 0.39$ (l) $\zeta = 0.2$, $Re_m = 110$, $f_1/f_n = 0.39$.

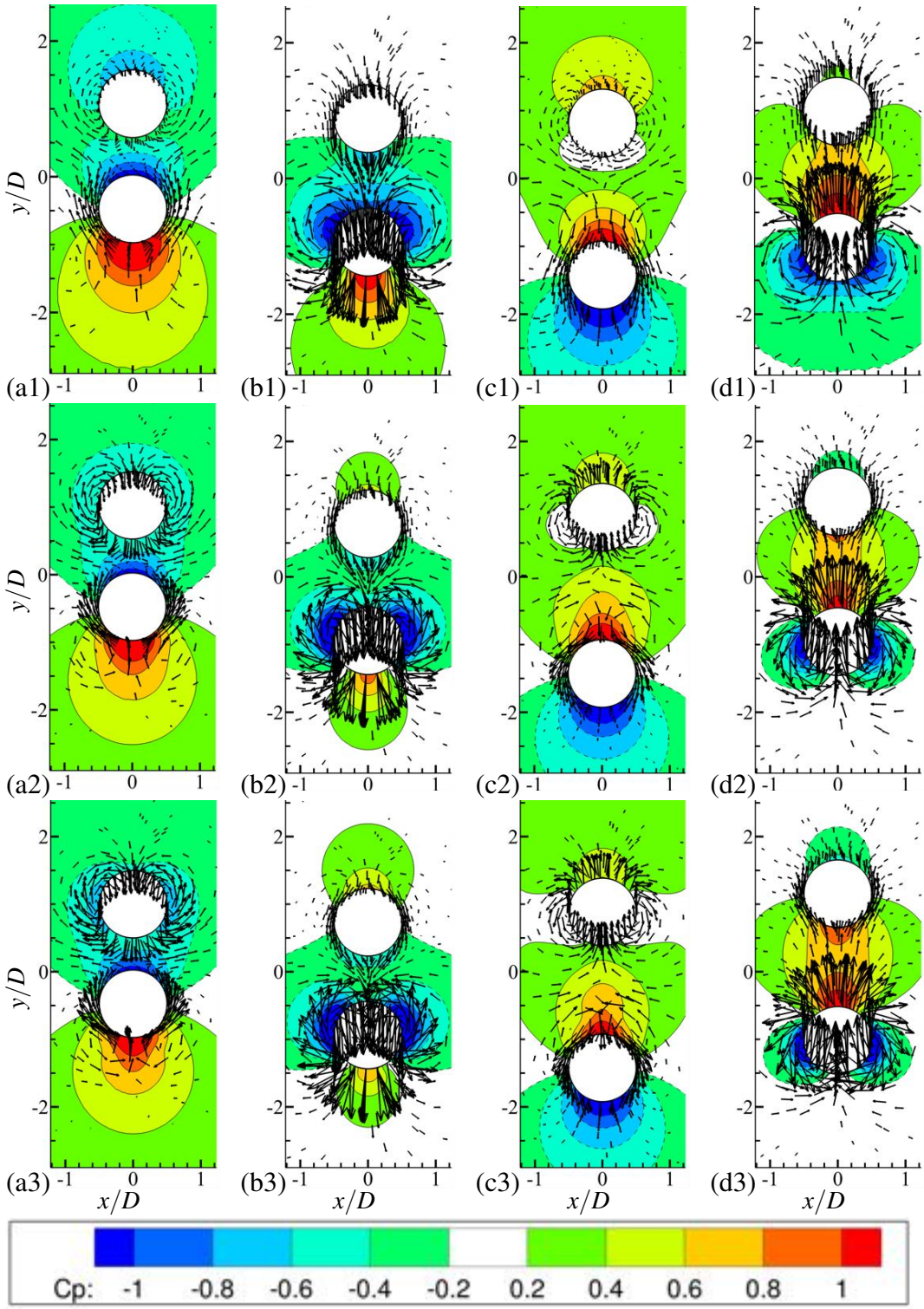

Fig. 5.15 Pressure coefficient contours and velocity vectors at $G/D = 0.9, A_1/D = 0.477, m^* = 2, \zeta = 0$ and (1) $Re_m = 10, f_1/f_n = 0.7$, (2) $Re_m = 50, f_1/f_n = 0.745$, (3) $Re_m = 110, f_1/f_n = 0.765$, (a) $\phi_1 = 0°$ (b) $\phi_1 = 90°$ (c) $\phi_1 = 180°$ (d) $\phi_1 = 270°$. Primary resonance occurs at around $f_1/f_n = 0.75$ and the damping factor is zero.

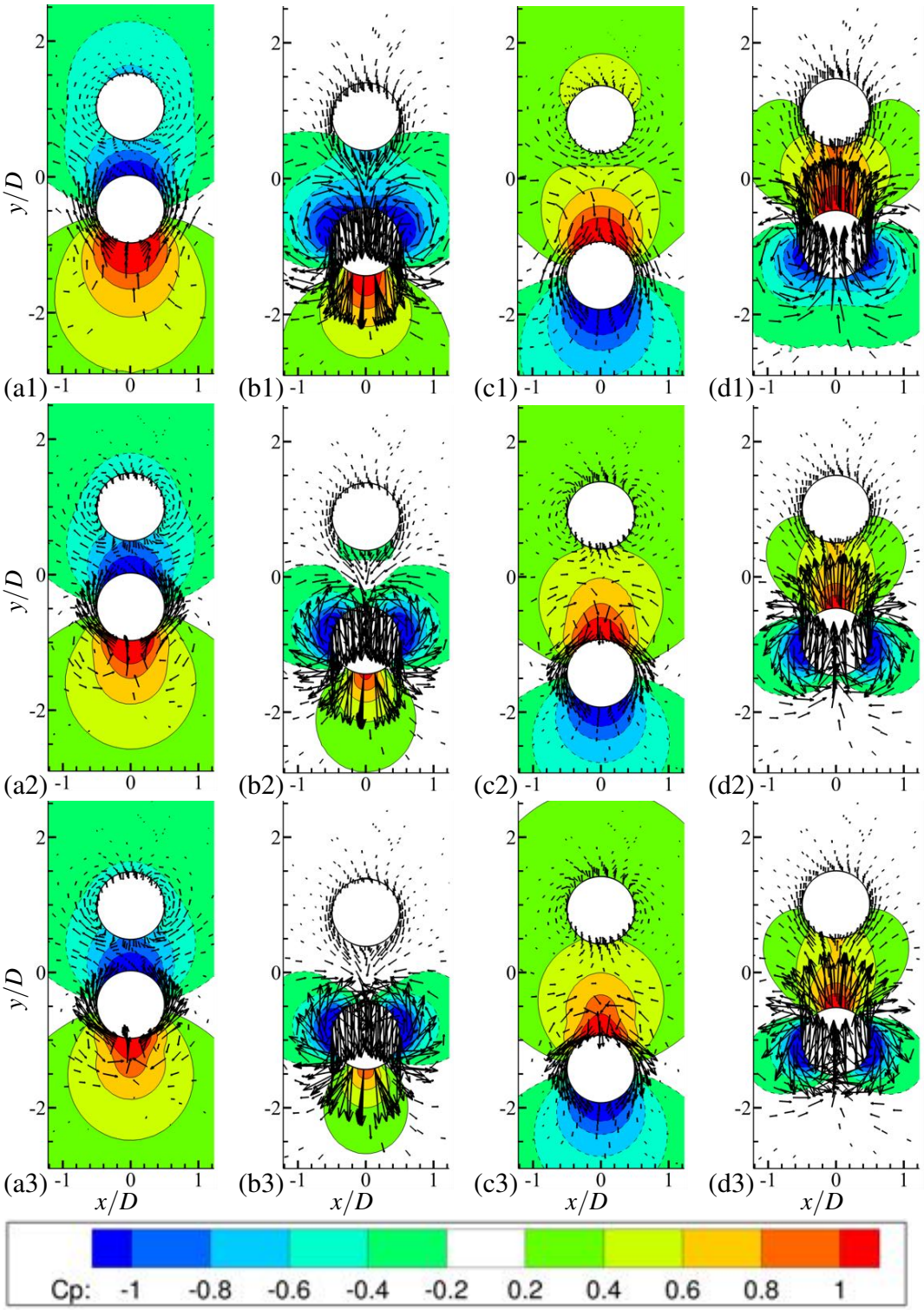

Fig. 5.16 Pressure coefficient contours and velocity vectors at $G/D = 0.9, A_1/D = 0.477, m^* = 2, \zeta = 0.2$ and (1) $Re_m = 10, f_1/f_n = 0.73$, (2) $Re_m = 50, f_1/f_n = 0.775$, (3) $Re_m = 110, f_1/f_n = 0.795$, (a) $\phi_1 = 0°$ (b) $\phi_1 = 90°$ (c) $\phi_1 = 180°$ (d) $\phi_1 = 270°$. Primary resonance occurs at around $f_1/f_n = 0.75$ and the damping factor is relatively high at $\zeta = 0.2$.

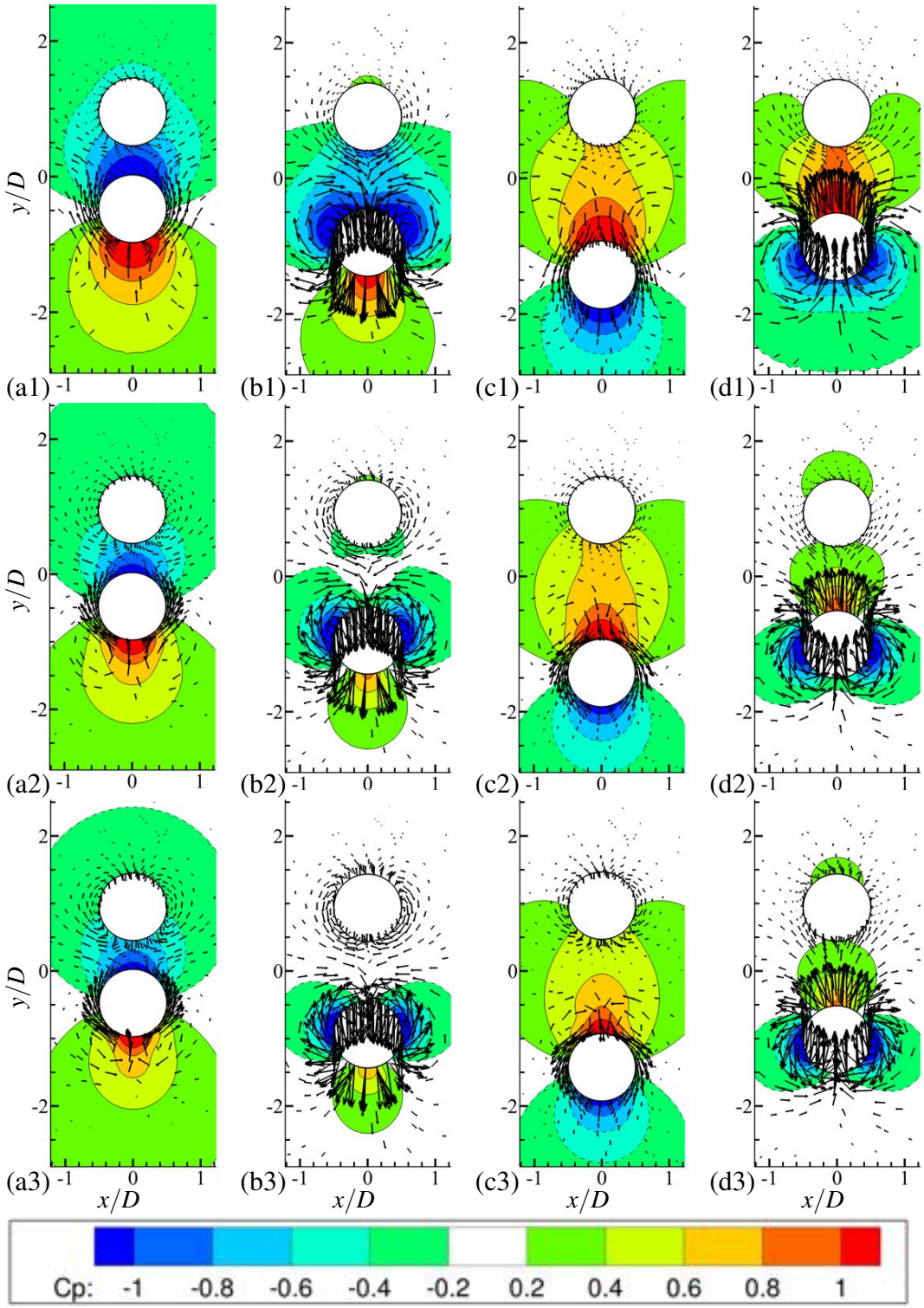

Fig. 5.17 Pressure coefficient contours and velocity vectors at $G/D = 0.9, A_1/D = 0.477, m^* = 2, \zeta = 0, f_1/f_n = 0.39$ and (1) $Re_m = 10$, (2) $Re_m = 50$, (3) $Re_m = 110$, (a) $\phi_1 = 0^\circ$ (b) $\phi_1 = 90^\circ$ (c) $\phi_1 = 180^\circ$ (d) $\phi_1 = 270^\circ$. Secondary resonance occurs at $f_1/f_n = 0.39$ and the damping factor is zero.

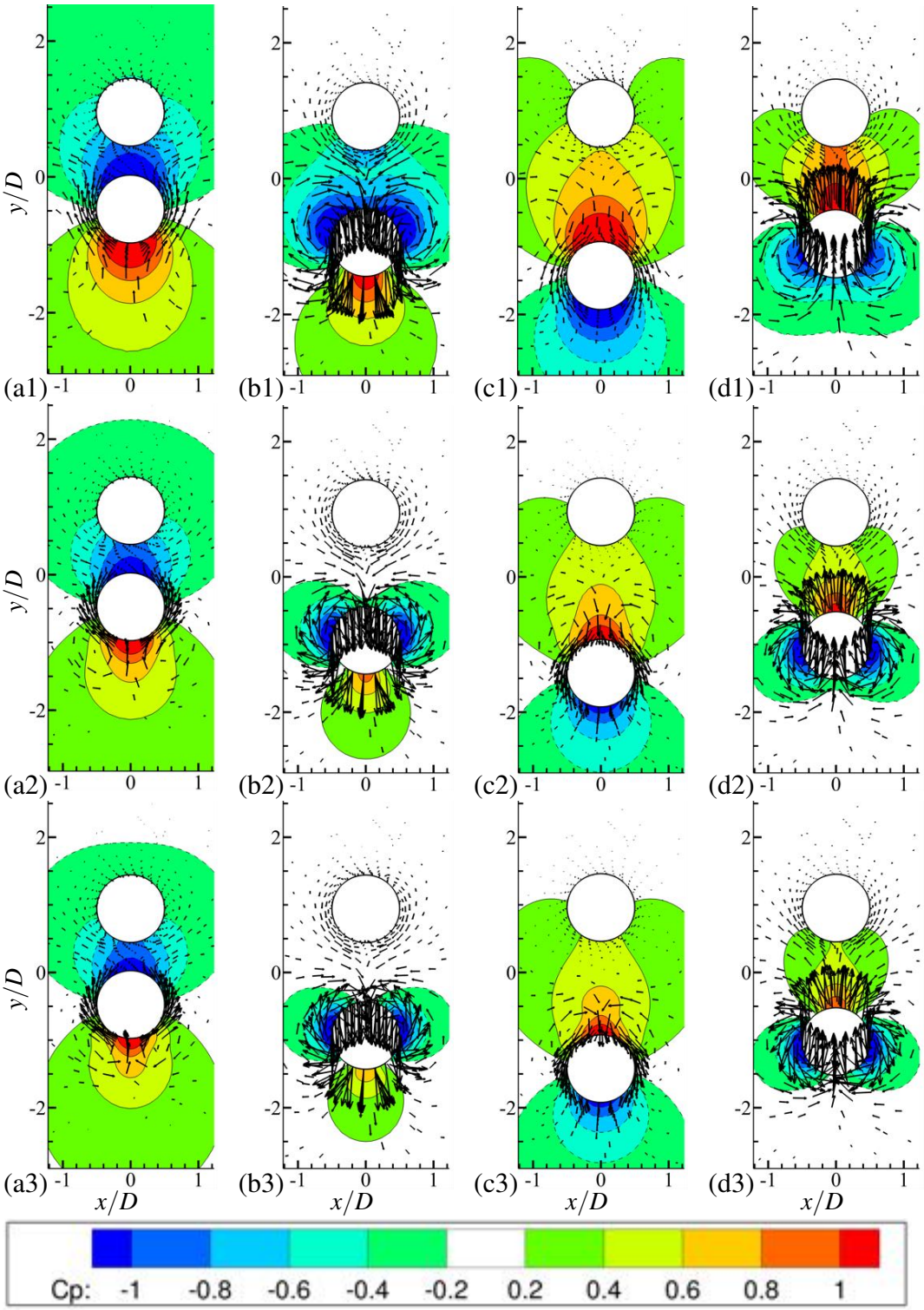

Fig. 5.18 Pressure coefficient contours and velocity vectors at $G/D = 0.9, A_1/D = 0.477, m^* = 2, \zeta = 0.2, f_1/f_n = 0.39$ and (1) $Re_m = 10$, (2) $Re_m = 50$, (3) $Re_m = 110$, (a) $\phi_1 = 0°$ (b) $\phi_1 = 90°$ (c) $\phi_1 = 180°$ (d) $\phi_1 = 270°$. Secondary resonance occurs at $f_1/f_n = 0.39$ and the damping factor is relatively high at $\zeta = 0.2$.

5.3 Gap Distance

In terms of the initial clear gap distance G/D, the passive cylinder vibration amplitude A_2/D decreases with the gap ratio G/D, as shown in Fig. 5.19. At a low frequency of the active cylinder oscillation $f_1/f_n < 0.6$, G/D barely affects A_2/D. At a high frequency $f_1/f_n > 1.0$, the passive cylinder amplitude is more sensitive to G/D compared with that at a low active cylinder frequency frequency $f_1/f_n < 0.6$. At the resonance frequency, G/D is most influential to A_2/D.

The gap ratio G/D does not affect much the phase difference, as shown in Fig. 5.20, which means the distance between the two cylinders can hardly influence the phase difference. The variation of ζ has no qualitative influence on the dependence of the amplification factor on initial gap distance G/D, as seen in Fig. 5.21a. Regardless of damping ratio ζ, G/D controls neither the resonance frequency nor $\Delta\phi_{21}$, as shown in Fig. 5.20 and Fig. 5.21b.

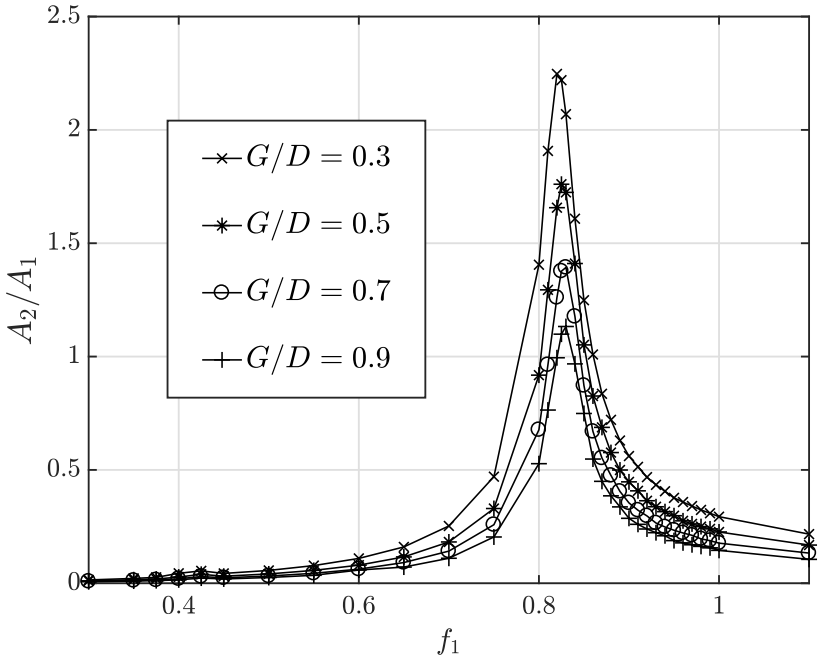

Fig. 5.19 Variation of A_2/A_1 with f_1/f_n and G/D at $m^* = 2.5, A_1/D = 0.05, Re_m = 100, \zeta = 0$. A_2/D decreases with G/D.

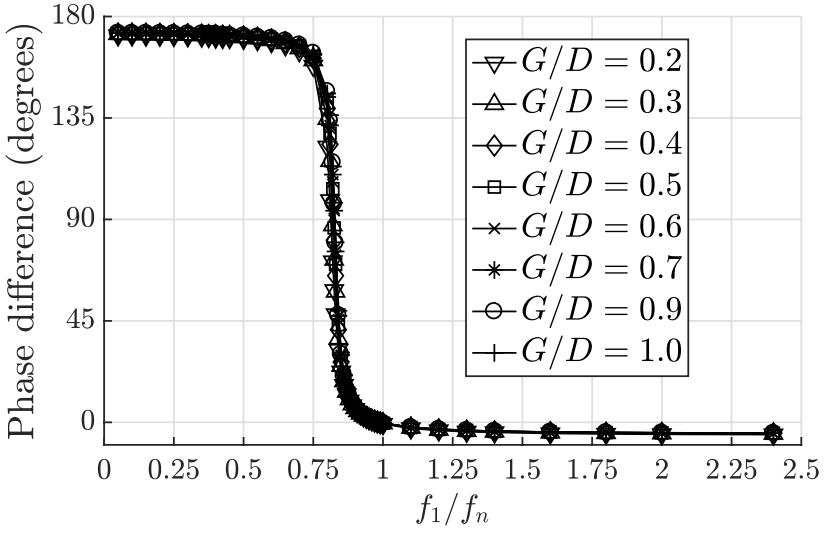

Fig. 5.20 Variation of the oscillation phase difference between the two cylinders with f_1/f_n at $A_1/D = 0.05, m^* = 2.5, G/D = 0.2 - 1.0, Re_m = 100, \zeta = 0$. G/D does not affect much the phase difference.

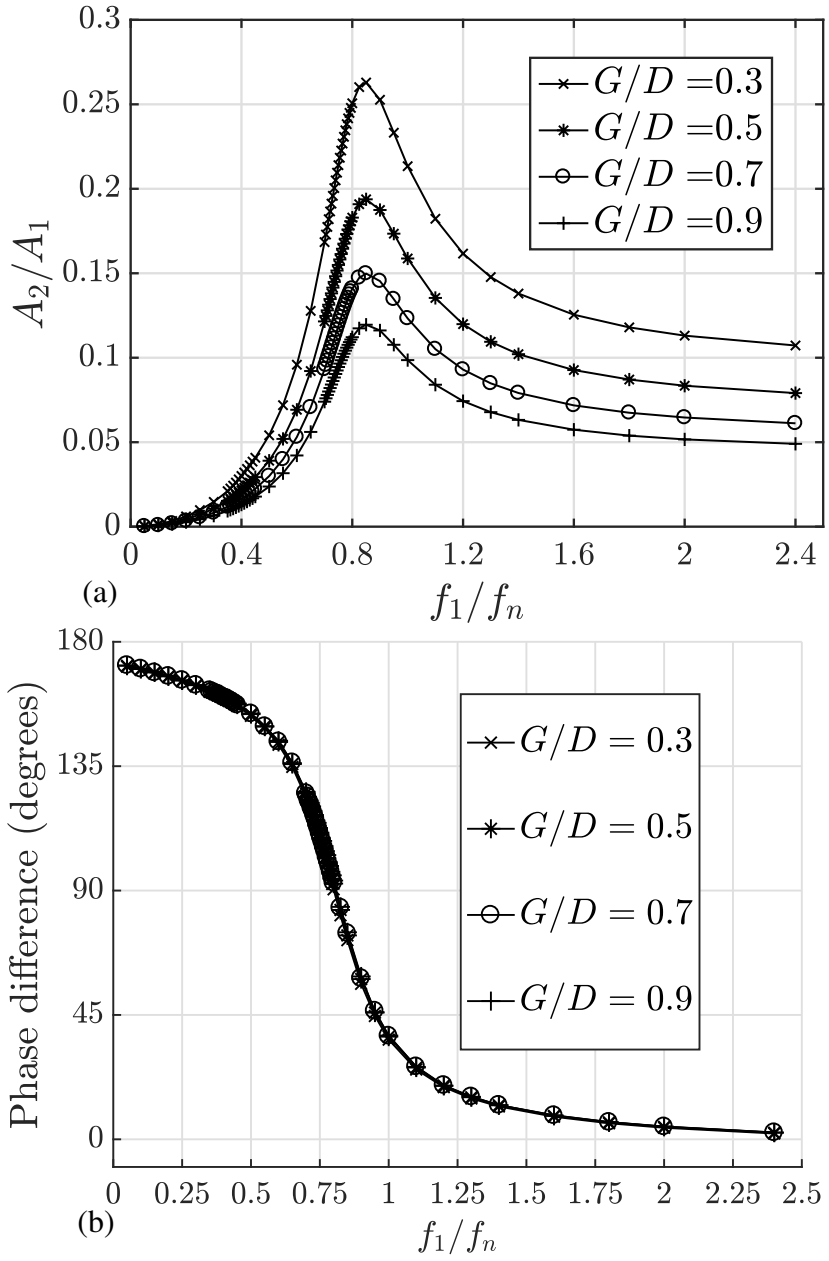

Fig. 5.21 (a) Variation of A_2/A_1 with f_1/f_n, and (b) variation of displacement phase difference $\Delta\phi_{21}$ between the passive cylinder and the active cylinder (for frequency components with $f/f_n = f_1/f_n$) with f_1/f_n at $G/D = 0.3-0.9, A_1/D = 0.05, m^* = 2.5$, and $\zeta = 0.2$. A_2/A_1 decreases with G/D, but the initial gap distance has little effect on $\Delta\phi_{21}$. This pattern is exactly the same as the undamped cases.

5.4 Chapter Summary

This chapter studies the effects of non-dimensional groups associated with the intermediate fluid, i.e. the Reynolds number Re_m and the gap ratio G/D, upon flow-mediated interactions between two cylinders immersed in an otherwise still fluid. Compared with the gap ratio, the Reynolds number is found to convey a much more complicated and significant impact upon the flow-mediated interaction.

For the vibration centre drift, a critical Reynolds number is discovered, beyond which the passive cylinder is repelled away from the active cylinder and below which the the passive cylinder is attracted towards the active cylinder. Here, the "attraction" and "repelling" indicate that the passive cylinder vibrates steadily with its vibration centre maintaining a certain distance away from its initial position and the vibration centre does not change with time. The existence of the critical Reynolds number is particularly obvious at high frequencies $f_1/f_n > 1$, while at the resonance regime this pattern is not significant. At the secondary and the primary resonance regimes, the passive cylinder tends to be attracted towards the active cylinder. When the Reynolds number is greater than $Re_m = 100$, the change of Re_m can hardly cause the vibration centre drift of the passive cylinder.

Both the passive cylinder's resonance amplitude and resonance frequency are found to increase with the Reynolds number with a damping ratio less than 0.1. The phase difference between the passive cylinder and the active cylinder decreases with Reynolds number. A critical damping factor is discovered, below which the resonance amplitude *increases* with the Reynolds number and beyond which the amplitude *decreases* with the Reynolds number. The increase of the mass ratio shifts the vibration amplitude curves to high-frequency region, but the mass ratio does not affect the overall trend of the relationship between the Reynolds number and the passive cylinder's vibration.

At the resonance regime, the passive cylinder is increasingly attracted towards the active cylinder with the increase of the damping factor. This effect can be amplified at small Reynolds numbers. The damping factor does not significantly influence the vibration centre drift at high frequencies $f_1/f_n > 1$. With the increase in the mass ratio, the passive cylinder keeps approaching to its initial position. Contrary to the influence of the damping factor, the effect of the mass ratio upon vibration centre shift grows with the increase of f_1/f_n.

The increase of the Reynolds number can result in more and stronger vortices to be generated in the gap. At high Reynolds numbers, the secondary vortices in the gap are generated, causing the fluid to flow towards the passive cylinder, contributing to the repelling force on the passive cylinder. The increase of the frequency causes the active cylinder to vibrate more violently, and also amplifying both the repelling and the attracting action on the passive cylinder.

At resonance, the increase of Reynolds number leads to a decreased amplitude for shear force and an increased amplitude for pressure force. At $\zeta = 0$, the increase in pressure force amplitude can outweigh the drop in shear force amplitude, thus causing a resonance amplitude positively correlated to Re_m. Whereas at $\zeta = 0.2$, this is not the case, resulting in a negative correlation between resonance amplitude and Re_m. This explains why the critical damping factor exists.

The effects of gap ratio is less significant than the Reynolds number. The passive cylinder's vibration amplitude on the whole decreases with G/D, especially at resonance. Being counter-intuitive, the gap ratio between the passive cylinder and the active cylinder turns out to not affecting the vibration phase difference between the two cylinders at all. The gap ratio does not affect the resonance frequency as well. This independence of the phase and resonance frequency upon gap ratio is not altered by the variation of any other non-dimensional group in all the cases. Gap ratio only affects the amplitude of the passive cylinder.

Chapter 6

Effects of Active Cylinder's Amplitude and Frequency in Less Regular Regimes

In this chapter, the parametric exploration is extended into the regimes where the flow pattern is more complicated with vortex shedding that significantly impacts the vibration of the passive cylinder. An overview in the passive cylinder's response is given on the effects of various Keulegan-Carpenter Number $KC = 2\pi A_1/D$ and the active cylinder's oscillation frequency f_1/f_n with the Stokes Number fixed at $\beta = Re_m/KC = 35$. After that, the effects of the active cylinder's oscillation frequency f_1/f_n is discussed with the KC and β chosen to be in regime C, E, F, G. Both the vortex dynamics and the response of the passive cylinder is examined in detail. 2176 combinations of parameters are simulated and examined, but only representative cases are discussed. Here, the active cylinder's oscillation amplitude is represented by KC rather than A_1/D for the convenience of comparison with previous research.

6.1 Overview of KC Effects

This section gives an overview of the effects caused by varying the KC on the responding vibration of the passive cylinder. In general, the passive cylinder vibrates increasingly complicated and aperiodic with KC, as seen in Fig. 6.1.

In regime A, as discussed in the previous chapters regard periodic regimes, the flow-mediated interaction between the two cylinders reaches a steady state after several initial periods of transition, as shown in Fig. 6.1, and the vibration centre shift can hardly be identified. In regime A at $KC \approx 4$, although the interaction is still steady and repetitive after initial transition, the passive cylinder can be attracted towards or repelled away from the

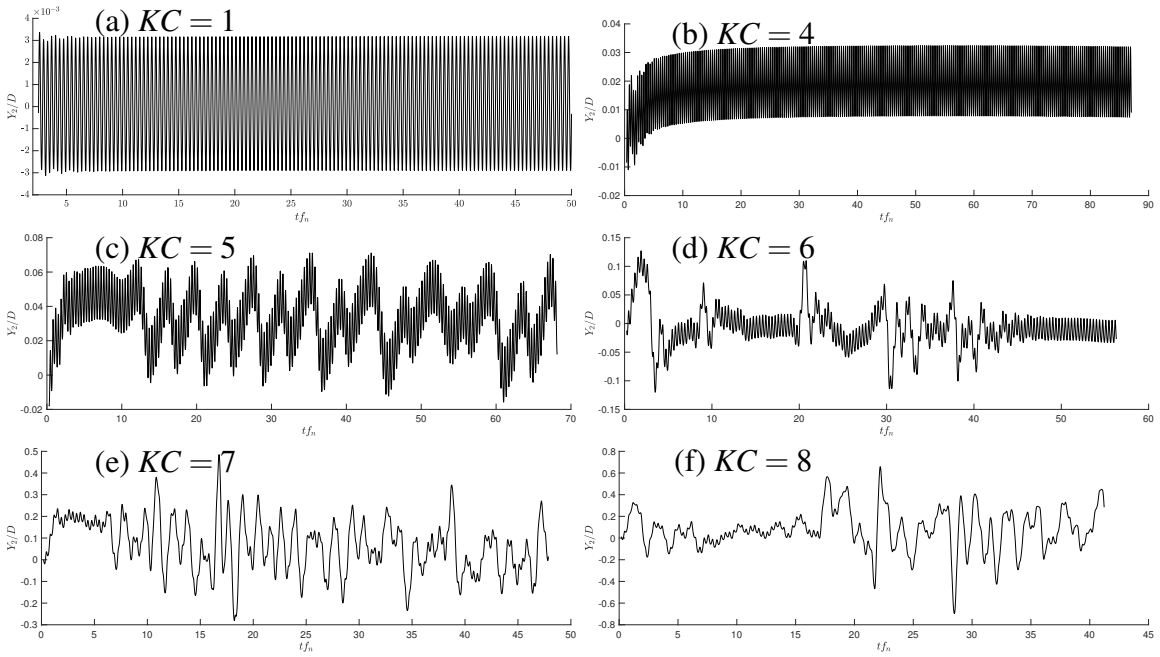

Fig. 6.1 Typical time histories of passive cylinder's vibration for $G/D = 2.5, m^* = 2, \zeta = 0, \beta = 35, f_1/f_n = 2.8$, (a) $KC = 1, Re_m = 35, A_1/D = 0.159$, (b) $KC = 4, Re_m = 140, A_1/D = 0.637$, (c) $KC = 5, Re_m = 175, A_1/D = 0.796$, (d) $KC = 6, Re_m = 210, A_1/D = 0.955$, (e) $KC = 7, Re_m = 245, A_1/D = 1.114$, (f) $KC = 8, Re_m = 280, A_1/D = 1.273$

active cylinder depending on the Re_m, as discussed in Chapter 5. In regime C at $KC = 5$, even though the response of the passive cylinder is on the whole repetitive, irregularity starts to appear for the drift of the vibration centre. It is not entirely independent of time any more, and the vibration centre starts to drift up and down rather than standing still. In regime E at $KC = 6$, the passive cylinder vibrates steadily in some parts of the history, but irregular displacement can occur from time to time. The passive cylinder is slightly attracted towards the active cylinder rather than repelled away as in $KC = 4-5$. In regime F at $KC = 7-8$, the response has become very irregular without any periodic vibration identified. The irregularity of the passive cylinder's response in regimes C, E, F, G is due to unstable vortex shedding from the active cylinder, which will be discussed later.

The effects of KC can also be reviewed in the frequency domain, as seen in Fig. 6.2. With the increase in KC, the irregularity clearly increased, and frequency component associated with the irregular vibration concentrated in the low-frequency band $f/f_n < 1$, and tend to peak at the immersed natural frequency $f/f_n \approx 0.77$. The fundamental pattern of harmonics and resonance, as discussed in Chapter 3, always exists regardless of the superimposed irregular frequency components. The increase of KC and f_1/f_n can both add to the irregularity. The frequency component with $f/f_n \approx 0$ represents the significance of the vibration centre drift,

which grows with the *KC* in regime A and C from $KC = 3$ to 5, as shown in Figs. 6.2a-6.2c. However, the magnitude of vibration centre shift drops significantly at $KC = 6$, because the flow structure in regime E is fundamentally different from regime A and C, favouring the attraction of the passive cylinder. In regime F at $KC = 7-8$, the vibration centre drift grows large again. Resonance amplitude increases with *KC* as expected. In short, the overall irregularity and vibration amplitude increase with *KC*.

Despite the growth of absolute responding amplitude with *KC*, amplification factor and phase difference for the harmonic components is at large independent of *KC*, as seen in Figs. 6.3 and 6.4. At $KC = 1-7$, linear relationship persists between the oscillation amplitude of the passive cylinder A_2 and the active cylinder A_1. At the minor and major resonance peaks, the linearity is weakened, which is coherent with the pattern in the periodic regimes Chapter 3. The amplification at the major resonance experiences a relatively large decrease from $KC = 6$ to 7. The phase difference only slightly decreases across all the frequencies with *KC*. The magnitude of decrease is less than 10°. Similar patterns can be observed for both damped and undamped cases demonstrated in Fig. 6.3 and Fig. 6.4 respectively. The vibration amplitude is extracted from the time history of the passive cylinder's displacement. The data processing method is discussed in Section 2.5.

In summary, the irregularity and the overall amplitude for the vibration of the passive cylinder increase with $KC = 1-7$ at $\beta = 35$. However, the amplification factor and the phase difference of the harmonic components barely changes with *KC* at both damped and undamped conditions. The following sections discuss the response patterns of the passive cylinder and the flow structure. The vortex shedding mechanism is examined in detail

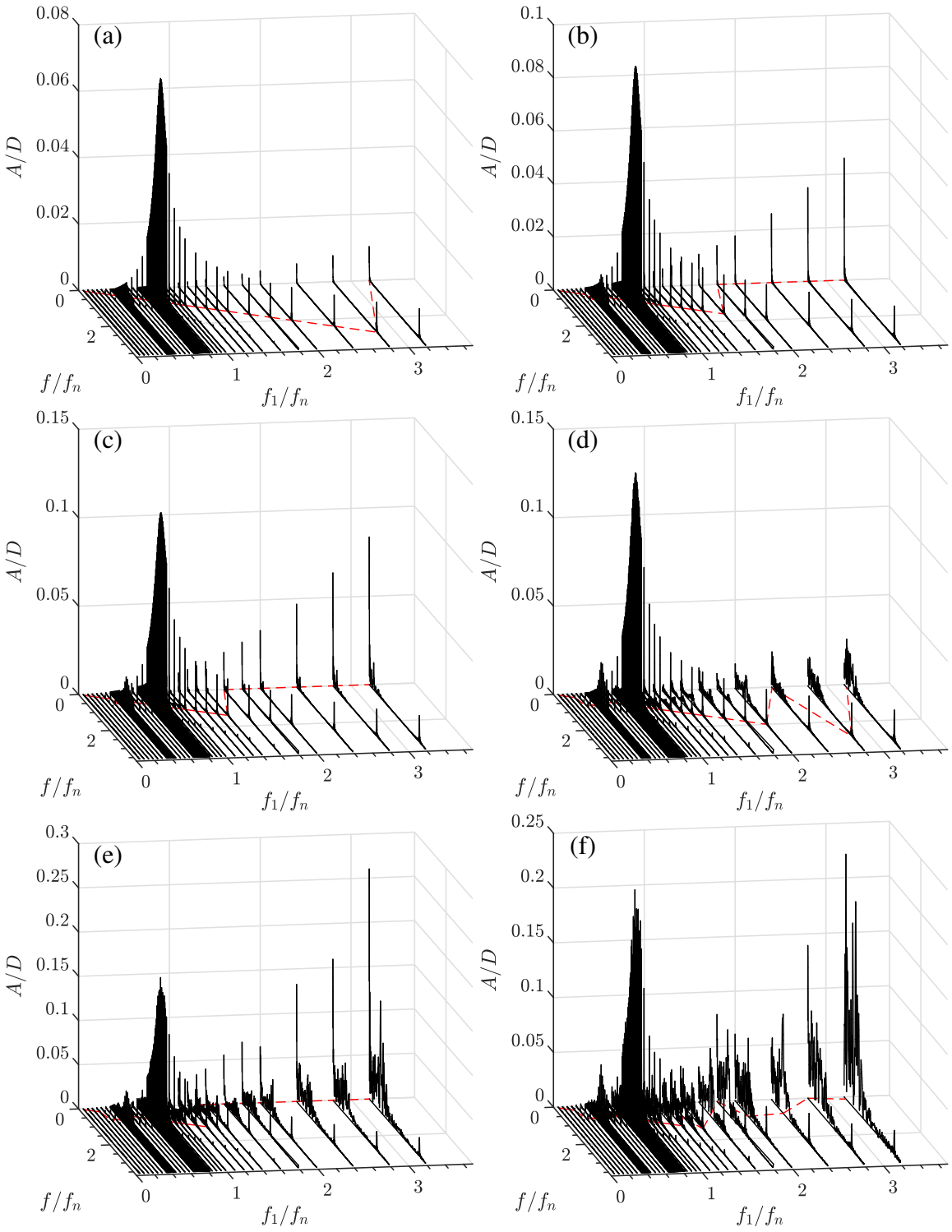

Fig. 6.2 Amplitude spectra for the displacement histories of the passive cylinder at $G/D = 2.5, m^* = 2, \zeta = 0, \beta = 35$, (a) $KC = 3$ in regime A, (b) $KC = 4$ in regime A, (c) $KC = 5$ in regime C, (d) $KC = 6$ in regime E, (e) $KC = 7$ in regime F, (f) $KC = 8$ in regime F

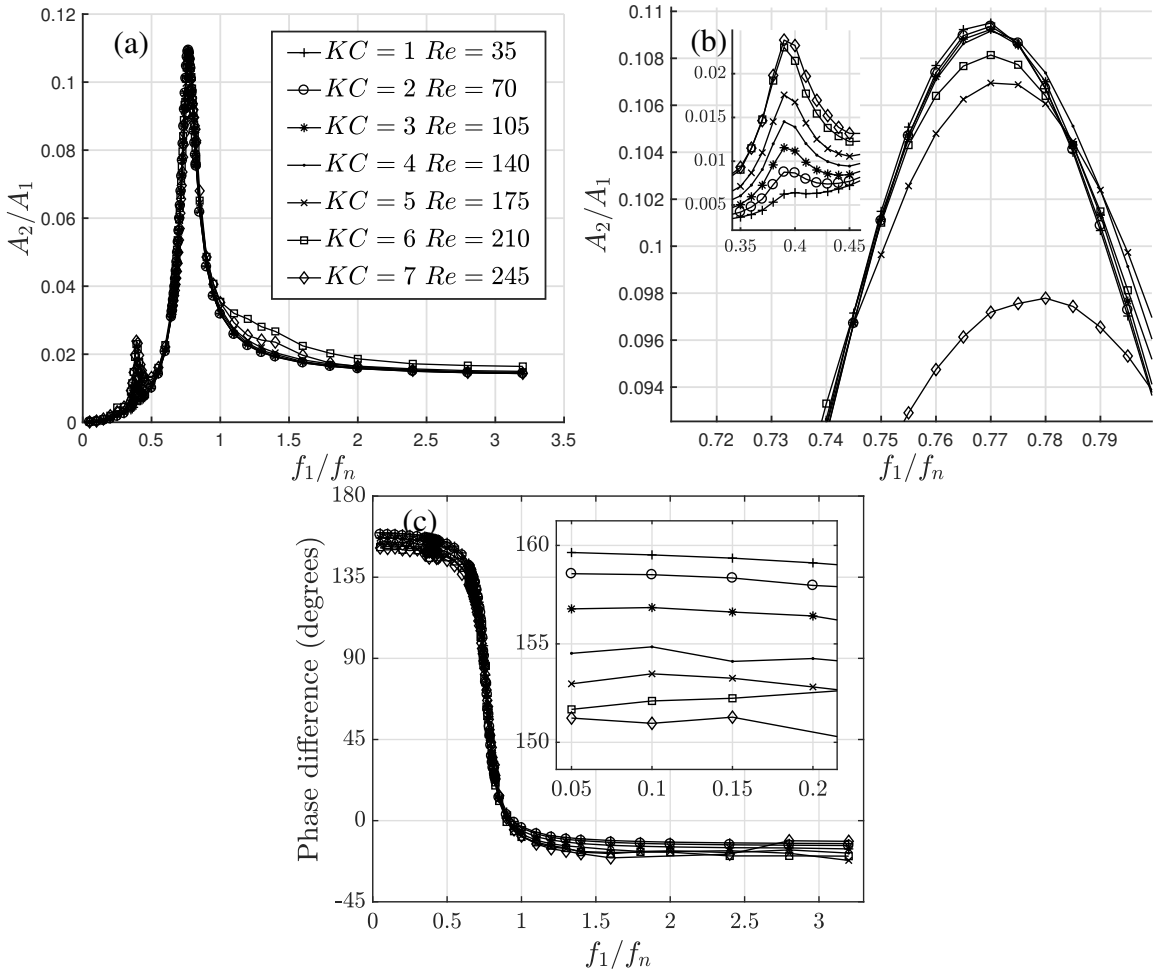

Fig. 6.3 At structural damping $\zeta = 0$, (a) Variation of amplification factor A_2/A_1 for only the harmonic components with f_1/f_n (b) Zoom-in for resonance (c) Variation of oscillation phase difference between the two cylinders $\Delta\phi_{21}$ with f_1/f_n (for the frequency components with $f/f_n = f_1/f_n$) with f_1/f_n at $G/D = 3.0, A_1/D = 0.159 - 1.114, m^* = 2.0, \zeta = 0, Re_m = 35 - 245$ and $KC = 1 - 7, \beta = 35$. The amplitude of the harmonic components is extracted by filter out the low-frequency components by FFT. The data processing method is discussed in Section 2.5.

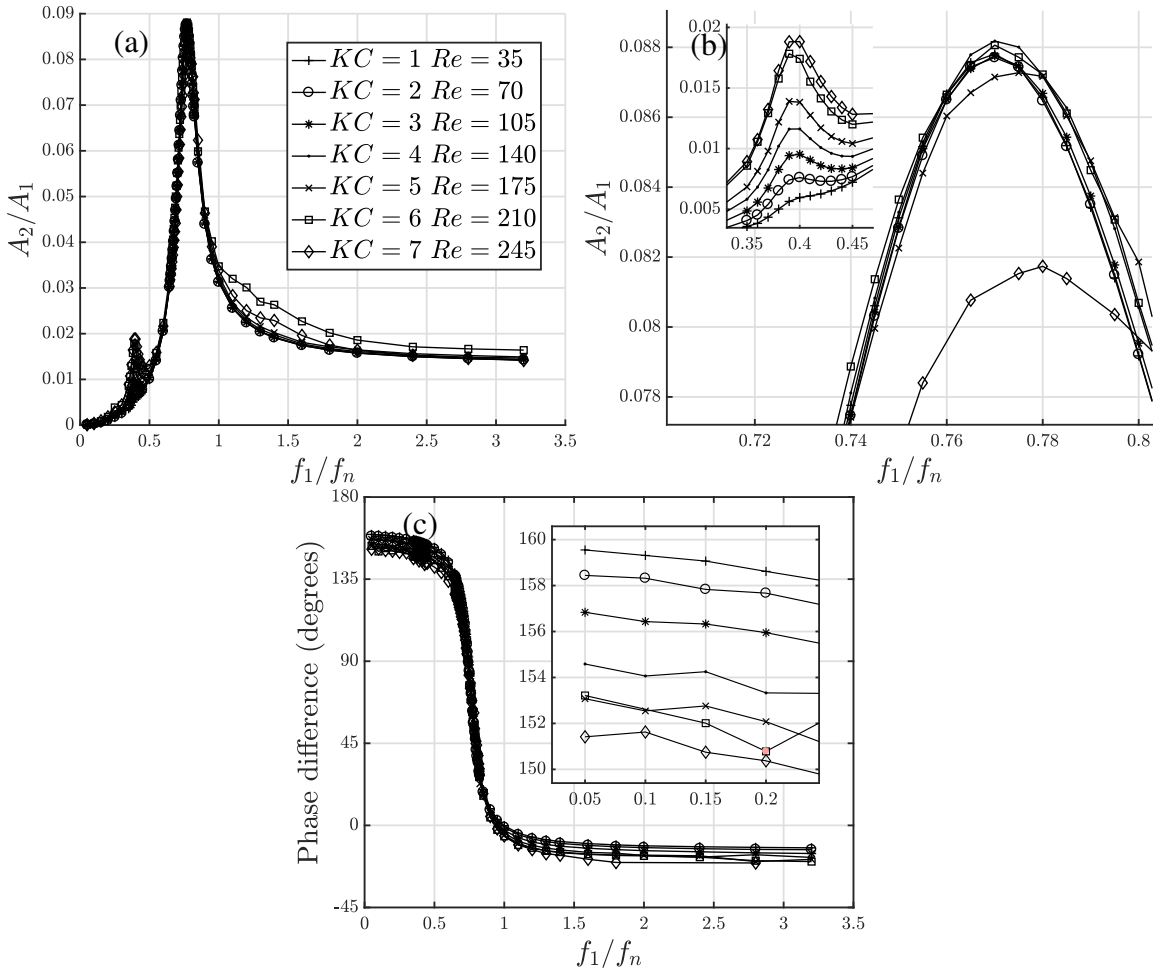

Fig. 6.4 At structural damping $\zeta = 0.02$, (a)Overview and (b)Zoom-in for variation of amplification factor A_2/A_1 with f_1/f_n and KC. (c) Variation of oscillation phase difference between two cylinders $\Delta\phi_{21}$ (for the harmonic component with $f/f_n = f_1/f_n$) with f_1/f_n and KC at $G/D = 3.0, A_1/D = 0.159 - 1.114, m^* = 2.0, Re_m = 35 - 245$ and $KC = 1 - 7, \beta = 35$.

6.2 Regime C

In regime C, $KC = 5$ is a threshold above which the irregularity of the displacement time history is significantly increased and can no longer be approximated as purely periodical.

With the increase of frequency ratio, the vibration of the passive cylinder gradually changes from a relatively sinusoidal pattern to pulse beating and the irregularity becomes more and more apparent, as seen in Fig. 6.5. At $f_1/f_n = 0.05$ to 1.0, the vibration of the passive cylinder is dominantly repetitive with only minor pulse beats. At $f_1/f_n = 1.2$ to 2.0, the pulse beats are relatively strong compared with low frequency. At $f_1/f_n = 2.4$ to 3.2, the pulse beating is significant with its amplitude becomes larger than the vibration at the active cylinder's frequency. The passive cylinder's vibration centre drift towards the far side significantly increases with the active cylinder's oscillation frequency at $f_1/f_n > 1.2$. Resonance of the passive cylinder still occurs at about the immersed natural frequency $f_1/f_n = 0.77$. The increase of irregularity can also be shown in the amplitude spectra of the displacement histories in Fig. 6.6. 2 minor frequency components with their frequency being 10th and 20th of the active cylinder's oscillation frequency are observed at $f_1/f_n \geq 1$, which will be discussed later. Harmonics are more obvious when the active cylinder's oscillation frequency is very low.

At $KC = 5$, vortices shed from the active cylinder becomes stronger with the increase of its frequency f_1/f_n, as seen in Fig. 6.7. Although the switch of skewing pattern is discovered, the vortex shedding process is on the whole repetitive and stable. 2 pairs of vortices rotating in opposite directions are shed from each oscillation cycle of the active cylinder. The strength of the vortices increases with the active cylinder's oscillation frequency, causing a stronger stream and thus a more significant pulse beating. The mechanism of pulse beating will be discussed later. The vorticity generated by the passive cylinder is the strongest at $f_1/f_n = 0.77$ where resonance occurs.

The skewing pattern of the vorticity contours switches left and right periodically, as seen in Fig. 6.8. The switch occurs after approximately 10 cycles of the active cylinder's forced oscillation, as seen in Fig. 6.9a. This periodical switching matches the pulse beating of the passive cylinder's vibration. The vorticity skewing switching can also take place for every 20 cycles of the active cylinder. The skewing switching occurs intermittently between 20 and 10 cycles of the active cylinder's oscillation. The vibration of the passive cylinder thus has 2 minor frequency components at 10th and 20th of the active cylinder's oscillation frequency, as highlighted in Fig. 6.9b. The switching vorticity pattern indicates the periodical change of the flow structure, which causes the low-frequency beating of the passive cylinder. The periodical switching of flow structure can be observed in all frequencies f_1/f_n in Regime C. With the increase of the active cylinder's frequency, the beating frequency tends to become

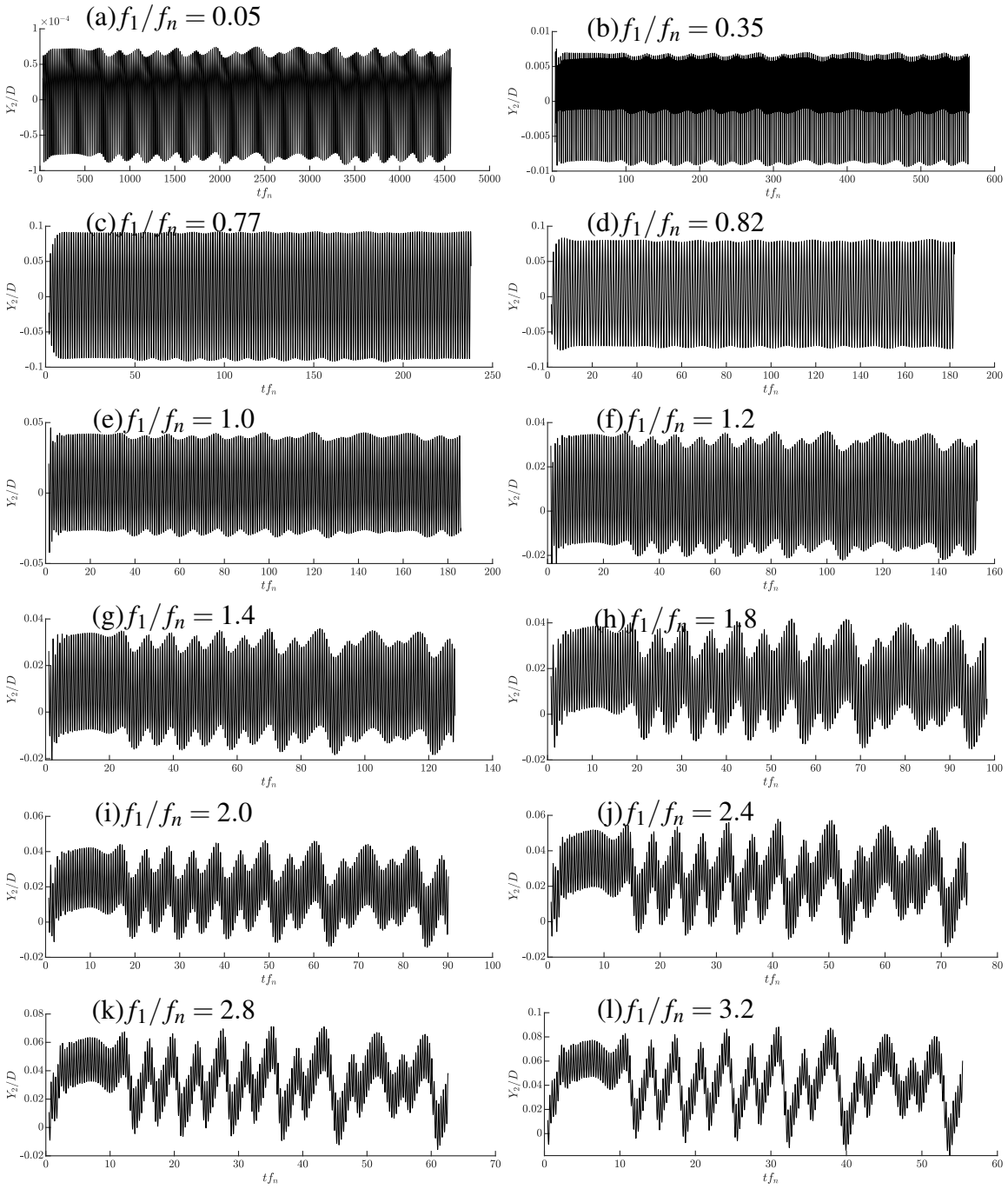

Fig. 6.5 Displacement time history of the passive cylinder in regime C with $KC = 5, \beta = 35, G/D = 2.5, A_1/D = 0.796, m^* = 2, \zeta = 0, Re_m = 175$ with (a)$f_1/f_n = 0.05$, (b)$f_1/f_n = 0.35$, (c)$f_1/f_n = 0.77$, (d)$f_1/f_n = 0.82$, (e)$f_1/f_n = 1.0$, (f)$f_1/f_n = 1.2$, (g)$f_1/f_n = 1.4$, (h)$f_1/f_n = 1.8$, (i)$f_1/f_n = 2.0$, (j)$f_1/f_n = 2.4$, (k)$f_1/f_n = 2.8$, (l)$f_1/f_n = 3.2$. $KC = 5$ is a critical value that above which the irregularity of the displacement time history is significantly increased. With the increase of frequency ratio, the vibration of the passive cylinder gradually changes from a repetitive pattern to pulsed beating.

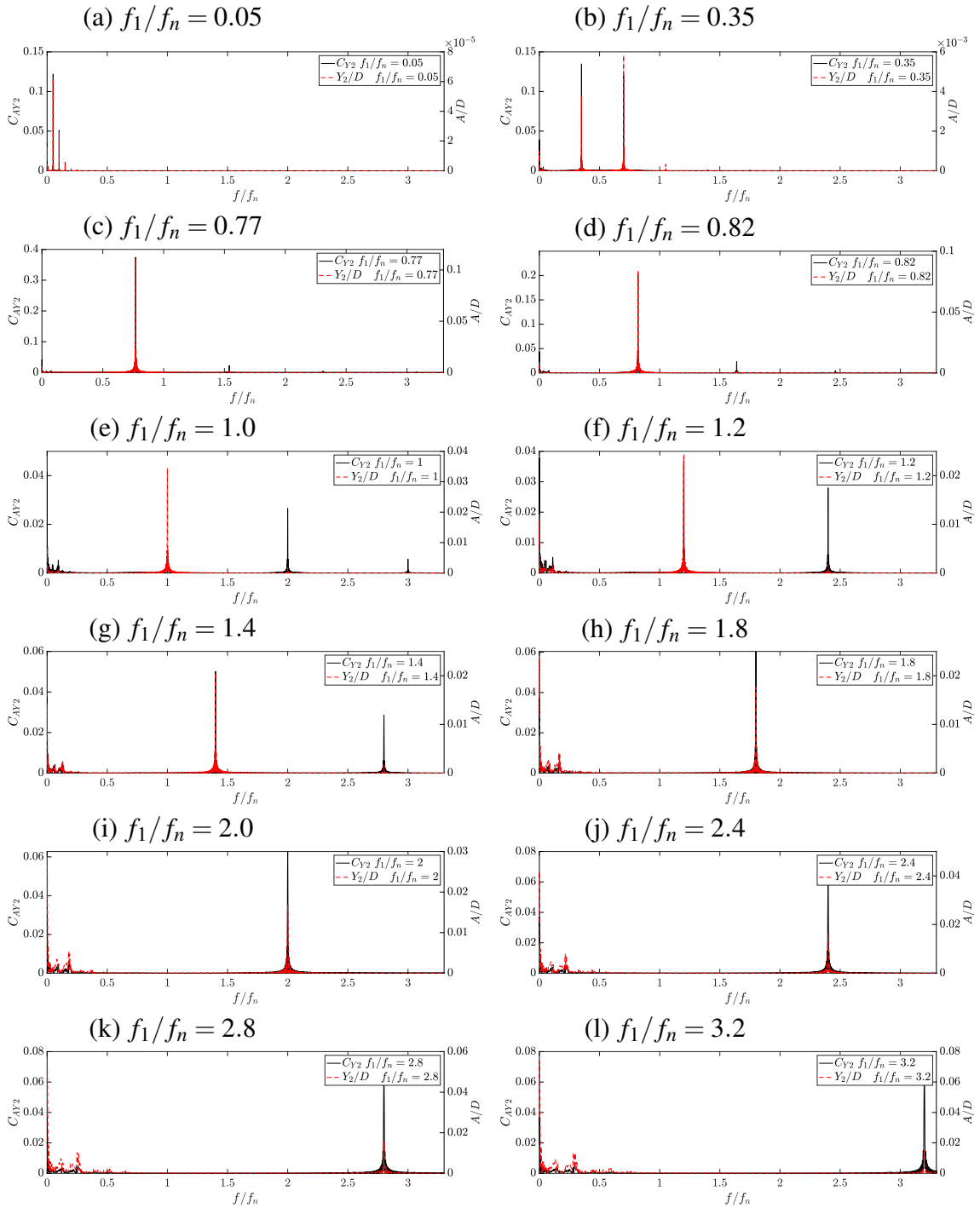

Fig. 6.6 Amplitude spectra of the passive cylinder's displacement In regime C with $KC = 5, \beta = 35, G/D = 2.5, A_1/D = 0.796, m^* = 2, \zeta = 0, Re_m = 175$ with (a)$f_1/f_n = 0.05$, (b)$f_1/f_n = 0.35$, (c)$f_1/f_n = 0.77$, (d)$f_1/f_n = 0.82$, (e)$f_1/f_n = 1.0$, (f)$f_1/f_n = 1.2$, (g)$f_1/f_n = 1.4$, (h)$f_1/f_n = 1.8$, (i)$f_1/f_n = 2.0$, (j)$f_1/f_n = 2.4$, (k)$f_1/f_n = 2.8$, (l)$f_1/f_n = 3.2$.

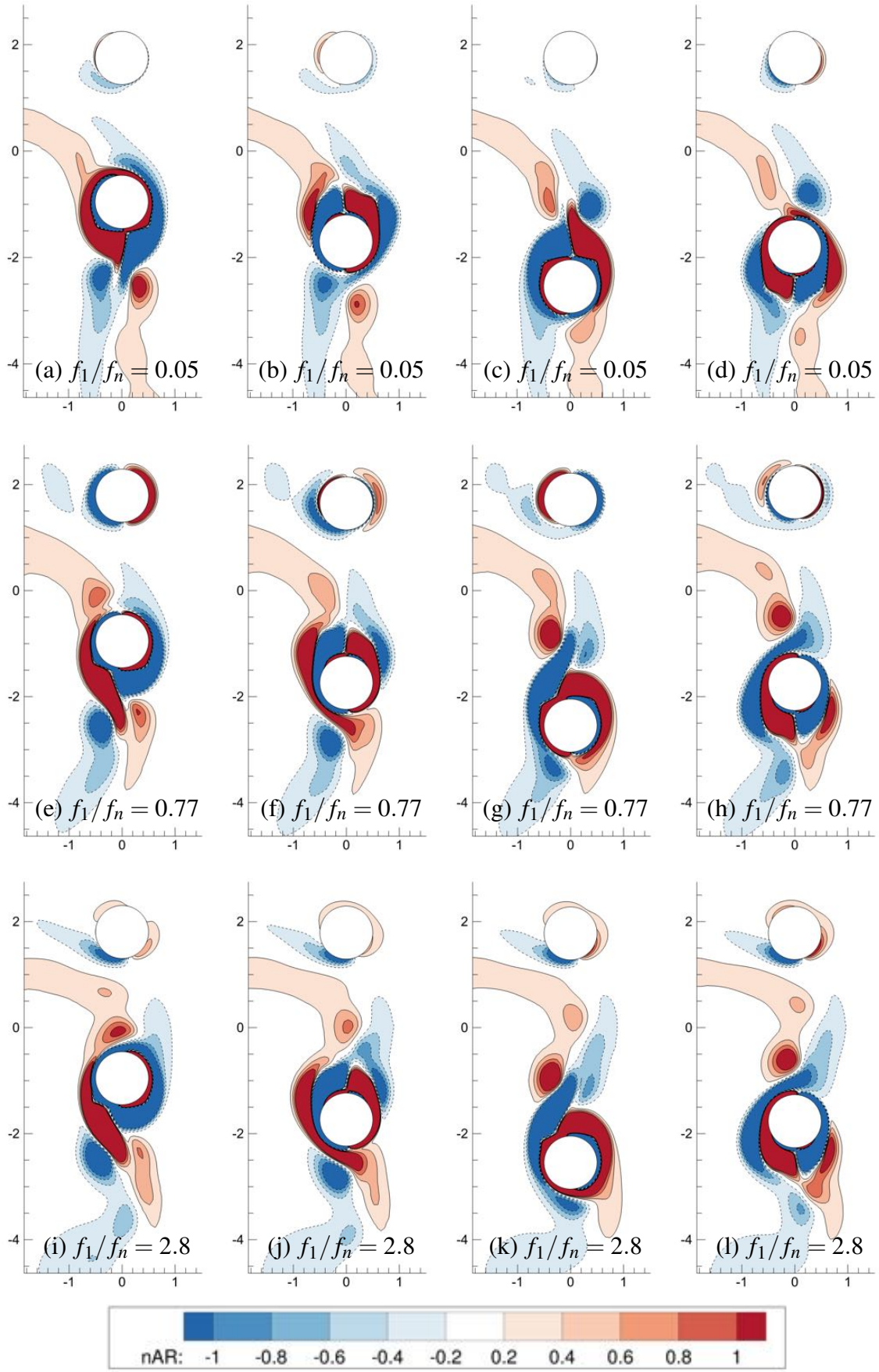

Fig. 6.7 Vorticity contours In regime C with (a-d) $f_1/f_n = 0.05$, (e-h) $f_1/f_n = 0.77$, and (i-l) $f_1/f_n = 2.8$ with (a & e & i) $\phi = 0°$ (b & f & j) $\phi = 90°$ (c & g & k) $\phi = 180°$ (d & h & l) $\phi = 270°$ at $KC = 5, \beta = 35, G/D = 2.5, A_1/D = 0.796, m^* = 2, \zeta = 0, Re_m = 175$.

lower than 10th and 20th of f_1/f_n. This periodical switch of the streaming and vorticity contours skewing direction was not found when only the active cylinder exists neither in regime C nor in other identified regimes (Tatsuno and Bearman, 1990).

The mechanism of the beating is examined in further details at $f_1/f_n = 3.2$ as seen in Fig. 6.10 and Fig. 6.11. At relatively high Reynolds number, the flow structure causes the passive cylinder to drift away from the active cylinder, as described in Chapter 5. The vortex pairs shed from the active cylinder produce a stream that pushes the passive cylinder away. In regime C, the stream produced by the active cylinder periodically changes direction, swinging from slight left to slight right and back to left, which is unlike in regime A and A^*, the direction of the stream is always along the centre line of cylinders. Typically a full beating can take 20-30 oscillations of the active cylinder. High f_1/f_n cases can take more oscillations. At instant A Fig. 6.11a, the streaming direction points at the passive cylinder, so the vibration centre of the passive cylinder drifts away from the active cylinder, as seen in Fig. 6.11. At instants B-D, the vortex pairs are shed towards the left side of the active cylinder. Since the negative vortex, i.e. rotating clockwise, the passive cylinder is slightly attracted towards the active cylinder, reaching the lowest position at instant C. At instant E-F, the streaming direction switch to the right. Notably, left-to-right switching is faster than right-to-left. So the passive cylinder is pushed away again, reaching highest position at instant E, but not as high as the position at instant A. At instant F, the positive vortex at the right side of the passive cylinder creates a downward flow, attracting it towards the active cylinder, reaching the lowest position at instant F, but not as low as instant C. In a nutshell, the periodical switching of the streaming direction causes the passive cylinder to be repelled and attracted periodically, resulting in the beating pattern of in its time histories.

This section has shown the flow-mediated interaction in regime C. On the whole, the vibration is regular with only minor irregularity appearing when the active cylinder is vibrating at a high frequency $f_1/f_n \geq 1.2$. The switch of the streaming direction leads to the pulse beating in the displacement time histories of the passive cylinder. The amplitude of the beating increases with the the active cylinder's frequency f_1/f_n. This gradual switch of the streaming direction was not observed when the passive cylinder does not exist (Tatsuno and Bearman, 1990). In each of the active cylinder's oscillation, 2 vortex pairs were shed. The switch of the streaming direction corresponds with the switch of the vortex shedding direction. In a nutshell, the flow-mediated interaction in regime C is at large regular. The slight irregularity is added by the switch of streaming direction, since each switch does not always take the same number of the active cylinder's oscillations.

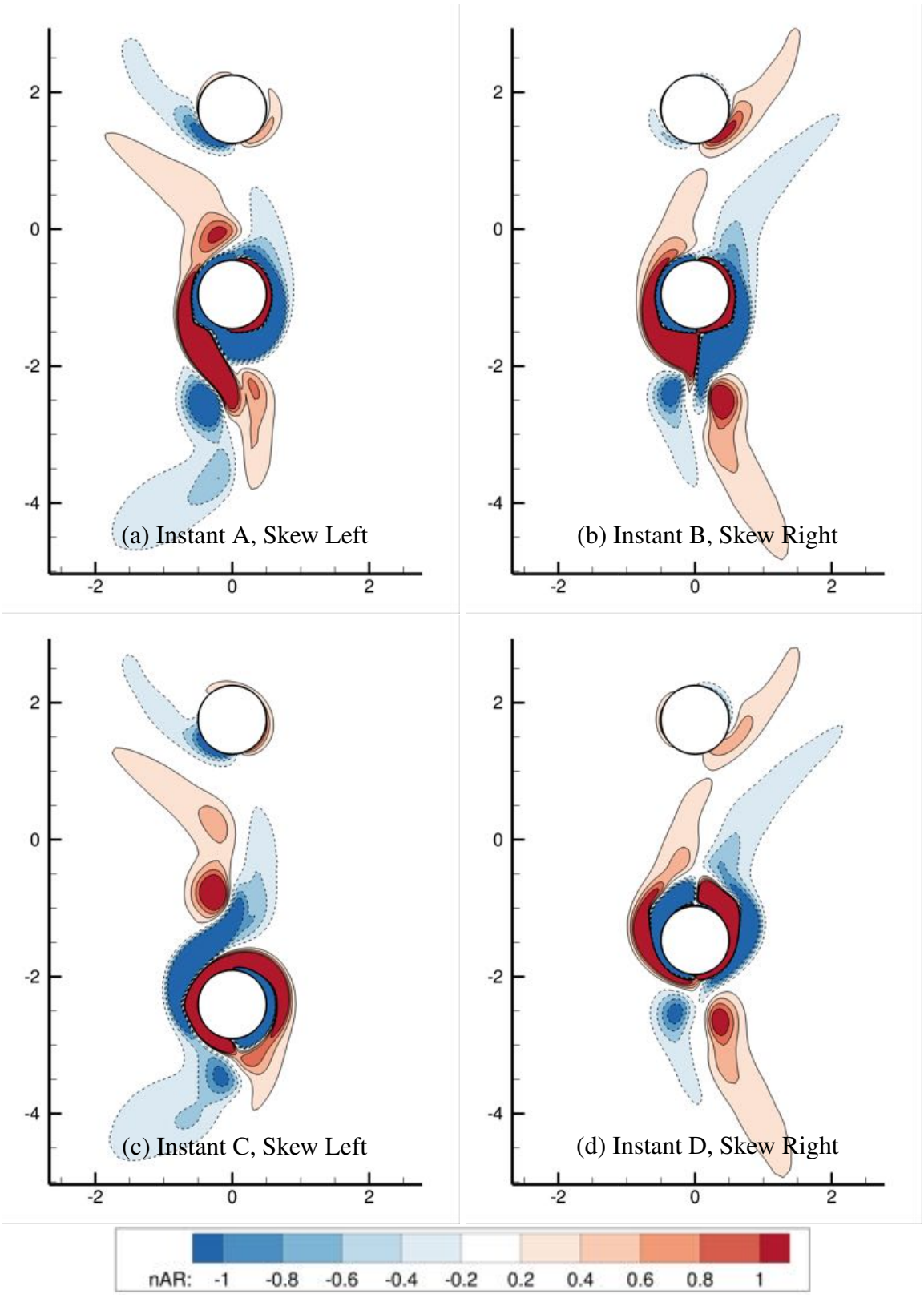

Fig. 6.8 Non-dimensional Vorticity Contours in Regime C with $f_1/f_n = 0.05$ and $KC = 5, \beta = 35, G/D = 2.5, A_1/D = 0.796, m^* = 2, \zeta = 0, Re_m = 175$, corresponding to instants (a)A (b)B (c)C (d)D in Fig. 6.9. The shape of vorticity contours switch the direction of skewing for approximately every 10 periods.

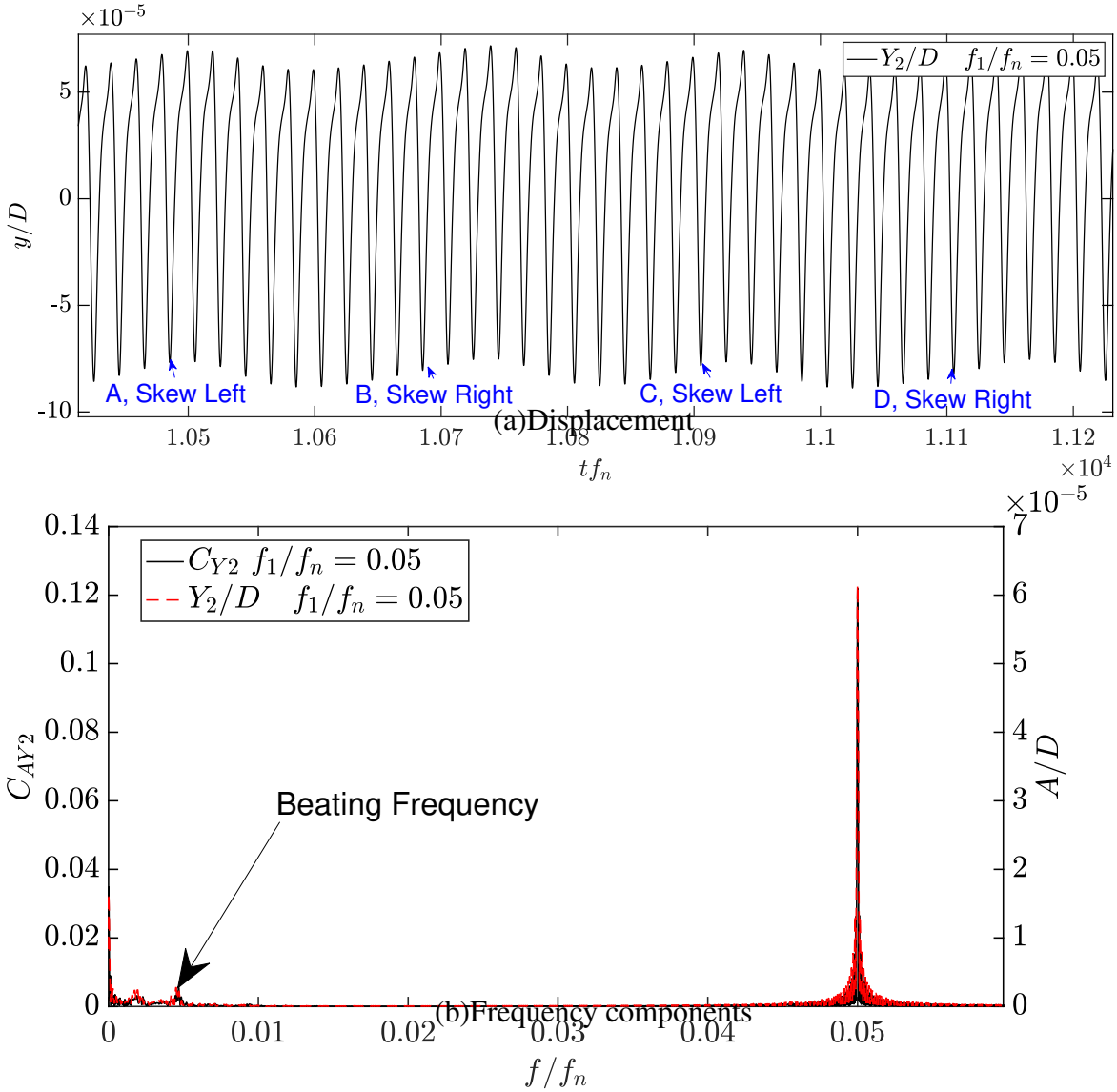

Fig. 6.9 (a)Displacement time history and (b) amplitude spectra of the passive cylinder in Regime *C* with $f_1/f_n = 0.05$ and $KC = 5, \beta = 35, G/D = 2.5, A_1/D = 0.796, m^* = 2, \zeta = 0, Re_m = 175$. The marked locations in (a) corresponds to the instants $a-d$ in Fig. 6.8.

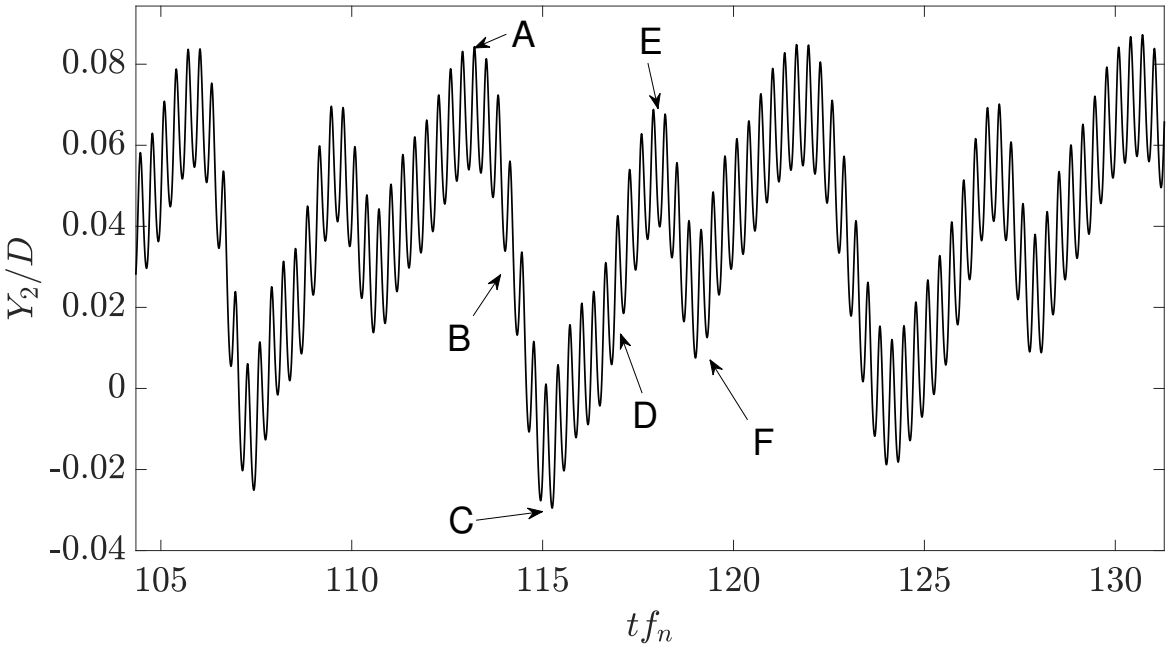

Fig. 6.10 Displacement time history of the passive cylinder in Regime *C* with $f_1/f_n = 3.2$ and $KC = 5, \beta = 35, G/D = 2.5, A_1/D = 0.796, m^* = 2, \zeta = 0, Re_m = 175$. The marked locations $A - F$ corresponds to the Figs. 6.11a-6.11f.

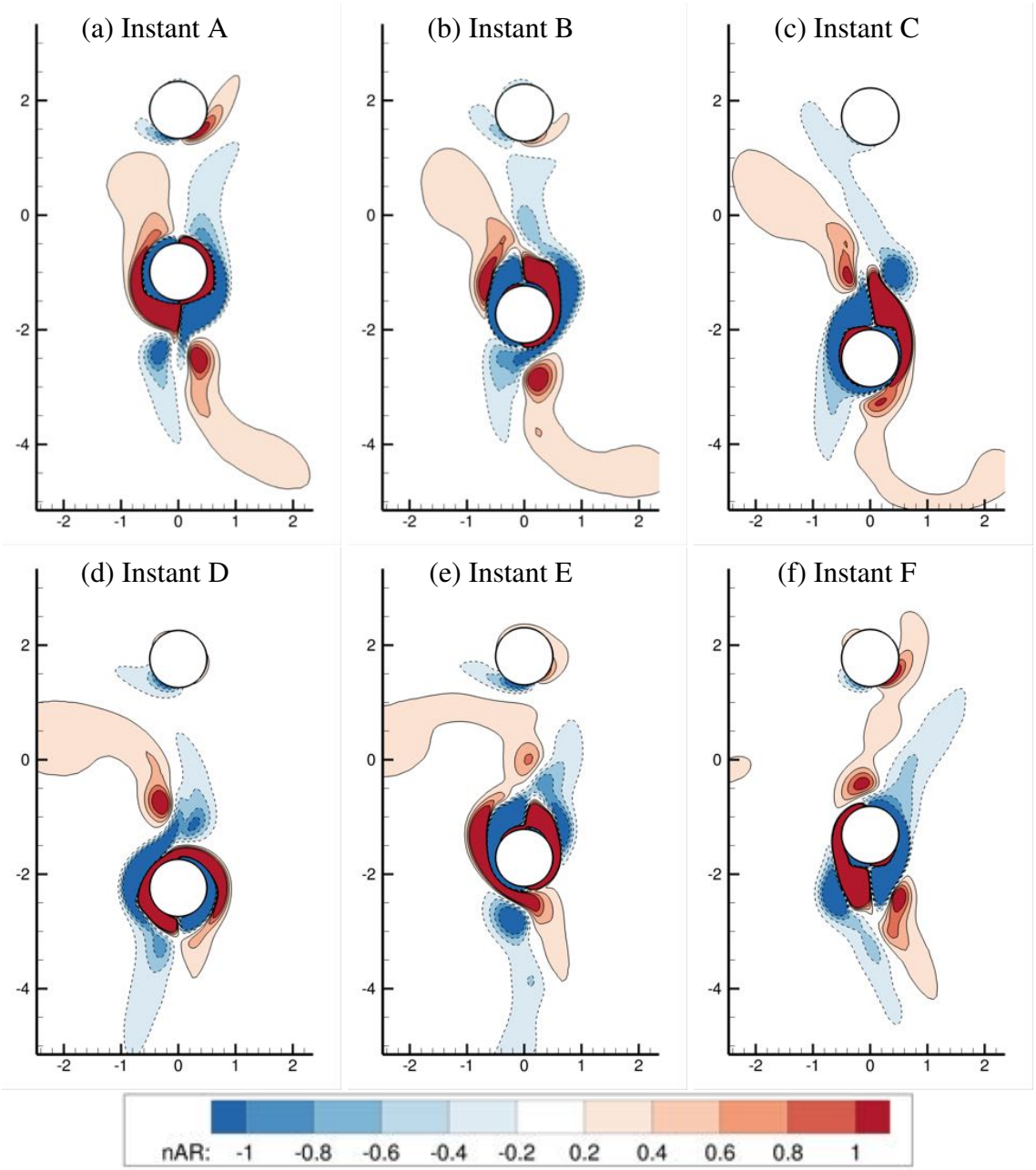

Fig. 6.11 Vorticity Contours for a typical cycle of beating in Regime *C*, corresponding to instants (a)A (b)B (c)C (d)D (e)E (f)F in Fig. 6.10 with $f_1/f_n = 3.2$ and $KC = 5, \beta = 35, G/D = 2.5, A_1/D = 0.796, m^* = 2, \zeta = 0, Re_m = 175$. The passive cylinder is pushed further away when the streaming direction is pointing at it.

6.3 Regime E

At regime E with $KC = 6$, the displacement time histories become more irregular, i.e. less periodic with more random motions, compared with regime C $KC = 5$, especially at high frequency f_1/f_n, as seen in Figs. 6.12 and 6.13. The relatively stable beating pattern can no longer be observed in regime E, as shown in Fig. 6.12. Intermittent large displacements of the passive cylinder are discovered. With the increase in active cylinder's oscillation frequency f_1/f_n, the abrupt large displacements occur more frequently, and the displacement scale relative to the steady small vibration grows as well. The distribution of frequency components is increasingly concentrated at typically $f/f_n \leq 1$. The dominant frequency of the passive cylinder's vibration shifts from equalling the active cylinder's oscillation frequency f_1/f_n or its harmonics to being very low at $f_1/f_n > 2.0$. It is also interesting to note that the vibration centre shift in regime E is less significant than that in regime C, despite the increase of the Reynolds number.

In regime E, the vortex pairs are shed from only one side of the active cylinder, as seen in Fig. 6.15, which is coherent with the scenario with only the active cylinder (Tatsuno and Bearman, 1990). In general, the vortex shedding is steady and asymmetric that it only takes place at one side of the cylinders. However, the flow pattern changes between one pattern and its mirror-image intermittently, as seen in Fig. 6.14. During the transition between the 2 patterns, the vortex shedding can make a direct impact on the passive cylinder. The vortices shed from consecutive cycles can sometimes merge to create a stronger vortex. As a result, the vibration of the passive cylinder is much less steady and become more irregular during the transition, e.g. corresponding to the irregular vibration shown in the time history in Fig. 6.12.

Irregularity increases with the oscillation frequency of the active cylinder f_1/f_n. Between each transition, the passive cylinder vibrates steadily for a few periods. The number of these continuous steady cycles is reduced by increasing the frequency of the active cylinder's oscillation f_1/f_n, corresponding to the more irregular displacement time history as seen in Fig. 6.12. The magnitude for the abrupt large vibration amplitude increases with f_1/f_n as well. During the transition between one pattern and its mirror-image, vortices can merge to create a stronger vortex. When it comes close to the passive cylinder, larger vibration displacement is induced. This process is similar to the vortex shedding in regime G.

The variation of the active cylinder's oscillation frequency can alter the vortex shedding pattern during the steady-state of the oscillation, as seen in Fig. 6.15. With the increase in f_1/f_n, the vortex shedding at the temporary steady state becomes more curved, and the streaming more circular. At $f_1/f_n = 0.05$, vortices shed below the active cylinder travel along a straight line at an angle of 45° to the x-axis. At $f_1/f_n = 0.77$, these vortices travel on a line that is slightly curved to the left, rather than along a straight line, which results in

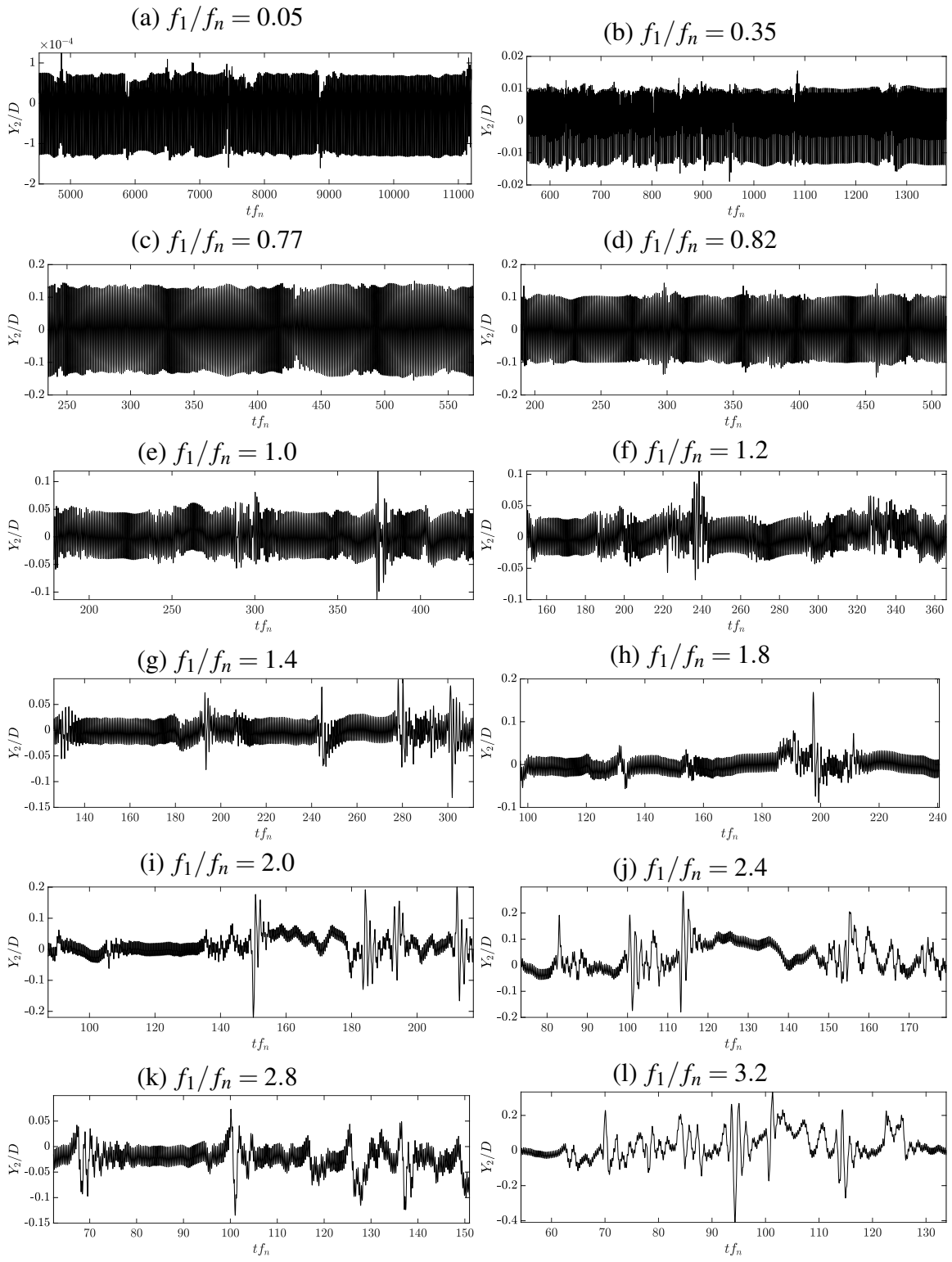

Fig. 6.12 Displacement time history of the passive cylinder in Regime E with $KC = 6, \beta = 35, G/D = 2.5, A_1/D = 0.955, m^* = 2, \zeta = 0, Re_m = 210$ with (a)$f_1/f_n = 0.05$, (b)$f_1/f_n = 0.35$, (c)$f_1/f_n = 0.77$, (d)$f_1/f_n = 0.82$, (e)$f_1/f_n = 1.0$, (f)$f_1/f_n = 1.2$, (g)$f_1/f_n = 1.4$, (h)$f_1/f_n = 1.8$, (i)$f_1/f_n = 2.0$, (j)$f_1/f_n = 2.4$, (k)$f_1/f_n = 2.8$, (l)$f_1/f_n = 3.2$. At $KC = 6$, the time histories become more irregular compared with $KC = 5$, especially at high frequency f_1/f_n.

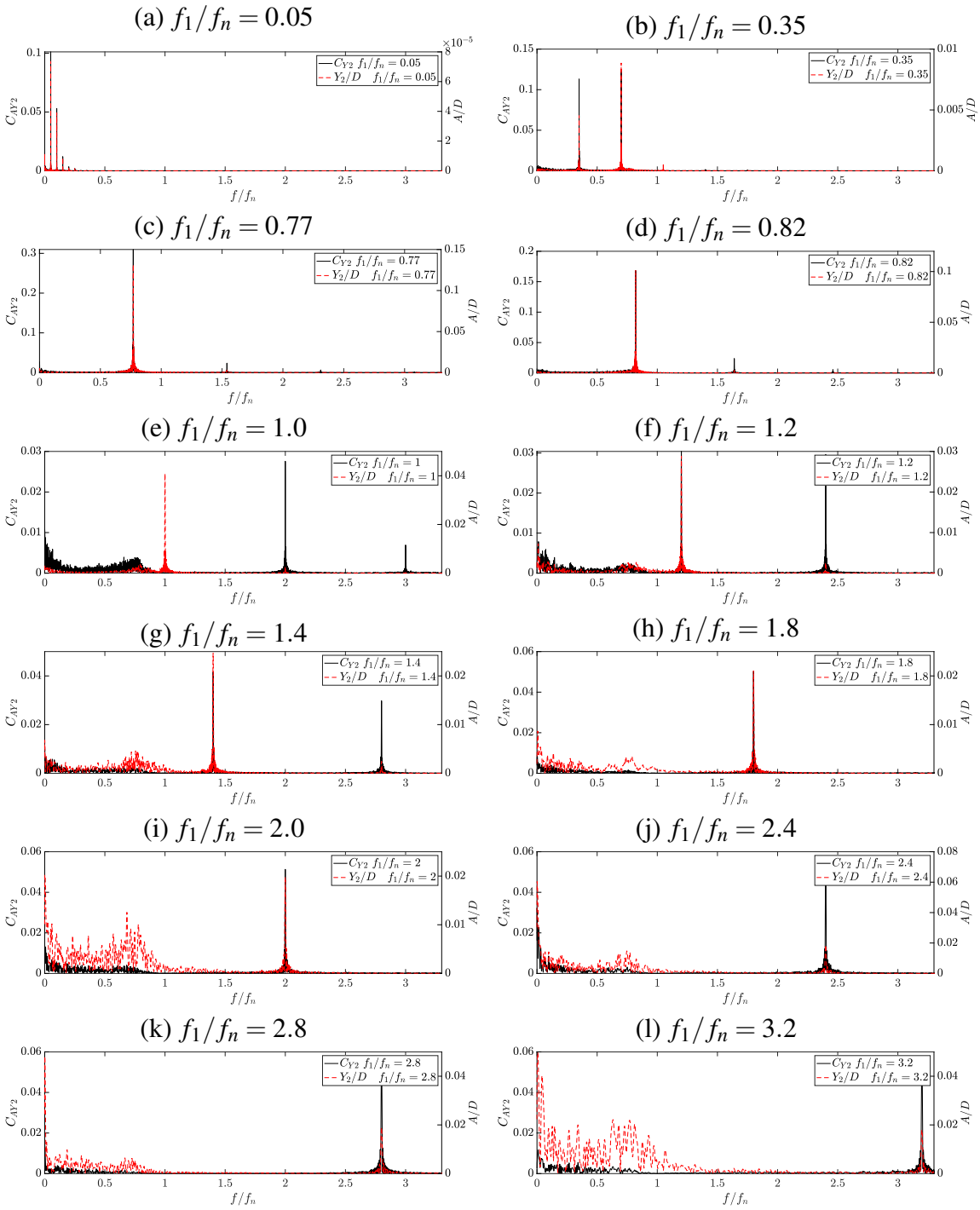

Fig. 6.13 Amplitude spectra of the passive cylinder's displacement in Regime E with $KC = 6, \beta = 35, G/D = 2.5, A_1/D = 0.955, m^* = 2, \zeta = 0, Re_m = 210$ with (a)$f_1/f_n = 0.05$, (b)$f_1/f_n = 0.35$, (c)$f_1/f_n = 0.77$, (d)$f_1/f_n = 0.82$, (e)$f_1/f_n = 1.0$, (f)$f_1/f_n = 1.2$, (g)$f_1/f_n = 1.4$, (h)$f_1/f_n = 1.8$, (i)$f_1/f_n = 2.0$, (j)$f_1/f_n = 2.4$, (k)$f_1/f_n = 2.8$, (l)$f_1/f_n = 3.2$.

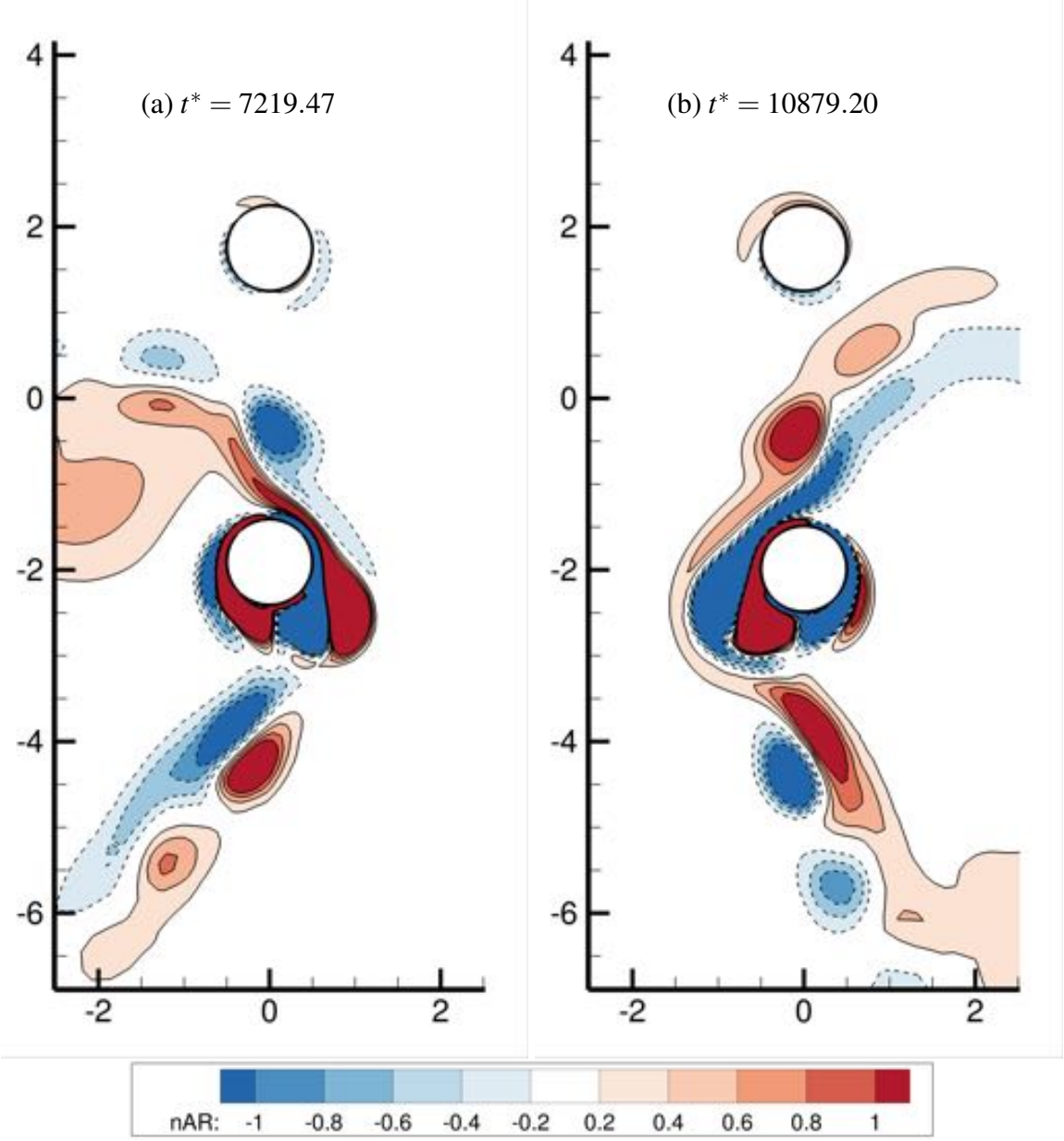

Fig. 6.14 Vorticity contours in Regime E with $f_1/f_n = 0.05$ at $KC = 6, \beta = 35, G/D = 2.5, A_1/D = 0.955, m^* = 2, \zeta = 0, Re_m = 210$. The flow pattern changes between one pattern and its mirror-image intermittently. With the increase of the f_1/f_n, the interaction remains steady for less cycles of the active cylinder oscillation and the passive cylinder's vibration becomes more irregular as well.

a vortex accumulated on the left side of the active cylinder. At $f_1/f_n = 3.2$, the curvature is more severe with strong vortex appear to the left of the active cylinder. The vortex can accumulate both above and below the active cylinder. The vortices shed on the outer skirt of the circular streaming keeps separated from each other, whereas the vortices in the inter side of the vortex shedding curve tend to be distorted and merged. Since the curvature for the vortex shedding path increases with f_1/f_n, consecutive vortices merge more easily. The basic vortex shedding mechanism is however not altered by f_1/f_n.

In regime E, chaotic vibration of the passive cylinder is observed at $KC = 6$. In Fig. 6.16a, we see that the time histories with $\zeta = 0$ and $\zeta = 0.02$ almost exactly overlap each other despite the difference of damping factor, whereas, in Fig. 6.16b, we see that the minor difference of initial condition, i.e. damping factor, leads to dramatic deviation of time history after $tf_n = 18$, which is an indication of chaos.

In summary of this section, the flow-mediated interaction in regime E is more irregular than that in regime C. The one-side "2P" vortex shedding mechanism and intermittent switching of shedding direction are coherent with the single-cylinder cases. During the switching, the vortices can have a direct impact on the passive cylinder, disrupting its steady vibration with a frequency identical to the active cylinder. With the increase in the active cylinder's oscillation frequency, the switching of the vortex shedding direction occurs more frequently, taking place after fewer cycles of the active cylinder's oscillation. The streaming becomes more circular as well. At high f_1/f_n, vortices shed from consecutive cycles merge more often. Accompanied with the frequent switch of the shedding direction, the passive cylinder's vibration can become very irregular, i.e. dominantly influenced by the vortices rather than the oscillation of the active cylinder. Additionally, with the slight variation of the structural damping ratio from $\zeta = 0$ to 0.02, the time history of the passive cylinder's vibration indicates the emergence of chaos.

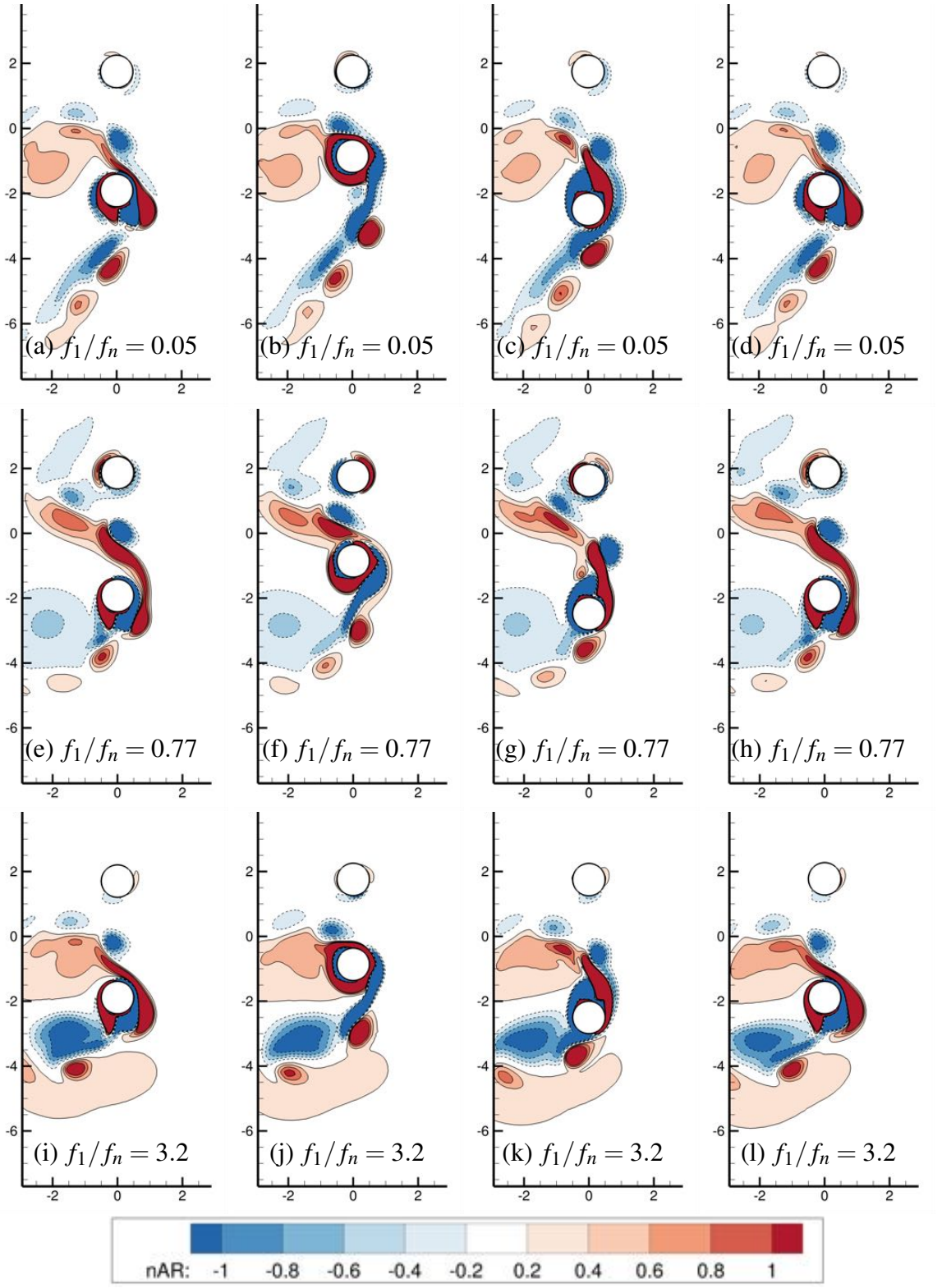

Fig. 6.15 Vorticity contours in Regime E with (a-d) $f_1/f_n = 0.05$, (e-h) $f_1/f_n = 0.77$, and (i-l) $f_1/f_n = 3.2$ at $KC = 6, \beta = 35, G/D = 2.5, A_1/D = 0.955, m^* = 2, \zeta = 0, Re_m = 210$. Sub-figures in the same column are at the similar state of vortex shedding process. With the increase in f_1/f_n, the vortex shedding at the temporary steady state becomes more curved, and the streaming more circular.

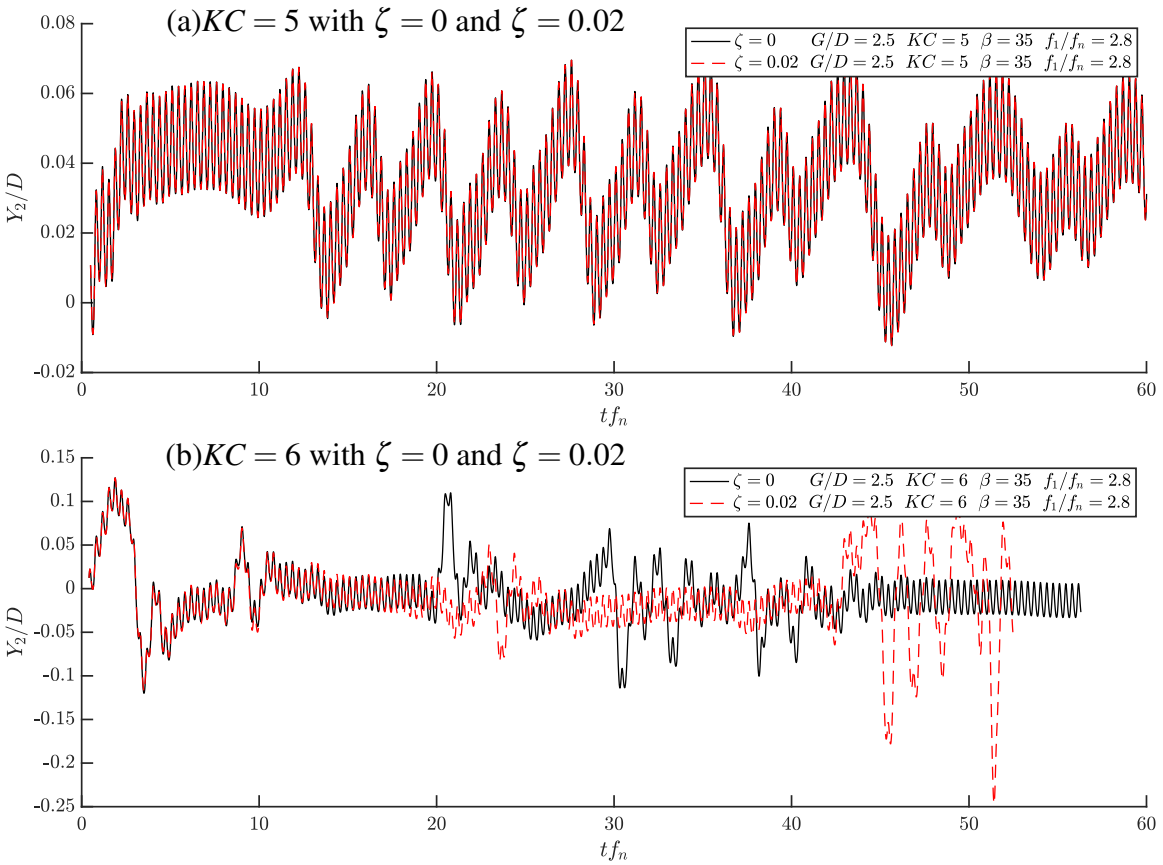

Fig. 6.16 Typical time histories of passive cylinder vibration for $G/D = 2.5, m^* = 2, \zeta = 0, \beta = 35$ (a)$KC = 5$ with $\zeta = 0$ and $\zeta = 0.02$, (b)$KC = 6$ with $\zeta = 0$ and $\zeta = 0.02$. In (a), we see that the time histories with $\zeta = 0$ and $\zeta = 0.02$ almost exactly overlap each other despite the difference of damping factor, whereas, in (b), we see that the minor difference of initial condition, i.e. damping factor, leads to dramatic deviation of time history after $tf_n = 18$, which is an indication of chaos.

6.4 Regime F

In regime F, the irregularity becomes more severe compared with regime E. Even if the active cylinder oscillates at a low frequency, the irregularity can still be apparent, as seen in Fig. 6.17. The amplitude of the sudden disruptions in the vibration time history of the passive cylinder is enlarged with the increase in active cylinder's oscillation frequency f_1/f_n. The distribution of the passive cylinder's vibration frequency is more and more concentrated around its immersed natural frequency, as seen in Fig. 6.17. The vibration centre of the passive cylinder is in general slightly attracted towards the active cylinder, which will be discussed later by viewing the vortex patterns.

For single-cylinder cases, the flow in regime F is stable and repetitive. The typical flow pattern can be seen in Fig. 6.19 by Zhao and Cheng (2014). In each cycle, 2 vortex pairs are shed from the oscillating cylinder towards two opposite directions along a diagonal line. This vortex shedding pattern was also referred as "2P" by Williamson (1985) and "Diagonal" by Obasaju et al. (1988).

For two-cylinder cases in this study, the flow pattern switches between steady patterns and irregular ones. The transition among different steady patterns is accompanied by very irregular flow-mediated interactions between the two cylinders. For steady states, 3 patterns are identified, as seen in Fig. 6.20. The first pattern is referred to as Pattern F1. A typical cycle can be seen in Figs. 6.20a-6.20d. The pattern looks similar to that of the single-cylinder case, since vortex pairs are also convected towards the diagonal direction. The vortices being shed downwards demonstrate a similar pattern to that of the single-cylinder cases, where a vortex pair is shed from half cycle of the forced oscillation and the vortex shedding occurs only on one side of the active cylinder. Nevertheless, vortex pairs convected upwards are shed with a different mechanism. The vortices are generated from both the left side and the right side of the active cylinder, which is more similar to the pattern in regime A, as seen in Fig. 6.20b. The second pattern is referred to as Pattern F2, as seen in Figs. 6.20e-6.20h. For vortex shedding pattern above the active cylinder, in each cycle, one vortex pair is shed on the left side of the active cylinder, and an additional minor negative vortex is generated and convected to merge with the negative one of the vortex pair. Vortex shedding pattern below the active cylinder is similar to that of the Pattern F1 and the single-cylinder cases with one vortex pair shed from the left side of the active cylinder. So for the Pattern F2, 2 vortex pairs together with an extra negative vortex are shed during each cycle. As for the Pattern F3 in Figs. 6.20i-6.20l, one major vortex pair together with an additional minor vortex is shed below the active cylinder, and the major vortices are shed from both sides of the active cylinder. The vortex pairs shed above the active cylinder is similar to the single-cylinder cases. The mirror-image of these patterns can also occur. For all 3 patterns of the steady state,

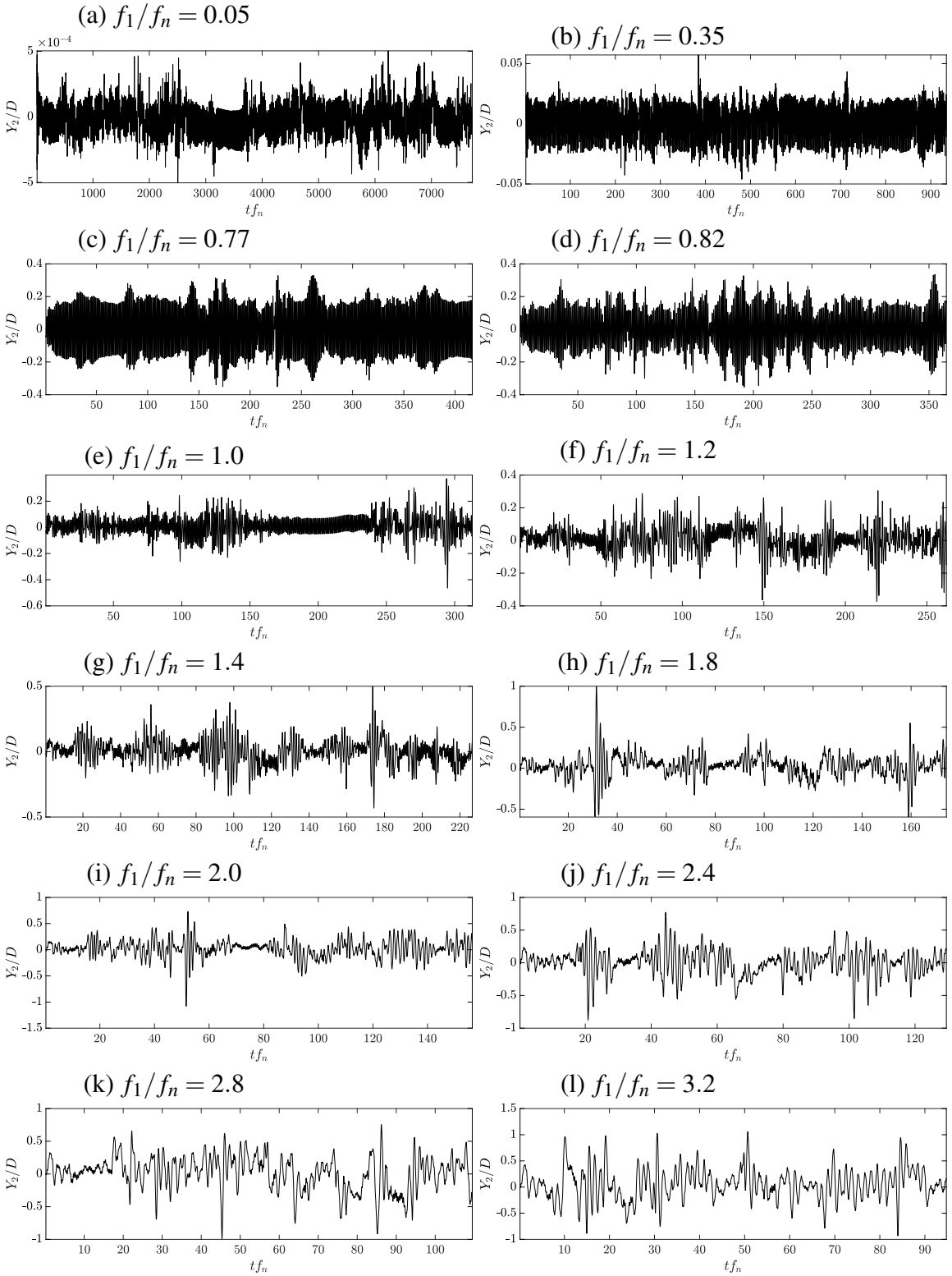

Fig. 6.17 Displacement time history of the passive cylinder in Regime F with $KC = 8, \beta = 35, G/D = 2.5, A_1/D = 1.273, m^* = 2, \zeta = 0, Re_m = 280$ with (a)$f_1/f_n = 0.05$, (b)$f_1/f_n = 0.35$, (c)$f_1/f_n = 0.77$, (d)$f_1/f_n = 0.82$, (e)$f_1/f_n = 1.0$, (f)$f_1/f_n = 1.2$, (g)$f_1/f_n = 1.4$, (h)$f_1/f_n = 1.8$, (i)$f_1/f_n = 2.0$, (j)$f_1/f_n = 2.4$, (k)$f_1/f_n = 2.8$, (l)$f_1/f_n = 3.2$. At $KC = 8$, irregularity is apparent even at very low frequency.

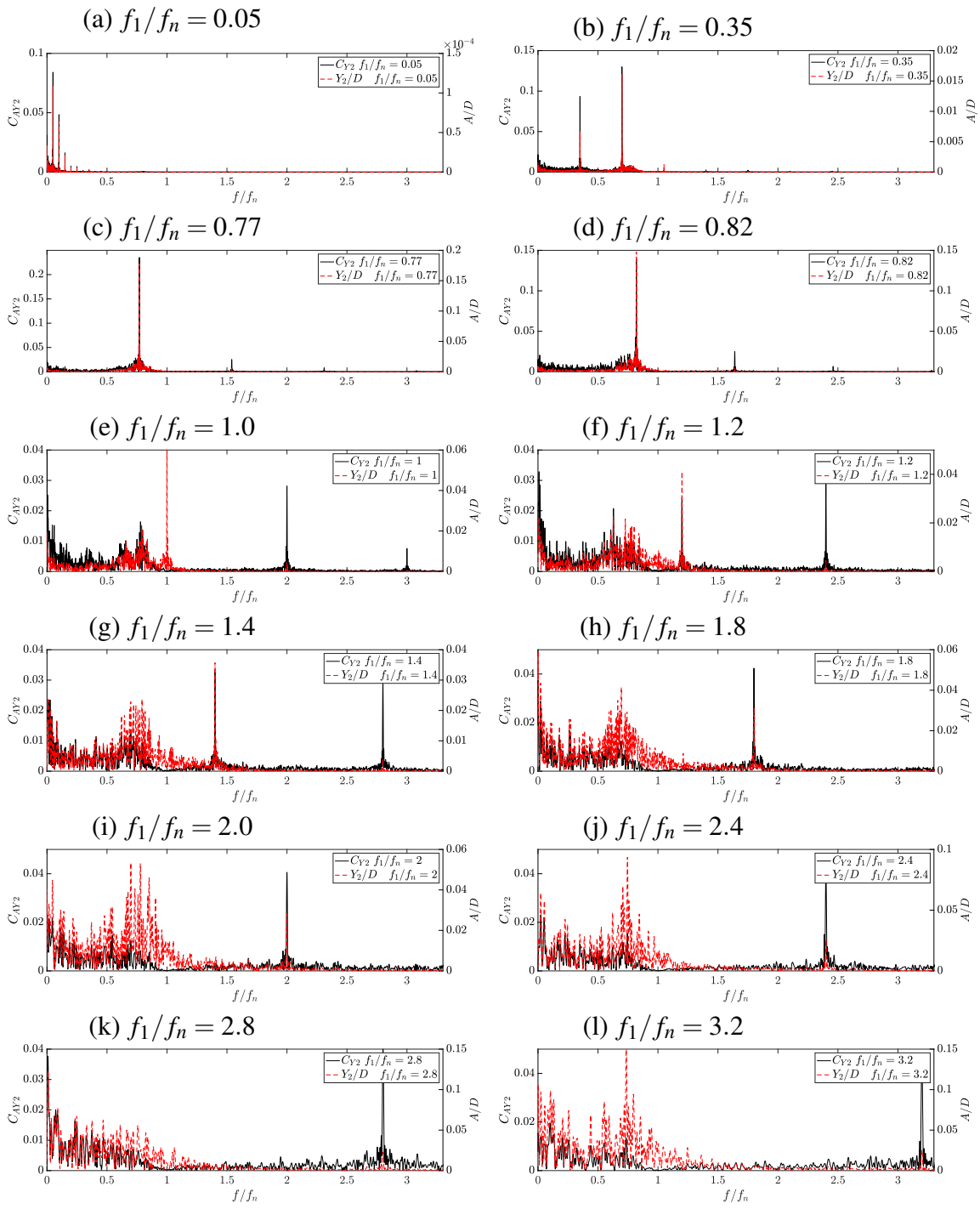

Fig. 6.18 Amplitude spectra of the passive cylinder's displacement in Regime F with $KC = 8, \beta = 35, G/D = 2.5, A_1/D = 1.273, m^* = 2, \zeta = 0, Re_m = 280$ with (a)$f_1/f_n = 0.05$, (b)$f_1/f_n = 0.35$, (c)$f_1/f_n = 0.77$, (d)$f_1/f_n = 0.82$, (e)$f_1/f_n = 1.0$, (f)$f_1/f_n = 1.2$, (g)$f_1/f_n = 1.4$, (h)$f_1/f_n = 1.8$, (i)$f_1/f_n = 2.0$, (j)$f_1/f_n = 2.4$, (k)$f_1/f_n = 2.8$, (l)$f_1/f_n = 3.2$. At $KC = 8$, irregularity is apparent even at very low frequency.

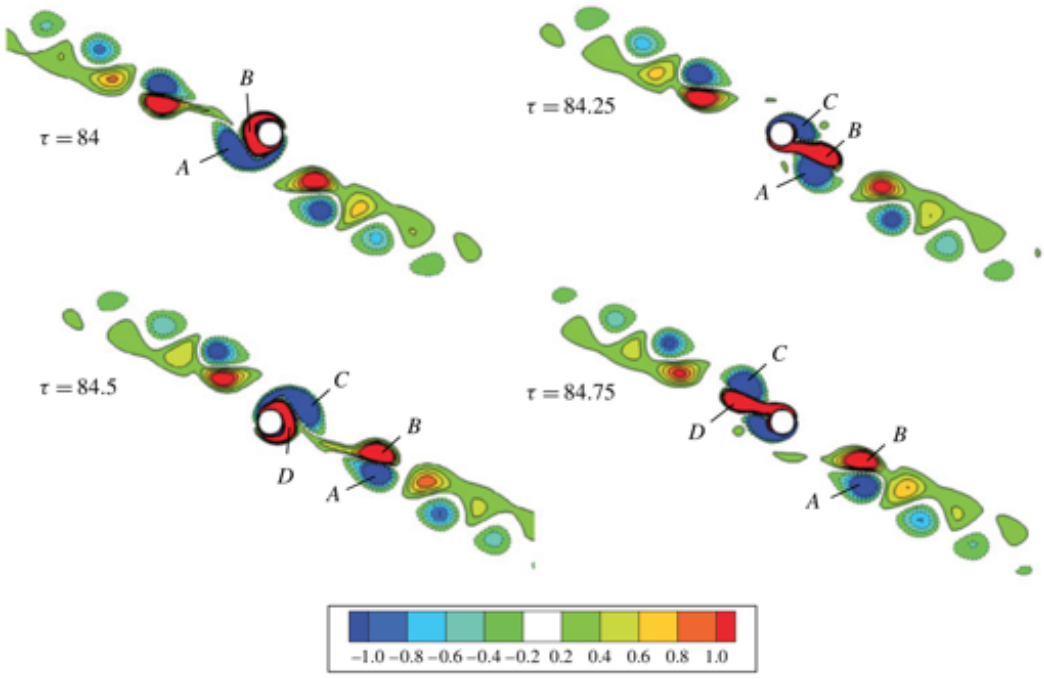

Fig. 6.19 Vorticity contours for a typical regime F flow with only one forced oscillating cylinder at $Re = 150$, $KC = 12$ and $\beta = 12.5$. (Zhao and Cheng, 2014). The flow oscillates on the horizontal direction.

the vortices have a direct impact on the passive cylinder, making its displacement irregular. During the unsteady phase, the flow structure is unpredictable and several vortices shed from consecutive cycles can merge to more severely interfere the vibration of the passive cylinder, plucking the passive cylinder and enlarging the amplitude of its vibration frequency components at about its immersed natural frequency, which is also observed in regime G. The existence of the passive cylinder has disrupted the flow structure, making it switching among several steady patterns and unsteady transition phase, which is dissimilar to the pattern previously observed in the single-cylinder cases.

In summary, the flow-mediated interaction in regime F can switch between being steady and being unstable. 3 steady patterns are identified. Typically, only the vortex shedding pattern on one side of the active cylinder is similar to that for the single-cylinder cases, whereas on the other side, the pattern can be different that vortex pairs can be shed from both the left and the right of the active cylinder. An additional minor vortex can also be observed in 2 of the 3 steady patterns. Irregular flow occurs during the transition from one steady pattern to another. Corresponding to the vortex dynamics, the vibration of the passive cylinder is steady and periodic when the steady vortex shedding patterns take place and the

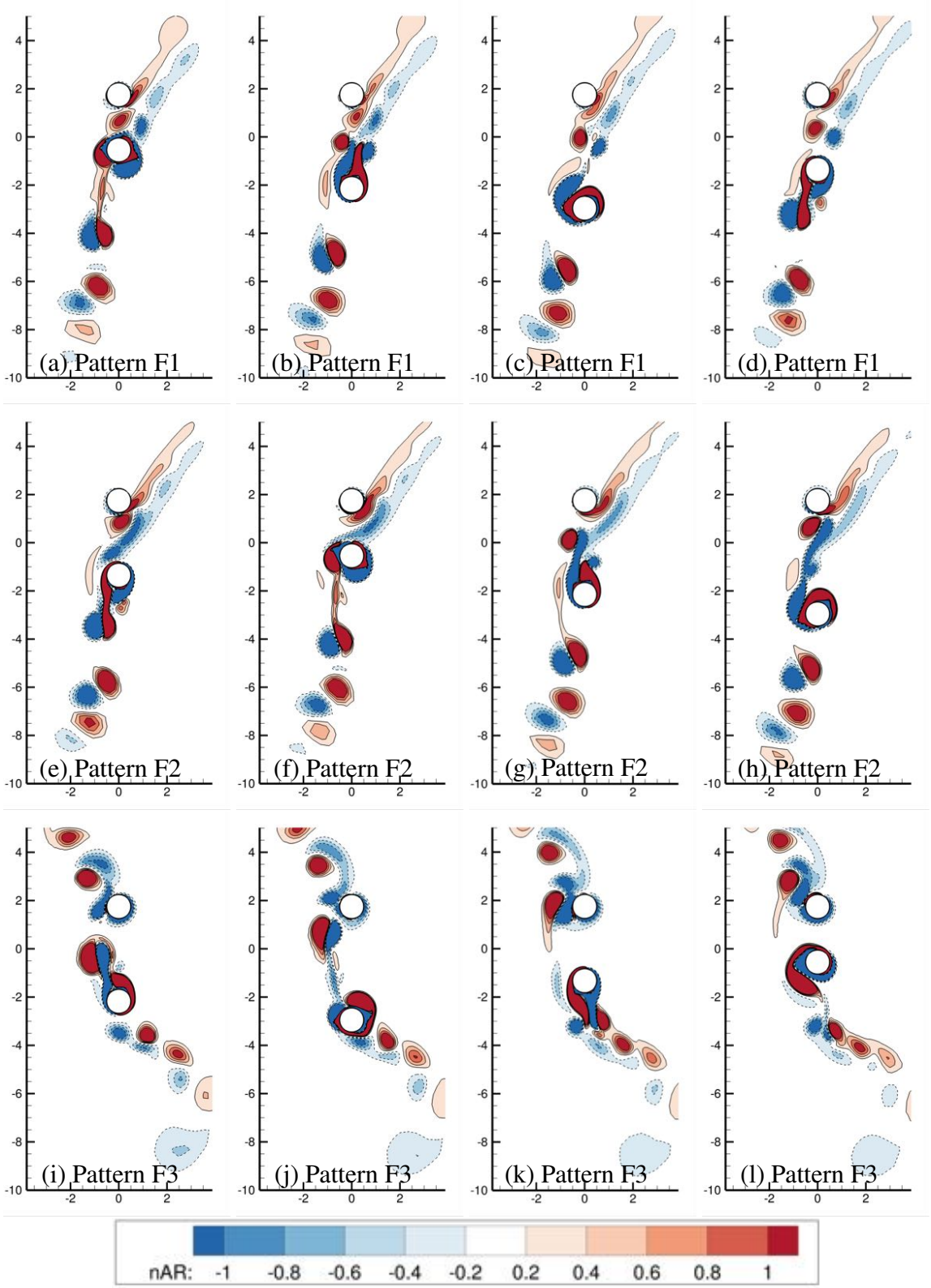

Fig. 6.20 Vorticity contours for vortex shedding patterns in Regime F with $f_1/f_n = 0.05, KC = 8, \beta = 35, G/D = 2.5, A_1/D = 1.273, m^* = 2, \zeta = 0, Re_m = 280$ (a-d) Pattern F1, one vortex pair shed from both sides convected upward and another pair shed from the left side convected downward (e-h) Pattern F2, one pair + one negative vortex shed upward and one pair shed downwards from the left side (i-l) Pattern F3, one pair shed upwards from the left side, and one pair + one negative vortex shed downward. The mirror-images of these patterns can also occur.

abrupt surge of the amplitude occurs when the vortex shedding is irregular, causing several vortices to merge and significantly impact the dynamics of the passive cylinder.

6.5 Regime G

In regime G, the vibration of the passive cylinder is very irregular as seen in Fig. 6.21 and Fig. 6.22. Irregular pulse beating can be observed in the time histories, e.g. when the active cylinder oscillates at $f_1/f_n = 0.77$ from $t^* = 20$ to $t^* = 80$. As the active cylinder oscillates at a higher frequency, the frequency components of the passive cylinder are more and more concentrated in the low-frequency band at $f/f_n \leq 1$.

In regime G, most commonly, 2 major vortex pairs are shed from each oscillation cycle of the active cylinder, and each pair is shed from opposite sides of the active cylinder, as seen in Fig. 6.23. An additional minor vortex can accompany each vortex pair. Due to the unsteady flow, a pair of major vortices can sometimes be shed from both sides of the active cylinder. Sometimes, two vortex pairs are shed from the same side of the active cylinder rather than two different sides.

In regime G, the direction of the vortex shedding changes irregularly, and is not stably diagonal as in regime F of the single-cylinder cases in relative sinusoidal flow. Due to interactions with irregular vortex shedding of the active cylinder, the vibration of the passive cylinder becomes irregular as well, as seen in Fig. 6.24. The amplitude of the passive cylinder's vibration can suddenly increase, for example, as seen in Fig. 6.24 between the instants A and P. The corresponding vorticity contours demonstrate that the sudden increase of the amplitude is caused by the interaction between the passive cylinder and the vortices shed from the previous cycles of the active cylinder as seen in Fig. 6.25. The streaming in regime G is very circular with vortices travelling on elliptical trajectories, and the vortices have a high chance to merge and become a very large vortex. Instants A and P in Fig. 6.25 corresponds to Figs. 6.25a and 6.25p, respectively. From instant A at time $t^* = 79.69$, 3 negative vortices shed from consecutive cycles of the active cylinder merges around the passive cylinder and carries the passive cylinder away, as seen in Fig. 6.25a-6.25h. This is because circulatory streaming allows the vortices to stay around the passive cylinder and merges together to create a powerful drive. For occasions without the significant amplitude, as exemplified in Figs. 6.25m-6.25p, the vortex pairs do not directly impact the passive cylinder and thus do not result in its significant displacement. It is also seen that the direction of vortex shedding from the active cylinder is unstable, causing the irregular displacement time history of the passive cylinder. It is worth noticing that through instants A-P in Figs. 6.25m-6.25p, at the bottom right corner, a positive vortex is growing. This is because the vortices shed from each oscillation cycle of the active cylinder stays there due to circular streaming and positive vortices shed from consecutive cycles merge and gradually forming a larger and larger vortex.

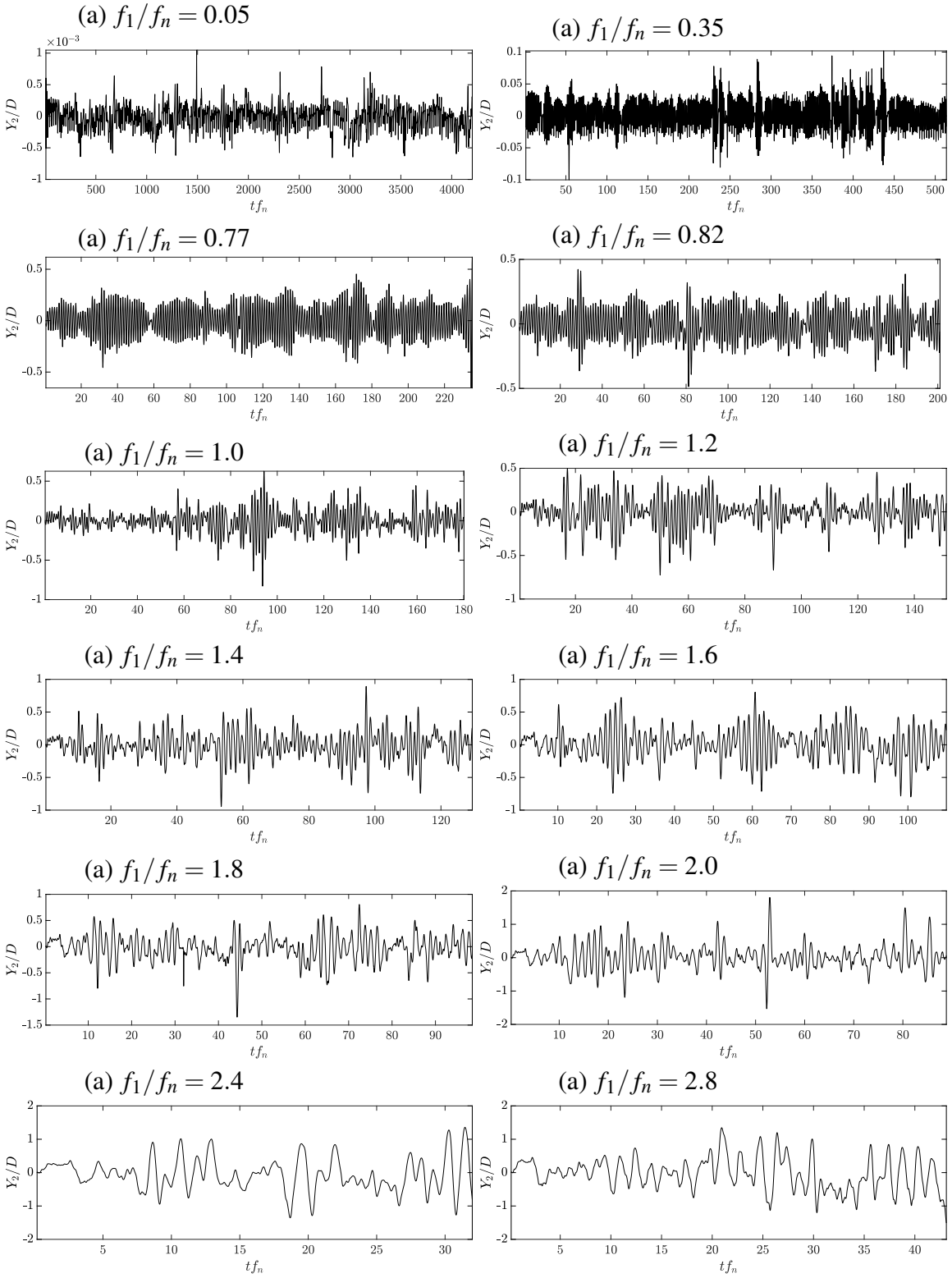

Fig. 6.21 Displacement time history of the passive cylinder in Regime G with $KC = 9, \beta = 35, G/D = 2.5, A_1/D = 1.432, m^* = 2, \zeta = 0, Re_m = 315$ with (a)$f_1/f_n = 0.05$, (b)$f_1/f_n = 0.35$, (c)$f_1/f_n = 0.77$, (d)$f_1/f_n = 0.82$, (e)$f_1/f_n = 1.0$, (f)$f_1/f_n = 1.2$, (g)$f_1/f_n = 1.4$, (h)$f_1/f_n = 1.6$, (i)$f_1/f_n = 1.8$, (j)$f_1/f_n = 2.0$, (k)$f_1/f_n = 2.4$, (l)$f_1/f_n = 2.8$.

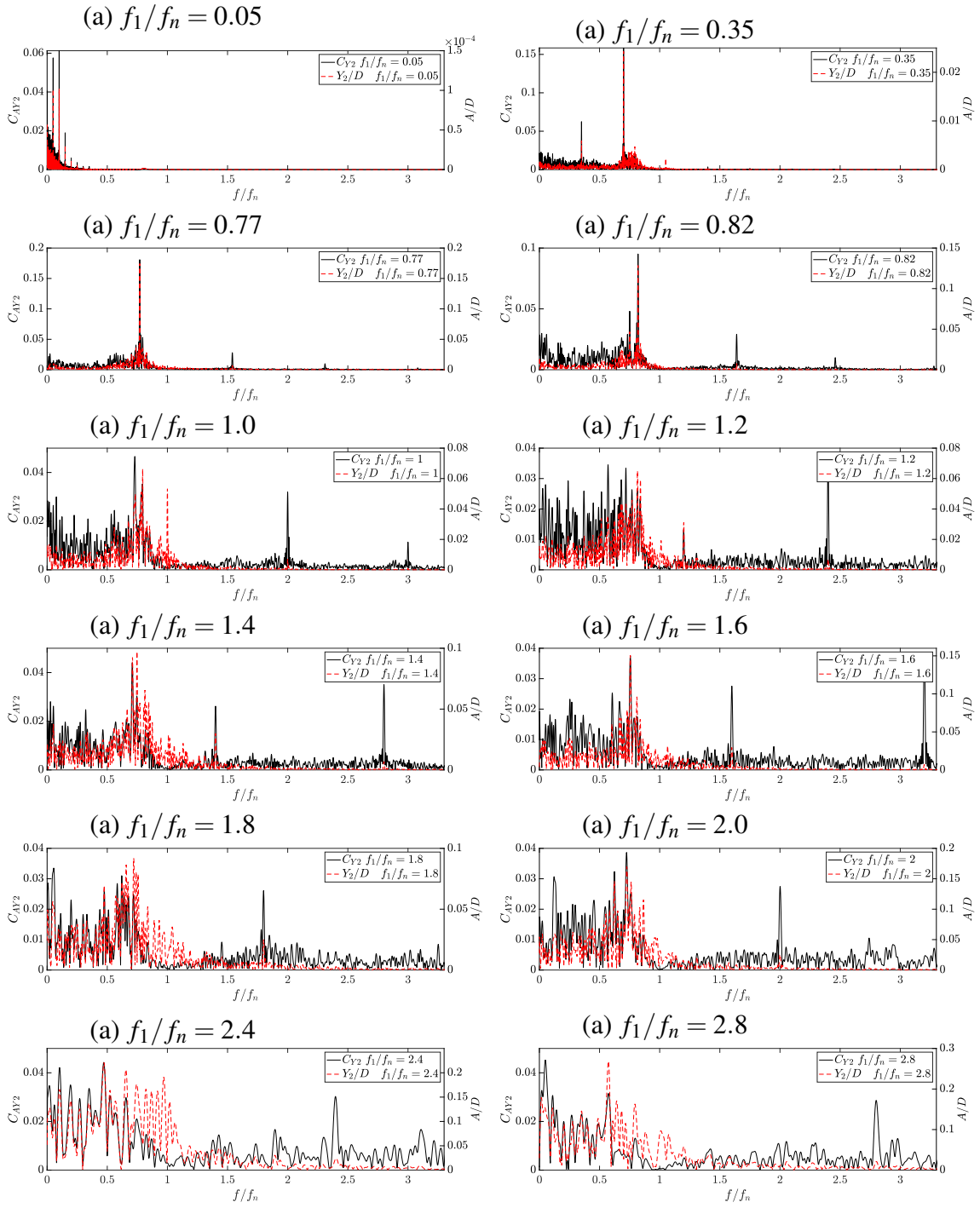

Fig. 6.22 Amplitude spectra of the passive cylinder's displacement in Regime G with $KC = 9, \beta = 35, G/D = 2.5, A_1/D = 1.432, m^* = 2, \zeta = 0, Re_m = 315$ with (a)$f_1/f_n = 0.05$, (b)$f_1/f_n = 0.35$, (c)$f_1/f_n = 0.77$, (d)$f_1/f_n = 0.82$, (e)$f_1/f_n = 1.0$, (f)$f_1/f_n = 1.2$, (g)$f_1/f_n = 1.4$, (h)$f_1/f_n = 1.6$, (i)$f_1/f_n = 1.8$, (j)$f_1/f_n = 2.0$, (k)$f_1/f_n = 2.4$, (l)$f_1/f_n = 2.8$. The dominant frequency of the passive cylinder's vibration becomes equivalent to its immersed natural frequency at $f_1/f_n \geq 1.0$.

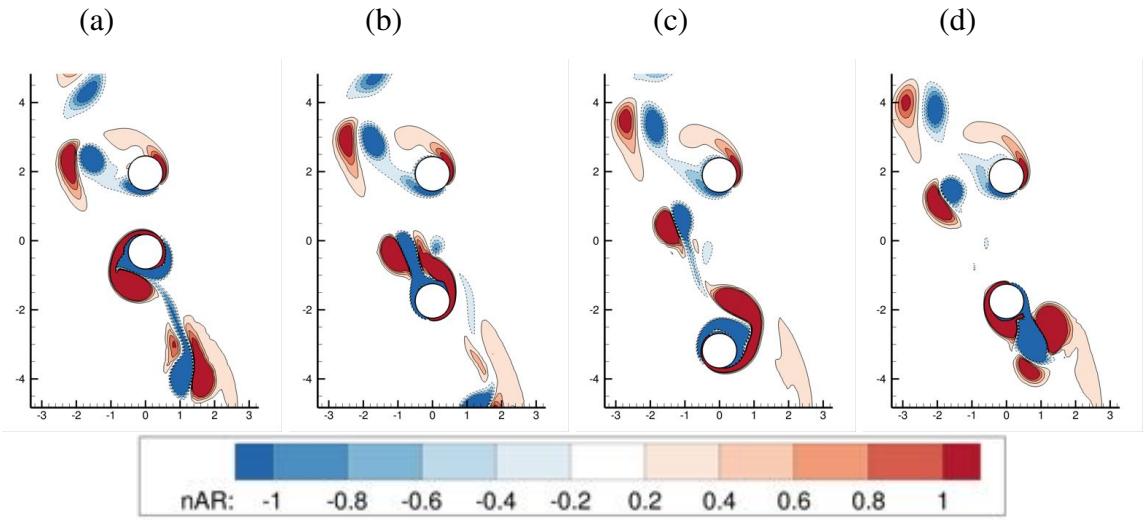

Fig. 6.23 Non-dimensional vorticity contours for regime G with $KC = 9, \beta = 35, G/D = 2.5, A_1/D = 1.432, m^* = 2, \zeta = 0, Re_m = 315, f_1/f_n = 2.0$.

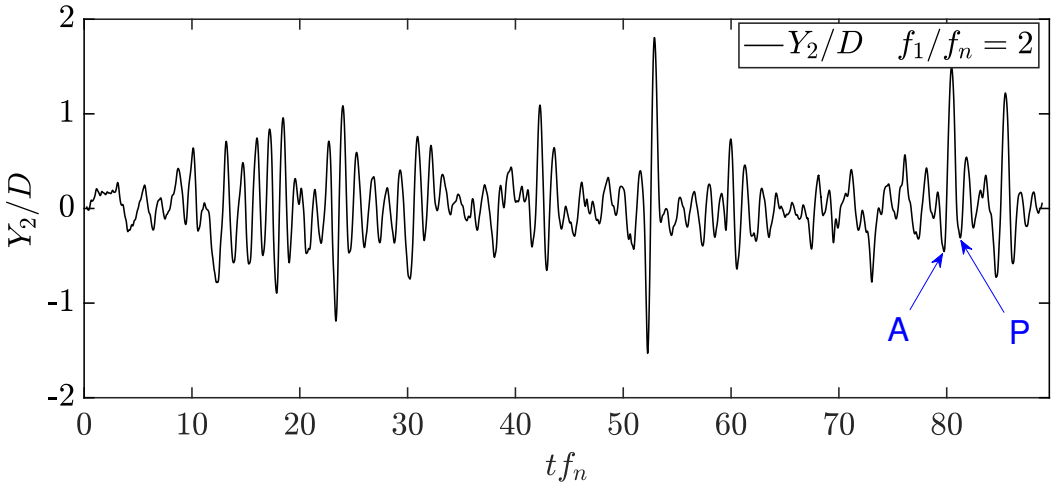

Fig. 6.24 Passive cylinder's vibration time history in Regime G with $KC = 9, \beta = 35, G/D = 2.5, A_1/D = 1.432, m^* = 2, \zeta = 0, Re_m = 315, f_1/f_n = 2.0$. The instants *A* and *P* corresponds to Figs. 6.25a and 6.25p, respectively.

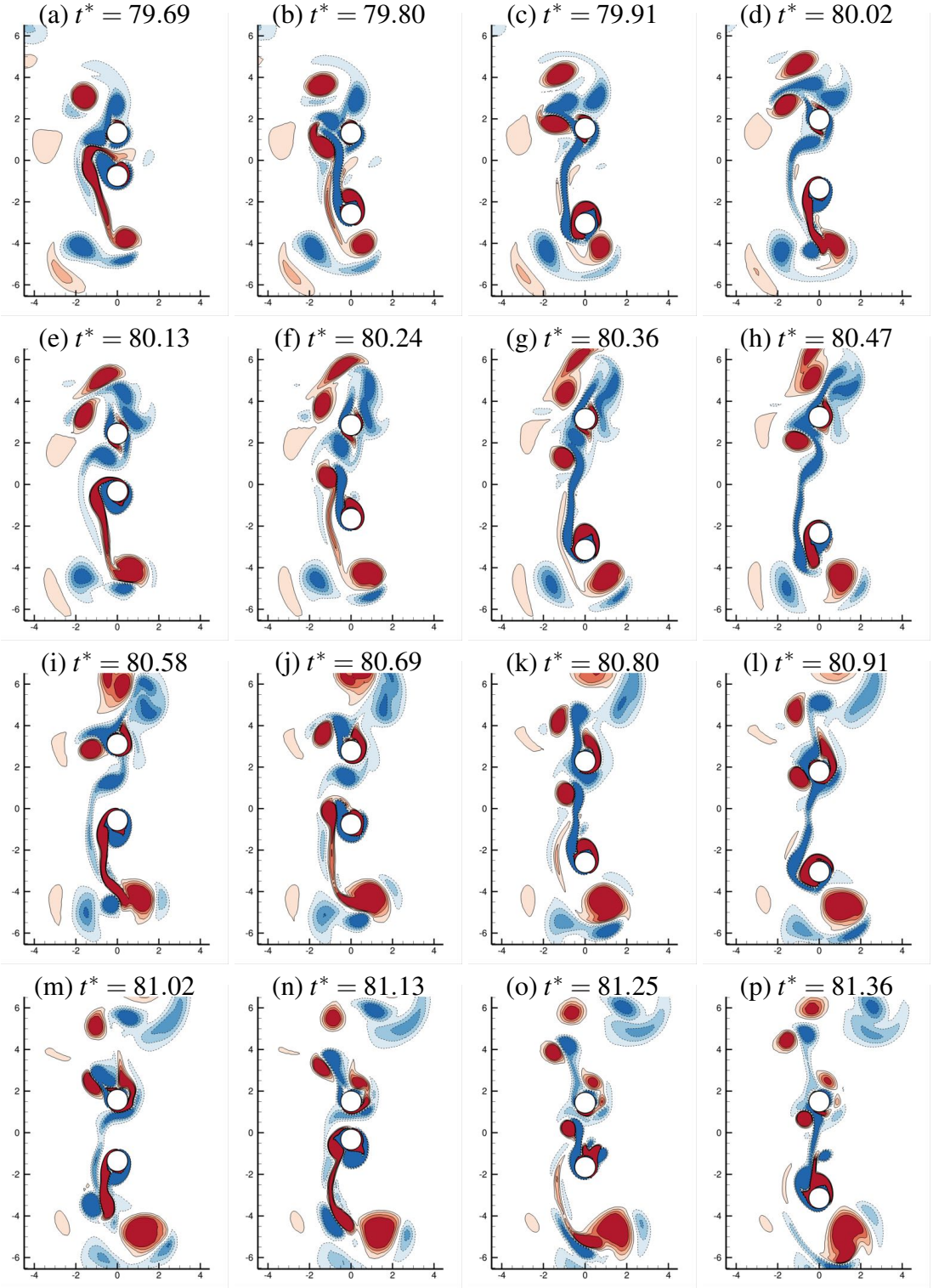

Fig. 6.25 Non-dimensional vorticity contours in Regime G with $KC = 9, \beta = 35, G/D = 2.5, A_1/D = 1.432, m^* = 2, \zeta = 0, Re_m = 315, f_1/f_n = 2.0$. (a-h) Multiple negative vortices shed from the active cylinder merges around the passive cylinder and pushes it away. (i-p) The vortex pairs shed from the active cylinder goes around the passive cylinder without causing its significant displacement. Instants A and P in Fig. 6.25 corresponds to Figs. 6.25a and 6.25p, respectively.

6.6 Chapter Summary

To summarise this chapter, the irregularity and the overall amplitude for the vibration of the passive cylinder increases with $KC = 1-7$ at $\beta = 35$. However, the amplification factor and the phase difference of the harmonic components barely changes with KC at both damped and undamped conditions. Regime C features pulse beating in the response of the passive cylinder due to the almost periodic gradual switch of the streaming direction, and the vortex shedding occurs for both sides of the active cylinder. In regime E, the passive cylinder responds steadily most of the time with irregularity occurs intermittently. This corresponds to the intermittent switching between one flow pattern and its mirror-image. During switching, the flow structure and vortex shedding are fairly irregular. In every cycle, 2 vortex pairs are shed from the active cylinder. In terms of regime F, the irregularity is of another level. Only a few periods of steady interactions can be observed. At least 3 steady patterns can be identified. In a single cycle, a vortex pair can be shed from one side of the active cylinder like in regime E and another vortex pair can emerge from both sides of the active cylinder like in regime C. During the steady state, the flow structure is diagonal in coherence with the single-cylinder cases. The transition between the steady patterns is very irregular with little pattern identifiable. In regime G, the flow is very irregular. Most of the time, 2 vortex pairs are shed from opposite sides of the active cylinder in one cycle. The flow is also very circular, enabling vortices shed from consecutive cycles to merge, becoming a much stronger vortex. Such large vortex can directly impact the passive cylinder, causing its significant displacement as shown in the time histories.

Chapter 7

Conclusions

This chapter provides a summary of the entire thesis and then draws conclusions on how the 6 non-dimensional groups influence the resonance phenomena and the vibration centre drift of the passive cylinder and the corresponding flow characteristics. At last, potential future work is suggested.

7.1 Overview

This study focuses on the representative case of the flow-mediated interactions between two cylinders immersed in a quiescent fluid. The active cylinder undergoes forced vibration with a specified amplitude and frequency, whereas the passive cylinder is elastically-mounted with a damper. Both cylinders are only allowed to vibrate along the centreline connecting the two cylinders. For this representative case, 6 non-dimensional groups are identified by dimensional analysis.

This study uses an in-house finite element code to simulate this problem of flow-mediated interaction. Simulations are conducted for a range of combinations of parameters. The active cylinder's oscillation frequency f_1/f_n ranges from 0.05 to 3.2; the amplitude of the active cylinder A_1/D varies from 0.025 to 1.432; the mass ratio of the passive cylinder m^* takes the value of 1.5, 1.7, 2.0, 2.2 or 2.5; the structural damping factor of the passive cylinder ranges from 0 to 1.4; Reynolds number Re_m varies from 10 to 310; the gap ratio G/D ranges from 0.2 to 3. The range of Keulegan-Carpenter number and the Stokes number of the active cylinder can then be calculated to be $KC = 0.16 - 9$ and $\beta = Re_m/KC = 3.3 - 637$, respectively. In total, 23,400 combinations of parameters are examined. This parametric space is chosen to reflect the values usually seen in engineering applications.

7.2 Parametric Study in Periodic Regimes A and A*

Active cylinder's forced oscillation frequency f_1/f_n is the most significant parameter. The vibration frequency of the passive cylinder is usually synced to f_1/f_n, thus adjusting f_1/f_n can cause resonance of the passive cylinder, greatly amplifying its vibration amplitude. Oscillation of the active cylinder also causes harmonics of the passive cylinder, resulting in secondary resonance.

Reynolds number Re_m governs the drifting of the vibration centre. Its variation can alter the flow structure, causing the passive cylinder to be attracted towards or repelled away from the active cylinder.

Structural damping factor ζ can significantly suppress the amplitude of the passive cylinder with a slight increase of value. It is also capable of affecting how other parameters influence the passive cylinder's vibration. It can alter the relationship between other non-dimensional groups and the vibration pattern of the passive cylinder. It also can lead to less intensive the pressure oscillation at the far side of the active cylinder.

The mass ratio of the passive cylinder m^* determines immersed natural frequency of the passive cylinder, and thus controlling its resonance frequency. At cases where the passive cylinder is structurally undamped, it can not influence the passive cylinder's amplitude at resonance. However, at the damped case, it can reduce the overall responding amplitude, including at resonance.

Active cylinder's oscillation amplitude A_1/D is generally linearly correlated with that of the passive cylinder, except at resonance and with very low structural damping.

Gap distance G/D is negatively correlated the responding vibration amplitude of the passive cylinder. However, it turns out not to influence the phase difference between the passive cylinder and the active cylinder.

7.3 Interactions in Less Regular Regimes C, E, F and G

The overall flow structures exhibited in less regular regimes are fundamentally different from that in the periodic regimes aforementioned. However, despite the irregular frequency components discovered in the amplitude spectra of the passive cylinder's vibration, the harmonics previously discussed is persistent and always distinguishable. So the previous conclusions regarding harmonics and major and minor resonance still apply. The vibration centre shift pattern may, however, change due to the alteration of flow structure.

Regime C features the passive cylinder's pulse beating due to the switching between the skewed "L" shape flow pattern and its mirror-image, and the vortex shedding occurs for both

sides of the active cylinder. In regime C, the switching of flow pattern is gradual, so the irregular transition in the following regimes does not occur. This pattern is fundamentally different from that of a single oscillating cylinder.

In regime E, the passive cylinder vibrates steadily most of the time, even though irregularity may take place from time to time. This response pattern corresponds to the intermittent switch of the flow structure between one pattern and its mirror-image. During the transition, the flow structure and vortex shedding are fairly irregular. In every cycle, two vortex pairs are shed from the active cylinder.

In terms of regime F, the irregularity further increases. Only a few periods of steady interactions can be observed. At least 3 steady patterns can be identified. In a single cycle, a vortex pair can be shed from one side of the active cylinder like in regime E with another vortex pair emerged from both sides of the active cylinder like in regime C. A minor extra vortex can be observed when the vortex pair is shed from both sides. During the steady-state, the flow structure is diagonal in coherence with the single-cylinder cases. The transition between the steady patterns is very irregular with little pattern identifiable.

In regime G, the flow is highly irregular. Most of the time, two vortex pairs are shed from opposite sides of the active cylinder in one cycle. Sometimes, two vortex pairs can also be shed from a single side. The flow is also very circular, enabling vortices shed from consecutive cycles to merge becoming a much stronger vortex. Such a large vortex can directly impact the passive cylinder, causing its significant displacement as shown in the time histories.

The existence of the passive cylinder disrupts the flow pattern, since the flow structure is more irregular compared with the single-cylinder cases and in some regimes, the flow pattern is very different from the single-cylinder cases.

7.4 Future Work

A few areas are suggested to be further explored in the future, including 3D simulation, artificial intelligence, Floquet analysis, bio-engineering and vortex-induced vibration energy harvesting.

3D simulations at higher KC and β can be conducted to explore regimes with more complicated 3D flow features and to provide a more comprehensive understanding of the flow-mediated interaction phenomena. The configuration of the two cylinders that are not parallel to each other can be studied.

Artificial intelligence can be useful in summarising a large number of CFD results. Machine learning or even deep learning may be applied to find patterns in the data, since

a large amount of data are generated in such parametric studies. Image processing may be used to check the flow fields and to identify interesting phenomena, thus reducing the human labour in processing such an amount of data.

Floquet analysis can be applied to further investigate the symmetry breaking in this two cylinder case.

The simulation of the swimming organisms can be simulated in the future, for example, the sperms and fishes.

Interaction among cylinders in vortex-induced vibration energy harvesting devices and the relationship between the parameters and the efficiency can be further explored.

References

Bampalas, N. and Graham, J. M. R. (2008). Flow-Induced Forces Arising During the Impact of Two Circular Cylinders. *Journal of Fluid Mechanics*, 616:205–234.

Bernitsas, M. M., Raghavan, K., Ben-Simon, Y., and Garcia, E. M. H. (2008). Vivace (Vortex Induced Vibration Aquatic Clean Energy): A New Concept in Generation of Clean and Renewable Energy From Fluid Flow. *Journal of Offshore Mechanics and Arctic Engineering*, 130(4):041101.

Brooks, A. N. and Hughes, T. J. (1982). Streamline Upwind/Petrov-Galerkin Formulations for Convection Dominated Flows With Particular Emphasis on the Incompressible Navier-Stokes Equations. *Computer Methods in Applied Mechanics and Engineering*, 32(1-3):199–259.

Choi, J. I., Oberoi, R. C., Edwards, J. R., and Rosati, J. A. (2007). An Immersed Boundary Method for Complex Incompressible Flows. *Journal of Computational Physics*, 224(2):757–784.

Cui, Z., Zhao, M., and Teng, B. (2014). Vortex-Induced Vibration of Two Elastically Coupled Cylinders in Side-By-Side Arrangement. *Journal of Fluids and Structures*, 44:270–291.

Donea, J., Giuliani, S., and Halleux, J. P. (1982). An Arbitrary Lagrangian-Eulerian Finite Element Method for Transient Dynamic Fluid-Structure Interactions. *Computer Methods in Applied Mechanics and Engineering*, 33(1-3):689–723.

Dütsch, H., Durst, F., Becker, S., and Lienhart, H. (1998). Low-Reynolds-Number Flow Around an Oscillating Circular Cylinder at Low Keulegan–Carpenter Numbers. *Journal of Fluid Mechanics*, 360:249–271.

Elston, J. R., Blackburn, H. M., and Sheridan, J. (2006). The Primary and Secondary Instabilities of Flow Generated by an Oscillating Circular Cylinder. *Journal of Fluid Mechanics*, 550:359–389.

Elston, J. R., Sheridan, J., and Blackburn, H. M. (2004). Two-Dimensional Floquet Stability Analysis of the Flow Produced by an Oscillating Circular Cylinder in Quiescent Fluid. *European Journal of Mechanics, B/Fluids*, 23(1):99–106.

Gazzola, M., Chatelain, P., van Rees, W. M., and Koumoutsakos, P. (2011). Simulations of Single and Multiple Swimmers With Non-Divergence Free Deforming Geometries. *Journal of Computational Physics*, 230(19):7093–7114.

Gazzola, M., Mimeau, C., Tchieu, A. A., and Koumoutsakos, P. (2012). Flow Mediated Interactions Between Two Cylinders at Finite *Re* Numbers. *Physics of Fluids*, 24(4):043103.

Gazzola, M., Tchieu, A. A., Alexeev, D., de Brauer, A., and Koumoutsakos, P. (2016). Learning to School in the Presence of Hydrodynamic Interactions. *Journal of Fluid Mechanics*, 789:726–749.

Guilmineau, E. and Queutey, P. (2002). A Numerical Simulation of Vortex Shedding From an Oscillating Circular Cylinder. *Journal of Fluids and Structures*, 16(6):773–794.

Gyrya, V., Aranson, I. S., Berlyand, L. V., and Karpeev, D. (2010). A Model of Hydrodynamic Interaction Between Swimming Bacteria. *Bulletin of Mathematical Biology*, 72:148–183.

Hall, P. (1984). On the Stability of the Unsteady Boundary Layer on a Cylinder Oscillating Transversely in a Viscous Fluid. *Journal of Fluid Mechanics*, 146:347–367.

Hirt, C. W., Amsden, A. A., and Cook, J. L. (1974). An Arbitrary Lagrangian-Eulerian Computing Method for All Flow Speeds. *Journal of Computational Physics*, 14(3):227–253.

Honji, H. (2006). Streaked Flow Around an Oscillating Circular Cylinder. *Journal of Fluid Mechanics*, 107:509–520.

Hughes, T. J. R., Liu, W. K., and Zimmermann, T. K. (1981). Lagrangian-Eulerian Finite Element Formulation for Incompressible Viscous Flows. *Computer Methods in Applied Mechanics and Engineering*, 29(3):329–349.

Huygens, C. (1660). Oeuvres completes de Christiaan Huygens. *M. Nijhoff (Ed.)*, 17:156–189.

Iliadis, G. and Anagnostopoulos, P. (2002). Numerical Visualization of Oscillatory Flow Around a Circular Cylinder at $Re = 200$ and $KC = 20$ - an Aperiodic Flow Case. *Communications in Numerical Methods in Engineering*, 14(3):181–194.

Ishikawa, T., Simmonds, M. P., and Pedley, T. J. (2006). Hydrodynamic Interaction of Two Swimming Model Micro-Organisms. *Journal of Fluid Mechanics*, 568:119–160.

Jester, W. and Kallinderis, Y. (2003). Numerical Study of Incompressible Flow About Fixed Cylinder Pairs. *Journal of Fluids and Structures*, 17(4):561–577.

Justesen, P. (1991). A Numerical Study of Oscillating Flow Around a Circular Cylinder. *Journal of Fluid Mechanics*, 222:157–196.

Keulegan, G. and Carpenter, L. (1958). Forces on Cylinders and Plates in an Oscillating Fluid. *Journal of Research of the National Bureau of Standards*, 60(5):423–440.

Kim, D. and Choi, H. (2006). Immersed Boundary Method for Flow Around an Arbitrarily Moving Body. *Journal of Computational Physics*, 212(2):662–680.

Kim, K. H. and Choi, J. I. (2019). Lock-In Regions of Laminar Flows Over a Streamwise Oscillating Circular Cylinder. *Journal of Fluid Mechanics*, 858:315–351.

Koch, D. L. and Subramanian, G. (2011). Collective Hydrodynamics of Swimming Microorganisms: Living Fluids. *Annual Review of Fluid Mechanics*, 43:637–659.

Lamb, H. (1932). *Hydrodynamics*. Cambridge University Press, Cambridge, 6th ed. edition.

Liao, J. C. (2003). Fish Exploiting Vortices Decrease Muscle Activity. *Science*, 302(5650):1566–1569.

Lin, X. W., Bearman, P. W., and Graham, J. M. (1996). A Numerical Study of Oscillatory Flow About a Circular Cylinder for Low Values of Beta Parameter. *Journal of Fluids and Structures*, 10(5):501–526.

Lin, Z., Liang, D., and Zhao, M. (2016). Numerical Study of the Interaction Between Two Immersed Cylinders. In *The 12th International Conference on Hydrodynamics*, page 55, Egmond aan Zee, The Netherlands.

Lin, Z., Liang, D., and Zhao, M. (2017). Interaction Between Two Vibrating Cylinders Immersed in Fluid. In *Proceedings of the Twenty-seventh (2017) International Ocean and Polar Engineering Conference*. OnePetro.

Lin, Z., Liang, D., and Zhao, M. (2018a). Effects of Damping on Flow-Mediated Interaction Between Two Cylinders. *Journal of Fluids Engineering*, 140(9):91106–91112.

Lin, Z., Liang, D., and Zhao, M. (2018b). Flow-Mediated Interaction Between a Vibrating Cylinder and an Elastically-Mounted Cylinder. *Ocean Engineering*, 158:389–402.

Meneghini, J. R., Saltara, F., Siqueira, C. L., and Ferrari, J. A. (2001). Numerical Simulation of Flow Interference Between Two Circular Cylinders in Tandem and Side-By-Side Arrangements. *Journal of Fluids and Structures*, 15(2):327–350.

Meting, T. S., Dalheim, J., and Others (1997). Numerical Prediction of the Response of a Vortex-Excited Cylinder at Low Reynolds Numbers. In *The Seventh International Offshore and Polar Engineering Conference*. International Society of Offshore and Polar Engineers.

Metzger, B., Nicolas, M., and Guazzelli, É. (2007). Falling Clouds of Particles in Viscous Fluids. *Journal of Fluid Mechanics*, 580:283–301.

Morison, J., Johnson, J., and Schaaf, S. (1950). The Force Exerted by Surface Waves on Piles. *Journal of Petroleum Technology*, 2(5):149–154.

Nair, S. and Kanso, E. (2007). Hydrodynamically Coupled Rigid Bodies. *Journal of Fluid Mechanics*, 592:393–411.

Noh, W. (1964). CEL: A Time-Dependent, Two Space Dimensional, Coupled Eulerian–Lagrange Code. Technical report, Lawrence Radiation Lab., Univ. of California, Livermore.

Obasaju, E. D., Bearman, P. W., and Graham, J. M. (1988). A Study of Forces, Circulation and Vortex Patterns Around a Circular Cylinder in Oscillating Flow. *Journal of Fluid Mechanics*, 196:467–494.

Pang, Y., Kai, W., Yuan, W., and Shen, G. (2015). Effects of Dynamic Fluid-Structure Interaction on Seismic Response of Multi-Span Deep Water Bridges Using Fragility Function Method. *Advances in Structural Engineering*, 18(4):525–541.

Peña Ramirez, J., Fey, R. H., Aihara, K., and Nijmeijer, H. (2014). An Improved Model for the Classical Huygens' Experiment on Synchronization of Pendulum Clocks. *Journal of Sound and Vibration*, 333(26):7248–7266.

Riffell, J. a. and Zimmer, R. K. (2007). Sex and Flow: The Consequences of Fluid Shear for Sperm-Egg Interactions. *Journal of Experimental Biology*, 210:3644–3660.

Sarpkaya, T. (1977). In-Line and Transverse Forces on Smooth and Sand-Roughened Cylinders in Oscillatory Flow at High Reynolds Numbers. *Journal of Ship Research*, 21(4):200–216.

Sarpkaya, T. (1986). Force on a Circular Cylinder in Viscous Oscillatory Flow at Low Keulegan-Carpenter Numbers. *Journal of Fluid Mechanics*, 165:61–71.

Sarpkaya, T. (2002). Experiments on the Stability of Sinusoidal Flow Over a Circular Cylinder. *Journal of Fluid Mechanics*, 457:157–180.

Sarpkaya, T. (2005). On the Parameter $\beta = Re/KC = D^2/\nu T$. *Journal of Fluids and Structures*, 21(4):435–440.

Sarpkaya, T. (2006). Structures of Separation on a Circular Cylinder in Periodic Flow. *Journal of Fluid Mechanics*, 567:281–297.

Tatsuno, M. and Bearman, P. W. (1990). A Visual Study of the Flow Around an Oscillating Circular Cylinder at Low Keulegan–Carpenter Numbers and Low Stokes Numbers. *Journal of Fluid Mechanics*, 211:157–182.

Trulio, J. G. (1966). Theory and Structure of the AFTON Codes. *Kirtland Air Force Base Rept. No. AFWL-TR-66-19*.

Van Rees, W. M., Novati, G., and Koumoutsakos, P. (2015). Self-Propulsion of a Counter-Rotating Cylinder Pair in a Viscous Fluid. *Physics of Fluids*, 27(6):063102.

Voth, G. A., Bigger, B., Buckley, M. R., Losert, W., Brenner, M. P., Stone, H. A., Gollub, J. P., and Gollub, J. P. (2002). Ordered Clusters and Dynamical States of Particles in a Vibrated Fluid. *Physical Review Letters*, 88(23):2343011–2343014.

Weck, O. D., Il, Y., De Weck, O., and Il, Y. (2016). Finite Element Method MIT Lecture Note. Technical report, Massachusetts Institute of Technology.

Weihs, D. (2004). The Hydrodynamics of Dolphin Drafting. *Journal of Biology*, 3(2):8.

Williamson, C. H. K. (1985). Sinusoidal Flow Relative to Circular Cylinders. *Journal of Fluid Mechanics*, 155:141–174.

Yang, J. and Balaras, E. (2006). An Embedded-Boundary Formulation for Large-Eddy Simulation of Turbulent Flows Interacting With Moving Boundaries. *Journal of Computational Physics*, 215(1):12–40.

Zhao, M. (2013). Flow Induced Vibration of Two Rigidly Coupled Circular Cylinders in Tandem and Side-By-Side Arrangements at a Low Reynolds Number of 150. *Physics of Fluids*, 25(12):123601.

Zhao, M. and Cheng, L. (2014). Two-Dimensional Numerical Study of Vortex Shedding Regimes of Oscillatory Flow Past Two Circular Cylinders in Side-By-Side and Tandem Arrangements at Low Reynolds Numbers. *Journal of Fluid Mechanics*, 751:1–37.

Zhao, M., Cheng, L., Teng, B., and Dong, G. (2007). Hydrodynamic Forces on Dual Cylinders of Different Diameters in Steady Currents. *Journal of Fluids and Structures*, 23(1):59–83.

Zhao, M., Cheng, L., and Zhou, T. (2009). Direct Numerical Simulation of Three-Dimensional Flow Past a Yawed Circular Cylinder of Infinite Length. *Journal of Fluids and Structures*, 25(5):831–847.

Zhao, M., Cheng, L., and Zhou, T. (2013). Numerical Simulation of Vortex-Induced Vibration of a Square Cylinder at a Low Reynolds Number. *Physics of Fluids*, 25(2):023603.

Zhao, M. and Yan, G. (2013). Numerical Simulation of Vortex-Induced Vibration of Two Circular Cylinders of Different Diameters at Low Reynolds Number. *Physics of Fluids*, 25:083601.

Appendix A

Data Processing Scripts

Thousands of lines of mini MATLAB programmes were created to execute the pre-processing and post-processing of the CFD simulations. The following sections present examples for many data processing scripts.

A.1 Generation of Time History and Amplitude Spectra

This is the most frequently used mini MATLAB programme for post-processing.

```
clear all
close all
fclose all;
global autocut_switch xlimax
global cutlength
autocut_switch=0;% 0 is to turn off autocut
cutlength=2;%first periods to cut off
syscount=0;%counter to go throught diff directories
xlimax=3.3;% maximum value on x-axis
for syscount=1:1
    if syscount==1
        sysdir % data part_2
    elseif syscount==2
        sysdir2 % data part_3
    end
    sys_pwd=pwd;
    list0=dir('g*a*m*d*e*r*'); %9326-9340
    n0=length(list0);
    s=0;resc=0;
    nstart=1;
    for j=nstart:n0 %1:n0
```

```
        cd(sys_pwd)
        cd (list0(j).name)
        listf1=dir('0*');
        n=length(listf1);
        cd ('../')
        str=list0(j).name;
        gamr=s2gamr(str);
        G=gamr(1);
        A1=gamr(2);
        m=gamr(3);
        damp=gamr(4);
        Re=gamr(5);
        taskid=gamr(6);
        cphs=zeros(1,n);
        yphs=zeros(1,n);
        f1s=zeros(1,n);
        for i=1:n % i=1:n
            f1=str2double(listf1(i).name);
            f1s(i)=f1;
            close all
            cd(sys_pwd)
            dirnamef=[list0(j).name,'/',listf1(i).name,'/'];
            cd(dirnamef)
            disp(pwd);
            fdir=pwd;
            cd('G:\My Drive\High_KC_Anime_Research_Figure_Plot');
            tempo=['plotting_both/',list0(j).name];
            mkdir(tempo)
            cd (tempo)
            disp(tempo)
            ttl=['G=',num2str(G),'  A_1=',num2str(A1),'  m=',num2str(
m),'  f1=',listf1(i).name,'  Cylinder 2'];
            pdir=pwd;
            pname=[list0(j).name,'_',listf1(i).name];
            fdir=fdir;pname=pname;pdir=pdir;
            zpf=[];ttl_p=[];
            start=0;
            f1=f1;A1=A1;
            nT=4;%nT last periods will be displayed
            ylimfftl=[];ylimfftr=[];
            ylimthl=[];ylimthr=[];
            mr=m;
```

```
63              [err,stperiods,cphs(i),yphs(i)]=checkplot_CY_and_Y(fdir,
    zpf,start,pdir,ttl_p,pname,ylimfftl,f1,nT,ylimthl,A1,ylimfftr,
    ylimthr,mr);
64              if err~=-1
65                  saveas(gcf,[ttl,'.fig'])
66              end
67              resc=resc+1;
68              result(resc,:)=[gamr(1:3) f1 gamr(4) Re stperiods -1];
69              cd ('../')
70              cd ('../')
71              csvwrite(['gamfr_Re_stperiods.dat'],result)
72          end
73          figure
74          plot(f1s,cphs)%plot phase of force coefficient (dominant
    frequency with largest amplitude)
75          plot(f1s,yphs)%plot phase of displacement
76          plot(f1s,cphs-yphs) % plot phase difference
77      end
78  end
79  function [err,stperiods,cphs,yphs]=checkplot_CY_and_Y(fdir,zpf,start,
    pdir,ttl_p,pname,ylimfftl,f1,nT,ylimthl,A1,ylimfftr,ylimthr,mr)
80  cphs=0;yphs=0;
81  global autocut_switch xlimax
82  setlatex
83  if ~exist('pname','var') || isempty(pname)
84      pname='';
85  end
86  if ~exist('fdir','var') || isempty(fdir)
87      fdir=pwd;
88  end
89  cd(fdir)
90  if ~exist('start','var') || isempty(start)
91      start=1;
92  end
93  [t1,y1]=textscan_ft(A1,f1);% 1 denotes force coefficient
94  dt1=t1(20)-t1(19);
95  [t2,y2,v2]=textscanty;          % 2 denotes displacement
96  dt2=t2(20)-t2(19);
97  fdname='Verification';
98  t1=t1(4000:(end-4000));
99  y1=y1(4000:(end-4000));
100 t2=t2(4000:(end-4000));
101 y2=y2(4000:(end-4000));
```

```
if autocut_switch;[t1,y1,t2,y2]=autocut_for_irregular(f1,t1,y1,t2,y2)
    ;end
note1='Cy02';
note2='Y';
L = length(y2); %total points after cut
stperiods=floor(L/(1/f1/dt1));% number of steady periods
if L-ceil(1/f1.*10/dt1)<=0
    disp('force less than 10 steady periods') ;err=-1;
    return;
else
    err=1;
end
if L-ceil(1/f1.*10/dt2)<=0
    disp('disp less than 10 steady periods') ;err=-1;
    return;
else
    err=1;
end
hold off
figure(6)
h(2)=plot(t2,y2,'color','k','LineStyle','-');
ylabel('$y/D$','Interpreter','LaTex','FontSize',20)
xlabel('$tf_{n}$','Interpreter','LaTex','FontSize',20)
axr = gca;axr.YColor = 'k';%set color of yaxis
hold off
if ~exist('ylimthl','var') || isempty(ylimthl); else; yyaxis left;
    ylim(ylimthl); end
if ~exist('ylimthr','var') || isempty(ylimthr); else; yyaxis right;
    ylim(ylimthr); end
if ~exist('f1','var') || isempty(f1)
else
    temp=['$f_1/f_n=',num2str(f1),'$'];
    hl = legend(['$Y_2/D$\ \ \ ',temp]);
    set(hl,'Interpreter','latex','FontSize',15)
end
if ~exist('ttl','var') || isempty(ttl); else; title(ttl); end
if ~exist('pdir','var') || isempty(pdir); else; cd(pdir);
    printpdf(gcf,[pname,'_',note2,'_Disp_Only_Time_history_all_used.
    eps']);
    saveas(gcf,[pname,'_',note2,'_Disp_Only_Time_history_all_used.fig
    '])
end
figure(7)
cphs=0;
```

```
[f, P1]=fftzp2(t1,y1);
plot(f,P1,'color','black')
xlim([0 3.7]);
if ~exist('ylimfft','var') || isempty(ylimfftl)
else
    ylim(ylimfftl);
end
if ~exist('ttl','var') || isempty(ttl)
else
    title(ttl);
end
xlabel('$f_2/f_n$','Interpreter','LaTex','FontSize',20)
ylabel('$C_{AY2}$','Interpreter','LaTex','FontSize',20);
hold on
yyaxis right
yphs=0;
[f, P1]=fftzp2(t2,y2);plot(f,P1,'color','r','LineStyle','--');
xlim([0 xlimax]);
if ~exist('ylimfftr','var') || isempty(ylimfftr)
else
    ylim(ylimfftr);
end
axr = gca;axr.YColor = 'k';%set color of yaxis
if ~exist('f1','var') || isempty(f1)
else
    temp=['$f_1/f_n=',num2str(f1),'$'];
    hl = legend(['$C_{Y2}$ ',temp],['$Y_2/D$\ \ \ ',temp]);
    set(hl,'Interpreter','latex','FontSize',15)
end
xlabel('$f/f_n$','Interpreter','LaTex','FontSize',20)
ylabel('$A/D$','Interpreter','LaTex','FontSize',20);
if ~exist('pdir','var') || isempty(pdir)
else
    cd(pdir)
    printpdf(gcf,[pname,'_',note1,'_FFT_.eps']);
end
end
```

Listing A.1 Mini MATLAB programme used to process simulation data into figures for time histories and amplitude spectra

A.2 Mesh Generation by Gmsh

The following Gmsh script was used to generate the structured and unstructured mesh used for simulations.

```
Mesh.ColorCarousel=2;

//input
G=2.5;//clear gap ratio
length=30;//length*2=computational domain boundary length
rt2=0.08;//mesh size around smaller square
ref80=1.8;//mesh size on far square boundaries 3.0

Spc_sixth_cylinder=28;//Spc_sixth_cylinder*6=total transfinite around
    one cylinder
Pr=1.065;//radiate lines progression rate
Spr=54;//radiate lines transfinite num

scale=G*1.2; //enlarge factor for smaller square

Spc=Spc_sixth_cylinder*2;
Cy=G/2+0.5;
ms=0.0001;//reference element size 0.3 (useless as it is overwritten)
sq2d4=0.35355339059327376220042218105242;

dx=0.25;
dy=0.43301270189221932338186158537647;
dx2=Cy/1.7320508075688772935274463415059;
dy3=0.81649658092772603273242802490196*Cy;


//Point(36) = {-0.4, 0, 0, 0.001};//local refinement

//square boundary
Point(1) = {-length, length, 0, ref80};
Point(2) = {length, length, 0, ref80};
Point(3) = {length, -length, 0, ref80};
Point(4) = {-length, -length, 0, ref80};
Line(1) = {1, 2};
Line(2) = {2, 3};
Line(3) = {3, 4};
Line(4) = {4, 1};

//Cylinders
```

```
Point(5) = {0, 0.5+G/2, 0, 1.0};
Point(6) = {0, -0.5-G/2, 0, 1.0};

Point(7) = {-dx, Cy+dy, 0, 1.0};
Point(8) = {dx, Cy+dy, 0, 1.0};
Point(9) = {dx, Cy-dy, 0, 1.0};
Point(10) = {-dx, Cy-dy, 0, 1.0};

Point(11) = {-dx, -Cy-dy, 0, 1.0};
Point(12) = {dx, -Cy-dy, 0, 1.0};
Point(13) = {dx, -Cy+dy, 0, 1.0};
Point(14) = {-dx, -Cy+dy, 0, 1.0};

Circle(15) = {7,5,8};
Circle(16) = {8,5,9};
Circle(17) = {9,5,10};
Circle(18) = {10,5,7};
Circle(19) = {14, 6, 13};
Circle(20) = {13, 6, 12};

Circle(21) = {12, 6, 11};
Circle(22) = {11, 6, 14};

//small block around cylinder
Point(23) = {dx2, 2*Cy, 0, ms};
Point(24) = {-dx2, 2*Cy, 0, ms};
Point(25) = {-dx2, 0, 0, ms};
Point(26) = {dx2, 0, 0, ms};

Point(27) = {dx2, -2*Cy, 0, ms};
Point(28) = {-dx2, -2*Cy, 0, ms};
//Point(29) = {-1.5, 0, 0, ms};
//Point(30) = {1.5, 0, 0, ms};

//Line(23) = {25, 24};
Circle(23) = {25, 5, 24};
//Line(24) = {24, 23};
Circle(24) = {24, 5, 23};
//Line(25) = {23, 26};
Circle(25) = {23, 5, 26};
Line(26) = {26, 25};
//Line(28) = {25, 28};
Circle(28) = {25, 6, 28};
//Line(29) = {28, 27};
```

```
Circle(29) = {28, 6, 27};
//Line(30) = {27, 26};
Circle(30) = {27, 6, 26};
Line(31) = {7, 24};
Line(32) = {10, 25};
Line(33) = {9, 26};
Line(34) = {8, 23};
Line(35) = {14, 25};
Line(36) = {13, 26};
Line(37) = {12, 27};
Line(38) = {11, 28};

//block lines tran
Transfinite Line {23, 24, 25, 28, 29, 30} = Spc Using Progression 1;
//Cylinder lines
Transfinite Line {22, 20, 21, 18, 16, 15} = Spc Using Progression 1;
//radient lines tran
Transfinite Line {32, 31, 34, 33, 35, 36, 38, 37} = Spr Using
   Progression Pr;
//edit
Transfinite Line {21,29,15,24,19,26,17} = Spc_sixth_cylinder Using
   Progression 1;

Line Loop(39) = {38, 29, -37, 21};
Plane Surface(40) = {39};
Line Loop(41) = {20, 37, 30, -36};
Plane Surface(42) = {41};
Line Loop(43) = {19, 36, 26, -35};
Plane Surface(44) = {43};
Line Loop(45) = {22, 35, 28, -38};
Plane Surface(46) = {45};
Line Loop(47) = {17, 32, -26, -33};
Plane Surface(48) = {47};
Line Loop(49) = {16, 33, -25, -34};
Plane Surface(50) = {49};
Line Loop(51) = {15, 34, -24, -31};
Plane Surface(52) = {51};
Line Loop(53) = {18, 31, -23, -32};
Plane Surface(54) = {53};

Recombine Surface {54, 52, 50, 48, 44, 46, 42, 40};

Transfinite Surface {48};
Transfinite Surface {50};
```

```
Transfinite Surface {52};
Transfinite Surface {54};

Transfinite Surface {40};
Transfinite Surface {42};
Transfinite Surface {44};
Transfinite Surface {46};

Line Loop(79) = {55, 56, 57, 58};
Line Loop(80) = {24, 25, -30, -29, -28, 23};
Plane Surface(81) = {79, 80};
Line Loop(82) = {1, 2, 3, 4};
Plane Surface(83) = {80, 82};

Recombine Surface {83};
Coherence;

//refinement around the cylinders
Point(84) = {-scale, (Cy+scale), 0, rt2};
Point(85) = {scale, (Cy+scale), 0, rt2};
Point(86) = {-scale, -(Cy+scale), 0, rt2};
Point(87) = {scale, -(Cy+scale), 0, rt2};

//+
Line(88) = {84, 85};
Line(89) = {85, 87};
Line(90) = {87, 86};
Line(91) = {86, 84};

Line{88} In Surface{83};
Line{89} In Surface{83};
Line{90} In Surface{83};
Line{91} In Surface{83};

Coherence;

//Boundary Condition
Physical Line("Cylinder 1", 2) = {19,20,21,22} ;
Physical Line("Cylinder 2", 3) = {15,16,17,18} ;
Physical Line("Outer Wall", 4) = {1,2,3,4} ;

//Mesh nodes
```

```
167 Physical Surface("Main mesh", 1 ) = {83, 46, 40, 42, 44, 48, 50, 54,
      52};
```

Listing A.2 Mini MATLAB programme used to process simulation data into figures for time histories and amplitude spectra